STRUCTURAL AND MAGNETIC PROPERTIES OF ULTRATHIN EPITAXIAL NICKEL FILMS GROWN ON IRON (001) SURFACES

by

Stephen Thomas Purcell
B.Sc.(Physics), Dalhousie University, 1978
M.Sc., University of British Columbia, 1982

A THESIS SUBMITTED IN PARTIAL FULFILLMENT OF
THE REQUIREMENTS FOR THE DEGREE OF
DOCTOR OF PHILOSOPHY
in the Department
of
Physics

SIMON FRASER UNIVERSITY
March 1989

APPROVAL

Name: Stephen Thomas Purcell

Degree: Doctor of Philosophy

Title of Thesis: Structural and Magnetic Properties of Ultrathin Epitaxial Nickel Films Grown on Iron (001) Surfaces

Examining Committee:

Chairman: E. D. Crozier

A. S. Arrott
Senior Supervisor

B. Heinrich

G. Kirczenow

J.F. Cochran

B.T. Jonker
External Examiner
Naval Research Laboratory, Washington, D.C.

Date Approved: March 9, 1989

PARTIAL COPYRIGHT LICENSE

Title of Thesis/Project/Extended Essay

Structural and Magnetic Properties of
Ultrathin Epitaxial Nickel Films Grown on
Iron (001) Surfaces

Author:
(signature)

STEPHEN PURCELL
(name)

Mar 16, 89.
(date)

ABSTRACT

Ultrathin epitaxial films of Ni were grown by Molecular Beam Epitaxy (MBE) on Fe (001) single crystals and on ultrathin epitaxial Fe (001) films that were grown on Ag (001) single crystals. The growths were monitored by means of reflection high energy electron diffraction (RHEED), X-ray photoelectron spectroscopy and Auger electron spectroscopy. The Ni grew in the body-centered-cubic (bcc) structure for the first 3 to 6 monolayers (ML) and then reconstructed into a more complicated phase for larger Ni thicknesses. Only face-centered-cubic (fcc) Ni exists in nature and hence bcc Ni is a new phase synthesized by MBE.

The magnetic effects of the Ni overlayers were studied using Ferromagnetic Resonance (FMR). The Ni on bulk Fe created an effective pinning of the magnetization at the Ni/Fe interface which perturbs the Fe resonance. The full theory of FMR in ferromagnetic metals was used to extract the Ni magnetic parameters as a function of the Ni film thickness. In the ultrathin Ni/Fe films (bilayers) on Ag (001) the directions of the Ni and Fe magnetizations were strongly coupled by interface exchange and this formed a new magnetic material. The theory of FMR for exchange-coupled bilayers in the limit of the film thickness being much smaller than the microwave skin depth is presented. It is shown that for strongly exchange-coupled bilayers the magnetic properties are given by a linear combination of the magnetic properties of the individual layers. The coefficients for each layer are given by the product of the magnetic moment per atom and the number of monolayers in that layer divided by the total moment of the bilayer. The bilayer theory and the known magnetic parameters of the Fe layers were used to determine the Ni magnetic parameters.

The pure bcc Ni overlayers had only small effects on the FMR. Reconstructed Ni overlayers created a large 4-fold in-plane magnetic anisotropy with the easy axis along the Fe [100] crystallographic direction. The anisotropy was ten to twenty times larger then the bulk fcc Ni. The anisotropy was studied as a function of thickness and temperature for the Ni films grown on the bulk Fe single crystals. The anisotropy started to increase rapidly with thickness at ~ 15 Å and then saturated at ~35 Å. The anisotropy was found to be approximately three times larger at 77 K than at room temperature. The 4-fold anisotropy scaled with layer thickness in agreement with the theory. Its value could be controlled by the appropriate choice of the individual layer thicknesses. These large 4-fold in-plane anisotropies are exceptional in 3-d transition metals. It is shown by detailed FMR studies that they are a result of dislocations created during the Ni lattice reconstruction.

Oscillations in RHEED intensity were discovered to accompany the epitaxial growth of metals; such RHEED oscillations have been studied in connection with the growth by MBE of semiconductors. The period of oscillations is equal to the time of formation of a single monolayer and is the result of the necessary roughening of the surface at partial monolayer filling. The oscillations were studied as a function of the angle of incidence of the electron beam and the substrate temperature to check the predictions of simple two layer kinematic scattering.

Acknowledgements

The work reported in this thesis is very much the result of a collaborative effort by our research group. I gratefully acknowledge the guidance and assistance of my supervisors Anthony Arrott and Bret Heinrich. They provided the research facilities and the major goals of the projects and spent many long hours working on the experiments. It has been a pleasure, an honour and an educational experience to have worked with them.

I received a lot of help from other members of the group as well. Ken Urquhart participated in the experiments and also provided invaluable computer assistance. Jeff Rudd helped me a great deal with the theory and practice of ferromagnetic resonance. I thank John Cochran for the use of his ferromagnetic resonance apparatus and computer programs and for a careful reading of this manuscript. Ken Myrtle built a lot of the apparatus and helped maintain and expand the MBE system. Neal Alberding analysed the data from the REELFS studies. also thank Don Hunter and John Dutcher for valuable disscussions and Xuanzeng Li for growing the Fe whiskers.

TABLES OF CONTENTS

LIST OF TABLES

LIST OF FIGURES

List of Abbreviations used in the Text

AES - Auger electron spectroscopy

bcc - body-centered cubic

CMA - Cylindrical Mirror Analyser

EXAFS - extended X-ray absorption fine structure

fcc - face-centered cubic

FMAR - ferromagnetic antiresonance

FMR - ferromagnetic resonance

MBE - molecular beam epitaxy

ML - monolayer

n.n.d. - nearest neighbour distance

REELFS - reflection electron energy loss fine structure spectroscopy

RHEED - reflection high energy electron diffraction

UHV - ultra high vacuum

XPS - X-ray photoelectron spectroscopy

Chapter 1

Introduction

The study of the structure and magnetic properties of surfaces and ultrathin epitaxial layers is new and exciting [1.1]. (Epitaxial growth refers to the oriented growth of one crystal upon another.) Researchers have been examining magnetic thin films (usually polycrystalline and several thousands of Å thick) for some time, but only since about 1980 have they begun to use the methods of ultra high vacuum (UHV) and molecular beam epitaxy (MBE) technologies to prepare clean surfaces and well defined magnetic single crystal overlayers. These samples can now be more easily linked to calculations based on fundamental models of surface band structures [1.2]. This closer connection between experiment and theory has been one driving force behind the increase in surface magnetism research. Another has been the realization that materials with new structures may be fabricated by using the substrate lattice to define the initial growth of the overlayer, and these materials may have new magnetic properties [1.3].

In this thesis we describe studies of the structural and magnetic properties of ultrathin epitaxial Ni layers grown on the (001) face of Fe single crystals and epitaxial Ni/Fe bilayers grown on Ag (001). A chronological sketch of the work our group has done is useful in understanding how the experiments fit together. Dr. Heinrich proposed that ferromagnetic overlayers on Fe (001) single crystals could be studied by ferromagnetic resonance (FMR) because of the relative sharpness of the Fe resonance. The resonance would be sensitive to exchange interactions between substrate and overlayer. Also, Ni would be an interesting overlayer on Fe because its density is close to Fe and it might be possible to synthesize body centered cubic nickel, which does not occur in nature. The samples would be interesting from three points of view: (1) would the Fe substrate resonance be sensitive to the overlayer magnetic properties? (2) could bcc Ni be synthesized? and (3) what would be its magnetic properties?

The initial growths of Ni on bulk Fe were monitored by in-situ reflection high energy electron diffraction (RHEED) (see sections 3.3-3.5) and showed that the Ni indeed maintained the in-plane structure of the bcc Fe substrate for the initial growth stages (3-6 monolayers). At thicker coverages faint superlattice streaks became visible which were more noticeable at other than principal azimuthal diffraction angles. The intensity of the superlattice streaks increased with coverage but the main bcc diffraction spots always remained. We termed the thicker layers as "reconstructed bcc Ni" and referred to the thinner layers as pure bcc Ni.

The next step was to verify that the FMR of the Fe substrate was sensitive to the Ni overlayers. As most of the FMR measurements were to be done outside of vacuum where large fields were available, the samples were covered with Au to protect them from oxidation. An in-situ 9.5 GHz FMR apparatus [1.4] was used to measure the effect of the Au overlayer. These measurments showed that the Au overlayers h`ad no discernible effects on the resonance. Strong shifts and splittings of the Fe resonance were observed for a reconstructed 60 Å Ni overlayer. After this initial success we began the hard work needed to improve sample preparation both in and out of the vacuum, and to characterise more carefully the crystal structure and to measure the magnetic properties.

To a first approximation, RHEED is sensitive to the first few layers only. During Ni growth we observed diffraction patterns corresponding to cubic in-plane coordination, but with definite features of a roughened or 3 dimensional growth. The current level of understanding of RHEED is not sufficient to relate quantitatively the three dimensional nature of the RHEED patterns to surface roughness. To determine if Ni grows layer by layer, we studied Auger and X-ray photoelectron spectra of the Fe substrate and Ni overlayer at increments in the growth (see section 3.6). The intensities followed simple exponentials as a function of thickness of the overlayer. The exponentials were fitted with parameters that show the films grew uniformly with little interdiffusion or clumping of the overlayers.

RHEED analyzes mostly the in-plane film structure. To study structure averaging over the perpendicular direction as well, we employed the relatively new method of reflection electron energy loss fine structure [1.5] (REELFS, see section 3.7). In principle this gives interatomic distances similar to extended X-ray absorption fine structure (EXAFS), except that it uses electrons instead of x-rays. In practice we could determine only the first nearest neighbour distance (n.n.d.). The bulk n.n.d. in fcc Ni is 2.49 Å and in bcc Fe it is 2.48 Å. We found the same n.n.d. in the thick Ni overlayers as in bcc Fe and fcc Ni, within experimental uncertainty.

To find the magnetic parameters of the overlayers (saturation magnetization, exchange, anisotropy constants and Gilbert damping parameter) the theory of a ferromagnetic overlayer coupled to a ferromagnetic substrate had to be worked out. This was done in a paper by Cochran, Heinrich and Arrott [1.6] that serves as a basis for interpreting the Ni on bulk Fe results. When the FMR data for a 60 Å reconstructed overlayer was analyzed by fitting the experimental lineshapes to lineshapes calculated using a computer program based on the analysis in the paper, we found the values of cubic magnetocrystalline anisotropy to be ~10 times the bulk values of fcc Ni [1.7-8]. The other parameters were not uniquely determined because combinations of them have similiar effects on the curve fitting.

At this time we installed a photomultiplier to record the intensity of the specular diffraction spot during growth of Ni on Fe to see if the RHEED oscillations that occur during the growth semiconductors by MBE could be detected. We found that the intensity oscillates with a period corresponding to the formation of a monolayer [1.9]. Though this method had become widely used for analysis of semiconductor MBE, this was the first time oscillations had been clearly seen during metal epitaxy. The effect allows precise determination of overlayer thickness and reflects the quality of crystal growth. We also found that the oscillations decreased in both intensity and period between the third and sixth layer of growth depending on the conditions. The superlattice streaks appeared in the RHEED patterns at approximately the same layer as the RHEED oscillation amplitude and period decreased.

As an offshoot to our Ni work we studied the oscillations during metal epitaxy on various substrates including Fe whiskers. These nearly perfect single crystal surfaces make excellent substrates for MBE growths, electron diffraction studies and RHEED intensity oscillation studies [1.10]. This work contributed much to our understanding of RHEED, but most of it is to be published separately rather than to expand this thesis.

To gain confidence in the theory of FMR for overlayers, we looked for consistency in the dependence of the resonance upon sample thickness. We grew Ni overlayers of 8.5 Å, 19 Å, 35 Å and 60 Å on Fe (001) and measured FMR at microwave frequencies of 36 and 73 GHz at both room and liquid nitrogen temperatures. By scaling the effect with thickness we predicted the 8.5 Å Ni film would shift the Fe resonance by ~30 Oe to higher fields. To measure such resonance shifts we increased our precision in field and frequency calibrations and in sample positioning. We found in fact that the 10 Å Ni overlayer shifted the resonance to lower fields. Such an effect could be explained if the Ni overlayers caused a reduction in the surface pinning at the Fe surface and had a much smaller cubic magnetic anisotropy than the thicker Ni films. From curve fitting we found that the anisotropy of the films is negligible below ~10 Å and then rapidly increases to a saturated value of 10-20 times the bulk fcc value at thicknesses of 25~35 Å. The anisotropy remains relatively constant up to ~ 60 Å which were the thickest films we grew.

As a preliminary to the FMR of Ni on Fe, careful FMR measurements of the surfaces of UHV prepared bulk Fe (001) substrates were carried out. These showed that the large perpendicular uniaxial surface anisotropy found in recent work on ultrathin epitaxial Fe films [1.11-13] also exists at the surfaces of well prepared Fe single crystals [1.14]. Previous attempts by researchers over many years had failed to show the existence of this surface anisotropy, presumably because of the difficulty of preparing and characterizing good surfaces. Hence the anisotropy found for the ultrathin samples is intrinsic to the electronic properties of Fe surfaces and not the result of some structural defects from sample preparation.

The magnetic properties of Ni layers thinner than ~10 - 15 monolayers were difficult to determine because they had a relatively small effect on the bulk Fe resonance. We therefore decided to grow Ni on ultrathin Fe layers that had been grown on Ag (001) [1.15]. The magnetic properties of the thin Fe layers on Ag (001) had been previously determined by our group [1.12]. These were strongly affected by adding the ferromagnetic Ni overlayers.

We constructed a theory of FMR in a bilayer of ferromagnetic materials in two ways: firstly, by making the assumption that the Ni and Fe layers are both continuous media which are exchange-coupled at their mutual interface; secondly, by considering each monolayer of the films as if it were a collective spin with its own magnetic moment, subject to a local anisotropy and coupled by exchange to its nearest neighbour monolayers. We compared the results of the two theories and experiment (see chapter 5) to unravel the magnetic properties of the thin epitaxial Ni layers. 10 ML thick Ni overlayers are characterized by approximately 10 times the bulk fcc Ni anisotropy. This large increase in anisotropy exists in thinner Ni layers that are part of the bilayers than in the Ni layers grown on bulk Fe (001). For a 3.5 ML Ni overlayer that was a part of a bilayer, which we term pure bcc Ni, we could not extract any of the magnetic properties or even determine that these layers are magnetic.

A brief outline of the thesis is as follows. Chapter 2 contains descriptions of the MBE facility used to grow and characterise the samples, the microwave setup used to measure the FMR, and the preparation of substrates both external to the UHV system and in the UHV system. The studies of the structural properties of the epitaxial layers are described in Chapter 3 including the methods of RHEED, RHEED intensity oscillations, the measurements of Auger and X-ray photoelectron spectral line intensities as a function of overlayer thickness and REELFS. In Chapter 4 the results for Ni on bulk Fe are given. Chapter 4 contains an introduction to the theory of FMR and how the theory applies to the case of a ferromagnetic overlayer exchange-coupled to a thick ferromagnetic substrate, a presentation of the FMR measurements and an analysis of the measurements to give the magnetic properties Ni overlayers as a function of overlayer thickness. A section on the determination of the surface anisotropy at the (001) face of bulk Fe single crystals is also presented. In chapter 5 the results on Ni/Fe bilayers grown epitaxially on Ag (001) single crystals are given. Sections in chapter 5 are devoted to the FMR theory of exchange-coupled ferromagnetic bilayers in a continuum approximation, the novel treatment of the FMR theory in which each monolayer as acts a spin coupled to its nearest neighbours, the results of FMR measurements on various samples of different thicknesses and the interpretation of the FMR measurements using the theory to give the magnetic properties of the individual layers.

Chapter 2

Experimental Apparatus and Substrate Preparation

2.1 The Molecular Beam Epitaxy System

We start with an overview of the apparatus followed by brief descriptions of the working principles of the various components. A more detailed account of the MBE equipment can be found in the thesis of Chian Liu [2.1]. The epitaxial films were grown in a Physical Electronics (PHI) Model 400 MBE System originally developed for the growth of GaAs. The layout of the system is shown in Fig. 2.1. The bulk of the MBE machine is formed by two interconnected vacuum chambers, one for analysis and one for growth. The vacuum is maintained by an ion pump connected to the analysis chamber and a cryogenic pump connected to the growth chamber. The background pressure was ~(4-8)x10^{-11} Torr when no evaporation furnaces were turned on and ~5x10^{-10} Torr during evaporation.

The analysis chamber is equipped with an ion gauge for pressure measurements, a Mg-Al X-ray source and Cylindrical Mirror Analyzer (CMA) with a self contained electron gun for angular resolved Auger Electron Spectroscopy (AES) and X-ray Photoelectron Spectroscopy (XPS), and an ion sputtering gun for cleaning the substrate. It is also possible to remove the CMA and insert a 0-3 kOe magnet and a waveguide with a microwave cavity assembly for in-situ ferromagnetic resonance measurements at 9.5 GHz. Two sorption pumps are attached through valves to the analysis chamber for roughing out the system from atmospheric pressure to ~3x10^{-4} Torr before the cryogenic and ion pumps are opened.

The growth chamber contains an ion gauge, a 3-10 keV electron gun and SnO$_2$ coated phosphor screen for low angle (0-5^{o}) Reflection High Energy Electron Diffraction, a temperature controlled quartz thickness monitor for measuring film thicknesses, a tungsten heater for annealing substrates, a quadrupole mass analyzer for checking the background gases and sometimes monitoring flux and the evaporation furnaces enclosed in a liquid N$_2$ cooled shroud.

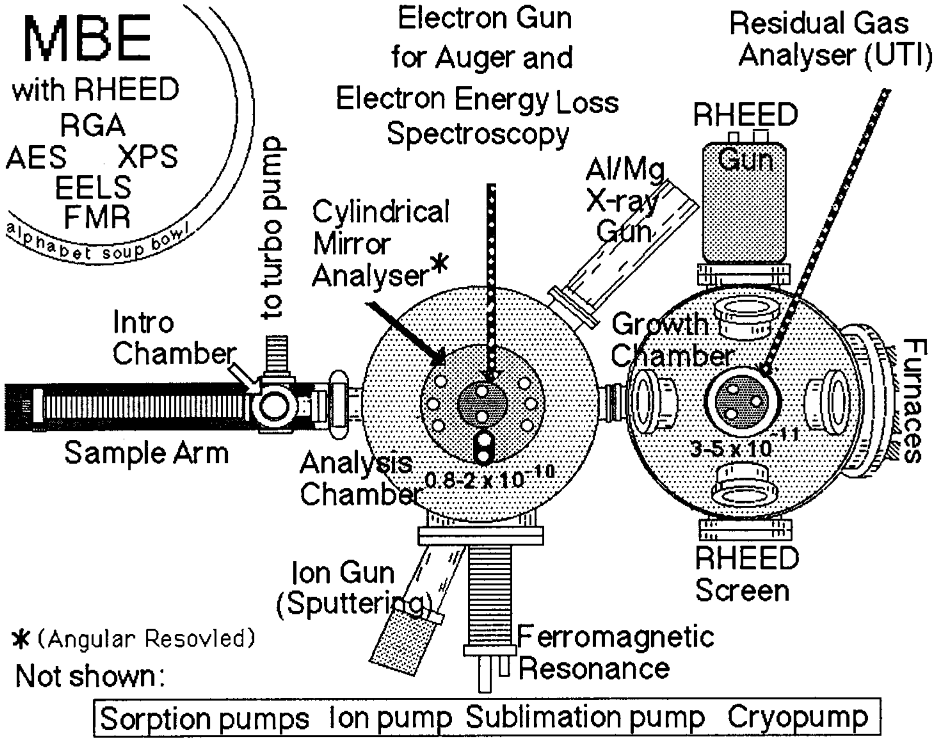

Fig 2.1 Schematic drawing of the top view of the PHI-400 MBE facility

Samples are introduced to the system via an introduction chamber which is connected by a pressure driven valve to the ultra high vacuum system. The substrates are first mounted on Mo holders which are then screwed to the manipulator end of the transfer rod in the introduction chamber. This chamber is connected to a N_2 flow line during sample mounting to reduce contamination. The long body of the transfer rod is contained within a bellows which is continuously pumped by a turbo pump. After a sample is mounted the introduction chamber is sealed and then pumped out by the turbo pump to $\sim 10^{-6}$ Torr. The transfer rod is connected to an electric motor which drives the sample into the UHV where it can be sputtered or annealed or analyzed by XPS and AES. The arm and manipulator allow the sample to be rotated about the center axis of the rod, flipped 90° to face the CMA or moved into the growth chamber for RHEED analysis and growth. The manipulator also contains a filament behind the substrate holder for annealing the substrates. Temperatures are measured by means of a thermocouple pressed loosely against the back of the substrate holder and were considered only marginally accurate. Temperatures can reach ~650-700 C with the substrate heater but higher temperatures are achievable when it is used in conjunction with the tungsten heater in the growth chamber.

The analysis and growth chambers can be covered with a heat resistant tent in which two electric heaters are also placed to heat the entire system to ~150 C. This is done after the system has been opened to atmospheric pressure (purified N_2) to desorb gases from the inner chamber walls so they can be collected by the pumps. This is termed "bakeout" and was usually done for 14 hours. It is a necessary procedure if pressures $\sim 5\times10^{-11}$ Torr are to be acheived.

The cryopump (Air Products and Chemicals, Inc. model HV-202) traps gases by adsorption on a cold trap cooled to 14-16 K. The trap is cooled by means of a Solvay cycle refrigeration system using He as the active gas. The cryopump retains all molecules except He that impinge upon its 30 cm diameter opening.

The ion pump consists of a pair of cathodes and an anode with a potential difference of 5~7 keV placed in a magnetic field (~several kOe). Electrons emitted from the cathode spiral towards the anode at high speed, ionizing molecules in their path. The positive gas ions then bombard the cathode where they form stable compounds with the metal atoms of the cathode. A titanium evaporation unit which can evaporate a titanium film from a filament is combined with the ion pump. The film getters gases such as H_2, O_2, N_2 and CO_2 at fairly poor vacuum ($>1\text{x}10^{-9}$ Torr) and is usually used during bakeout.

The sorption pumps are filled with absorbents such as 5A molecular sieve and processed oxides of Al and Si. When the absorbent is cooled by liquid N_2 it absorbs large volumes of gases due to its large surface area. The turbomolecular pump (PHI model 67 turbo pump station) is a powerful mechanical pump consisting of a high speed rotor unit (43,000 rpm) with a standard mechanical backing pump. The blades of the spinning rotor sweep the gases into the exhaust of the pump.

Both XPS and AES are used to determine the elemental and chemical composition and distribution at a sample surface. This is done using the CMA (PHI model 15-255GAR) to analyze the energy of electrons emitted from the energy levels of the substrate atoms after bombardment by electrons (AES) or by X-rays (XPS). Determination of the elements is possible because each atomic species has a unique set of energy levels. Measured spectra are compared with a set of standard spectra listed in handbooks published by PHI [2.2]. Both these techniques are sensitive to the first 5-30 Å of the surface because electrons have only a short inelastic mean free path in solids.

The CMA filters the electrons by means of an electrostatic field. The analyzer consists of two concentric cylinders that have a variable potential difference applied between them. Electrons are accepted into the entrance of the analyzer at roughly 42^{o} with respect to the axis of the analyser. Those with the selected energy will travel a curved path between the cylinders and pass through two holes, one halfway along the axis of the cylinder and one at the end of the cylinder, and then enter an electron multiplier. In AES data is collected by a lock-in amplifier with a modulation voltage applied to the outer cylinder. XPS data is collected using electron counting. The energy resolution is $\cong$ 1eV in the XPS mode depending on the choice of analyzer settings and ≅ .6% of the kinetic energy in the AES mode. Because the X-ray beam is not focused the spatial resolution in XPS is relatively poor. It is collimated to a circular analysis area of roughly 5 mm in diameter. Spatial resolution in AES is determined by the focusing of the the electron gun which has a spot ≅ .2 mm in diameter.

The Mg-Al X-ray source (PHI model 04-548) produces Kα X-rays by bombarding water-cooled Mg or Al targets with 10 keV electrons. The Mg Kα line is at 1253.6 eV with a line width of .7 eV and the Al Kα line is at 1486.6 eV with a line width of .8 eV. We usually used the Mg X-rays because of the sharper linewidth. The geometry of the gun roughly collimates the X-rays into a beam ~5 mm in diameter which is aimed at the substrate. The X-rays cause electrons to be photoemitted from energy levels with binding energy less than the X-ray energy. Thus the kinetic energy of a photoemitted electron is $E_k = h\upsilon - E_B - \phi_s$ where $h\upsilon$ is the X-ray energy, E_B is the binding energy of the electron before excitation referenced to the Fermi energy and ϕ_s is the spectrometer work function [2.2].

In AES a high energy electron beam impinges upon the sample to cause the ionization of core levels. The vacant states are then filled by the relaxation of electrons from higher energy states. The energy given up in the relaxation can be transferred to another electron (the Auger electron) which may then possess enough energy to leave the sample and hence be collected by the spectrometer (the emission of a fluorescent X-ray is a minor competing process in this energy range and it occurs less than one percent of the time). Since the energy of the ejected electron is characteristic of the parent atom it can be used to identify the composition of the solid surface. The kinetic energy of the ejected electron is given by $E_k = E_{BC} - E_{BR} - E_{BA} - \phi_s - U_{eff}$ where E_{BR}, E_{BC} and E_{BA} are the binding energies of the relaxing electron, the original core electron and the Auger electron respectively (considered positive), ϕ_s is the spectrometer work function and U_{eff} is an effective Coulomb interaction between the two final vacancy states. The origin of U_{eff} is the difference in the effective Coulomb potential between an N electron atom and the same atom having N-1 electrons.

To use the sputtering gun (PHI model 04-191) the chamber is first filled with argon to a pressure of 5×10^{-5} Torr. Argon atoms then diffuse into the ionization chamber of the gun where they are ionized by collision with electrons emitted from a filament. The ions are accelerated to energies in the range of .5-5 keV and collimated into a beam which strikes the substrate, and removes the surface contaminants. The beam can be electronically deflected to raster over approximately one square cm area of the sample. Typical rates of removal from the target are ~1 ML/min. A fresh Fe single crystal takes ~1/2 hour for initial removal of the oxide and C layers that form during ex-situ handling.

The in-situ magnet and 9.5 GHz FMR setup has been described in a paper by Heinrich, et al. It was used in this work mainly to confirm that the Au overlayers we used to protect our samples from oxidation have negligible effect on the magnetic properties of the films.

The RHEED apparatus is shown in more detail in Fig. 2.2. With this arrangement and choice of electron energy (10keV) the diffraction is sensitive only to the top few layers of the sample because of the low angles of incidence (see section 3.3). Also the diffraction can be observed during growth without interfering with the evaporation. The phosphor screen is coated with conducting SnO_2 to reduce charging from the electron beam. The angle of incidence of the electron beam can be varied from 0-5°. The focused beam spot diameter was ~.2 mm on the screen and the sample to screen distance was 30.5 cm. RHEED intensities and profiles were measured during growth similar to Van Hove, et.al. [2.3] using a microscope objective with a ~1:1 magnification to focus the screen onto a 50 μm pinhole placed between the objective and a photomultiplier. Another photomultiplier was later added so that accurate lattice spacing measurements could be made by observing two streaks simultaneously. The photomultipliers were mounted on independent micrometer driven x-y translators to locate them at diffraction features. There also was a set of Helmholtz coils to deflect the electron beam when the shapes of diffraction features were to be recorded. The deflection coils and photomultiplier tubes were interfaced with an IBM clone personal computer.

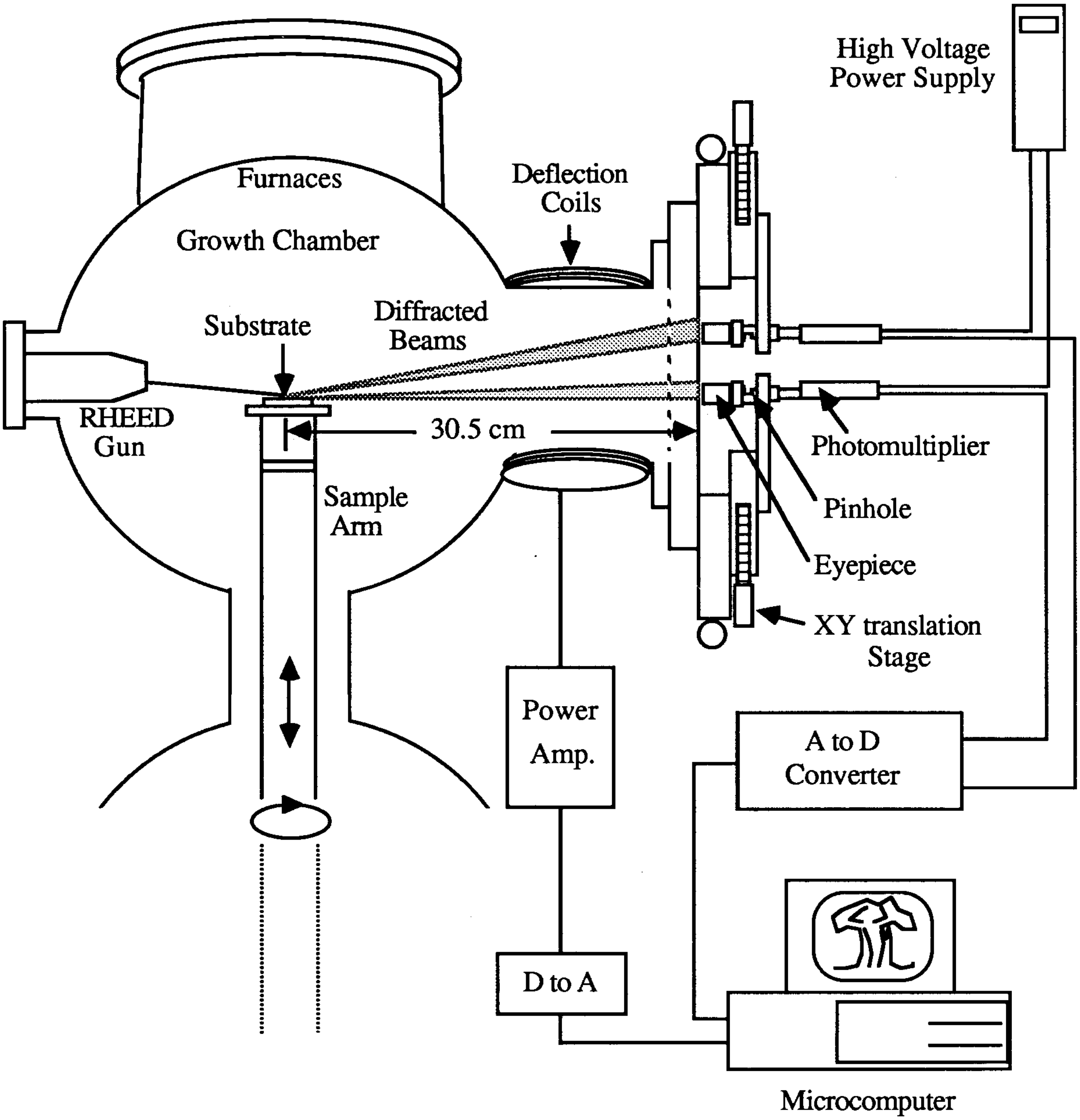

Figure 2.2 RHEED components and the photodetection system

We used a Mathis model TM-100 thickness monitor to measure film thicknesses. It used a piezoelectric quartz crystal as part of a 6 MHz resonant circuit. The crystal was placed in the atom flux that deposits on the substrates. When mass is deposited on the crystal the resonant frequency changes. This is electronically compared with a reference crystal and the frequency difference is calibrated by the manufacturer in terms of actual mass deposited. The crystal monitor is mounted on extendable bellows above the sample position for RHEED and growth. This allows the quartz crystal and furnace to be moved into and in front of the sample position respectively for calibration and annealing. Since the quartz crystal does not actually sit at the sample position during growth, the difference in the atom flux between the monitoring and the sample positions must be measured. The constant of proportionality between the two fluxes is called the "tooling factor". This was also checked against RHEED oscillations (see section 3.4). A major difficulty with the thickness monitor is that the crystal is very sensitive to temperature (~1Å/degree C at 30 C). This sensitivity was a problem in these experiments because our films were in the monolayer thickness range. Thus we controlled the temperature of the crystal monitor head with circulating water from a controlled bath. We used a Haake model 000-5713 all-in-one temperature controller and pump. It was also necessary to control the temperature of the electronics using the same bath. Because the tubes that carry water to the monitor head are only 1/8" ID the Haake pump was not strong enough to deliver a fast water flow. Thus an industrial pump was added in parallel. This pump in turn generated heat and had to be cooled from tap water. The water that passes through the auxiliary pump was then colder than the bath and had to be heat exchanged with the bath before traveling to the monitor head. One incidental advantage of this system was that it controlled the temperature of the monitor head if the room temperature was below or above the bath temperature since the cooled auxiliary pump always provided cold water to the bath through the heat exchanger. Temperature stabilization removed the drifts in the monitor reading due to the quartz crystal temperature except for varying heat loads to the front surface of the crystal. Cooling the cryo shrouds that surrounded the furnaces or opening the furnace shutters when the furnaces were heated also caused changes in the thickness reading. Cooling the cryo shroud caused a 2-3 Å decrease in the thickness monitor (TM) reading, and which requires roughly 1.5 hours to stabilize. When a furnace shutter was opened (or closed) there was a 1-2 Å decrease (increase) in the reading due to the radiation from the furnaces. The thickness monitor absorbed heat during the growth which also causeed an increasing offset in TM reading of the order of 1-3 Å depending on the duration of the growth. This also required ~1-1.5 hours before a constant reading was reached. The procedure used to obtain accurate thickness measurements was: (1) cool the cryo shrouds for ~1.5 hours until the TM reading stabilized; (2) record the TM reading just before growth; (3) grow sample; (4) wait ~.5 - 1.5 hours after growth, depending on the duration of the growth, for reading to settle with the cryo shields still cooled. Using this procedure, thickness readings agreed to ±1/8 monolayer with the thicknesses determined from RHEED oscillations.

Two types of evaporation furnaces were used. Fe and Ni were evaporated from resisitively heated tungsten filaments and Au and Ag were evaporated from boron nitride crucibles which were heated by tungsten coils enclosing the crucibles. The boron nitride furnaces were purchased from PHI (model 04-410). The filament furnaces are shown in Fig. 2.3. Fine wires of Ni (.25 mm) and Fe (.5 mm) were wound around .5 mm tungsten wire which was then bent into shape and spot welded to tungsten support posts. The filament furnaces were used for Fe and Ni because the boron nitride crucibles gave off N_2 at the high temperatures necessary to evaporate these metals. About 80 watts of power was run through a furnace for a typical evaporation and this yielded growth rates at the substrate of about 1 Å/min. The furnaces were equipped with electrically controlled air-driven shutters which can initiate or terminate the growth in a fraction of a second. Because we grew our samples at rates of about one monolayer per minute the shutters could be used to control the deposition to better than .01 Å.

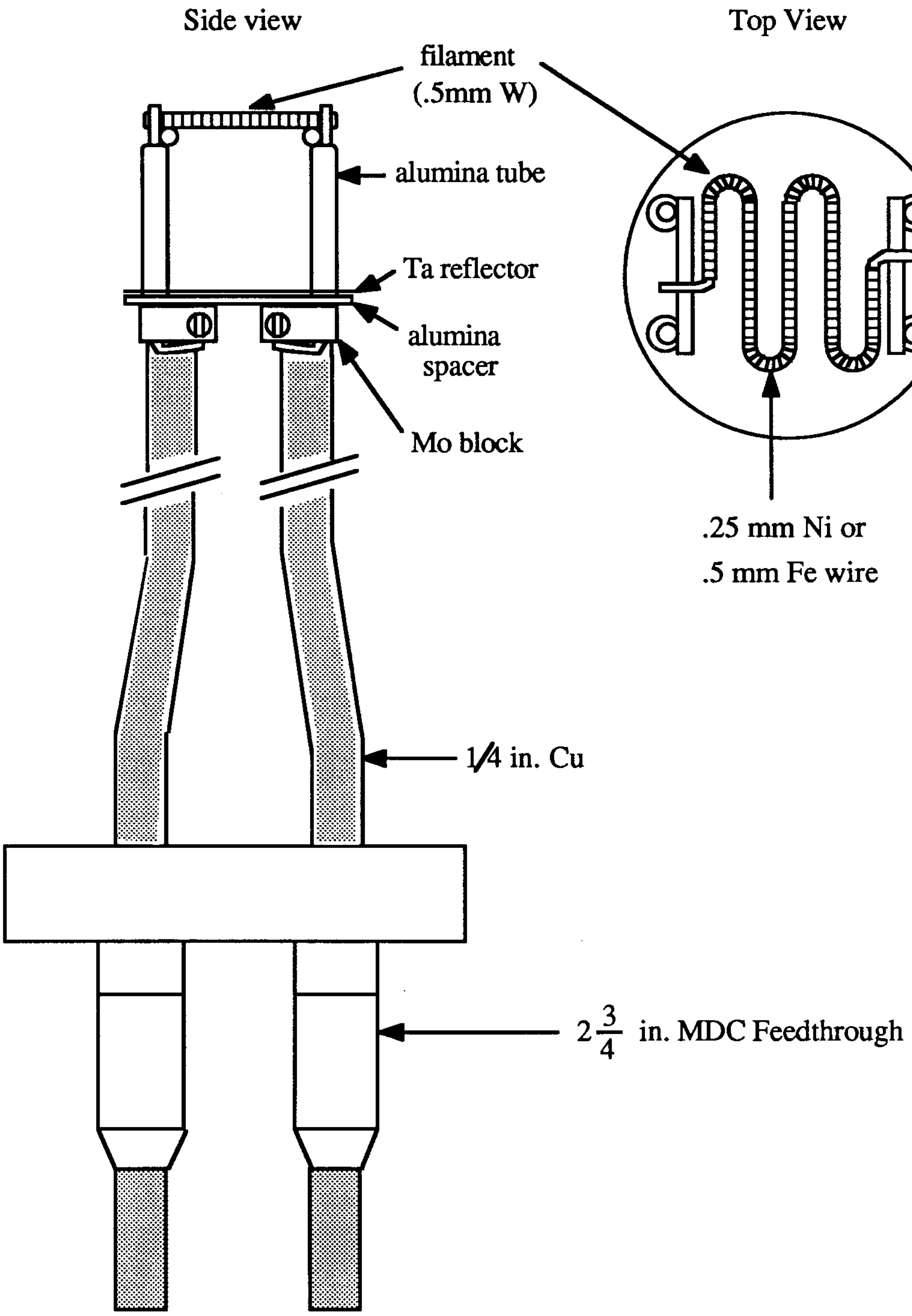

Fig. 2.3 Tungsten Filament furnace used for evaporating Ni or Fe

2.2 Ferromagnetic Resonance Apparatus

The 73 GHz FMR setup is shown in Fig. 2.4. Similar setups that ran at 36.6, 24.0 and 9.5 GHz were used for some of the experiments. Microwaves are generated by the klystron and pass into the waveguide. They pass through an isolator which prevents microwaves from reflecting back into the klystron, a variable attenuator and then a three port circulator which routes the waves down to the cavity. The cavity resonates in the cylindrical TE_{01n} mode (the "doughnut mode") and is tuned to resonate at the frequency at which the klystron power output is a maximum. The cavity is equipped with a tuning rod to change its length and hence the resonant frequency. Because the cavity is a resonant circuit the microwave magnetic field at the sample is much larger than that generated by the klystron. The cavity is coupled to reflect ~10-50% of the incident microwave amplitude; enough so that the sensing diode responds to amplitude rather than power. A sample forms the endwall of the cavity. At FMR the sample absorption increases and as a result causes a small change in the reflectivity of the cavity. We measure this change in reflectivity to observe FMR. The reflected microwaves are routed by means of the circulator to a frequency meter and two point contact diodes (1N53B). The diodes convert the microwaves into a DC signal. We use phase sensitive detection to improve the signal to noise ratio. This is done by modulating the applied magnetic field at 130 Hz. Also we use the output from the stabilzation diode to lock the klystron frequency to the cavity resonant frequency by modulating the klystron reflector voltage at a frequency of ~70 kHz.

A glass Dewar fits over the cavity for low temperature measurements. The cavity is filled with He gas to prevent condensation on the sample. The teflon seal shown in the Fig. 2.4. isolates the cavity end of the waveguide from the atmosphere.

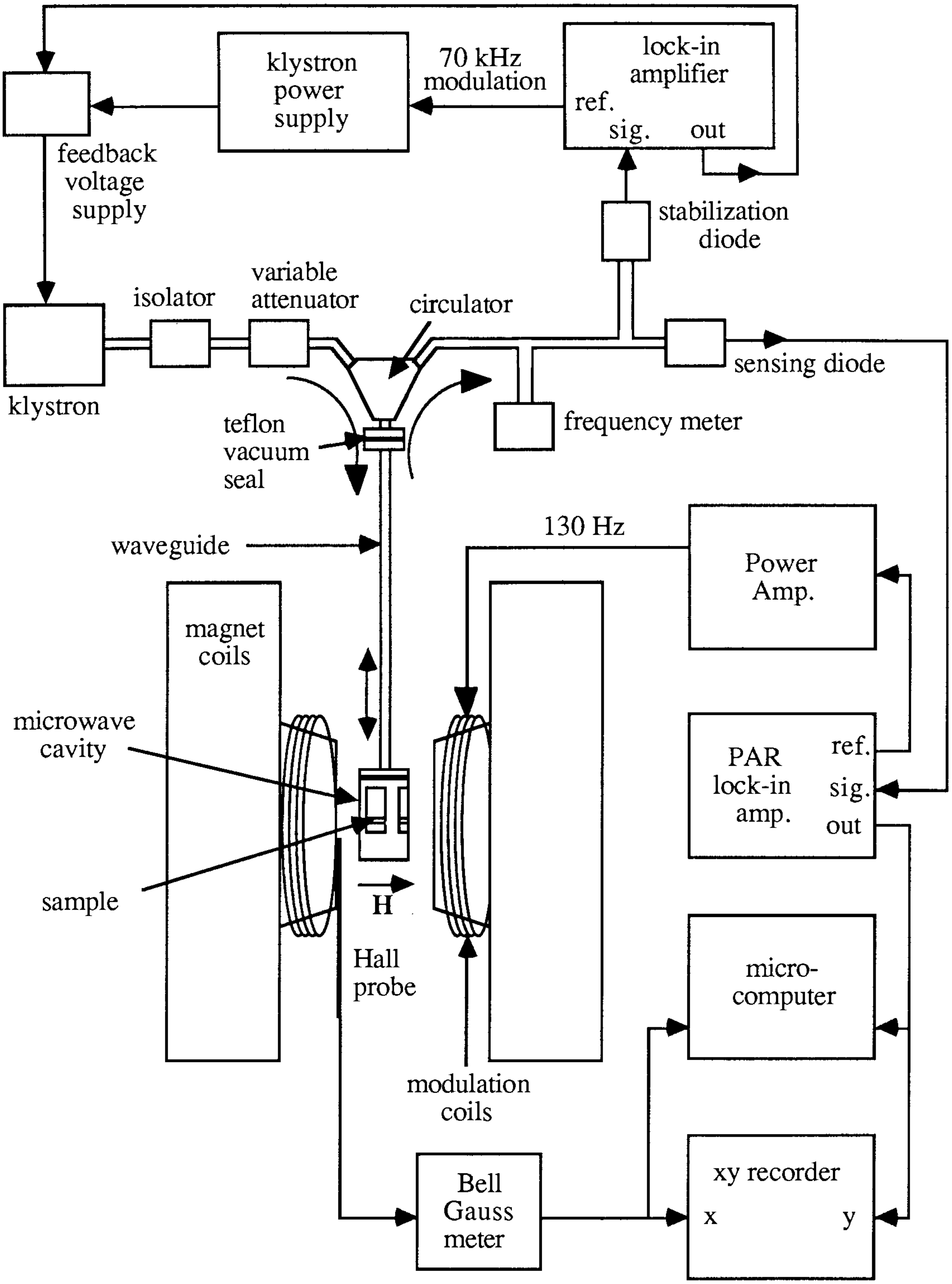

Fig. 2.4 73 GHz Ferromagnetic resonance system with a donut cavity, phase sensitive detection and klystron frequency stabilization.

2.3 Substrate Preparation

The Ni overlayers were grown on the (001) faces of various Fe and Ag single crystals which have approximately the same square surface lattice spacing (2.867 Å for Fe and 2.889Å for Ag). Disk-shaped Fe and Ag substrates were used for growth and FMR studies. Fe single crystal "whiskers" were used as near ideal substrates for growth studies. A few growths were carried out on a Ru (0001) single crystal and a Ni (001) single crystal. The disk-shaped substrates are listed and described in Table 1.

Table 1: Substrates used in MBE and FMR experiments

Sample	Diameter mm	Thickness mm	Misorientation deg	Mosaic deg	Final external polish
Fe (001) 1	13	.35	<.5	<.5	colloidal silica
Fe (001) 2	18	.25	~2	~1	"
Fe (001) 3	18	.7	2.7±.2	~1	"
Ag (001) 1	15	3.	~2	~1	electropolish
Ag (001) 2	15	3.	<.2	<.5	"
Ru (0001)	7	1.	~2	~2	3 micron diamond on cloth
Ni (001)	20	1.	1	<.5	H_2SO_4 based electropolish

The Fe disks were cut from single crystal plates grown by means of strain-anneal [2.4]. The misorientations of Fe samples 2 and 3 were set by the plates from which they were cut. By reducing the diameter of Fe sample 1, accurate alignment of the (001) axis with the crystal normal was possible. The sample was mounted on a polishing jig which had accurate sample tilting capability and can in turn be mounted on the Laue camara. To align the (001) direction of the sample to better than .2° with respect to the x-ray beam, Laue photos were taken with different rotations of the jig in the X-ray goniometer. This removed error due to misalignment of the Laue camara. Also the sample to film distance was increased to 10 cm to increase the angular resolution of the photos. The degree of misalignment was then determined by the accuracy with which the Laue photos could be marked and by the mosaic spread. Careful alignment was important because it determines the average terrace length on the growth surface (~60 atoms at 1° and 300 atoms at .2°).

After X-ray alignment, the Fe samples were rough polished on 600 grit sandpaper, then polished with 6 μm and 1 μm diamond paste on soft tin plates using a turntable type polishing machine. There was a spiral groove in each of the plates, ~1/2 mm wide and 1 mm spacing, that collected particles pushed from the polishing surface. In principle this feature reduced scratching. The bottom surface of the jig was an annular-shaped hardened steel polishing plate that acted as a conditioning ring. After the diamond paste was applied to the plate, the jig was mounted and run for ~1 hour with the sample raised to condition the polishing surface. The advantage of this type of jig was that the sample was already mounted during the conditioning stage and was then simply lowered to the polishing surface by adjustment of the jig. The next polishing stages used 3 μm and 1 μm diamonds on a soft felt pad. It is important to use high quality soft pads. We used Microcloth pads from Buehler. The pads were conditioned for ~1/2 hour after application of the diamond paste before the sample was lowered. If this is not done a large number of diamonds can become imbedded in the Fe. Approximately 20 to 30 min polishing at each step produced progressively shinier mirror surfaces and removed all the damage from the previous polish. No scratching was visible to the eye after the 1 μm step, but fine scratches as well as many small pits were visible under 400x magnification particularly if oblique illumination was used. We used a scanning Auger microprobe to show that the pits contained O_2. We believe that they were Fe oxide conglomerates that formed during bulk crystal growth. However they cover only a small percentage of the surface. The samples were given a final polish using a commercial technique developed for Si wafers. The polishing agent was a colloidal silica slurry from RODEL Products applied to their adhesive backed Politex pads. The average particle size was 50-70 nm. The sample was polished for 2-6 min with several checks using the microscope to watch for the disappearance of scratches. If polished too long a fine grain etching occurs. The best polish balances the removal of final scratching with the onset of etching. A final 30 sec polish with distilled water was used to remove a buildup of colloidal silica near the edges of the samples. Because the samples were polished only lightly on the cloth pads they were rounded only minimally on the edges. A standard Fe chemical polish consisting of 47 ml distilled H_2O, 5 ml HNO_3 (48%) and 80 ml H_2O_2 (50%) [2.5] was also used. Though it produced a brighter surface and a superior finish at 400x magnification it always lead to macroscopic etching and an "orange peel" surface. Which final polish produced the best surface for MBE and FMR work is not clear, but we chose the colloidal silica as our standard. The quality of the polish is indicated by the RHEED streaks and FMR lines being as narrow as any we or anyone else had obtained for bulk crystals.

The Fe whiskers were grown by the Brenner method [2.6] of flowing H_2 gas over $FeCl_2$ filled iron "boats" at 700-710 C.

Final preparation of the Fe samples takes place in the UHV. This consists of argon sputtering to remove impurities and annealing to produce flat single crystal surfaces. The surface impurity concentrations (C, O_2, S, N) were determined by means of AES and XPS with detection limits ~1%. Argon sputtering roughens the surface yet gives a clean sample. High temperature annealing (~700 C - 750 C) produces a smooth surface yet allows impurities present in the bulk Fe to diffuse to the surface. Therefore a balance is sought between surface impurities and crystal perfection. In our early work sputtering and annealing were carried out separately and left impurity levels O_2/C/Fe ~ 1/2/40 at best. The samples were sputtered for 30-60 min. at normal incidence using beam voltages of 2-5 keV and current densities of 8μA/cm^2. They were then annealed ~1/2 hr. at 500-600 C. Using 2-3 cycles did not cause improvements. Later we learned that by sputtering and annealing at the same time we could improve the surface quality. Our final preparation sequence after initial insertion of the sample consisted of a 30-40 min sputter at 8 μA/cm^2; a 30-40 min anneal at 750 C; one or two cycles of 20-30 min combined sputter-anneal at 750 C; a 30 min anneal at 750 C to get a sharp diffraction pattern; a final 2-5 min sputter to remove impurities (S,N) that diffuse to the surface during the previous anneal. The minor damage caused to the surface during by the final sputter is mostly annealed out as the sample cooled to room temperature. Final impurity levels were as low as O_2/C/Fe-1/2.5/100.

The Ag(001) substrates were 15 mm in diameter and 3.5 mm thick. They were spark cut from a single crystal boule having a mosaic spread of ≈ 20 mRad. The substrates were ground and polished mechanically before a final electropolish using a cyanide-free solution [2.7] which produced a strain-free, smooth, mirror-like surface. The Ag substrates were sputter etched using an Ar^+ ion beam at 2 keV and 8 $\mu A/cm^2$ for 30 min. The surface damage induced by ion milling was removed by annealing at 450 C in ultrahigh vacuum (low 10^{-10} Torr) for 20 min. The preparation of the Ag substrates used in our growth studies has been described in more detail elsewhere [2.8].

Chapter 3

Structural Characterization

3.1 Introduction

In this chapter we will describe experiments used to characterize the structure of the Ni films grown on Fe (001) single crystal surfaces. We will also describe more general studies of the structure of metal crystal surfaces and epitaxial films. These studies are worth reporting on their own and provide a useful introduction to the discussion of Ni on Fe. The technique we have used most is RHEED and there will be a strong emphasis on this technique in this chapter.

Section 3.2 contains a qualitative description of substrate surfaces with varying degrees of crystal perfection and a discussion of epitaxial growth at moderate temperatures. RHEED is discussed in section 3.3. This section begins with the simple single elastic scattering of a plane wave from a two dimensional lattice of points. We then introduce the finite penetration of the electron beam into the surface by including exponential damping of the wave as it enters the solid. Photographs of RHEED patterns from different surfaces are shown next with an analysis of the surface structures they represent. In section 3.4 we discuss the oscillations in RHEED intensity that occur during deposition because of the cyclic roughening and smoothing of the surface as monolayers nucleate and fillup. We show measurements made on various metal-metal epitaxial systems. In section 3.5 we describe the RHEED results on Ni on Fe. This includes photographs of RHEED patterns, RHEED oscillations and lattice spacing measurements. In section 3.6 the homogeneity of the films is discussed. This is determined by measurements of the decrease in the Auger and XPS signals from the substrate as a function of Ni thickness. Section 3.7 contains a description of the reflection electron energy loss fine structure experiments. These experiments give a measure of the local order of the Ni films. In section 3.8 the Ni film structure is discussed by summarizing the information from sections 3.5 to 3.7. In section 3.9 we discuss the growths of the Ni/Fe bilayers on Ag(001) single crystals.

3.2 Surface Structures and Epitaxial Growth

The formation of surface structure is driven by the minimization of the free energy A = E-TS where E is the potential energy, T is the temperature and S is the entropy. The extent to which surface free energy is reduced will depend on diffusion rates. In the simplest approximation the potential energy can be found by counting missing bonds. Creating a vacancy in an otherwise perfect surface increases the number of unpaired bonds and hence the potential energy. However, since the vacancy can move on the surface the configurational entropy will be increased. Formation of the surface is therefore a competition between reduction in the potential energy and an increase in the entropy. For simple metal surfaces and the low temperatures used in our experiments the potential energy is the dominant term. The free energy does not reach a global minimum but rather the atoms settle in positions of local equilibrium. The structures are metastable. The substrates generally get smoother when heated because the increased diffusion rates allow the atoms to rearrange themselves in lower energy configurations. Annealed surfaces generally consist of wide terraces separated by single atom high steps.

The substrate surfaces that are useful to visualize for this work are depicted in Figs. 3.1-3.2. The most basic and obvious one is the infinite periodic lattice. In Fig. 3.1(a) we show a simple cubic array. If this is the surface of a bcc lattice, creating a vacancy would break four nearest neighbour bonds, all from the plane below. If the atom removed from the vacancy were then placed on top of the surface it would complete four nearest neighbour bonds. Hence it is the second and further neighbour bonds that are responsible for the surface stability. A surface that is parallel to a set of low index lattice planes is termed a singular surface. A surface which is at a small angle to a principal plane is termed a vicinal surface. We work with fcc and bcc crystals cut at less than 2 degrees from the (001) planes. A vicinal surface is depicted in Fig. 3.1(b). It consists of a set of terraces separated by monolayer steps. Fig. 3.1(c) shows details of a terrace and step together with various defects. Each of the defects are held by different numbers of bonds and hence have different diffusion rates. Diffusion will

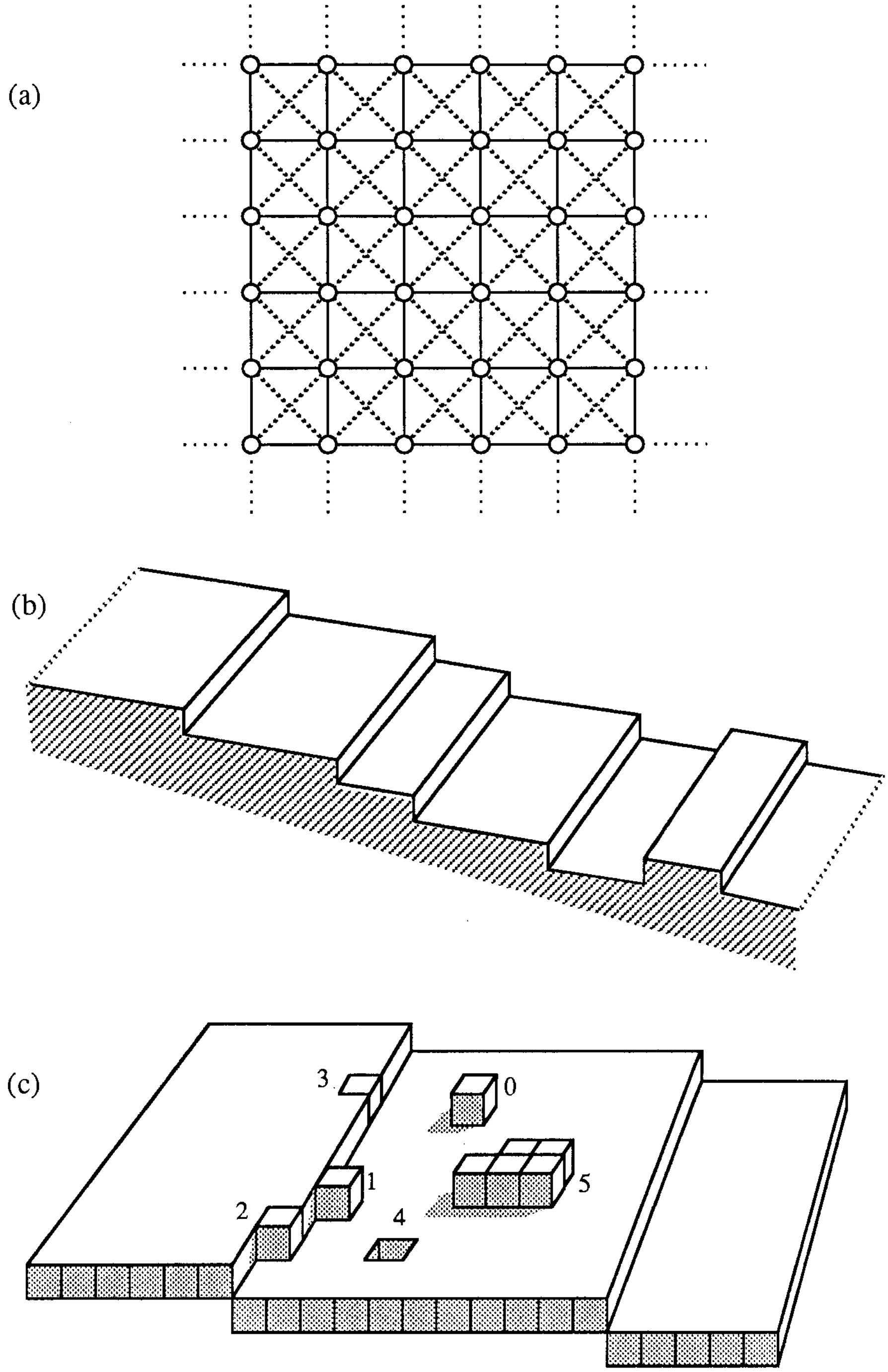

Fig. 3.1 (a) Top view of an ideal crystal surface with first and second nearest neighbour bonds.
(b) Vicinal surface showing terraces separated by somewhat randomized step faces.
(c) Different types of atomic positions with various bonding strengths

also be anisotropic because the steps will tend to trap atoms and hence atoms will move more freely parallel with the steps. Any cut and polished crystal surface will exhibit steps no matter how accurately it is cut because the polishing will introduce some waviness. However we will show evidence that the terrace width on Fe (001) whiskers can be as large as 1500-3500 Å. Besides simple terraces the surfaces can consist of multilayered interconnecting islands exhibiting varying degrees of flatness as depicted in Fig. 3.2(a) (see reference [3.1] for an excellent illustration). This configuration or surface structure is common when a sample is being annealed after sputtering, when a sample is raised to temperatures where configurational entropy is dominant, and during growth in which the surface diffusion rates are the limiting factor. These islands can assume a preferred shape depending on the symmetry, bonding and diffusion at the surface. For example, square or octagonal islands may be preferred (or not) on a cubic array. A freshly sputtered sample will be characterized by defects on a short length scale and by deep valleys as depicted in Fig. 3.2(b). The sample will tend to form small 3-dimensional islands having close-packed faces. Another common surface defect is a reconstruction as depicted in Fig 3.2(c). The surface atoms reduce the potential energy by means by slight relaxations of position. This often gives a new unit cell at the surface which is a multiple of the unreconstructed surface unit cell. This is particularly dramatic for the (001) surface of Au for which we show some RHEED data. RHEED is very sensitive to reconstructions. Surface impurities also often arrange themselves into regular arrays having a unit cell larger than the unit cell of the substrate surface. All of the above mentioned surface arrangements are formed on perfect substrate crystals. Metal single crystals grown by strain-anneal, Bridgman or Czochralski techniques contain bulk defects which we loosely label the mosaic spread. The lattices are not coherent over large distances. This is depicted schematically in Fig. 3.2(d). Large Fe single crystals cannot be grown from the melt because of the δ to γ and γ to α phase transitions so we use crystals grown by the strain-anneal technique. For some studies we use Fe single crystals whiskers which are grown by chemical vapor deposition. They are nearly perfect single crystals. Another type of defect in the Fe

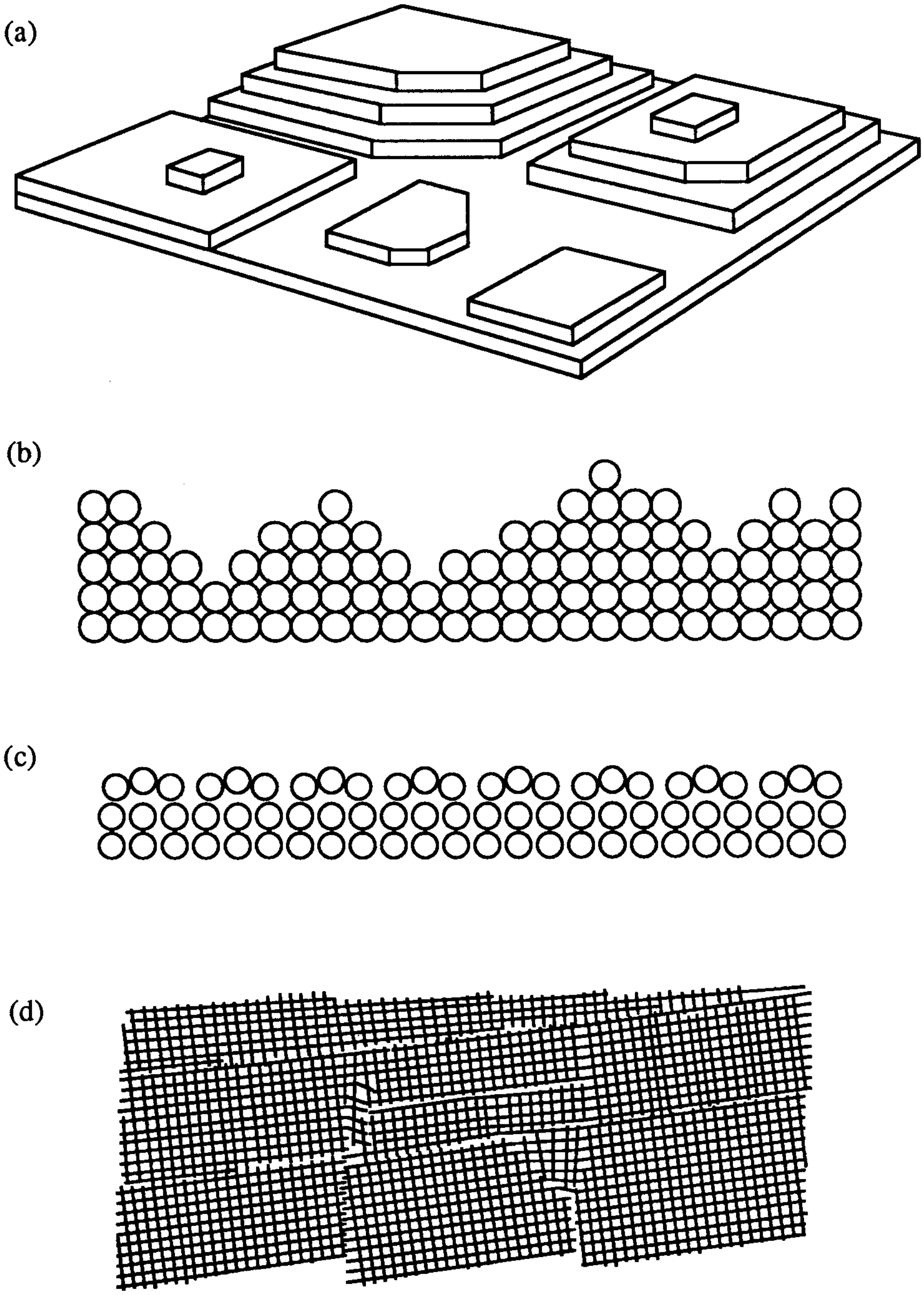

Fig. 3.2: (a) Surface with relatively large flat islands expected during uncompleted annealing; (b) Rougher surface of freshly sputtered sample; (c) Side view of simple three times surface reconstruction; (d) Artistic depiction of crystal with a mosaic spread.

crystals grown by the strain-anneal technique is the iron oxide precipitates which form during the crystal growth.

Different regimes of epitaxial growth are often loosely classified by discussing certain obvious surface parameters and processes such as the lattice misfits, the binding energies, the activation energy and the nucleation process (see [3.2-3.3]). Though such classifications are useful for providing a language in which to discuss epitaxial growth, in practice each substrate-overlayer system must be dealt with separately. We will not provide a general discussion of epitaxy but will concentrate on features pertinent to metal-metal epitaxy at moderate temperatures.

The lattice misfit is defined as the percentage difference in lattice spacings of the substrate and overlayer. Good epitaxial growth is anticipated when the overlayer and substrate lattices are well matched. Various types of lattice matching are possible. The first is when the overlayer and substrate have both similar lattice spacings and the same structure such as in the combinations Cr-Fe (bcc), Al-Ag-Au (fcc) or Ni-Cu (fcc). The lattices of these materials match on any plane. The atoms of the first layer of the overlayer will strain to adopt the lattice spacing of the substrate. Thicker overlayers will try to relax to the bulk equilibrium density. Relaxation may occur by the inclusion of a network of misfit dislocations as depicted for a simple cubic array in Fig. 3.3(a). Note that in this example a square network of dislocations is expected. An experimental realization of this is the Ag-Au system [3.4] which has a .2% lattice mismatch. A theory of the formation of the misfits based on elastic strain theory was developed J.H. van der Merwe [3.5]. Another possibility is the matching of particular planes such as occurs in the cases of Au, Al or Ag (100) on Cr or Fe (100) as shown in Fig. 3.3(b). In these cases substrate steps become sources of defects because there exists a vertical mismatch between the materials. Perhaps the most exciting possibility is when the substrate forces the overlayer to form a new metastable phase by providing a template for a particular crystal plane. Examples are fcc Fe [3.6] and Co [3.7] on (100) Cu and the work reported here on bcc Ni on (100) Fe. These new phases exhibit new material and magnetic properties. Their

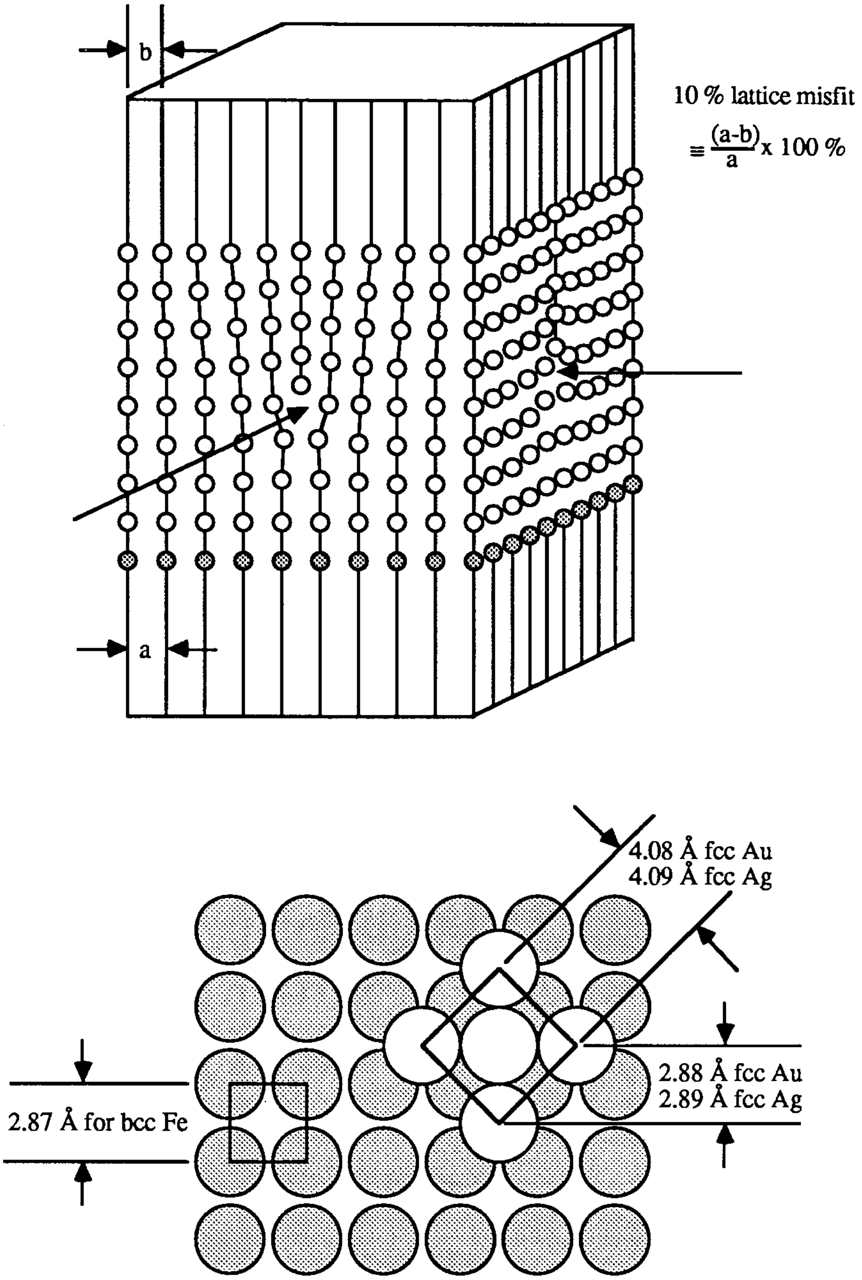

Fig. 3.3 (a) Epitaxy between two simple cubic arrays with a 10% lattice mismatch. This will tend to create a cubic array of misfit dislocations. (b) Epitaxial matching of a (001) fcc overlayer on a (001) bcc substrate.

synthesis and stability against phase transformation provide new challenges for experimentalists and theorists. Lattice misfit in this case will be determined by how closely the substrate surface lattice matches a plane of a lattice with approximately the same density as a bulk sample of the overlayer. This occurs when the nearest neighbour spacings are approximately the same in both crystals (2.483 Å for Fe and 2.492 Å for Ni) though there are many other possibilities. The formation of crystal defects will be driven by a combination of degree of lattice misfit and the tendency for a phase change to the true equilibrium phase. More complicated forms of epitaxy occur even if the lattices do not match. The substrate then provides only the crystal directions for overlayer growth. This is termed pseudomorphic growth.

The ratio of the binding energy of an overlayer atom to the substrate (E_I per nearest neighbour bond) to the binding energy between condensate atoms (E_C) will influence whether the deposited atoms will tend to stick together or to adhere to the substrate. That is, whether they wet the surface. If the ratio of energies is small epitaxial growth may not proceed even if the lattice spacings are matched. In our experiments we found that the Ni overlayers cover the Fe substrates without a disernible tendency for clumping or interdiffusion.

The energy barrier an atom must overcome to move one lattice site (the activation energy E_A) determines the rate of surface diffusion. Activation energies are some fraction of the binding energies are specific to the type of site (see Fig. 3.1(c)).

Epitaxial layers form by first nucleating stable islands. The minimum stable island size is determined by the binding energies and temperature of the substrate. Because metal bonding is not strongly directional, the substrate and overlayer atoms interdiffuse rather freely. Therefore we are forced to grow our films at rather low temperatures (usually at room temperature). This is more critical in the case of bcc Ni on Fe because we want to avoid a bcc-fcc phase transformation. Simple calculations of the diffusion rates based on the activation energy show that the minimum stable island size at metals is one atom at room temperature. This does not imply the films will grow in a completely random fashion. Firstly, the metal atoms will always locally arrange themselves into crystal forms. Small islands that touch can coalesce and thereby effectively increase diffusion rates. Experimentally, as observed by RHEED, we find that growths at low temperatures (~150 K) do produce rougher films than room temperature growth. Secondly, it has been recently suggested [3.8] that incoming atoms will gain a certain kinetic energy from condensation that allows them to move over the surface for a certain distance before coming to rest. Evidence of this comes from growths at low temperature which still occur in a layer-by-layer fashion. Finally, atoms will not tend to deposit upon small islands because they will have a high probability of transporting to the lower layers. Obviously atoms will not stick on islands of one, two or three atoms in a cubic array because they provide no stable sites.

The important point is that bcc Ni can form on Fe (001) without a gross strain because Ni and Fe have approximately the same nearest neighbour spacing. Later in this chapter we will show that bcc Ni grows for the first 3-6 ML before undergoing a phase transformation to an as yet undeciphered form.

3.3 Reflection High Energy Electron Diffraction (RHEED)

RHEED is the technique which we used most extensively to study the structure of epitaxial overlayers. The standard reference for RHEED is a review article by Bauer [3.9] and a recent extensive study of RHEED in the kinematic approximation can be found in the thesis of P. Pukite [3.10]. A schematic of the apparatus is shown in Fig. 2.2. A 5-10 keV electron beam strikes the sample at small angles of incidence and the diffracted beams are observed on a phosphor screen. At these energies electrons are strongly forward scattered and hence much of the diffracted intensity strikes the phosphor screen. This low angle scattering geometry makes RHEED very convenient for observation during growth because the diffraction apparatus does not place constraints on the placement of the evaporation furnaces. RHEED is sensitive to the surface because electrons interact strongly with matter and therefore penetrate only a few layers near the surface of the sample. The inelastic mean free path (IMFP) of electrons at 10 keV is

~50 Å (see equation 3.14). The attenuation by elastic scattering at the Bragg condition for diffraction is even stronger. In table 3.1 we show the penetration of 10 keV electrons as a function of angle assuming a simple exponential attenuation along the path into and out of the sample using the IMFP of 50 Å.

Table 3.1: Depth at which 10 keV electrons are attenuated by e^{-1} as a function of angle of incidence (θ_i). The depth is given by $L\sin(\theta_i)/2$ where L = 50Å is the inelastic mean free path.

θ_i (deg)	depth (Å)
0.5	.22
1.0	.44
1.5	.65
2.0	.87
3.0	1.3
4.0	1.7
5.0	2.2

From the table we see that RHEED is extremely sensitive to the surface, even more so than Low Energy Electron Diffraction (LEED) in which electrons of energies 50 - 150 eV impinge at normal incidence. RHEED has several other advantages over LEED [3.13]. LEED is not observed during growth mainly because of geometry but also because the low energy electrons can be affected by the magnetic fields from the evaporation sources. RHEED is less sensitive to the temperature of the sample than LEED because of a smaller Debye-Waller factor. That is, the intensity of a diffracted beam is proportional to the Debye-Waller factor = $\exp(-(\Delta K)^2/T)$ where ΔK is the scattering vector and T is the temperature. The ΔK are ~ 5 times larger in LEED than in RHEED because of the different scattering geometries. Therefore is more conveniently used at high temperatures. RHEED is more sensitive to surface roughness and exhibits characteristic transmission patterns when asperities are present. As we will explain below, RHEED can be used to resolve surface order over distances much larger than LEED.

LEED has several advantages over RHEED. A LEED pattern contains a much larger region of k-space than a RHEED pattern and hence complex surface unit cells can be more easily identified. The theory of LEED has been extensively developed to give a much more quantitative picture of the surface than is possible by means of RHEED, though improvements in RHEED theory are now being carried out [3.11].

We will now give a brief overview of the theory of RHEED in the kinematic approximation so that we can interpret our RHEED patterns in a qualitative way. Ideally RHEED can be considered as diffraction from a 2-dimensional array of scattering points because of the limited penetration of the electrons into the sample. We will discuss the diffraction from two points of view. First we will use a simple Laue construction for a 2-D array of scatterers to show where the diffracted beams are to be found. Then we will discuss, in the Born approximation of elastic scattering, how the diffracted intensity is a measure of the reciprocal space of the region of the surface sampled by the electron beam.

Consider the surface to be an ideal lattice of point scatterers as depicted in Fig. 3.4. All the points of the lattice are given by $\mathbf{R} = n_1\mathbf{a}_1 + n_2\mathbf{a}_2$, where n_1 and n_2 integers. $\mathbf{k}_i$ and $\mathbf{k}_f$ are the incident and reflected wavevectors respectively ($|\mathbf{k}_i| = |\mathbf{k}_f| = 2\pi/\lambda$). To have maximum constructive interference the phase difference between waves reflected from different points must be a multiple of 2π, i e.:

$$\phi = \mathbf{R}\bullet(\mathbf{k}_i - \mathbf{k}_f) = 2\pi m \tag{3.1}$$

The set of $\Delta\mathbf{K} \equiv \mathbf{k}_i - \mathbf{k}_f$ that satisfy equation (3.1) are the reciprocal lattice vectors of the 2-D lattice. Since $\mathbf{R}$ has only in-plane components (3.1) can be solved for the in-plane components of $\Delta\mathbf{K}$ independent of the normal component. $\Delta\mathbf{K}$ has the form $\Delta\mathbf{K} = m_1\mathbf{K}_1+m_2\mathbf{K}_2+m_3\mathbf{K}_3$ where m_1 and m_2 are integers. $\mathbf{K}_1$ and $\mathbf{K}_2$ are given by:

$$\mathbf{K}_1 = \frac{2\pi\mathbf{a}_2\times\hat{\mathbf{n}}}{|\mathbf{a}_1\times\mathbf{a}_2|} \qquad \text{and} \qquad \mathbf{K}_2 = \frac{2\pi\hat{\mathbf{n}}\times\mathbf{a}_1}{|\mathbf{a}_1\times\mathbf{a}_2|} \tag{3.2}$$

where $\hat{\mathbf{n}}$ is the unit normal vector. The normal component of $\Delta\mathbf{K}$ ($m_3\mathbf{K}_3$) is then found from conservation of energy (i e. $|\mathbf{k}_i|=|\mathbf{k}_f|$). Combining the conditions from equation (3.1) with

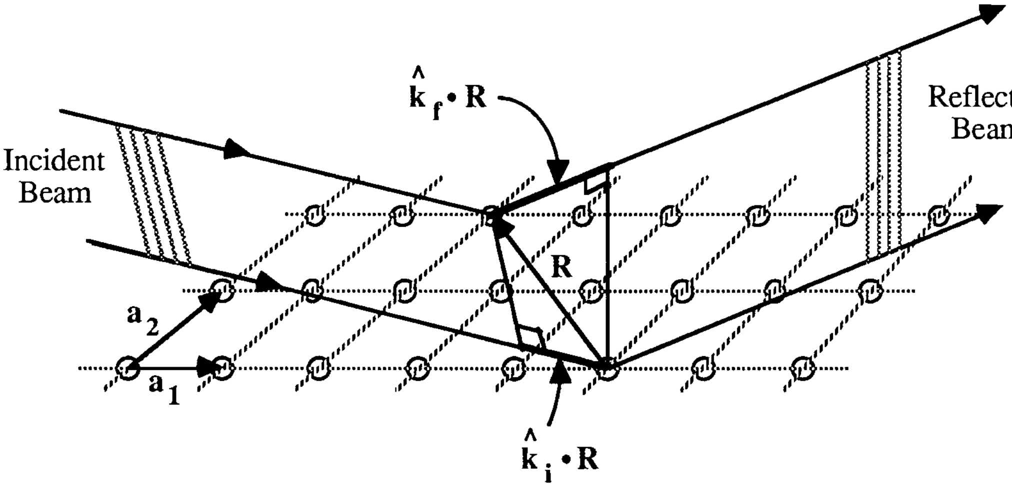

Fig. 3.4 Laue construction for a 2-dimensional lattice

$|\mathbf{k}_i|=|\mathbf{k}_f|$ gives three equations for the unknowns m_1, m_2, m_3. The possible $\Delta\mathbf{K}$ form a set of rods normal to sample surface. The Ewald construction is depicted in Fig. 3.5 to show the type of patterns seen on a screen. To form a mental image of the construction it is important to keep in mind that for RHEED $|\mathbf{k}_i|/\Delta K \sim$(lattice spacing)$/\lambda \sim 20$. The diffraction pattern characteristic of a two dimensional cubic array is a circular pattern of spots on the viewing screen. The reflection for which $\theta_i = \theta_f$ is termed the "specular reflection". It is of particular interest because it is the one for which intensity calculations are generally made and it is the reflection most often measured as a function of angle of incidence and growth time (see RHEED oscillations section 3.4).

If we consider reciprocal space loosely (see below) as the Fourier transform of the atoms in the surface region we would say that real space is periodic in the plane of the surface and hence that k-space has a discrete set of in-plane points. Since the surface is a delta function normal to the plane and the Fourier transform of the delta function is a constant, k-space is a constant in the z direction. Hence the reciprocal lattice is a set of rods oriented normal to the plane. Another way to look at this is the normal component of the electron's linear momentum is a continuous variable because of the broken symmetry at the surface and hence can have any value that satisfies energy conservation.

Now we follow Bauer [3.9] and consider diffraction more formally as the elastic scattering of a plane wave from a potential. The incident plane wave is given by $\exp(i\mathbf{k}_i\cdot\mathbf{r})$. Schrodinger's equation can be written in integral form for the wavefunction, $\Psi(\mathbf{r})$, far from the sample as:

$$\Psi(\mathbf{r}) \cong \exp(i\mathbf{k}_i\cdot\mathbf{r}) - \frac{\exp(i|\mathbf{k}_f|r)}{4\pi r}\int \exp(-i\mathbf{k}_f\cdot\mathbf{r}')V(\mathbf{r}')\Psi(\mathbf{r}')d^3r'$$

where $V(\mathbf{r}')$ is the potential and $|\mathbf{k}_i| = |\mathbf{k}_f|$. The complex scattering amplitude is defined as:

$$f(\mathbf{k}_f) \equiv -\frac{1}{4\pi}\int \exp(-i\mathbf{k}_f\cdot\mathbf{r}')V(\mathbf{r}')\Psi(\mathbf{r}')d^3r' \qquad (3.3)$$

In an experiment we are sensitive to the intensity $I \propto |f(\mathbf{k}_f)|^2$.

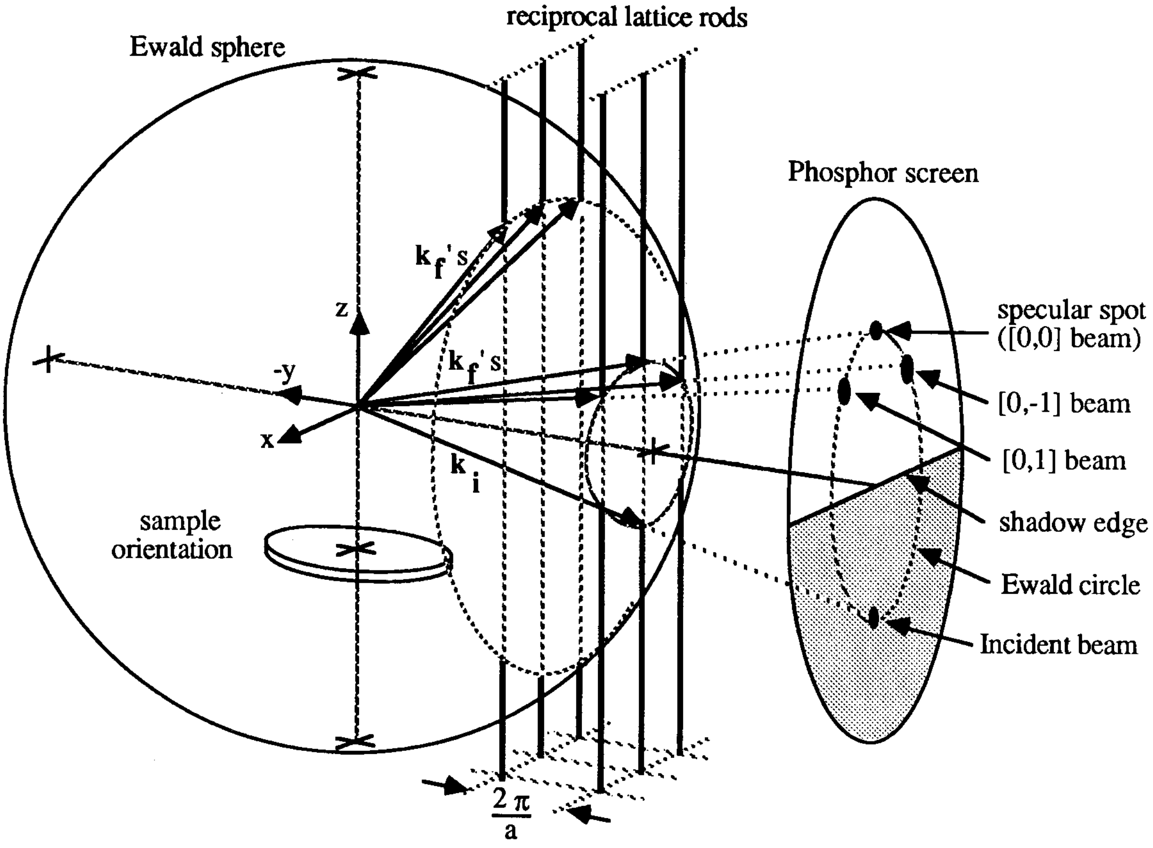

Fig. 3.5(a) Laue construction of 2-dimensional diffraction and depiction of observed patterns on a flat screen.

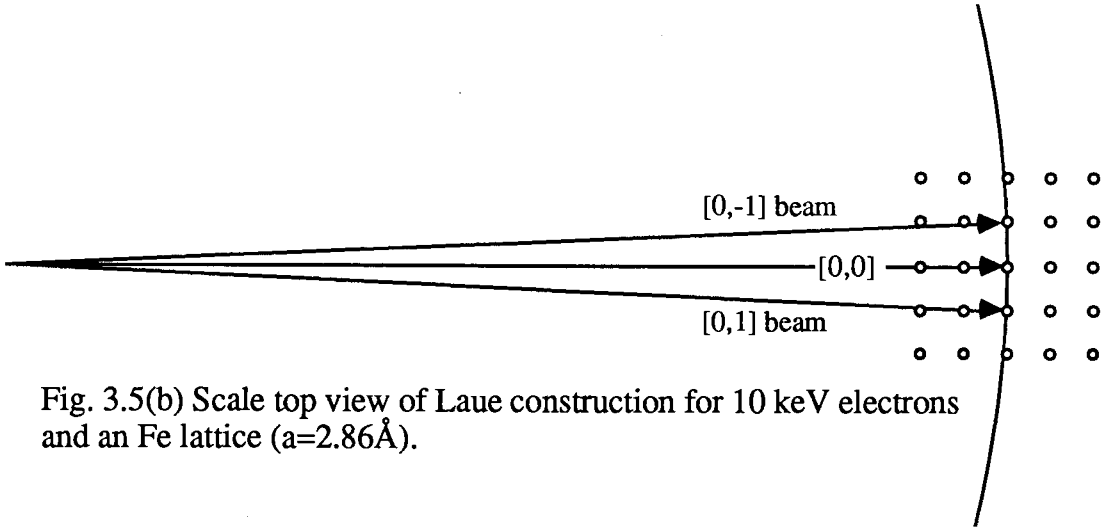

Fig. 3.5(b) Scale top view of Laue construction for 10 keV electrons and an Fe lattice (a=2.86Å).

The simplest approximation is to let $\Psi(\mathbf{r}') = \exp(i\mathbf{k}_i\cdot\mathbf{r}')$ in the integrand. This is the Born approximation and leads to the "kinematic" theory. Because of the strong interaction of electrons with matter the Born approximation is not valid for RHEED and intensities calculated do not match experiments. The wave within the crystal must be written as a series of plane waves which themselves become sources of multiple scattering. RHEED has been treated formally by Maksym and Beeby [3.11] by solving Schrodinger's equation including multiple scattering and will not be discussed here. It has been claimed that kinematic theory does determine the positions and lineshapes of diffraction peaks fairly well [3.27] and we will develop it here as a qualitative way to discuss RHEED.

In the Born approximation the scattering amplitude can be written as:

$$f(\mathbf{K}) = -\frac{1}{4\pi}\int \exp(-i\mathbf{K}\cdot\mathbf{r}')V(\mathbf{r}')d^3r' \tag{3.4}$$

with the scattering vector defined as $\mathbf{K} \equiv \mathbf{k}_f - \mathbf{k}_i$. The scattering amplitude becomes the Fourier transform of the potential. This is the same form as for x-ray and optical diffraction if the electron potential is replaced by the electron density and the optical transmission function respectively. The next step is to assume that the potential is periodic. That is:

$$V(\mathbf{r}) = V(\mathbf{r} + \mathbf{R}) \qquad \text{with} \quad \mathbf{R} = n_1 a_1 + n_2 a_2 + n_3 a_3 \tag{3.5}$$

The indices n_1, n_2 and n_3 are integers and run from 0 to N_1-1, N_2-1 and N_3-1 respectively where N_1,N_2,N_3 are the number of atoms in the 3 directions. Because of the periodicity of the potential we can rewrite equation (3.4) as

$$f(\mathbf{K}) = \left[\frac{-1}{4\pi}\int_{\text{cell}} \exp(-i\mathbf{K}\cdot\mathbf{r}')V(\mathbf{r}')d^3r'\right]\left[\sum_{n_1=0}^{N_1-1} e^{-i\mathbf{K}\cdot n_1 a_1}\sum_{n_2=0}^{N_2-1} e^{-i\mathbf{K}\cdot n_2 a_2}\sum_{n_3=0}^{N_3-1} e^{-i\mathbf{K}\cdot n_3 a_3}\right]$$

$$\equiv F(\mathbf{K})G(\mathbf{K}) \tag{3.6}$$

The intensity is now given by $I \propto |F(\mathbf{K})G(\mathbf{K})|^2$. F(K) is called the form factor and G(K) is called the structure factor. The summations in (3.6) are exactly the same as one would obtain for diffraction from a lattice of point scatterers so the form factor accounts for the interference within a unit cell. The form factor is strongly peaked for small **K** vectors and therefore the scattering is mostly in the forward direction for the high energies used in RHEED.

The sums are evaluated in standard books on optics and x-ray diffraction. In the case of RHEED or LEED the sum for the direction perpendicular to the surface must be handled separately because of attenuation (see below). For simplicity we assume $\mathbf{a}_3$ is perpendicular to the surface. The sums over n_1 and n_2 give:

$$I \ \alpha \ \frac{\sin^2(\frac{1}{2}N_1K_1a_1)}{\sin^2(\frac{1}{2}K_1a_1)} \cdot \frac{\sin^2(\frac{1}{2}N_2K_2a_2)}{\sin^2(\frac{1}{2}K_2a_2)} \tag{3.7}$$

where $K_i \equiv \mathbf{K} \cdot \mathbf{a}_i$. This the Laue interference function. If N is large this function is sharply peaked at values of K_1 and K_2 which satisfy the Bragg conditions $K_1a_1 = 2m_1\pi$ and $K_2a_2 = 2m_2\pi$ with m_1 and m_2 integers. These are the same conditions as for scattering from the two dimensional lattice. The intensity has a series of zeros and minor maxima on either side of the Bragg peaks. The zeros nearest to the main peaks are at $\delta K_1 = \pm\, 2\pi/a_1N_1$ and $\delta K_2 = \pm\, 2\pi/a_2N_2$ respectively. It is also easy to show that the FWHM is given by $\delta K_i(\mathrm{FWHM}) \cong \delta K_i$. Ignoring the z direction for now, the k-space rods can be said to be broadened in the K_1 and K_2 directions. The width of the peak gives a measure of the size of the regions of crystal coherence in the plane of the surface. In real samples the zeros are washed out by the mosaic spread and the randomness of steps and islands but the halfwidth of the peak can be roughly associated with the average island size. It can be determined most simply the ratio of the spacing between successive peaks to the width of a diffraction line. That is $K_i/\delta K_i(\mathrm{FWHM}) \cong (2\pi/a_i)/(2\pi/a_iM_i) = M_i$.

One of the advantages of the RHEED geometry is that it is very sensitive to the broadening of the rods [3.13]. This can be seen in the construction in Fig. 3.6. Because the Ewald sphere is almost to tangent to the rods it cuts the broadened rods over a large range of angles perpendicular to the surface ($\delta\theta$, see Fig 3.6). Any mosaic spread causes the ideal spots of Fig. 3.5(a) to be lengthened in a direction perpendicular to the surface by a factor of $1/\sin(\theta_i)$

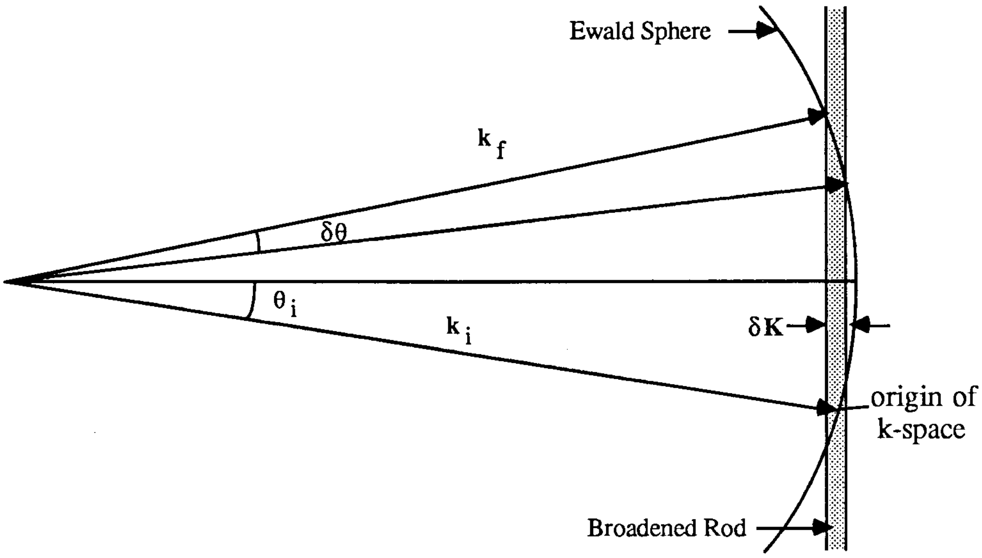

Fig. 3.6 (a) RHEED construction for a finite crystal for which the k-space rod possesses a finite width. Because of the range of possible outgoing k-vectors the diffraction pattern consists of streaks vertical to the sample surface.

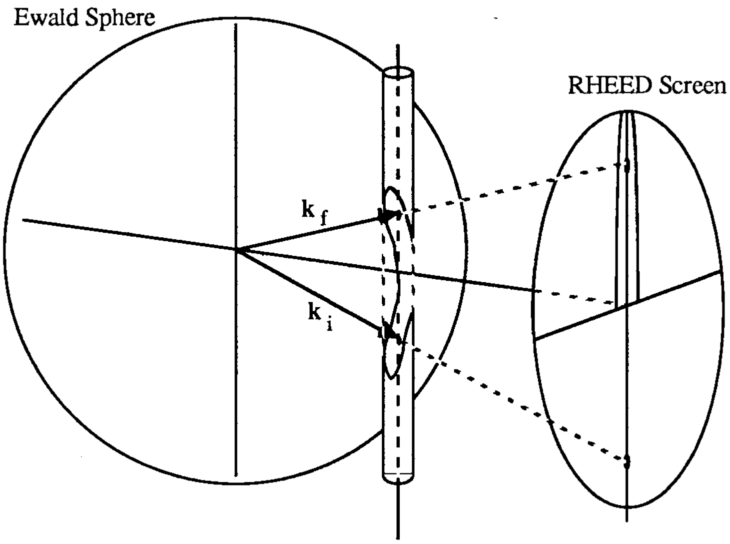

Fig. 3.6(b) Depiction of the intersection of a line and concentric cylinder with the Ewald sphere. The line and cylinder are an idealization of one rod in the k-space of a crystal surface covered by randomly shaped islands.

while they are broadened parallel to the surface only by the width of the rod. The spots of the Ewald construction then become streaks. $\delta\theta$ will be given approximately by:

$$\delta\theta \approx \delta K/k_i \sin(\theta_i) \approx 2\pi/Wk_i \sin(\theta_i) \tag{3.8}$$

if we neglect the angular spread of the incoming beam. δK is the width of the k-space rod and W is the average island size along the direction of the beam. With $\theta_i \sim 1^0 - 3^0$, for eg., the streak will be ~ 60 - 20 times longer perpendicular to the surface than parallel with the surface. This explains the most standard type of RHEED pattern obtained for a relatively high quality metal samples (see Figs. 3.7(c),(d)). The shortening of the streaks into spots can be seen beautifully in patterns from Fe whiskers (see Figs. 3.7(a),(b)).

There will be a modulation of the rods perpendicular to the surface because of the finite penetration of the beam. The deeper it penetrates the more the k-space rods evolve into 3-D points. The beam attenuates primarily because of elastic scattering but also due to inelastic processes. In either case the attenuation can be handled by including an imaginary term in the scattering vector. For the case of specular scattering for which K_1 and K_2 are zero we can write K_3 as:

$$K_3 = -(\kappa + i(\beta_E + \beta_A))\hat{z}$$

where $\kappa = -2k_i \sin(\theta_i)$. The absorption term β_A includes all processes that remove electrons from the elastic beams. The damping due to inelastic processes is given by $\beta_A = 1/L\sin(\theta_i)$ where L is the inelastic mean free path for intensity. The factor of two on conversion from intensity to amplitude is canceled by the factor of 2 which accounts for the sum of the paths in the material before scattering and after the scattering event. β_A increases with decreasing angle. The β_E term accounts for the diminishing of the elastic beam with depth because electrons are diffracted out of the crystal by elastic scattering.

For electrons to produce an imaginary term in the scattering vector it is necessary that an incoming electron meets the conditions that it is trying to propagate in an energy gap produced by the crystal potential. At the Bragg condition, that is if the scattering vector lies on the sphere

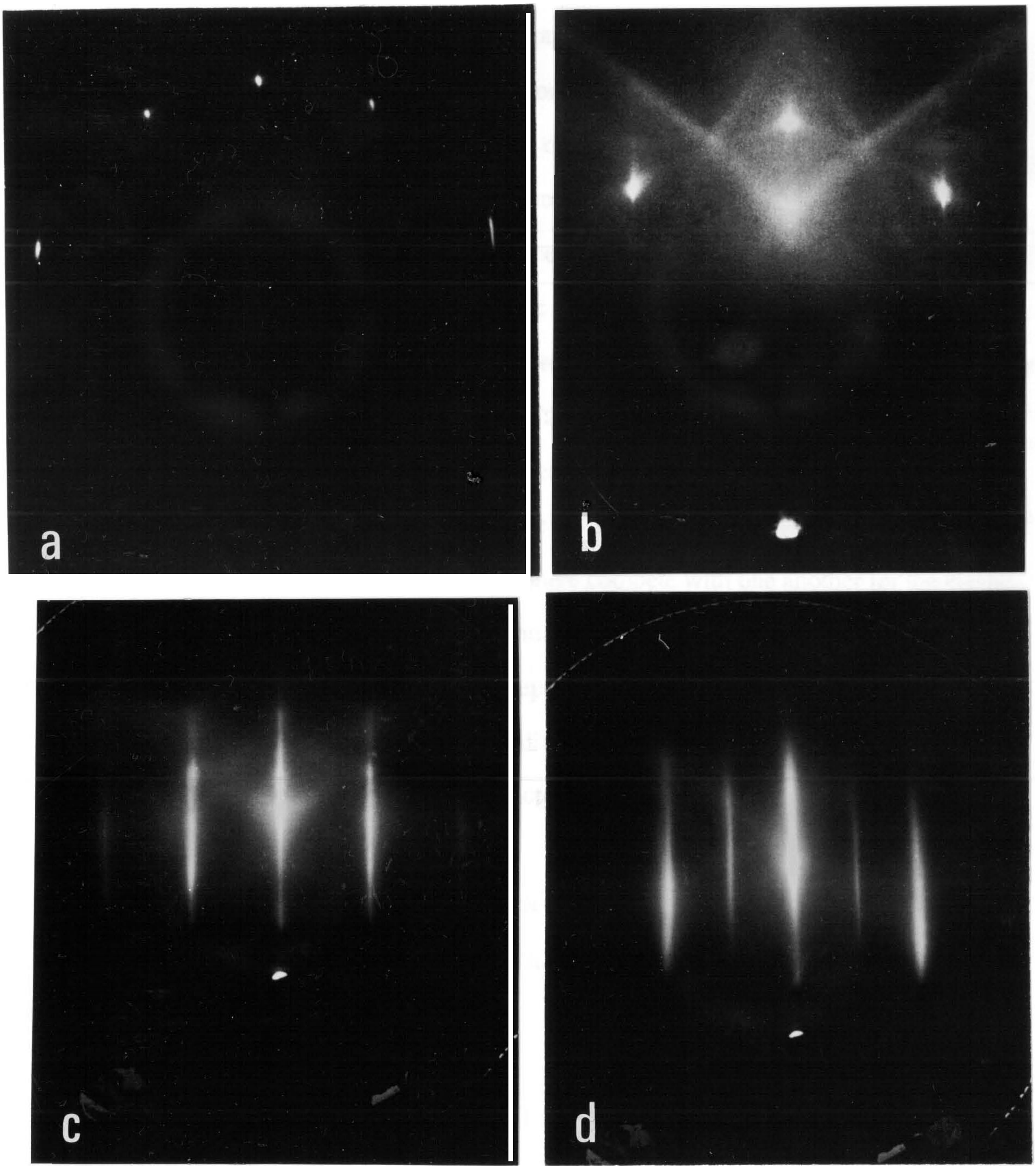

Fig. 3.7 (a),(b): RHEED patterns for diffraction from the (001) surface of an Fe whisker. In (a) the incident beam is along the [100] direction and in (b) the [110] direction. (b) is overexposed to reveal Kikuchi lines. (c),(d): [100] and [110] RHEED patterns respectively for a 2° vicinal Fe (001) single crystal grown by strain-anneal after preparation in UHV.

of reflection, the electron is in the center of the gap and β_E is a maximum. The width of the gap, and hence the angular width of the diffraction peaks, depends on the ratios of the Fourier components of the potential to the kinetic energy of the incoming electrons measured perpendicular to the surface. For x-rays and neutrons the gap energies are 5 to 6 orders of magnitude smaller than the kinetic energies. For electrons the gap energies are only two to three orders of magnitude smaller than the kinetic energy for electrons at 10 keV. In RHEED with 10 keV electrons the wavevector of the incoming beam and the radius of the Ewald sphere are ~50 $Å^{-1}$. The reciprocal lattice vectors lie on a grid whose spacing is ~5 $Å^{-1}$. There are many lattice points close to the sphere of reflection. The attenuation of the beam by both β_E and β_A elongate the reciprocal lattice points in the direction perpendicular to the surface. All of the reciprocal lattice points close to the Ewald sphere compete with one another for the elastic intensity. They all contribute to the elastic attenuation of the beam with depth. Exactly which ones contribute strongly to the scattering will depend on the angle of incidence, but to a first approximation the collective effect of all of the diffracted beams can be summed up in the elastic attenuation factor β_E. The attenuation factor due to elastic scattering for the intensity is approximately 20 Å for electrons in Fe [3.12].

Treating $\beta_E+\beta_A$ as a phenominological parameter for a given angle we can evaluate the sum over n_3 in equation (3.6). The limit of the sum can be extended from N_3-1 to infinity because the beam penetrates so little. We get:

$$\sum_{n_3=0}^{\infty} e^{-iK\cdot n_3 a_3} = \frac{1}{1-\exp(-iK_3 a_3)}$$

The intensity is proportional to the square modulus of the amplitude:

$$I \;\alpha\; \frac{1}{1-2\cos(\kappa a_3)\exp(-\beta a_3)+\exp(-2\beta a_3)} \tag{3.9}$$

This function has maxima corresponding to Bragg angles where $\kappa a_3 = 2n\pi$ as for the in-plane sums but the angular width is now determined by β and not by the crystal size. In the limit of small β it can be shown that the intensity decreases to 1/2 a maxima when $\delta\theta_i \approx \beta/2k_i$. Thus we see that the 3-D k-space points are broadened out along the normal direction to form modulated rods as β increases. The broadening increases with damping (i e. β) and is largest at low angles because of the $1/\sin(\theta_i)$ dependence of β. For a crystal of high quality the diffraction pattern is formed by the set of sharp intersections of the rods with the Ewald sphere because the in-plane width of the rods is small. The intensity of the diffraction features will change as θ_i is varied because the degree to which the reciprocal rods become extended in the z-direction is determined by β. The intensity does not follow equation (3.9) well in experiments because of dynamical diffraction effects from many beams being simultaneously excited and also because of the scattering giving rise to Kikuchi lines. However, the basic argument about the damping being the cause of the broadening of the spots normal to the surface is still valid in RHEED as it is in LEED.

We stated above that the width of the k-space rods in the plane of the specimen can be associated with the average island size. This is true if the islands are randomly displaced from one another so that we can use a random phase approximation. Then the intensities from each island add to form the overall diffraction pattern. This is the case for a crystal exhibiting a mosaic spread as shown in Fig. 3.2(d). However, in a system such as depicted in Fig. 3.2(a) the atoms are correlated over large distances because the substrate is correlated over large distances. One must take into account the effect on the diffraction patterns of the interference of waves scattered from different islands. We must introduce correlation functions to discuss diffraction from surfaces which are neither perfectly periodic nor a random collection of periodic islands. Lent and Cohen [3.14] have considered a simple two-level system in which a percentage of a monolayer is deposited on an otherwise perfect surface. They then consider the diffraction to come only from the surface atoms and uncovered atoms of the top layer of the substrate. The sums in equation (3.6) are then converted to

$$I \propto \left|\sum_{\mathbf{r}} p(\mathbf{r})\exp(i\mathbf{K}\cdot\mathbf{r})\right|^2 \qquad (3.10)$$

where $p(\mathbf{r})$ is 1 if a surface atom is at position $\mathbf{r}$ and 0 if the site is vacant. This can be rewritten approximately as [3.14]:

$$I \alpha \int C(\mathbf{r})\exp(i\mathbf{K}\cdot\mathbf{r})d^3\mathbf{r} \qquad (3.11)$$

where $C(\mathbf{r})$ is the pair correlation function defined as the probability that two atoms are separated by a distance $\mathbf{r}$. If the atoms stick together in islands $C(\mathbf{r})$ is relatively large at small $\mathbf{r}$ and then tapers off to a constant at large $\mathbf{r}$. Therefore $C(\mathbf{r})$ can be written as a constant for the long range order plus a term for the short range order. The diffracted intensity will then consist of a spike for the Fourier transform of the long range order plus a broader function for the transform of the short range order correlation function. The width of the spike will depend on the quality of the substrate crystal as discussed above. We will show photos of RHEED patterns which nicely demonstrate the separation of the diffraction into these two terms.

Another diffraction feature is Kikuchi lines. These are caused by scattered electrons that have lost a little energy through inelastic collisions with plasmons, phonons and valence electrons. These electrons cause light and dark bands to appear on the RHEED screen at various angles. Since we will not be analyzing them in this work we refer the reader to the literature (see [3.9] e.g.).

Now we will discuss RHEED patterns from various samples. A problem facing researchers wishing to use RHEED quantitatively to study metal epitaxy is that most metal single crystal substrates are not generally as good as semiconductor crystals. The RHEED streaks are elongated and broadened by the mosaic spread present in metal crystals grown by strain-anneal or by the Bridgman technique. However Fe whiskers are nearly perfect as can be seen from Fig. 3.7(a) - (b) and one of the themes in this section will be to point out how ideal the whiskers are for diffraction studies. The diffraction features are sharp points where the rods intersect the Ewald sphere. The diffracted spots are often no longer than the beam size at angles of incidence greater than 2 deg. The spots elongate at lower angles of incidence in accordance with the RHEED construction of Fig. 3.6 and equation (3.8). The maximum elongation is for the outgoing beam parallel to the crystal surface. The point at the top in both photos is the specular spot. The bright point at the bottom in Fig. 3.7(b) (masked off in Fig 3.7(a)) is the portion of the incident beam that misses the sample and hence the distance between this point and the specular spot is used to determine the angle of incidence. The diffraction features are often labelled, starting from the left of Fig. 3.7(a), as the [-2,0], [-1,0], [0,0], [1,0] and [2,0] beams. The pattern in Fig. 3.7(b) was overexposed to reveal the Kikuchi patterns. All the crystal faces of the whiskers we use are {001} to a high degree of accuracy as can be seen by the sharpness of the diffraction points and the lack of azimuthal asymmetries characteristic of stepped surfaces. J.M. Van Hove, et al. [3.13] determine average island size on well-prepared GaAs substrates from the θ_i dependence of the length of the RHEED streaks, i e. using equation (3.8). In Fig. 3.8 we show some preliminary measurements of the length of the specular spot as a function of the angle of incidence obtained for a well-prepared Fe whisker. Our results show terrace lengths of ~3700 Å. As a final note it is worth pointing out that these photos have the sharpest RHEED diffraction features from metal crystals published in the literature.

Fig. 3.7(c),(d) show RHEED patterns from an annealed Fe (001) single crystal (Fe sample 2) grown by strain-anneal. The patterns have the elongated streaks expected for a crystal which has a mosaic spread and a stepped surface. Fig. 3.7(d) shows an extra set of lines when the beam is oriented along the [110] azimuth. This occurs in samples when the impurity levels of C and O_2 becomes greater than 3 % of the surface atoms. The surface unit cell becomes two times larger than the bcc Fe surface cell and is rotated at 45 deg. It indicates that the impurities order into domains or the impurities force a reconstruction of the Fe surface. One possible surface ordering could be an impurity sitting at every second hollow site on the surface. The interesting thing for RHEED studies is that a reconstruction is observed at these relatively low levels of impurities. Extensive LEED studies [3.15] showed that much higher impurity levels of O_2 were necessary to create the doubling of the surface surface unit cell. This is direct evidence of the enhanced surface sensitivity of RHEED over LEED.

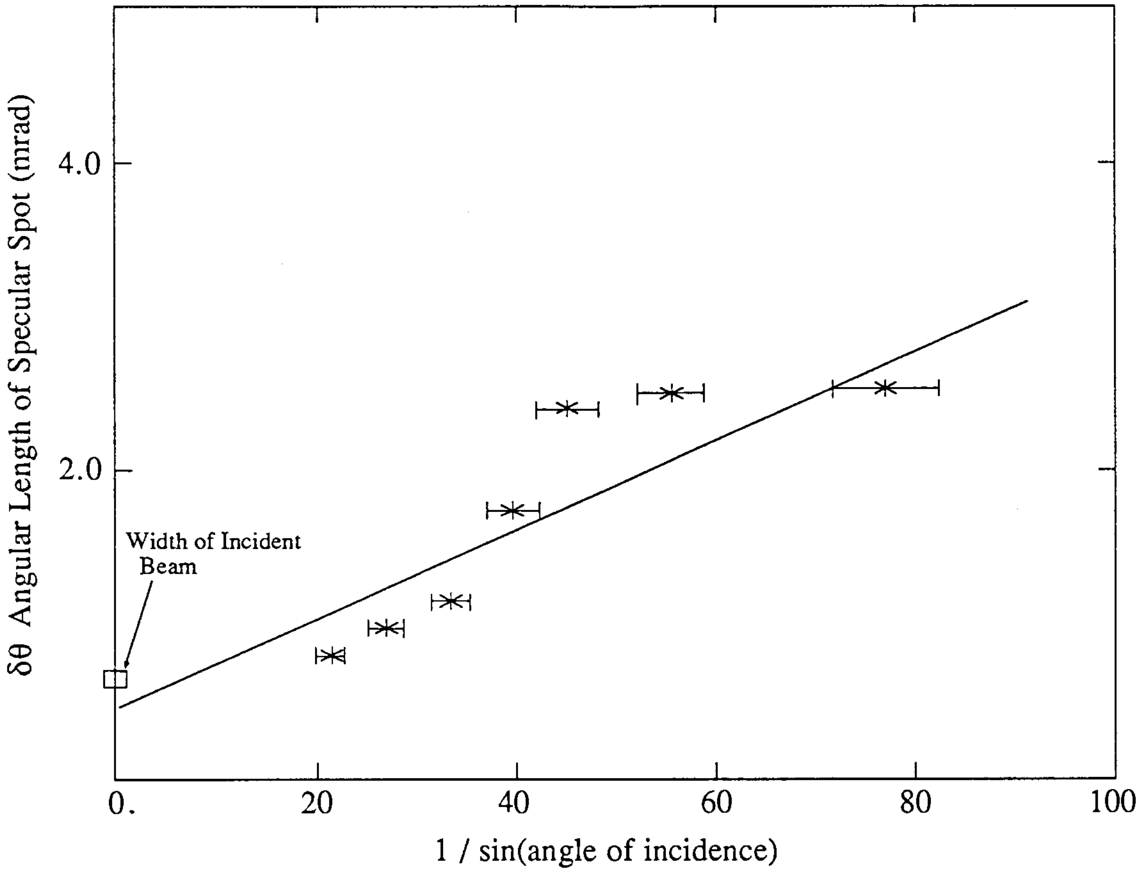

Fig. 3.8 FWHM of the specular spot plotted vs 1 / sin(angle of incidence) obtained for an Fe(001) whisker with the electron beam directed along the [110] axis. The slope of the line combined with equation (3.8) provides an estimate of the coherence length: W~3700 Å.

Figs. 3.9(a) and 3.9(b) show the RHEED patterns from a sputtered Fe (001) surface for an incident electron beam directed along the [100] and [110] azimuths respectively. The patterns show the features of the three dimensional k-space of the bcc lattice. The k-space of the bcc lattice is a fcc lattice. The photos in (a) and (b) are a result of the intersection of the Ewald sphere with the (100) and (110) planes of the fcc k-space unit cell respectively. The three dimensional nature of the crystal is revealed in the RHEED pattern because the disorder caused by sputtering makes the average island size smaller and also deepens the effective penetration of the beam. From the point of view of the simple diffraction theory, the in-plane dimensions of the average island size are small causing the rods to be broadened in the plane of the surface and the effective damping constant β has been decreased causing the rods to sharpen in the direction normal to the surface. An important point for epitaxy is that this type of pattern can arise because of the small in-plane size of the islands and can seen even during layer-by-layer growth. Such a pattern could also be seen if the surface were covered with small crystallites through which the beam penetrates to give transmission patterns.

In Figs. 3.9 (c) and (d) we show RHEED patterns for an Fe whisker on which 10 ML of Fe was deposited at room temperature. The patterns consist of the bright spots along the Ewald circle and sets of bands that are nearly perpendicular to the sample surface. This is direct evidence of the splitting of the diffraction into long range and short range correlations as mentioned previously. The k-space rods can be pictured as consisting of a narrow central line surrounded by a broader cylinder as depicted in Fig. 3.6(b) where we show the RHEED construction for this case. The cross section of the cylinder is roughly circular because roughly the same splitting is observed at all azimuths. This implies that the surface consists of randomly shaped islands. This makes sense at these low temperatures because the atoms will stick easily to the sides of clusters without becoming rearranged into square islands which are the low energy shapes on cubic surfaces. A similar k-space construction for submonolayers of Si on Si(001) surfaces have been studied as a function of temperature using high resolution LEED by Horn and Henzler [3.16]. They then Fourier transform the

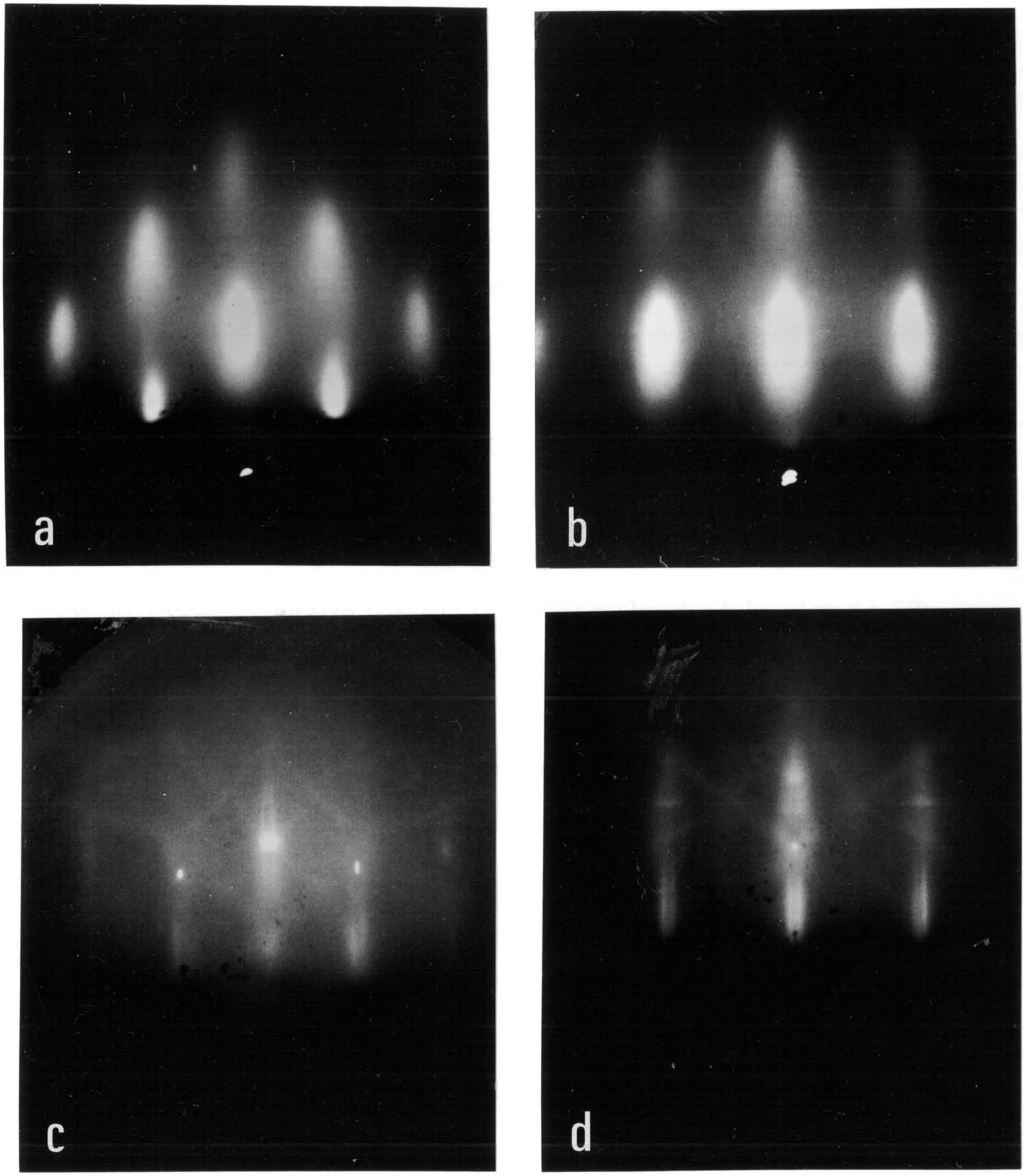

Fig. 3.9 (a),(b): [100] and [110] RHEED patterns repectively for a 2° vicinal Fe (001) single crystal grown by strain-anneal after sputtering in UHV. (c),(d): [100] and [110] RHEED patterns for an Fe (001) whisker after 10 ML of Fe have been deposited at room temperature.

diffraction intensity to derive the distribution of island dimensions as a function of temperature. Profiles taken across the streak for a pattern obtained for an Fe whisker before and after growth at $\theta_i = 22$ mrad are shown in Figs. 3.10(a)-(c). The width of the narrow central spike shown in (a) and (b) is the same before and after the growth. In Fig. 3.10(c) we show a profile across the split streaks away from the spectral spot which shows the dip in intensity visible in Figs. 3.9(c)-(d). Resolution of the dip in intensity in Fig. 3.10(b) near the spectral spot has been prevented by crossing of the Kikuchi lines as seen in Fig. 3.9(d). As we mentioned above the narrow peak is due to long range correlations of flat surfaces and the split peak is due to local roughness.

The photo in Fig. 3.11(a) shows what happens as the Fe whisker with a 10 ML deposit of Fe is annealed for about 10 minutes at 600 C. We observe that the split streaks of Figs.3.9(c-d) have disappeared and fans have developed that radiate from the main spots. The origin of these streaks have been explained by Pukite [3.10] and his explanation is based on the diffraction pattern of a square aperture. At this higher temperature the atoms appear to have rearranged into more nearly square-shaped islands. We will not depict the rather complicated RHEED construction here but simply state that observation of the fans along the [110] direction and not the [100] direction shows that the edges of the islands are oriented along the [100] direction. This is the low energy orientation on a cubic substrate as can be seen easily by drawing some simple surface island diagrams. A similar pattern of fans is observed for Fe whiskers covered with more than two monolayers of Au (see Figs. 3.11(b),(c)). The lattice misfit between Au (001) and Fe (001) is very small as depicted in Fig. 3.3 (b). The (001) face of a Au single crystal has the interesting property that it reconstructs into a close-packed plane which is modulated by the less dense cubic underlayer [3.17]. Though the exact structure of the surface is not precisely known it is believed to consist of relatively large unit cells of approximately square shape. These square shapes are responsible for the fans of diffracted intensity in Fig. 3.11(c). Two orientations of the unit cells, which have local hexagonal coordination, must exist on the surface to explain the overall cubic symmetry of the RHEED patterns. The fans are

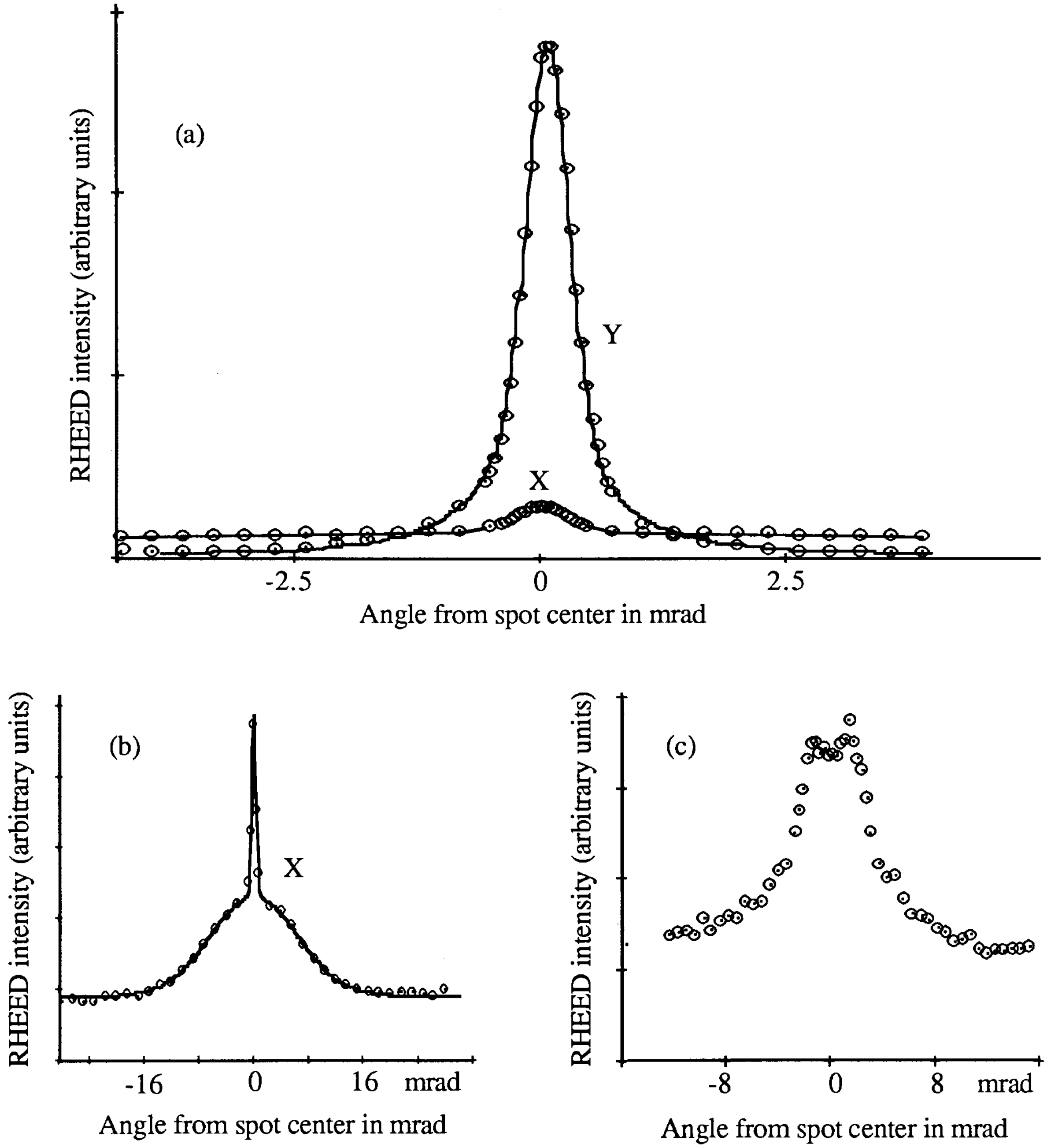

Fig. 3.10 Profiles of the RHEED intensity across the [0,0] streak reflected from an Fe (001) whisker. The electron beam was directed along the [011] direction. (a),(b): The profile measured before growth, labeled X in (a), is compared with the profile measured after the growth of 10 ML of Fe, labeled Y in (a) and (b). In (c) is shown a profile across the bands in the [0,0] streak that are visible in Fig. 3.9(d). The profile in (c) was measured away from the specular spot and the Kikuchi lines at approximately .5 cm from the shadow edge.

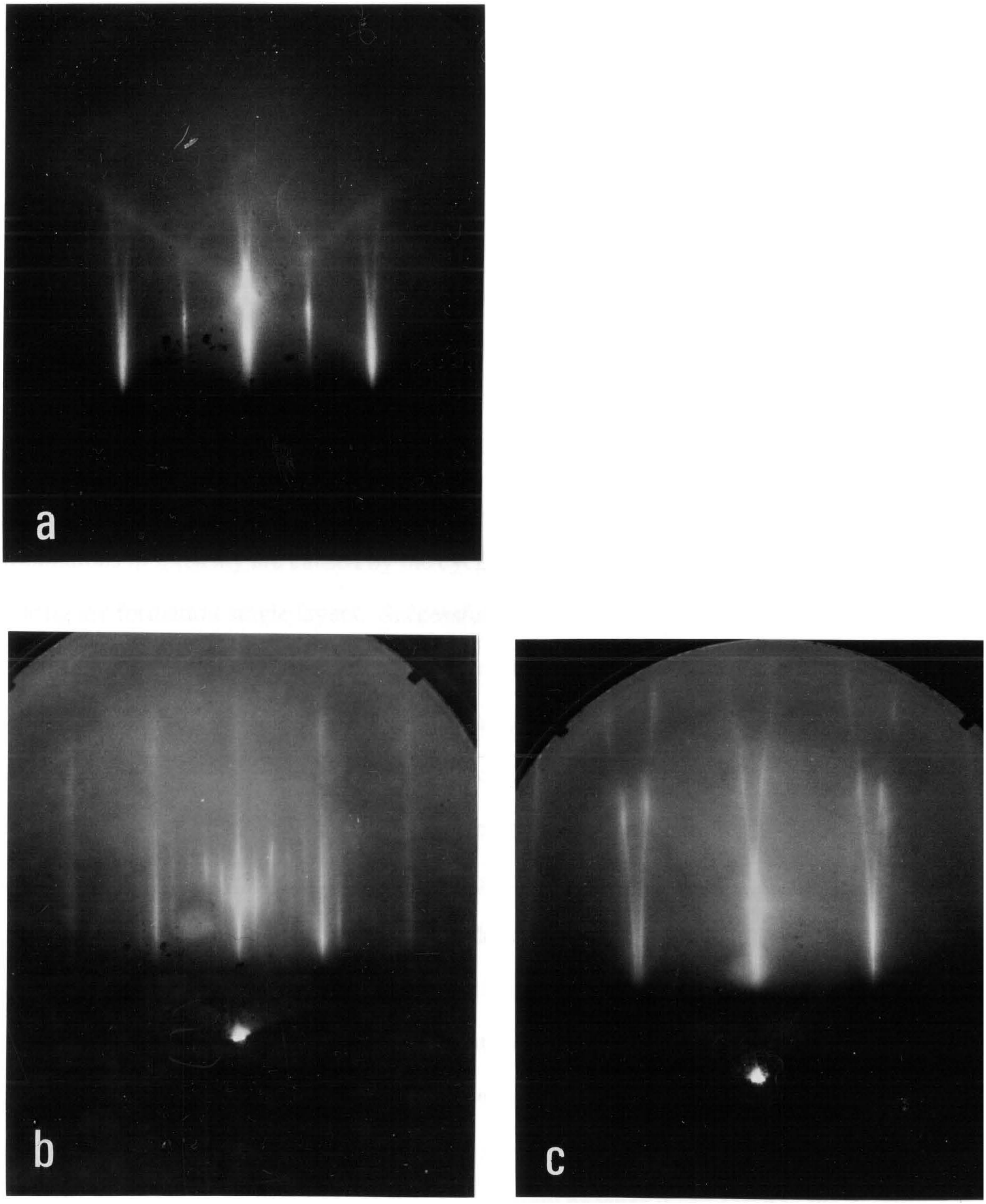

Fig. 3.11 (a) [110] RHEED pattern for an Fe (001) whisker after deposition of 10 ML of Fe at room temperature and approximately 10 minutes of annealing at 600 C. (b),(c) [100] and [110] RHEED patterns respectively for an Fe (001) whisker after deposition of 30 ML of Au.

composed of short streaks because the surface is a periodic array of the large unit cells. The important point for our work is that the streaks due to the cubic substrate are still the strongest feature even though the surface has a very different local coordination. This is because the diffraction still picks out the periodicities of the modulations of the overlayer created by the cubic substrate. Later we will propose that this idea may explain one of the major contradictions in the structural studies of Ni on Fe (001).

3.4 RHEED Oscillations

Oscillations in reflection high energy electron diffraction (RHEED) patterns during epitaxial growth of metals on metal substrates have recently been reported [3.18-19]. These oscillations in intensity are caused by the cyclic roughening and smoothing of the surface during the formation single layers. Successful observation of these oscillations indicates a strong degree of layer-by-layer growth. Their interpretation has established a tool for controlling and studying, in depth, the growth by molecular beam epitaxy (MBE) of IV [3.20, 3.21], III-V [3.22-24] and II-VI [3.25] semiconductor compounds and superlattices. A knowledge of their dependence on substrate temperature and flux rates as well as the method of phase locking growth to oscillations has improved crystal and interface properties.

Here we show: (1) RHEED oscillations during metal epitaxial growth exhibit the features observed during semiconductor growth but at lower temperatures; (2) oscillations are common to all the metal on metal substrate growths that we have studied at room temperature; and (3) the faces of Fe single crystal "whiskers" grown by chemical vapor transport provide a nearly ideal substrate for the study RHEED oscillations [3.26].

The observation of RHEED oscillations is timely because it can assist in the current efforts to control the growth of epitaxial metallic ultrathin films and superlattices. An obvious and common use for the phenomenom is for accurate control of film thicknesses. Even if oscillations are not observed during a particular system, a quartz thickness monitor can be calibrated for a given overlayer element by growing the element on its own single crystal where oscillations are likely. More importantly oscillations are linked to crystal quality which can then be correlated with magnetic properties.

The degree of layer-by-layer growth during metal epitaxy is usually determining by the difficult and time consuming method of looking for breaks in XPS or AES intensities of underlayers or overlayers vs growth time (see section 3.6). This involves detection of subtle deviations from exponential curves and does not take into acount the effects of variations in surface roughness upon electron emission. Oscillation studies have many advantages over these techniques.

The quality of metallic epitaxial growths does not usually match that of semiconductors. This can be seen by comparing typical RHEED patterns. Metals interdiffuse more freely. The substrates have a higher defect density. The growths often incorporate large lattice mismatches. The formation of metastable phases is sometimes attempted as in the Ni growths studied in this thesis. Choosing the best growth temperature is critical. One wants a temperature which is sufficient to allow movement of atoms to provide crystal quality but a low enough temperature to prevent interdiffusion or destruction of metastable phases. The study of the sensitive temperature dependence of oscillations can guide this choice.

In an ideal layer-by-layer growth, each layer is substantially completed before the growth of the next layer commences. The intensity of the RHEED pattern when the layer is partially filled will be changed by the interference between the beams reflected from the partially filled overlayer and from the substrate. Van Hove, et al. [3.27] proposed that the oscillations could be explained as a simple kinematic interference of the beam from the overlayer and the uncovered top surface. The intensity at coverage C (C=0 for no coverage and C=1 for full coverage) would then be:

$$I = |\Psi_0+\Psi_1|^2 = C^2 + (1 - C)^2 + 2C(1 - C)\cos(\phi) \qquad (3.12)$$

where $\Psi_0 = (1\text{-}C)\exp(-i\phi)$ is the wave reflected from the substrate layer and $\Psi_1 = C$ is the wave reflected from the overlayer. ϕ is the phase angle between the scattered beams from the adjacent planes. For the specular spot $\phi = 2k_ia_3\sin(\theta_i) \approx 2k_ia_3\theta_i$. In this simple model the RHEED oscillations for perfect layer-by-layer growth are a series of intersecting parabolas, with minima at half layer filling. The amplitude of the oscillations are zero at $\cos(\phi) = 1$ (the two waves are exactly in phase) and a maxima at $\cos(\phi) = -1$ (the two waves are exactly out of phase). The conditions $\phi = \pi, 3\pi$, etc. have been termed the first, second, etc. Bragg conditions and the conditions $\phi = \pi/2, 3\pi/2$, etc. have been termed the first, second, etc. anti-Bragg conditions.

If additional layers start to form before the first layer is completed, there is an accumulated effect that dampens the oscillations with the growth of each successive layer. This is more noticeable away from the anti-Bragg condition. If there is more than one layer growing at a time, the intensity in the kinematic model of diffraction would be given by

$$I = \left| \sum_{n=0}^{N} \{(C_n - C_{n+1})\exp(in\phi)\} \right|^2 , \tag{3.13}$$

where C_n is the coverage of the nth layer, starting from somewhere deep enough in the substrate that $C_0 = 1$ and stopping when $C_N = 0$.

Fe on Fe(100) Whiskers

This system closely approaches ideal metal epitaxy with no lattice mismatch, obviously. This is a base to study less perfect growths. Figs. 3.12 (a) - (c) show RHEED oscillations during several growths at room temperature. The electron beam is directed along the [110] direction. Note that the oscillations are strong; they are comparable in amplitude to the oscillations observed during the growth of semiconductors. The initial phase of the oscillations depends on the angle of incidence and the condition of the sample at the initiation of growth. We will discuss this in detail later. There are also starting transients of uncertain origins.

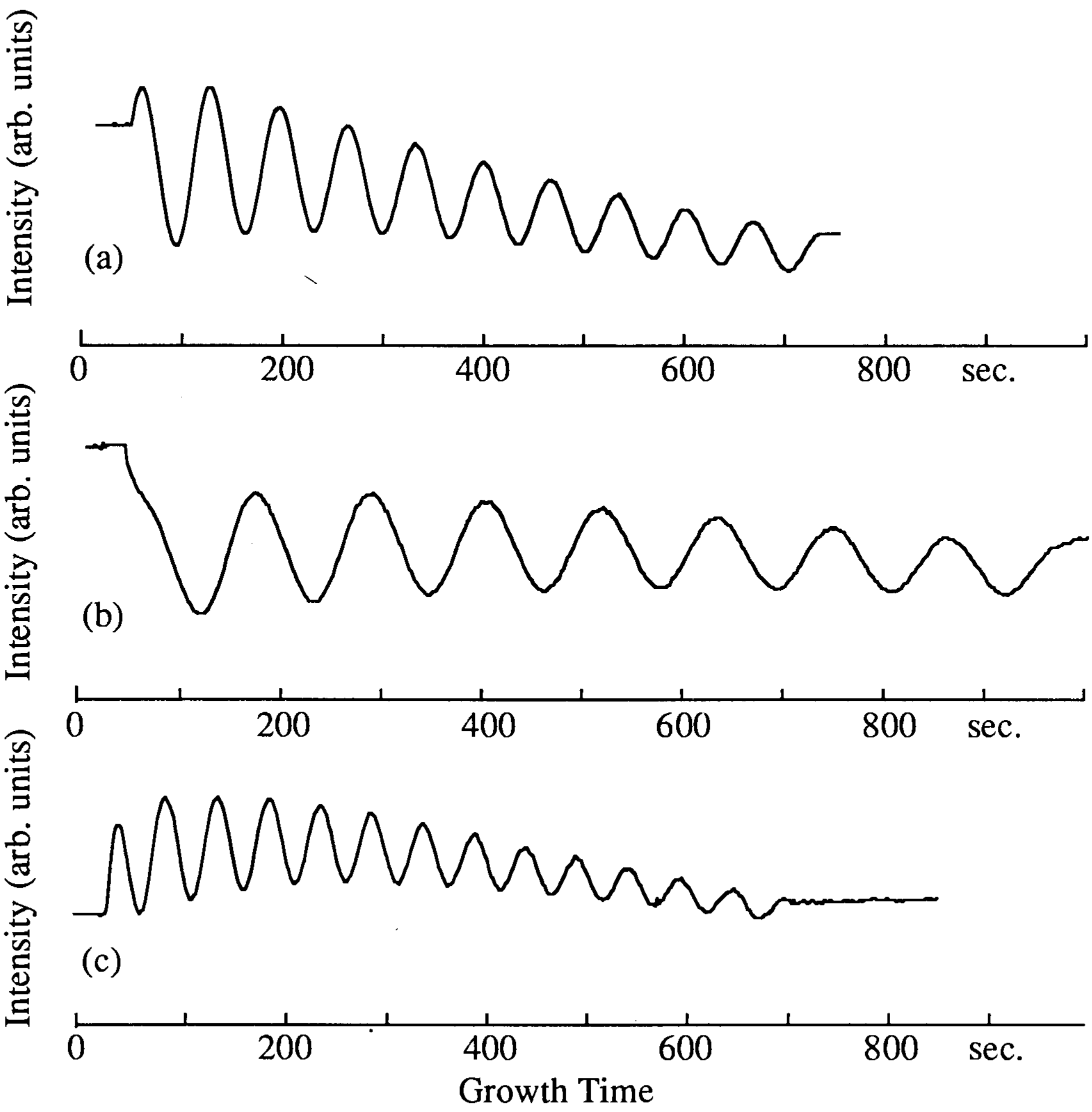

Fig. 3.12 RHEED intensity oscillations for room temperature growths of Fe on Fe(001) whiskers with the beam directed along the [110] direction approximately at the anti-Bragg condition. The growths shown in (c), (d) and (e) have varied starting oscillations which may be the result of different initial conditions of the surface or of slight variations in the angle of incidence of the electron beam.

Fig. 3.13 shows growths of Fe on an Fe (100) whisker and a 2.8° vicinal Fe sample at various temperatures. The Fe whisker has wide terraces and hence significant diffusion to step edges should occur only at relatively high temperatures. Figs. 3.13(a) and (b) show growths at 350 C and 450 C. The oscillations are much weaker at 450 C but are still visible. Neave, et al. [3.28] have explained the disappearance of oscillations at higher temperatures for GaAs as due to the growth taking place primarily from step edges. They use the known vicinal angle of their sample and the temperature at which the oscillations disappear to estimate the surface diffusion constants and activation energies for Ga. Studies of a 2.8° vicinal sample, Fig 3.13(d) and (e), show that the oscillations disappear at a much lower temperature due to the short terrace lengths (~30 Å). Yet that same substrate showed oscillations at 300 C after an anneal at 750 C without sputtering to remove the surface segregated impurities. Impurities (3% S) appear to enhance nucleation of islands, decreasing the probability of migration to the steps. This implies that one needs sensitive measurements of impurity levels before drawing conclusions about diffusion constants and growth mechanisms based upon the temperature dependence of RHEED oscillation studies as in semiconductors [3.29].

Fig. 3.14 shows the intensity of the spectral spot measured at different values of θ_i during a series of growths. The sample was rotated 6° azimuthally to avoid Kikuchi lines where large enhancements occur. The furnaces were closed between growths, but the sample was not reannealed. The phase of the oscillation was maintained on change of angle of observation. Most growths were stopped at oscillation maxima. Only slight subsequent variations of intensity were observed indicating that the Fe on Fe reanneals little at room temperature. Simple kinematic theory predicts a maximum of the oscillations at the anti-Bragg conditions and no oscillations at the Bragg conditions. We see this behaviour in Fig. 3.14, however, the angle of maximum oscillation occurs at less than anti-Bragg condition (1.3 deg). Indeed we have found that the oscillations exhibiting the largest amplitude occur for the angles of incidence much less than the first anti-Bragg condition.

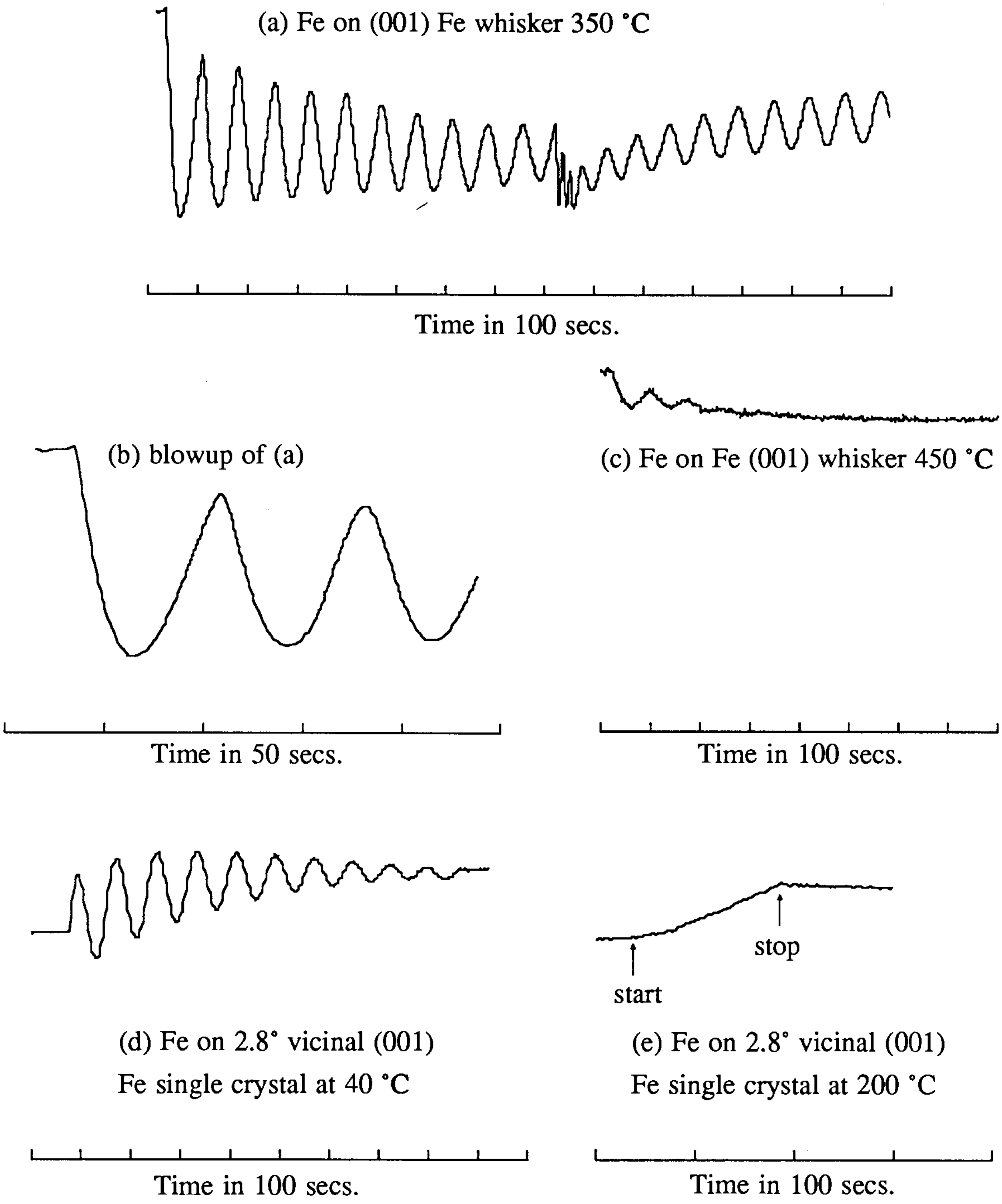

Fig. 3.13 Comparison of RHEED intensity oscillations during growth of Fe on various Fe single crystals at different temperatures. (a)-(c) Fe on Fe (001) whiskers (θ_i near anti-Bragg). (d),(e) Fe on 2.8° vicinal Fe (001) single crystal. The oscillations decrease more rapidly with temperature for vicinal surfaces of a bulk Fe (001) crystal than for an Fe (001) whisker. The first few oscillations of (a) are enlarged in (b) to show the cusp-like peaks. In the middle of growth (a) the heater wire gave a burst of Fe flux. The oscillations at 350 C recover with time.

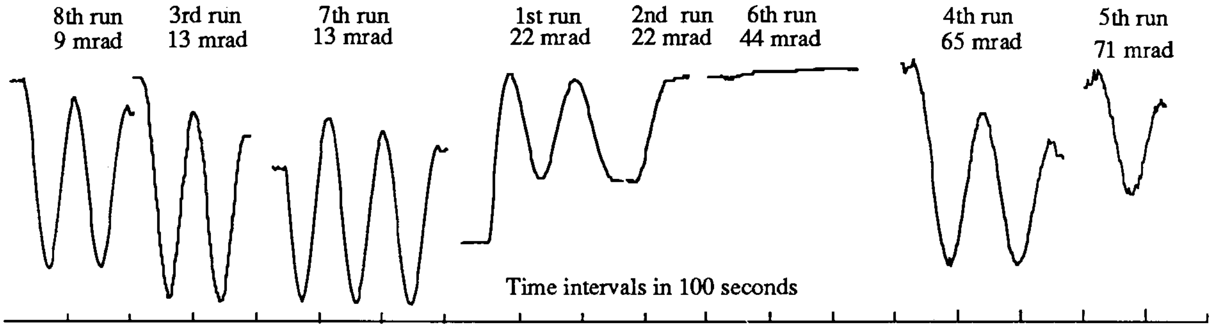

Fig. 3.14. Intensities of the spectral spot measured at different values of θ_i during a series of growths at room temperature. The data are presented in order of the angle θ_i to indicate the variation of the oscillation amplitudes with angle. The maximum intensity in each of the runs are in the ratios (1.2 / .91 / .63 / .05 / .04 / 2.7 / .26 / .17) for runs 1 through 8. The anti-Bragg angles are 22 and 65 mrad and the Bragg angle is 43 mrad.

Other Growths

The oscillations in Fig. 3.15(a) during Au growth on an Fe (001) whisker surface (.6% lattice misfit) in conjunction with the overall RHEED pattern show the onset of the Au reconstruction after starting from the Fe (001) substrate. The intensities undergo an initial complicated transient behavior before regular oscillations are established. The period then corresponds to monolayer growth. RHEED oscillations may reveal some of the dynamics of the Au reconstruction as well as yield a value for the number of surface atoms per underlayer atom.

Oscillations during the growth of Au on 5 ML of Ni grown on an Fe (001) whisker are shown in Fig. 3.15(b) and for Fe on 15 ML of Au on an Fe (001) whisker are shown in Fig. 3.15(c). Therefore even for the growth of overlayers on overlayers oscillations can be used for thickness calibrations. The initial sharp increase in (c) can be explained by the Au reconstruction rapidly reverting to (001) ordering and hence the diffraction intensity shifting from the streaks due to the reconstruction into the spectral spot .

Oscillations during less ideal epitaxial growth are often not as strong but are easily visible. As an example of a mis-matched (~4%) growth system, Fig. 3.15(d) shows the growth of Mn on Ru (0001). The bulk Ru gives long RHEED streaks characteristic of a sample exhibiting a large mosaic spread. The calibrated thickness monitor shows that the oscillations correspond to one Mn atom per Ru atom per oscillation. The first three layers are a continuation of the Ru structure. Then Mn forms a more complex structure which has been tentatively identified as a Laves phase [3.30]. The structural phase change is reflected in the disappearance of the RHEED oscillations.

Oscillations during the growth of bcc Ni on Fe (001) will be discussed in section 3.5.

These preliminary results show that in-depth oscillation studies as carried out by researchers in semiconductors can be exploited also for the study of epitaxial metallic systems. RHEED oscillations during metal and semiconductor growths show similar dependence on temperature, diffraction angles and surface impurities.

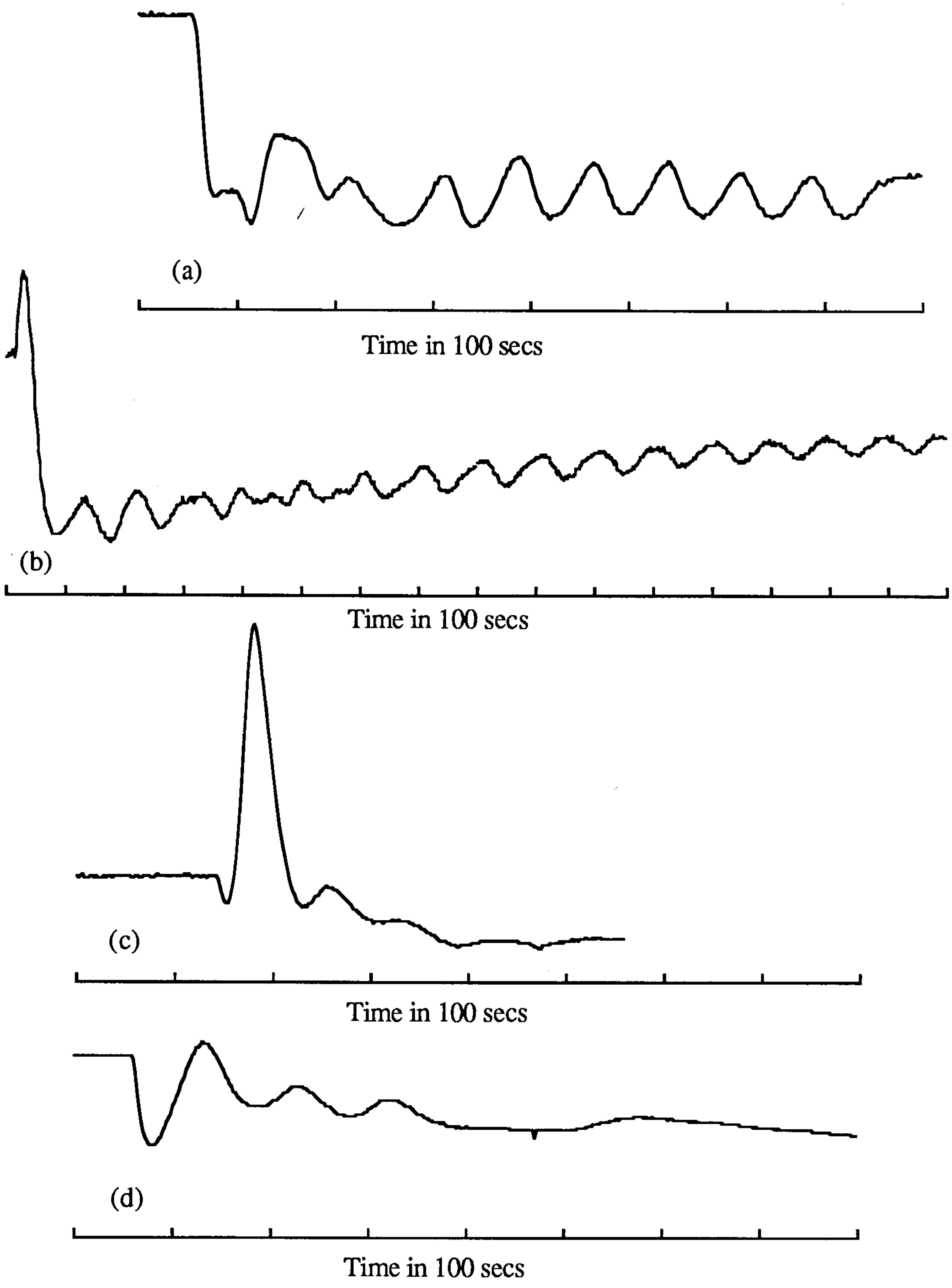

Fig 3.15 RHEED intensity oscillations during the growth at room temperature of: (a)Au on a Fe (001) Fe whisker; (b) Au on % ML of Ni on a Fe (001) whisker; (c) Fe on 15 Ml of Au on a Fe (001) whisker and (d) Mn on Ru (001). All growths were monitored at the anti-Bragg angle for the respective substrate crystals.

3.5 Ni on Fe (001) RHEED Results

Representative photos of RHEED patterns of Ni on Fe (001) single crystals are shown in Fig. 3.16 (a) - (b) for a 5 ML Ni overlayer and in (c) - (d) for a 37 ML Ni overlayer. Photos (c) - (d) have been overexposed to reveal more details of the diffraction patterns. The most obvious aspect of the patterns is that the bcc Fe (001) diffraction features are maintained for all overlayer thicknesses. This can be seen by comparing the patterns in Fig. 3.7 with those in Fig. 3.16. The streaks from the Ni covered samples are broader than the Fe substrate streaks indicating a smaller coherence length in the plane of the specimen. Also the maxima in intensity normal to the surface no longer fall on the Ewald circle but are more aligned with projections of the 3-dimensional k-space points of the bcc lattice. This is seen from the similarity between the patterns with the Ni overlayers and the patterns of sputtered Fe samples shown in Fig. 3.9. As we discussed in section 3.3, this indicates that the Ni films have a combination of a reduced in-plane coherence and a degree of roughness perpendicular to the surface. The Ni patterns however have elongated narrower streaks and hence are much smoother than the sputtered samples. In Fig. 3.17 we show a profile across the specular spot when the beam is directed along the [110] direction after 11 ML of Ni have been deposited at 200 C on the same Fe whisker used for the profiles shown in Fig. 3.10. The width of the streak has increased from ~.7 mrad for the uncovered whisker to ~2.3 mrad for the covered whisker. If we associate the angular width of the streak with the average block size as for a crystal with a mosaic spread the increase in width gives a block size of W~40 atoms. This is arrived at from the relation $W \approx K/\delta K \approx (2\sqrt{2}\pi/a)/k_i\delta\theta \approx (\sqrt{2}\lambda/a)/(2.3\text{-}.7)\text{x}10^{-3}$ where $\delta\theta$ is the angular halfwidth and $\sqrt{2}$ accounts for the fact that we measured the profile along the [110] direction. A final observation on the RHEED photos is that there are additional diffraction features visible in (c) and (d) that are not a part of the pattern from a bcc lattice. Along the [110] azimuth they are positioned between the main streaks with ~10% smaller spacing. These features are not present until the Ni overlayer reaches a critical thicknesses of 3-6 ML, varying from growth to growth, and their intensities gradually increase with Ni thickness. They have

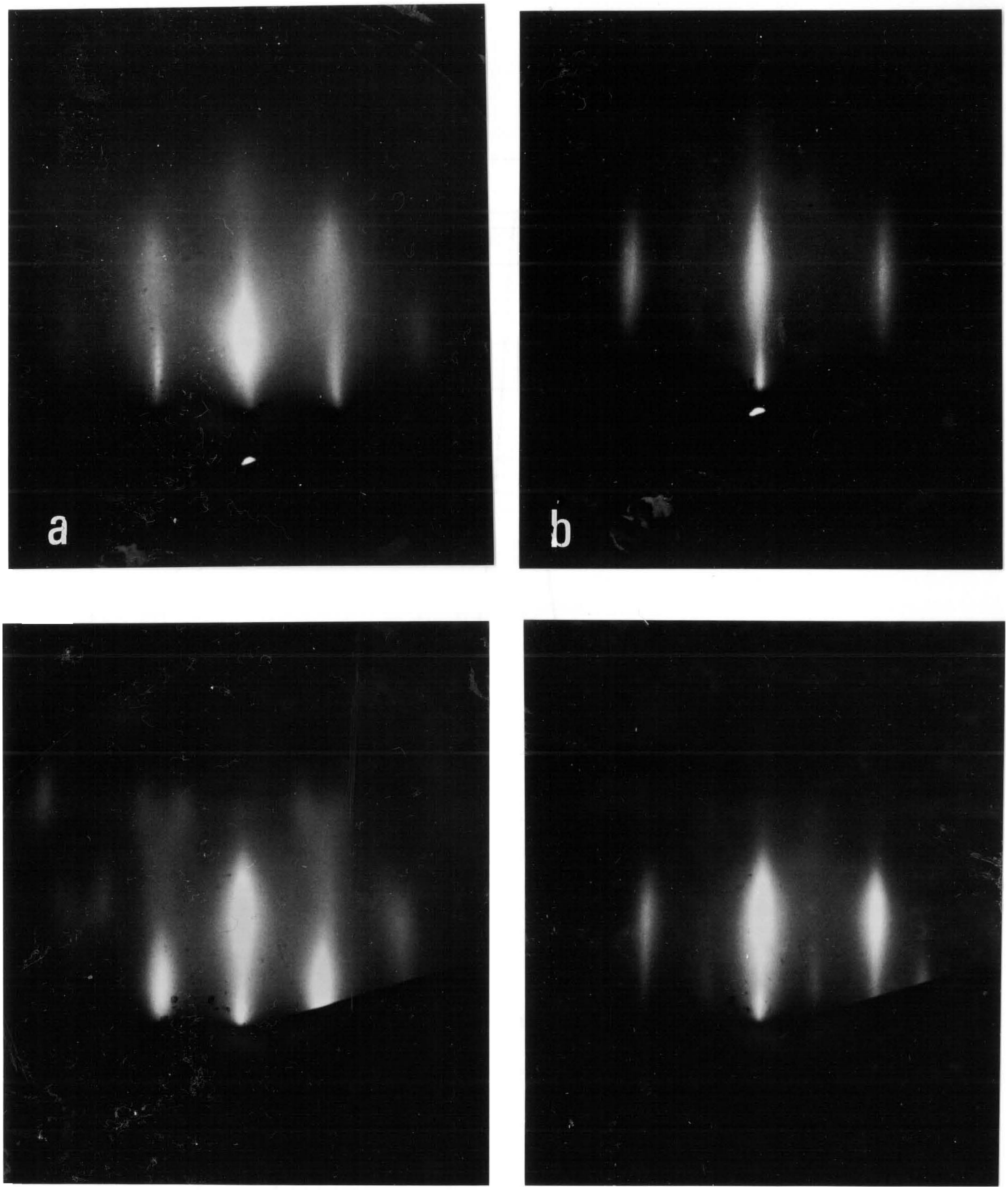

Fig. 3.16 (a),(b) [100] and [110] RHEED patterns respectively from Fe (001) sample 1 with a 5 ML overlayer of Ni grown at room temperature. (c),(d) [100] and [110] RHEED patterns from Fe (001) sample 3 with a 37 ML overlayer of Ni grown at room temperature.

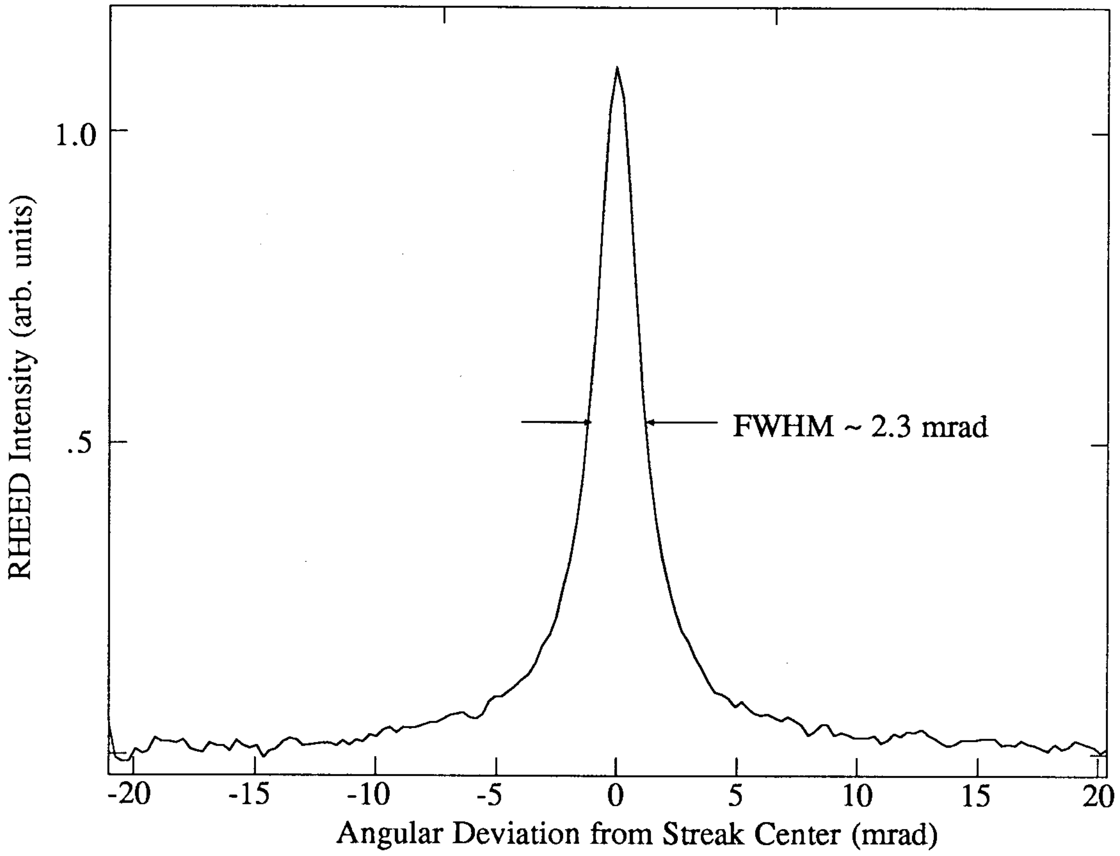

Fig. 3.17 Profile across the specular spot on a Fe (001) whisker after deposition of 11 ML of Ni at 200 C. The beam was along the [110] direction.

stronger intensities when the electron beam is directed off azimuth from the [110] and [100] directions and form a complex pattern. The spacings between the extra spots in the off azimuth patterns are a large fraction of the Fe bcc RHEED spacing indicating that the surface unit cell has increased to only several lattice spacings. At first we thought that the extra features reflected a mild reconstruction of the bcc Ni lattice similar to the reconstruction of the Fe substrates shown in Fig. 3.7(d) because the bcc features are so much more intense. We have found other evidence that the extra diffraction features may in fact represent major structural changes. Subsequent studies by Wang, et al. [3.31] using LEED also showed that the first 3-6 ML of the Ni on (001) Fe grows in a bcc structure identical to the Fe bcc lattice including the same interlayer relaxations normal to the surface. They found that the thicker layers formed a more complicated and as yet undeciphered structure. Magnetic studies discussed in Chapters 4 and 5 show that the reconstruction is connected with the unique magnetic properties of the Ni films. For brevity we will often refer to the reconstructed Ni layers as "bcc Ni", in quotation marks.

We also made careful lattice spacing measurements from the RHEED patterns during the growth of Ni on Fe. The method was originally used by Whalley, et al. [3.32] during measurements on GaAs and the setup is depicted in Fig. 2.2. Two photodetectors were placed at the [1,0] and [-1,0] streaks from a .5° vicinal Fe sample. The streaks were scanned during growth by means of a modulation of the magnetic field through which the diffracted electrons travel. We found that the spacing between the maxima of the streaks changed by only .6% during growth. Because the sample is slightly vicinal the streaks are not perfectly uniform but exhibit structure along the streak. Also Kikuchi lines cause interferences with the streaks. These effects cause the spacing between the streaks to vary along their length. The fine details in the streaks are washed out when a thick Ni overlayer is formed and the .6% change in streak spacing is well within the variation of the initial choice of the settings of the photomultipliers along the streak. The lattice spacing data shows that the main periodicities of the RHEED pattern for Ni on Fe are the same within experimental uncertainty as for the Fe (001) substrate.

RHEED Oscillations during growth of Ni on Fe (001)

RHEED intensity oscillations observed during the growth of Ni on Fe (001) whiskers and on a strain-anneal single crystal are shown in Figs. 3.18-19. Oscillations during the growth are large indicating a strong degree of layer-by-layer growth. The period during the first 2-6 ML corresponds to within experimental error (~2%) to one Ni atom per Fe atom per layer as measured by the thickness monitor calibrated using Ni on Ni (001) oscillations. At 2-6 ML the oscillations decrease more rapidly and the period decreases by ~5-20% (see Fig. 3.20) at the same time the RHEED pattern develops the additional weak incommensurate spots. The decrease in period shows that there are ~5-20% fewer atoms per layer in the modulated structure than in the bcc structure. The measurements show nicely how the RHEED oscillations tie the structural changes to a specific thickness.

We grew Ni on Fe at 200 C to see if the reconstruction would be suppressed. Observations of the RHEED patterns showed this was not the case. RHEED oscillations during this growth are shown in the insert in Fig 3.18. The rapid drop in amplitude to zero after the fifth oscillation is because the increased diffusion at 200 C allows the growth to proceed from the very short range defect structure. This is similar to the disappearance of oscillations during the growth of Fe on the vicinal Fe sample described in Fig. 3.13 (e).

Fig. 3.19 shows another interesting aspect of the oscillations during the growth of Ni on Fe. In Fig. 3.19(a),(b) we show oscillations from growth on a strain-anneal crystal with the specular spot monitored at less than the Bragg angle taken simultaneously with oscillations on the [10] beam. Comparison of the upper and lower curves in (a) or (b) reveal a clear phase shift of the oscillations (~π).

3.6 AES and XPS Intensities as a Function of Ni Overlayer Thickness

Ni overlayer growth was also studied by measuring the dependence of AES and XPS peak intensities of substrate and overlayer atoms on the added film thickness. This gave information about the uniformity of the overlayer and the degree of layer-by-layer growth. If the overlayer

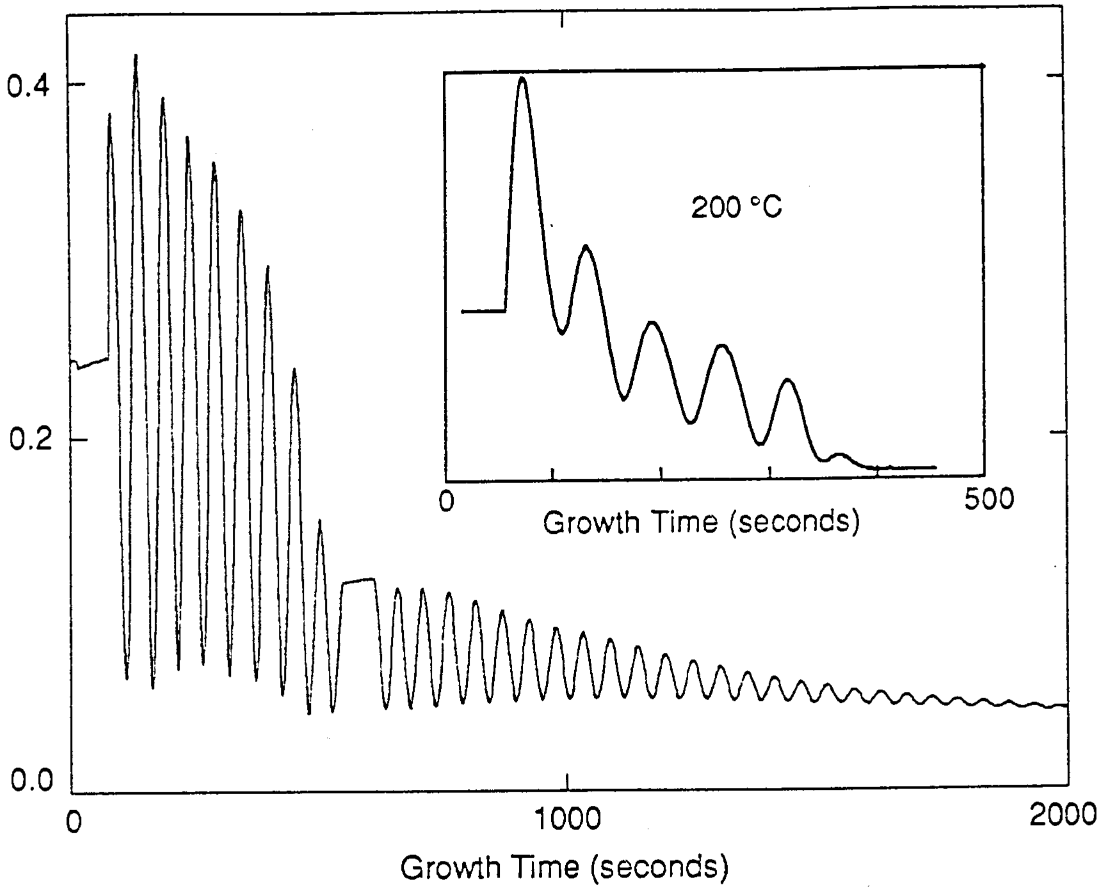

Fig. 3.18 Rheed Oscillations during the growth of metastable bcc Ni on Fe (001) whiskers at room temperature and 200 C. The oscillations decrease rapidly at 6-7 ML, where the RHEED pattern indicates a modulation of the bcc structure.

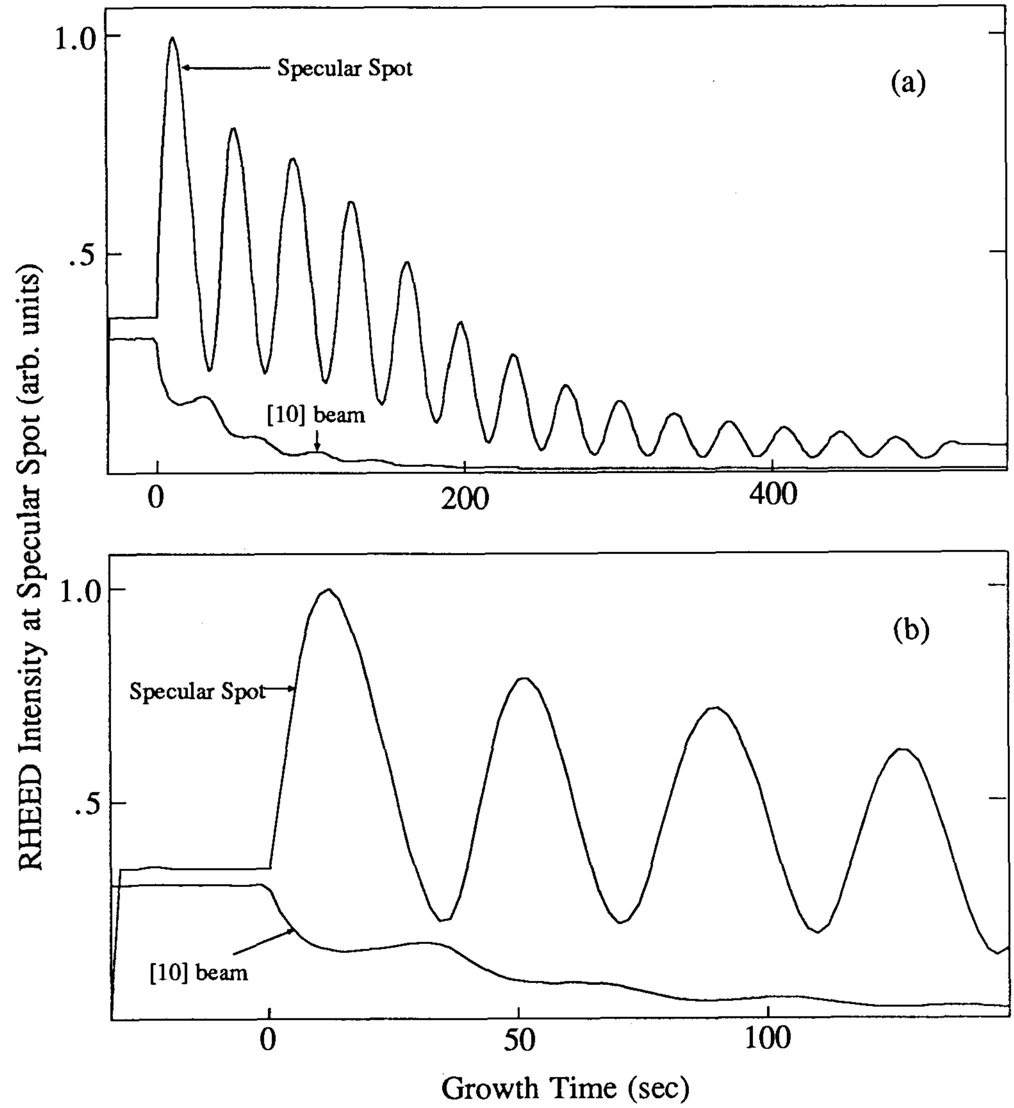

Fig. 3.19 RHEED intensity oscillations during the growth of Ni on a Fe (001) strain-anneal single crystal. The incident beam was rotated 6 deg azimuthally from the [110] direction in both growths to avoid Kikuchi lines. (a) and (b) show the intensity at the specular spot and [10] beam monitored simultaneously when the angle of incidence was 1 deg (less than the anti-Bragg angle). This clearly shows that the oscillations are out of phase (~180 deg). (b) is a blowup of the first four oscillations of (a) to show that the first oscillation is higher than the next few.

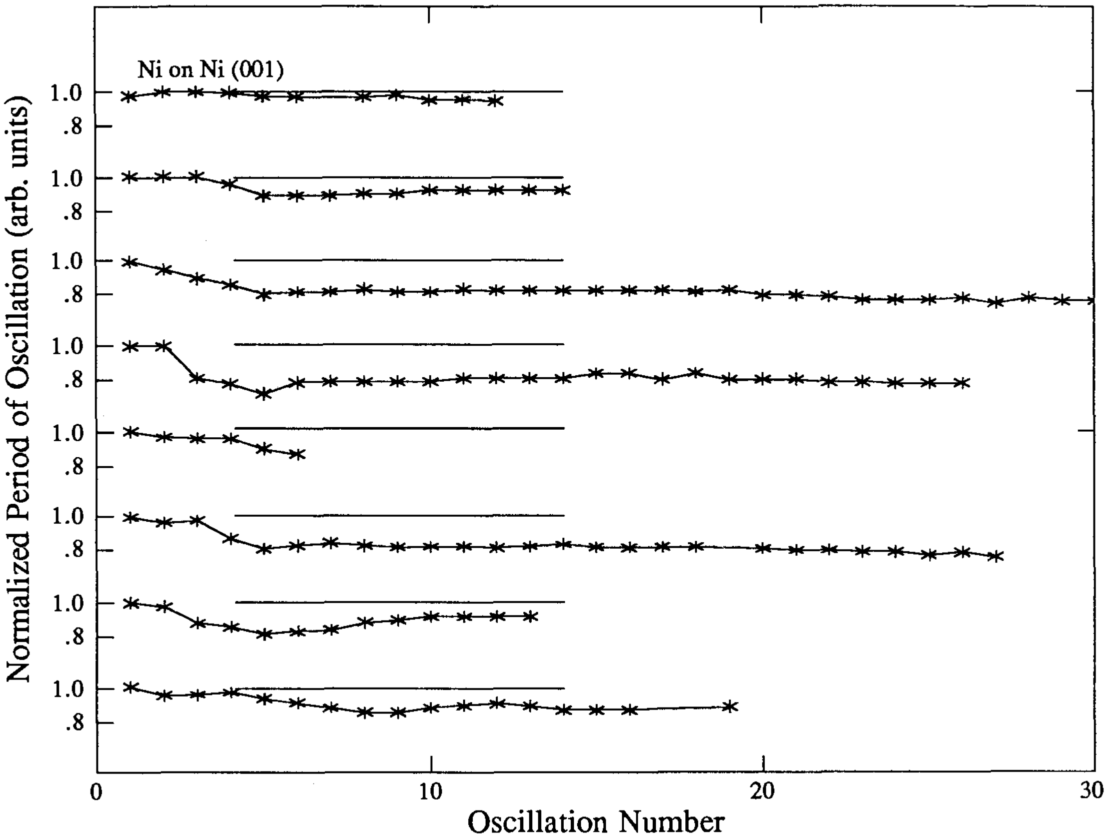

Fig. 3.20 Plot of the normalized periods of RHEED oscillations vs the chronological order of the oscillations for various growths of Ni on Fe (100) single crystals. The top set of data is for oscillations during the growth of Ni on a Ni (100) single crystal. All the data sets for Ni on Fe growth show that the period of oscillation decays after the second to fifth oscillation. The Ni on Ni (001) periods are displayed to show the constancy of the Ni furnace flux.

forms uniformly without clumping into islands or without migration of the substrate atoms to the surface, the substrate intensities will decrease approximately exponentially with increasing overlayer thickness and the overlayer intensities will increase roughly exponentially to a final constant value characteristic of very thick samples. If there is substantial completion of a layer before the next layer begins to form, the intensity curves will be a series of connected straight lines exhibiting decreasing slopes that fall roughly on the exponential curves. Breaks in the plots will occur at the times during growth corresponding to the completion of a monolayer.

The results for the AES Fe KLL line (45 eV), the XPS Fe $2p_{3/2}$ line (547 eV) and the XPS Ni $2p_{3/2}$ line (401 eV) peak intensity as a function of Ni mass are shown in Figs. 3.21 (a-c) respectively. The AES and XPS peak intensities of both the substrate and overlayer atoms follow an exponential dependence. For each data point we have to first deposit some mass on the sample in the growth chamber and then remove the sample to the analysis chamber to measure the AES or XPS intensities. This causes some uncertainties in the intensities and makes it difficult to distinguish breaks in the curves. In retrospect we should have measured the intensities at smaller increments of growth. Our best evidence for layer-by-layer growth is still the strong RHEED oscillations. It can be seen from the thickness dependence of the AES and XPS intensties that the overlayer grows uniformly without clumping or significant interdiffusion. To quantify this statement the exponential constants must be analyzed. The basic equations for the substrate and overlayer peak intensities are respectively:

$$I = I(0)\exp(-\sqrt{2}d/\lambda_s) \qquad I' = I'(\infty)(1-\exp(-\sqrt{2}d/\lambda_o) \tag{3.15}$$

where d is the overlayer thickness, λ_s and λ_o are the IMFP's of the electrons and the $\sqrt{2}$ accounts for the fact that the electron analyzer accepts emitted electrons at approximately 45° with respect to the sample surface. Estimates of the IMFP's in nanometers accurate to 20% can be made from the empirical formula [3.33]:

$$\lambda = \frac{A}{N^{1/3}E^2} + B\left(\frac{E}{N}\right)^{1/2} \tag{3.14}$$

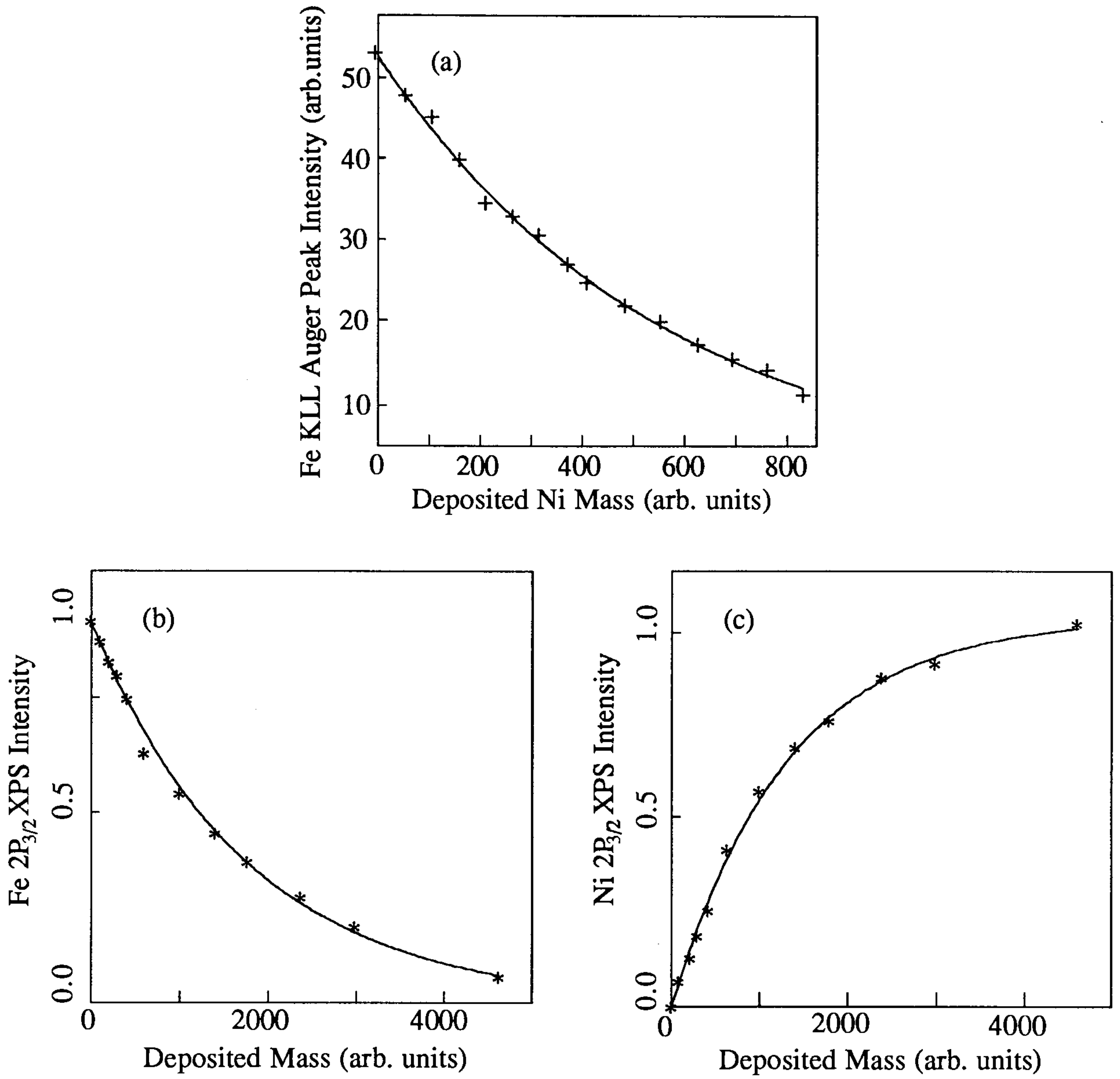

Fig. 3.21(a) The dependence of the intensity of the Auger KLL Fe substrate line on the mass of nickel deposited upon an Fe (001) substrate. (b) The decrease of the principal Fe XPS $3p_{3/2}$ peak signal and (c) the growth of the Ni $3p_{3/2}$ XPS signal vs the mass of nickel deposited (same growth for (b) and (c)). The mass scale was taken from the mass spectrometer output and was calibrated as 300 ± 10% mass units per ML by RHEED oscillations. The data points fall fairly well on the exponential curves.

where $A=538\ eV^2$, $B=.41\ nm^{-1/2}\ eV^{-1/2}$, N is the number of atoms per nm^3 (85.0 for Fe) and E is the kinetic energy of the electron. For the Fe 45 eV AES, Fe 547 eV XPS and Ni 401 eV XPS electrons passing through Ni assumed to have the same number density as Fe we calculate $\lambda = 2.9$ Å, 10.4 Å and 8.9 Å respectively. We got good agreement between the thicknesses measured from the calibrated mass units and the thicknesses determined from the exponential decrease (increase) of the spectral intensities. This would not be the case if the surface were significantly non-uniform. The mass spectrometer was used for thickness measurements (this was before we had installed a quartz thickness monitor). The calibration obtained was 1 ML Ni per 300±10% mass units as determined from RHEED oscillations. The comparisons at the 1/e values of the curves are: d=2.1 Å from the Fe AES intensity decrease vs 2.6 Å from mass units; d=7.4 Å from the Fe XPS intensity decrease vs 8.1 Å from mass units; d=6.2 Å from the Ni XPS intensity increase vs 6.3 Å from mass units. This demonstrates that the Ni films are indeed very uniform. Furthermore, the dependence of the Fe and Ni XPS peak intensities on the thickness of the bcc Ni overlayer clearly shows an exponential decrease for an overlayer coverage well in excess of six monolayers (see Fig. 3.21 (b),(c)). Therefore the decrease of the RHEED oscillation amplitude after the first six monolayers does not signify a dramatic change in the film uniformity.

3.7 REELFS Studies of Ni(001) and Fe(001) Single Crystals and Ni layers on Fe(001)

RHEED studies give information about the periodicity and coherence of the films particularly in the plane of the specimen. Reflection electron energy loss fine structure (REELFS) spectroscopy is an in situ technique which can be used to reveal the local structure around an individual atom [1.5,3.34,] similar to the more developed Extended X-ray Absorption Fine Structure (EXAFS) spectroscopy [3.35-36]. We used REELFS to study 30 ML thick Ni films grown on Fe (001). The results have been reported in detail elsewhere (see Heinrich, et al. [1.8]) and will be briefly summarized here.

A REELFS spectrum is obtained by directing an electron beam of kinetic energy E_P onto the sample at nearly normal incidence and measuring the reflected electrons as a function of energy. Some of the resulting reflected electrons have been knocked out of specific core levels of the atoms by the incident electrons. The electrons ejected from the core levels can have any kinetic energy, E_K, between zero and the difference between the incident energy and the binding energy (E_P - E_B). The spectrum is peaked at the ionization edge $E_K = E_P - E_B$ and tails off as $E_K \rightarrow 0$. In the tail there is a fine structure caused by the partial reflection of the emitted electrons by neighbouring atoms. The fine structure occurs because the final state wave function of the ejected electron is composed of an outgoing wave and the reflection of this wave from neighbouring atoms. The final state wave function at the central atom position is larger or smaller depending upon the phase change 2kr from the central atom to the reflecting atom and back, where k is the electron wavevector magnitude. Thus the modulation of the REELFS spectrum due to a neighboring atom is a sum of waves of the form $\sin[2kr + \delta(k)]$. $\delta(k)$ is a slowly varying phase shift that can be calibrated from measurements on known structures or estimated theoretically. A Fourier transform of the energy spectrum, after rescaling to a function of k, is a function of r showing peaks corresponding to the various near neighbour atomic shells around the central atom. The positions are slightly shifted because of the phase shift δ.

We measured spectra for the $2p_{3/2}$ states of Ni (001) and Fe (001) single crystals and ~30 ML of Ni on Fe (001). It would have been preferable to have made measurements on Ni films of 6 monolayers or less thick since we believe they are in the pure bcc form but the Fe $3p_{3/2}$ spectrum then interferes with the Ni $3p_{3/2}$ spectrum. Hence data was acquired for Ni films sufficiently thick so as to eliminate the Fe signal.

The principle conclusions regarding nearest neighbour positions can be drawn from examining the Fourier transform magnitude (Fig. 3.22). The large peaks at approximately 2.3 Å are caused by reflections from the nearest neighbour atoms. This implies a phase shift of ~.2 Å because the n.n.d.'s in bcc Fe are 2.48 Å and in fcc Ni 2.49 Å. Within the

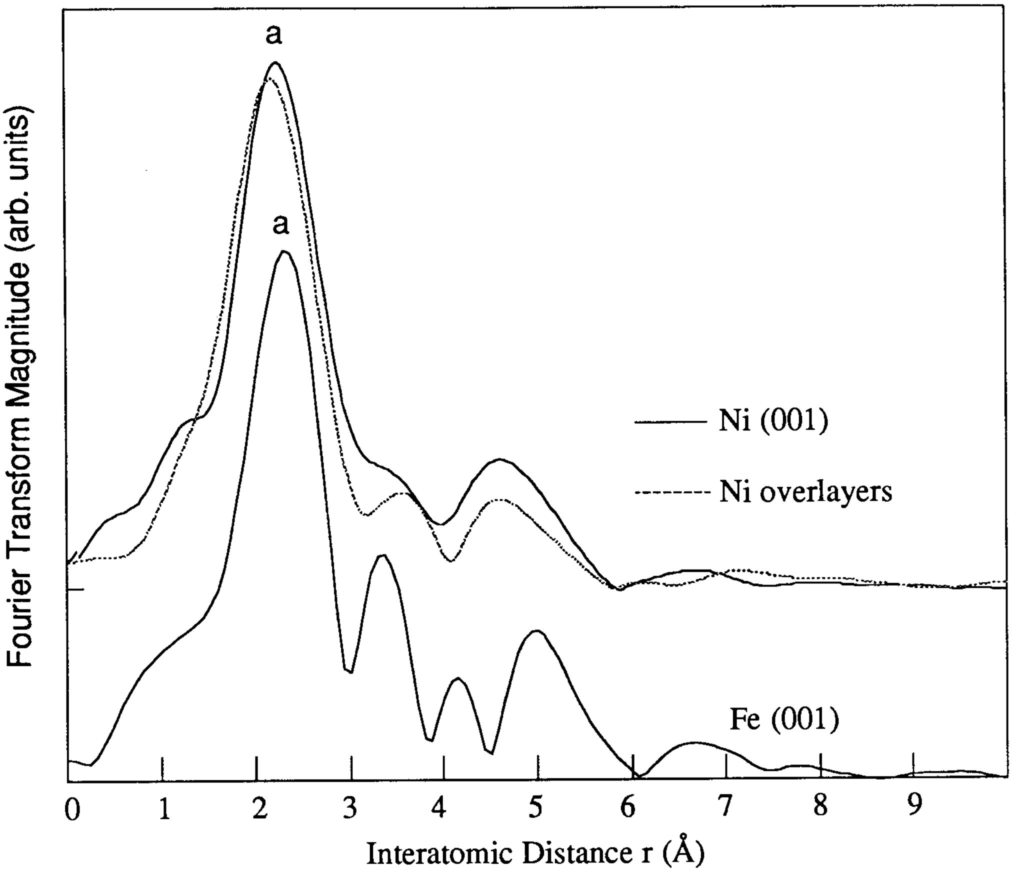

Fig. 3.22 The Fourier transforms of the REELFS spectra from fcc Ni, bcc Fe and 30 ML of Ni on Fe (001). The peaks in the Fourier transforms are related to neighbouring atomic positions around a central atom. The peaks labelled (a) correspond to the nearest neighbour distance of fcc Ni and bcc Fe.

experimental error (0.05 Å) the n.n.d. in the Ni overlayers is identical with that of ordinary fcc Ni or bcc Fe. It therefore follows that the nickel overlayers on Fe(001) cannot be simply an expanded form of the fcc lattice which would have a similar RHEED pattern. Positions of the atoms further than the n.n.d. are not in consistent agreement with the known structures of bcc Fe and fcc Ni if a phase shift of .2 Å is used. It appears that REELFS is reliable only for the first nearest neighbour. However, by inspection of Fig. 3.22 we see that the REELFS spectrum of the Ni overlayer more closely resembles fcc Ni than bcc Fe. If the REELFS spectra reflects the atomic structure then we would conclude that the thick Ni overlayers have more nearly a fcc ordering than a bcc ordering. Recent EXAFS measurements on a 37 ML film by Jiang, et al. [3.37] showed that the structure of the films was very close to the fcc order. This is in apparent contradiction with our RHEED patterns which show strong bcc order.

3.8 Summary of Ni on Fe (001) Structural Studies

The results from the RHEED, AES, XPS and REELFS studies can be summarized as follows. The first 3-6 ML of Ni grows layer-by-layer in the pure bcc form as determined by the symmetry of RHEED patterns, the period of the RHEED oscillations and the exponential dependence with overlayer thickness of the XPS/AES intensities. At a critical thickness of 3-6 ML extra diffraction features begin to appear which strengthen with thickness showing that the film has undergone a local restructuring to a more complicated form. The main bcc diffraction features remain in the pattern but become broader with increasing thickness indicating increasing disorder in the samples. The continuance of the RHEED oscillations after reconstruction and the exponential dependence of the XPS/AES intensities shows that the overlayer still forms mainly in a layer-by-layer fashion. From the decrease in the period of the oscillations it is deduced that the layers contain 5-20% fewer atoms per layer after reconstruction than the (001) bcc Fe substrate. The REELFS measurements show that the n.n.d. is the same in the thick overlayers as in fcc Ni or bcc Fe and the local order may be more similar to fcc Ni than to bcc Ni. The fcc local order of the top of the thick films has been confirmed by recent EXAFS experiments [3.36].

The above results do not allow complete determination of the structure of the reconstructed Ni films. However they do provide a reproducible set of data to which other growths can be compared and upon which the dependence of the magnetic properties can be quantified.

There are several possible explanations of the apparent disagreement between the RHEED patterns and the REELFS/EXAFS data. One explanation is suggested by our studies of reconstructed Au films on Fe (001). It is possible that the reconstructed Ni starts to grow in a distorted fcc structure having the same density. This structure must contain defects caused by the mismatch with the bcc substrate since there are no matching planes between the two lattices. Since the defects or distortions of the fcc lattice are tied to the substrate the diffraction will still pick up the bcc periodicity just as the diffraction from the reconstructed Au (001) surface. A possible fcc plane for growth is the (110) plane which for Ni has 7% fewer atoms than the (001) bcc Fe. This would explain part of the decrease in the number of atoms per layer that was determined from the decrease in the period of the RHEED oscillations. The rest of the missing atoms could be excluded from misfit dislocations at the edges of blocks of the (110) unit cells. Two perpendicular orientations of (110) blocks in the plane would have to exist to explain the cubic symmetry of the RHEED patterns. This would imply a cubic symmetry for the defect structure, and this requirement agrees with our magnetic measurements (see chapters 4 and 5). One potential problem with this theory is that in thicker films we clearly see three dimensional bcc periodicities. That is, the bcc structure is maintained normal to the plane as well as in the plane. The argument that bcc coordinated defects cause the bcc periodicity in the RHEED holds only in the plane. However the difference between the perpendicular spacing for (110) fcc Ni (1.25 Å) and (001) bcc Fe (1.43 Å) is only 13%. This would be hard to distinguish on RHEED patterns normal to the surface. Another possibility is that the film is a mixture of bcc and fcc phases which becomes more fcc with thicker coverages. This would explain the gradual increase in the intensities of the extra RHEED diffraction features and also the results of the REELFS and EXAFS data which are heavily weighted towards the region of the film closest to the surface. The defect structure would still have a loosely cubic symmetry because of the continued presence of the bcc form. Also there is the possibility that the REELFS and EXAFS data do not reflect the true structure of the films and that they are indeed slightly reconstructed bcc Ni. The equilibrium spacing of bcc Ni is likely to be somewhat different than bcc Fe and hence the films would develop elastic strain as Ni is deposited. At a critical thickness this strain may be reduced by the formation of a network of misfit dislocations as pictured ideally in Fig. 3.3(a). Finally there is the possibility that the unit cell is much more complicated and should not be thought of as either bcc or fcc-like. The EXAFS data provides reliable information only to about the third nearest neigbour. The apparent fcc ordering may be just a short range property of the larger unit cell.

It is clear that there will be strains in the Ni films because of the missing atoms and the matching of the larger unit cell to the bcc underlayer. This may be enhanced if the equilibrium spacing of the bcc Ni does not match bcc Fe. Strain is known to cause magnetic anisotropy in ferromagnetic materials. We will see in the next chapters that there is a strong correlation between the defects created in the overlayer at reconstruction and the existence of a large cubic magnetic anisotropy.

3.9 Growth Studies of Epitaxial Ultrathin Ni/Fe Bilayers Grown on Ag (001)

In this section we describe the growth of the Ni/Fe bilayers whose magnetic properties are discussed in detail in chapter 5. All depositions were carried out with the sample substrate held at room temperature (T = 300 K). The deposition rates were measured using the Mathis quartz crystal thickness monitor.

Fe overlayers can be grown epitaxially on bulk Ag substrates. However Ag(001) and Fe(001) lattices are well matched only in the (001) plane. There is an appreciable vertical mismatch due to the large tetragonal distortion between the fcc and bcc lattices. The presence of atomic steps affects the growth and magnetic properties of Fe on the bulk Ag(001). The

RHEED patterns obtained from 5.6 ML of Fe on Ag (001) are shown in Fig. 3.23(a),(b). The patterns show that the films have a degree of roughness greater than the annealed Fe (001) single crystal (see Fig. 3.7(c)(d)) because features of the three dimensional k-space are visible. The Fe films epitaxially grown on vicinal Ag substrates showed RHEED oscillations only after three to four atomic layers were deposited, see Fig. 3.24. Perhaps the complete bcc unit cell has to be formed before a well defined layer-by-layer growth is attained. Even though the lattice spacings of Ag(001) and Fe(001) match, the Fe atoms are not nearest neighbours in the (001) plane and the Fe-Fe bonding may be strong enough to pull the Fe atoms of the first layer from the four-fold hollow sites of the Ag (001) surface.

The growth of Ni on ultrathin Fe(001) on bulk Ag(001) was similar to the growth of Ni on bulk Fe(001). They exhibited similar RHEED patterns and the films had the same critical thicknesses at which reconstruction took place. Very thin Ni layers grow epitaxially in the pure bcc structure with the in-plane lattice spacing corresponding to pure bcc Fe (see Fig.3.23(c-d)). The Ni growth on ultrathin Fe films showed very weak RHEED oscillations when vicinal Ag substrates were used. However the Ni growth on ultrathin Fe on singular Ag substrates showed well defined RHEED oscillations during the entire growth, see Fig. 3.25, indicating that the growth of Ni overlayers proceeded layer-by-layer.

The decrease in intensities of dominant XPS and AES peaks of the substrate material during deposition was used to evaluate the overall homogeneity of deposited films. For the Fe on Ag samples the thicknesses determined from AES and/or XPS were in agreement to within 1/2 ML with those given by the thickness monitor. In addition, the AES and XPS spectra showed that the bulk Ag(001) substrates and epitaxially grown Fe and Ni films were free of surface contaminants (less than .05%).

Further information about the Ni/Fe bilayer structure was obtained from careful measurements of the Ag MNN (356 eV) and Fe LMM (703 eV) Auger peak intensities as a function of Fe and Ni overlayer thicknesses. Agreement of the thicknesses determined from the Ag Auger peak intensity, quartz thickness monitor and RHEED intensity oscillation showed

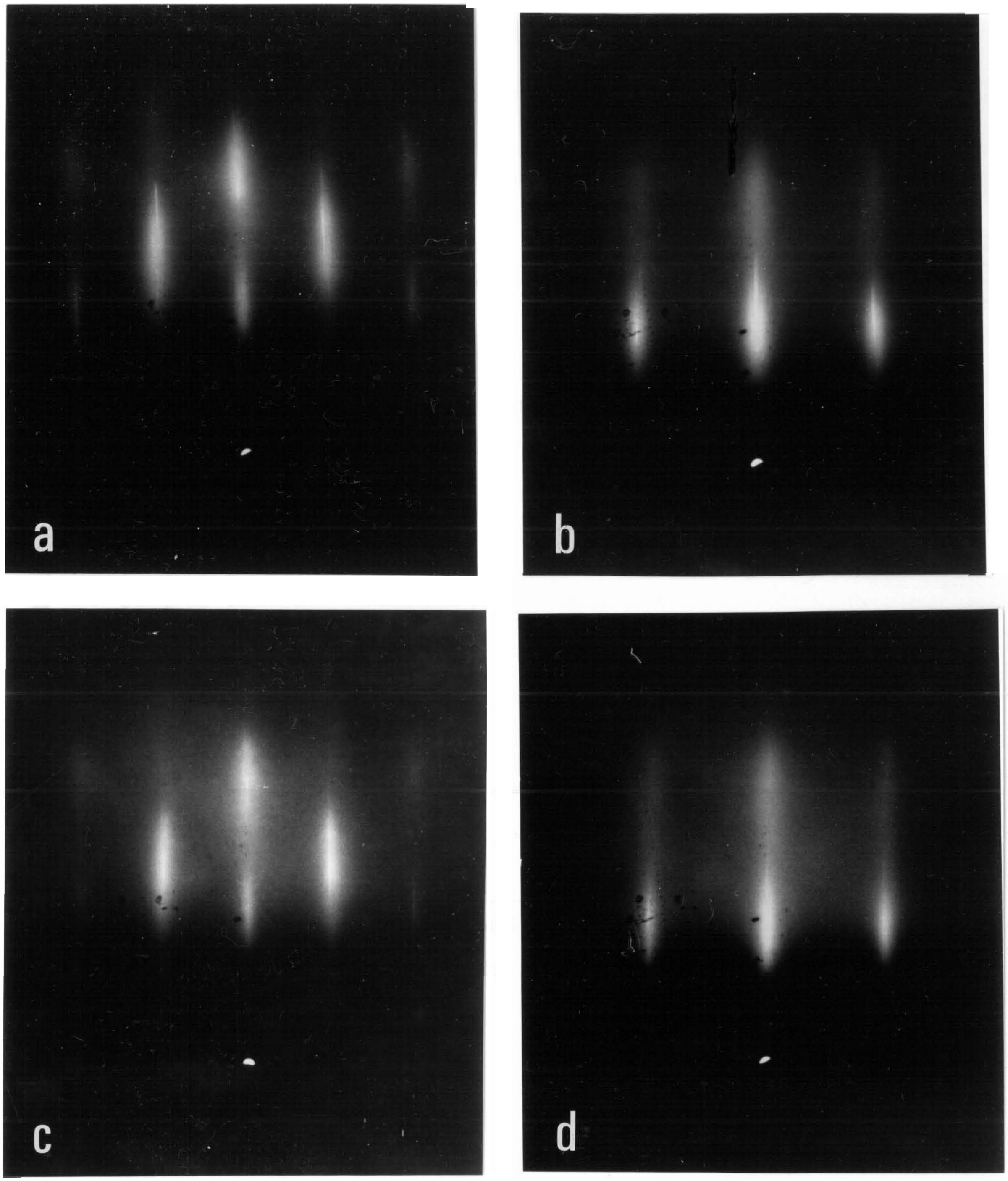

Fig. 3.23 (a),(b) RHEED patterns from sample NiFe(3.5/5.6): (a)-(c) 5.6 ML of Fe on Ag (001); and (d)-(f) 3.5 ML of Ni on the 5.6 ML Fe on Ag (001). The incident electron beam (10 keV) is directed along the Fe [100] azimuth in photos (a) and (d) and along the Fe [110] in (b) and (e). The Ni on Fe on Ag patterns are almost identical with the Fe on Ag patterns and display no extra diffraction streaks.

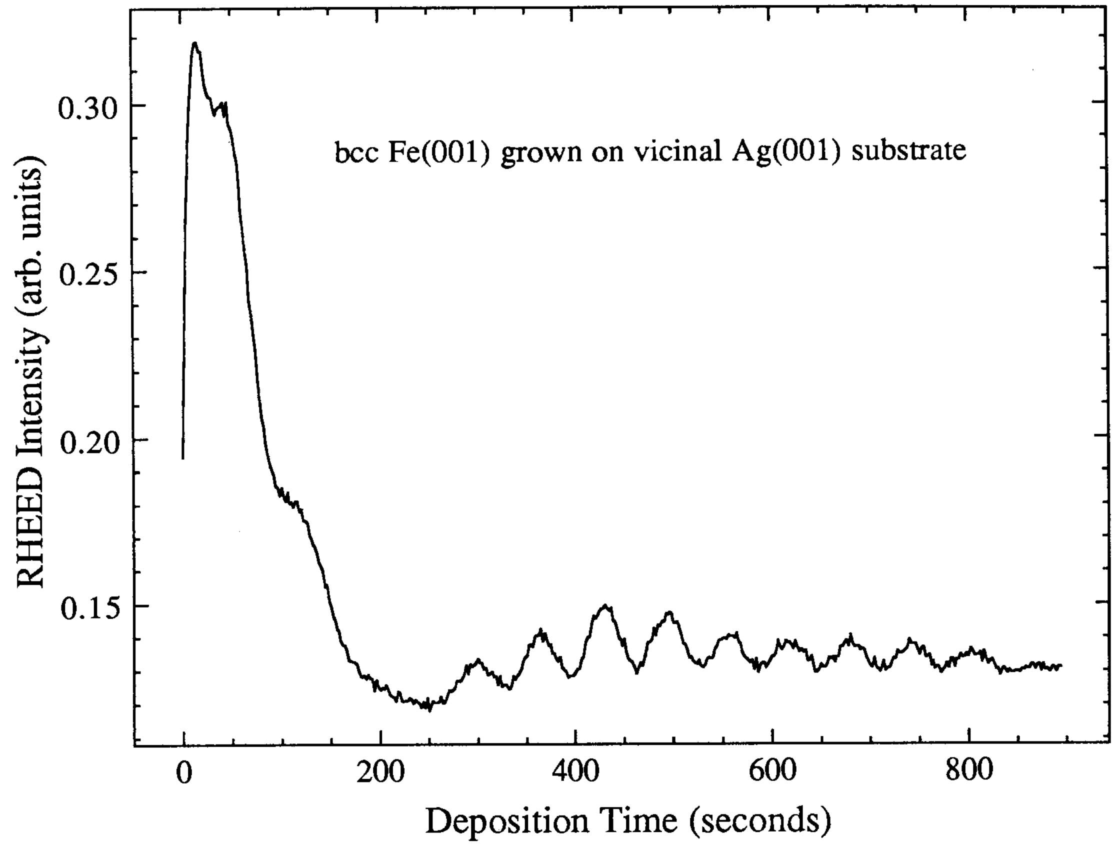

Fig. 3.24 Oscillations in the intensity of the spectral spot during the growth of Fe on a bulk vicinal Ag (001) substrate. The electron beam angle of incidence was 4° and was rotated 6° azimuthally from the Fe [110] to avoid interference with Kikuchi lines. After an initial transient period there are regular oscillations whose period corresponds to the deposition of (001) bcc Fe.

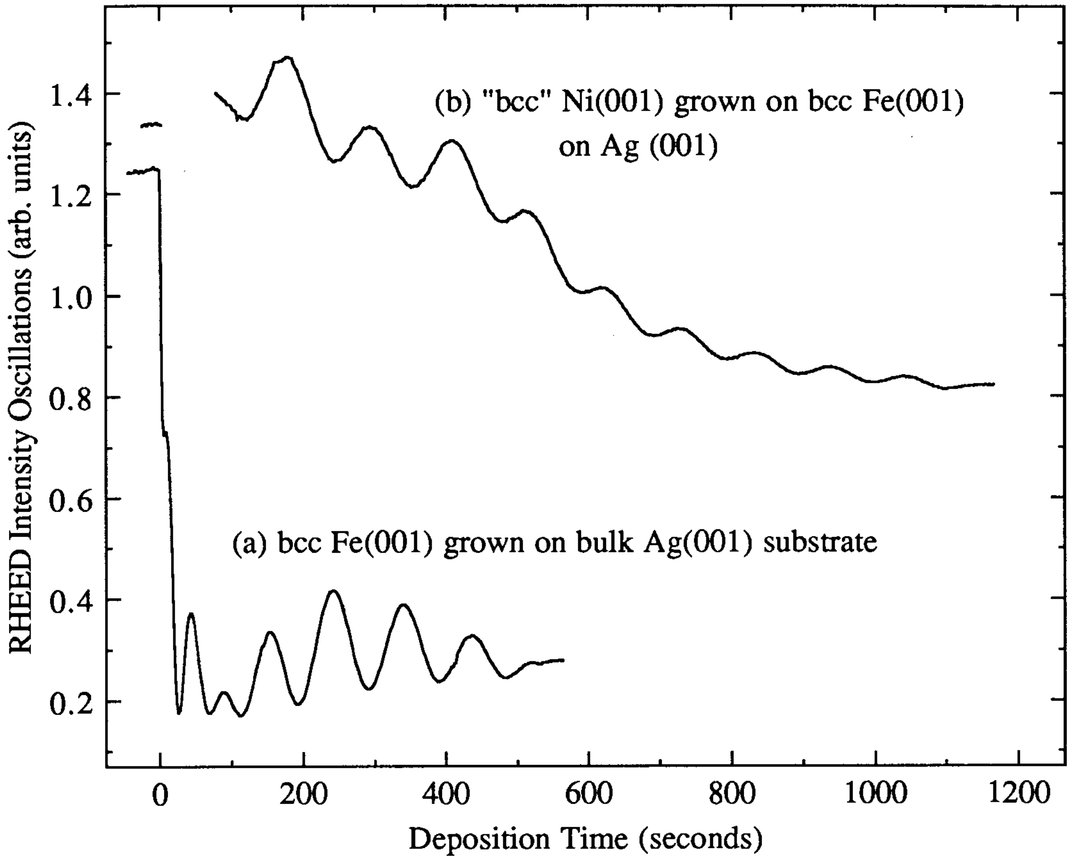

Fig. 3.25 RHEED oscillations during the growth of: (a) Fe on singular Ag (001); (b) Ni on the Fe overlayer of (a). Notice that the oscillations are present during the entire growths of both layers (data recording failed during first half monolayer in (b)). The angle of incidence of the electron beam was .9 deg, corresponding to the first anti-Bragg condition of Ag(001), and was directed along the Ag [110] direction.

that the Fe formed a homogeneous layer on the Ag. However, all reconstructed Ni overlayers grown on ultrathin Fe films showed a significantly smaller apparent Ni thickness, as determined from the Ag Auger peak intensity, than thicknesses from RHEED intensity oscillations and the quartz thickness monitor. The Ni thicknesses determined from the Fe Auger peak intensities were in excellent agreement with RHEED oscillations and the quartz thickness monitor measurements. Therefore the Ni covers the Fe homogeneously. These seemingly contradictory results can be explained by assuming either that the Ag substrate became somewhat exposed along misfit dislocations or that the Ag substrate atoms partly defused along misfit dislocations to the sample surface. In either case the dislocation would not be limited to the Ni overlayers but would propagate throughout the whole Ni/Fe bilayer structure. Further studies using angular resolved Auger and XPS measurements are needed to determine the behavior of Ag substrate atoms during "bcc Ni" lattice reconstruction. A model of the reconstructed Ni overlayer based on a text book picture of a relaxed bcc Ni lattice accompanied by a network of misfit dislocations is probably too crude. Other surface science tools, such as scanning tunneling microscopy, are needed to develop a more precise model for reconstructed Ni overlayers.

"Bcc Ni" overlayers can be epitaxially grown directly on Ag(001) substrates. When Ni was deposited on bulk Ag the large vertical mismatch between the Ag and Ni lattices resulted in a more three dimensional growth. Also additional superlattice RHEED streaks appeared with increasing Ni overlayer thickness. These additional features were not observed in Ni growths on Fe substrates.

Chapter 4

Ferromagnetic Resonance Studies of Fe (001) Single Crystals Covered with Epitaxial Ni Overlayers

4.1 Introduction

The main purpose of this chapter is to discuss the magnetic properties of Ni overlayers grown epitaxially on the (001) surfaces of bulk Fe single crystals [1.7-8]. The properties of interest are the saturation magnetization, the magnetocrystalline cubic and surface anisotropy constants, the g-factor, the exchange constant and the Gilbert damping constant. We used ferromagnetic resonance (FMR) to study these magnetic properties. The basis of the technique is that the magnetization has a characteristic frequency of precession that depends on the magnitude and direction of the total internal field. The effective internal field depends on the magnetic parameters of the material as well as upon the externally applied field. Microwaves of fixed frequency are used to drive the precessional motion in a ferromagnetic sample placed in an external magnetic field which is varied to change the characteristic frequency of precession. The absorption of microwaves is a maximum when the microwave frequency matches the characteristic precessional frequency. This absorption is measured as a function of applied field and is termed the ferromagnetic resonance. The resonance has a linewidth that depends on the damping processes.

Microwaves which fall upon the plane surface of a metallic sample are exponentially damped by eddy currents within a skin depth of the surface. The magnetic field dependence of the absorption is sensitive to the boundary conditions or "surface pinnings" that are imposed on the magnetization at the surface. This is analogous to a vibrating string which can have either fixed, free or partially free ends. In this series of experiments we are measuring the effect that an ultrathin Ni overlayer has on the FMR of an Fe single crystal as a result of changing the boundary conditions at the Ni-Fe interface. The Ni overlayer has an effect on both the resonance position and lineshape and this effect depends on the magnetic properties of the Ni.

Crucial to the experiments is that the intrinsic linewidth of Fe is sufficiently small so that the changes in the FMR due to an overlayer can be detected.

This chapter is organized as follows. Section 4.2 is an introduction to the theory of ferromagnetic resonance in metals with emphasis on the application to Fe. In section 4.3 we discuss measurements of FMR on Fe (001) single crystal surfaces prepared in UHV and covered with epitaxial overlayers of Au or Ag [1.13]. This was done as a preliminary to measurements of Fe with ultrathin Ni overlayers (~10Å) and to determine the surface anisotropy at a well-defined Fe interface. In section 4.4 we discuss the extension of FMR theory to the case of a ferromagnetic metal exchange-coupled to a ferromagnetic overlayer characterized by magnetic properties which are different from the bulk. Section 4.5 describes the FMR measurements of Fe covered by epitaxial Ni overlayers of various thicknesses. Also in this section the results are analysed using the theory of section 4.4 to deduce the magnetic properties of the Ni overlayers as a function of overlayer thickness. We conclude that "bcc Ni" as formed in thicknesses up to 60 Å appears to be a new magnetic material which exhibits a four fold anisotropy in the plane that is much larger than that found in other transition elements.

4.2 Ferromagnetic Resonance in Metals

There are many in-depth reviews of FMR available (see for eg. [4.1-3]). Our aim here is to describe briefly the relevant features of the rather involved theory to give the reader a feel for the subject and to form a basis for the interpretation of the experiments.

When a classical magnetic moment is immersed in a uniform magnetic field **H** and its magnetic moment μ is displaced from equilibrium, it precesses about the field direction with an angular frequency $\omega=\gamma H$ where γ is the gyromagnetic ratio. From elementary mechanics the equation of motion for this moment is $\tau = \mu \times H = \frac{d\hbar S}{dt} = -\frac{1}{\gamma}\frac{d\mu}{dt}$ where $\hbar S$ is the angular momentum. This classical result remains unchanged in quantum systems if the components of the magnetic moment are interpreted as expectation values.

In a ferromagnetic material the net magnetic moments of the atoms are strongly coupled by the exchange interaction to form the magnetization (moment per unit volume). The mutual interaction of the spins through exchange, dipole fields and spin-orbit coupling and the damping of the precessional motion by inelastic processes can be represented by an effective field. These effective fields combine with the applied field and the magnetization responds to the combined torque of the applied field plus the effective fields. The Landau-Lifshitz equation of motion (the LL equation) is used to provide a phenomenological description of the magnetization and total effective field. It is obtained from the torque equation by dividing μ by the volume per atom to give the magnetization **M** and by replacing the applied field by an effective field to be discussed below. In general γ includes an orbital contribution to the magnetic moment and therefore it may differ from the free spin value $\gamma_f = 1.7588\text{x}10^7$ (sec-Oe)$^{-1}$.

In FMR experiments we detect the reflected microwaves. The microwaves are absorbed more strongly when the magnetic field sweeps through the resonance and hence the reflected power is reduced. To calculate the reflected microwave power the LL equation must first be solved to find the effective permeability. This is then combined with Maxwell's equations to solve the boundary value problem for the fraction of the incident power reflected from the metal surface.

The geometry used for the FMR experiments reported in this work is shown in Fig. 4.1. The samples are thin disks having the [001] direction normal to the plane. The microwaves can be considered as normally incident onto the sample surface. This is because the index of refraction of metals is very large, causing the internal angle of propagation to be very close to the normal direction (~.01°). The static field and magnetization can be rotated in the plane of the surface. The field direction is chosen as the x axis. The [100] crystal axis makes an angle of φ with respect to the x axis. The sample can be idealized as having an infinite radius. For this type of symmetry the magnetization varies only in the z direction.

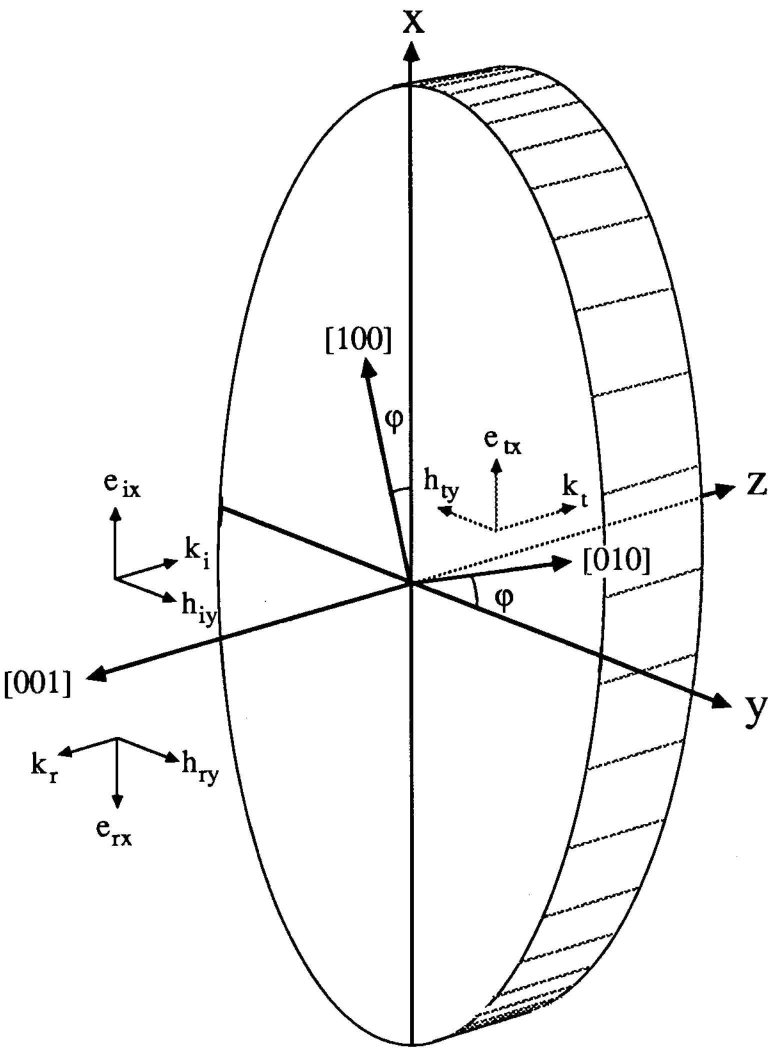

Fig. 4.1 Sample Geometry for ferromagnetic resonance

In FMR the magnetization makes only small deviations from the static equilibrium direction and we write:

$$\mathbf{M} = M_s\hat{x} + \mathbf{m} = M_s\hat{x} + m_y\hat{y} + m_z\hat{z} \qquad \text{where } |\mathbf{m}| \ll M_s.$$

The time and spatial variation of **M** is all contained in m_y and m_z.

The Landau Lifshitz (LL) equation can be written as:

$$-\frac{1}{\gamma}\frac{\partial \mathbf{M}}{\partial t} = \mathbf{M} \times \mathbf{H}_{\text{eff}} \tag{4.1}$$

where $\mathbf{H}_{\text{eff}}$ is the effective field. Note that the units of the equation are torque (or energy) per unit volume. The magnitude and direction of $\mathbf{H}_{\text{eff}}$ can be determined from a variational principle [4.4,4.5]. If we write the free energy per unit volume E as a function of **M** the effective field is given by

$$\mathbf{H}_{\text{eff}} = -\frac{\partial E}{\partial \mathbf{M}} = -\left[\frac{\partial}{\partial M_x}\hat{x} + \frac{\partial}{\partial M_y}\hat{y} + \frac{\partial}{\partial M_z}\hat{z}\right]E \tag{4.2}$$

We are not interested in fields that are parallel to **M** because they do not produce torques.

For our system $\mathbf{H}_{\text{eff}}$ is written symbolically as:

$$\mathbf{H}_{\text{eff}} = \mathbf{H}_0 + \mathbf{H}_D + \mathbf{H}_{K1} + \mathbf{H}_{Ex} + \mathbf{H}_G + \mathbf{h}\,. \tag{4.3}$$

$\mathbf{H}_0$ is the applied field, $\mathbf{H}_D$ is the static dipole demagnetizing field, $\mathbf{H}_{K1}$ is the magnetocrystalline anisotropy field hereafter called simply the anisotropy field, $\mathbf{H}_{Ex}$ is the exchange field, $\mathbf{H}_G$ is the damping field and **h** is the internal microwave field.

The static dipole demagnetizing field for a saturated ellipsoid is uniform and equal to:

$$\mathbf{H}_D = -\,(4\pi N_x M_x\hat{x} + 4\pi N_y M_y\hat{y} + 4\pi N_z M_z\hat{z}\,) \tag{4.4}$$

where N_x, N_y and N_z are given by the ellipticity of the sample. For an idealized thin sample $N_x = N_y = 0$ and $N_z = 1$ and there is no static demagnetizing field because $M_z = 0$ at saturation. Because our samples have a finite thickness, N_x and N_y have a finite values and hence there is a small static demagnetizing field $\mathbf{H}_D = -4\pi N_x M_x \hat{x} \cong \sim 2\pi(t/d)M_s\hat{x}$ where t is the thickness of the sample and d is the diameter. We add this field to the applied field in our calculations. There is also a dynamic demagnetizing field that is produced when the spin tilts out the surface during precession. This is taken into account through Maxwell's equations.

Magnetocrystalline anisotropy has its origin in the spin-orbit interaction which links the directions of the spin with the orbital angular momentum. The orbital states of the atoms in turn are tied to the crystal axes because of interatomic potentials generally referred to as crystal fields (electric). Hence the magnetization has preferred directions with respect to the crystal axes and the energy is a function of the angles between the magnetization and the crystal axes. We write the energy as a power expansion in the direction cosines between **M** and the axes. The lowest order term in a lattice with cubic symmetry is the fourth order term (see [4.1] e.g.):

$$E_{\text{cubic}} = K_1\left(\alpha_x^2\alpha_y^2 + \alpha_x^2\alpha_z^2 + \alpha_y^2\alpha_z^2\right) \tag{4.5}$$

where $\alpha_x = (M_x/M_s)$, etc. are the direction cosines of the magnetization with respect to the crystal axes. For bulk Fe this lowest order term is sufficient to describe the anisotropy. The anisotropy pulls the magnetization away from the direction of the applied field when the direction of the applied field does not coincide with a major crystal axis. Because this considerably compilcates the algebra we will not discuss this effect here. Our applied fields are sufficient to justify the assumption that in equilibrium **M** lies parallel with $\mathbf{H}_0$ for all orientations of $\mathbf{H}_0$. This requires only minor corrections at the large fields used in most of these experiments, and none when **M** is oriented along the major directions ([100], [110]). In chapter 5 we will include corrections which arise because **M** and **H** are not parallel. To find the effective field we first write the energy for small deviations of **M** from equilibrium. Then we take the gradient of this energy with respect to **M** to find the effective anisotropy field. The terms that give rise to terms that are linear in **m** are:

$$\mathbf{H}_{K_1} = \frac{K_1}{2M_s}\left[3+\cos(4\varphi)\right]\hat{x} + \frac{K_1}{2M_s}\left[\sin(4\varphi) + \frac{m_y}{M_s}(3-3\cos(4\varphi))\right]\hat{y} \tag{4.6}$$

The symmetry is lower at the surface of the sample. This gives rise to a second order anisotropy which will be incorporated through the boundary conditions.

The exchange energy increases if there are spatial variations in the magnetization. The macroscopic form can be found by averaging the microscopic exchange energy $-2JS_i \cdot S_j$ [4.5]. For a lattice of cubic symmetry the increase in exchange energy can be written:

$$E_{ex} = \frac{A}{M_s^2}\left((\nabla M_x)^2 + (\nabla M_y)^2 + (\nabla M_z)^2\right) \qquad (4.7)$$

where A is the macroscopic exchange constant given by $A=2JS^2/a$ for a bcc lattice having a lattice constant a. It can be shown [4.5] that the effective field for exchange is given by:

$$\mathbf{H}_{ex} = \frac{2A}{M_s}\left(\frac{\nabla^2 \mathbf{M}}{M_s}\right) \qquad \text{which simplifies to} \qquad \mathbf{H}_{ex} = \frac{2A}{M_s^2}\frac{\partial^2 \mathbf{M}}{\partial^2 z} \qquad (4.8)$$

for our geometry.

The effective damping field accounts for various inelastic processes which transfer energy from the precessing magnetization and transfers it to spin waves, conduction electrons and phonons. We use the Gilbert form for the damping field (see [4.6] for eg.):

$$\mathbf{H}_G = -\frac{G}{(\gamma M_s)^2}\frac{\partial \mathbf{M}}{\partial t} \qquad (4.9)$$

The appropriate forms of Maxwell equations are:

$$\nabla\cdot\mathbf{e} = 0 \;\; (a) \qquad \nabla\times\mathbf{e} = -\frac{1}{c}\frac{\partial\mathbf{b}}{\partial t} \;\; (b) \qquad \nabla\times\mathbf{h} = \frac{4\pi}{c}\mathbf{j} + \frac{\varepsilon}{c}\frac{\partial\mathbf{e}}{\partial t} \;\; (c) \qquad \nabla\cdot\mathbf{b} = 0 \;\; (d) \qquad (4.10)$$

with $\mathbf{j} = \sigma\mathbf{e}$ $\quad \mathbf{b} = \mathbf{h} + 4\pi\mathbf{m} = \tilde{\mu}\mathbf{h}$ $\quad$ and $\quad \mathbf{m} = \tilde{\chi}\mathbf{h}$.

$\tilde{\mu}$ and $\tilde{\chi}$ are the complex permeability and susceptibility tensors respectively ($\tilde{\mu} = 1 + 4\pi\tilde{\chi}$). We assume that **h,b,m** ~ exp(ikz-ωt) where k is complex to account for the damping of the wave into the sample. The exchange field becomes $H_{ex} = -(2Ak^2/M_s^2)\mathbf{m}$. From $\nabla\cdot\mathbf{b} = 0$, Gauss's theorem and b_z(external) = 0 we have that $0=b_z=h_z+4\pi m_z$. We substitute $h_z = -4\pi m_z$ and the effective fields into the LL equation. The system of linear equations can be solved for m_y, m_z and h_z in terms of h_y. These can be used to calculate the reflected power. The effective permeability, hereafter termed simply the permeability $\mu \equiv b_y/h_y$ is given by [4.3]:

$$\mu \equiv \frac{b_y}{h_y} = \frac{\left(B_0+H_1+\frac{2Ak^2}{M_s}-\frac{i\omega G}{\gamma^2 M_s}\right)\left(B_0+H_2+\frac{2Ak^2}{M_s}-\frac{i\omega G}{\gamma^2 M_s}\right)-\left(\frac{\omega}{\gamma}\right)^2}{\left(B_0+H_1+\frac{2Ak^2}{M_s}-\frac{i\omega G}{\gamma^2 M_s}\right)\left(H_0+H_2+\frac{2Ak^2}{M_s}-\frac{i\omega G}{\gamma^2 M_s}\right)-\left(\frac{\omega}{\gamma}\right)^2} \tag{4.11}$$

$$\text{where } B_0 \equiv H_0+4\pi M_s\,, \quad H_1=\frac{K_1}{2M_s}(3+\cos(4\varphi)) \quad \text{and} \quad H_2=\frac{2K_1}{M_s}\cos(4\varphi)\,. \tag{4.12}$$

The expression for μ displays a resonant behavior that depends on H_0 and the magnetic parameters of the sample: M_s, K_1, A, G and γ. Resonance occurs for a value of the applied H_0 for which the denominator in equation (4.11) is a minimum. The linewidth is determined by the damping term as well as by the exchange term because k is complex. It is useful to note that the resonance condition is approximately given by:

$$\left(\frac{\omega}{\gamma}\right)^2 \cong H_0 B_0 = H_0(H_0+4\pi M_s) \tag{4.13}$$

because H_0 and $4\pi M_s$ for Fe are much larger than the other effective fields (see Table 4.1). The addition of the exchange field complicates the analysis considerably because it makes the permeability dependent on k and, as we will see, k in turn depends on the permeability.

We will also be interested in the ratio of m_x to m_y, the ellipticity of the precession, which is given by [4.3]:

$$\frac{m_z}{m_y} = \frac{i\omega/\gamma}{H_0+4\pi M_s+H_1+2Ak^2/M_s-(i\omega G/\gamma_2 M_s)} \cong \frac{i\omega/\gamma}{H_0+4\pi M_s} \tag{4.14}$$

Another interesting value of H_0 occurs when the real part of the numerator of equation (4.11) goes to zero minimum. Neglecting exchange, damping and anisotropy this occurs at approximately $(\omega/\gamma)^2 = (B_0)^2$. This is termed ferromagnetic antiresonance (FMAR) [4.7] and is used in the next section to find an accurate value for the Gilbert damping parameter G.

Now we consider the boundary value problem. We can neglect the displacement current in (4.10c) because it is small in the microwave limit ($4\pi\sigma \sim 10^{18} >> \omega \sim 10^{11}$). Using $\mathbf{j} = \sigma \mathbf{e}$ and substituting (4.10b) into (4.10c) we get:

$$\nabla \times (\nabla \times \mathbf{h}) = -\frac{4\pi\sigma}{c^2}\frac{\partial \mathbf{b}}{\partial t}. \tag{4.15}$$

For our geometry $\nabla = \hat{z}\,(\partial/\partial z)$ which gives us $k^2(h_x, h_y) = i(4\pi\sigma\omega/c^2)(b_x, b_y)$. Combining this with (4.11) for the y components gives:

$$k^2 = \frac{4\pi i\sigma\omega\mu}{c^2} \equiv \frac{2i\mu}{\delta^2}. \tag{4.16}$$

$\delta = \sqrt{c^2/2\pi\sigma\omega}$ (the skin depth) is the distance into the sample at which the electric field amplitude falls by 1/e if $\mu=1$ because then $k=(1+i)/\delta$. For Fe at 73 GHz $\delta \cong 1.0\ \mu m$. At FMR, if we neglect the exchange and anisotropy terms in the permeability (equation 4.11), $\mu \cong 230i$ and then $1/k \cong .048\,i\ \mu m$ from equation 4.16. This is an underestimate of the penetration of the microwaves because the addition of exchange decreases μ and hence decreases the imaginary part of k.

Equation (4.16) is a sixth order polynomial in k because of the k dependence of μ. Hence there are six waves in the sample. The problem was first treated by Ament and Rado [4.8]. The nature of the waves are discussed in detail by Cochran, et al. [4.6]. Three of these travel in the -z direction (internally reflected waves) and are not excited in these FMR experiments because the the skin depth is much smaller than the thickness of the sample. They do exist in the overlayer discussed in sections (4.4-4.5). To calculate the amplitudes of the three waves plus the external reflected wave we need four boundary conditions. Two of these are provided by the continuity of the tangential components of **e** and **h** at the surface that come from equations (4.10b), (4.10c):

$$e_{ix} + e_{rx} = e_{tx} \qquad\qquad h_{iy} + h_{ry} = h_{ty} \tag{4.17}$$

where e_{tx} and h_{ty} are the sum of the amplitudes of the three propagating waves in the magnetic metal. We also have $e_{ix} = h_{iy}$ and $e_{rx} = h_{ry}$ since in free space the amplitudes of the electric and magnetic fields are equal. Also from (4.10c) $e_{jx} = Z_j h_{jy}$ for each wave where Z_j is the surface impedance for the jth internal wave of wavevector k_j given by :

$$Z_j = -\frac{i\omega\delta^2 k_j}{2c} \tag{4.18}$$

The other boundary conditions define the derivatives of **m** at the surface. These derivatives depend upon torques from the surface anisotropy and exchange fields which are considered separately from the bulk torques (see Rado and Weertman [4.9]).

First consider the surface anisotropy. Because of the broken symmetry at the surface the normal direction is not equivalent to the two in-plane cubic axes. Hence a second order magnetocrystalline anisotropy energy can exist at the surface. The spin-orbit coupling will not necessarily be the same for the surface atoms and near surface atoms. We assume this anisotropy acts on the surface and is given by an energy contribution:

$$E_{Ks} = -K_s\left(\frac{m_z}{M_z}\right)^2 \tag{4.19}$$

where K_s is in ergs/cm^2. Higher order surface anisotropies are also possible but we will neglect them. A positive K_s makes the surface spins tend to point out of the plane and a negative K_s makes them tend to stay in the plane. Taking the negative of the derivative with respect to **M** we find that the effective field is given by:

$$\mathbf{H}_{Ks} = 2\frac{K_s m_z}{M_s^2}\hat{z}. \tag{4.20}$$

Note that this field has units of Oe-cm and its contribution to the the LL equation will therefore have units of torque per unit area.

The surface exchange torque can be derived from variational techniques [4.9] and by using Green's functions [4.9]. We instead consider a microscopic derivation of the exchange field using Heisenberg-type exchange interaction. An atom on the (001) surface of a bcc lattice has four nearest neighbours displaced by a distance a/2 in the z direction. The exchange energy of this spin is $-8J\mathbf{S}_1\cdot\mathbf{S}_2$ (2J per pair interaction and four nearest neighbours) where $\mathbf{S}_1$ is the surface spin and S_2 denotes the second layer spins which are all parallel. We assume that the angle of the spin can be approximated by a continuous function of position. Since the spin angle changes slowly with position we can write the exchange energy of S_1 as:

$$\frac{E_{ex1}}{\text{moment}} = -8JS(0)\cdot\left(S(0) + \frac{a}{2}\frac{\partial S(0)}{\partial z} + \frac{1}{2}\left(\frac{a}{2}\right)^2 \frac{\partial^2 S(0)}{\partial z^2} + \ldots\right) \tag{4.21}$$

where a is the lattice spacing. Dropping the second order and higher order derivatives, multiplying by M^2/M^2, dividing by a^2 to convert to energy per unit area, and using the definition of $A=2JS^2/a$ we get:

$$\frac{E_{ex1}}{cm^2} \cong -\frac{4A}{aM_s^2}\mathbf{M}\cdot\mathbf{M} - \frac{2A}{M_s^2}\mathbf{M}\cdot\frac{\partial \mathbf{M}}{\partial z} \tag{4.22}$$

The first term is independent of the direction of **M** and therefore contributes nothing to the torque. The exchange field at the surface is given by:

$$H_{ex1} = \frac{2A}{M_s^2}\frac{\partial \mathbf{M}}{\partial z} \tag{4.23}$$

again in Oe-cm. In the bulk this field is canceled by the nearest neighbour spins on the other side which contribute a field of opposite sign. In the bulk it is the second derivatives which matter (the next highest order terms in the expansion (4.21)) because the spins on either side both contribute positive terms.

In equilibrium the sum of the torques from the surface exchange and anisotropy fields must be zero. From $\tau = \mathbf{M}\times\mathbf{H}(\text{surface}) = 0$ and equations (4.20,4.23) we get the boundary conditions for **M** as:

$$-\frac{K_s}{M_s}m_z = \frac{A}{M_s}\frac{\partial m_z}{\partial z} = \frac{A}{M_s}(ik_1m_{1z}+ik_2m_{2z}+ik_3m_{3z})$$

$$0 = \frac{A}{M_s}\frac{\partial m_y}{\partial z} = \frac{A}{M_s}(ik_1m_{1y}+ik_2m_{2y}+ik_3m_{3y}) \tag{4.24}$$

We can substitute for the components of m_{jy} and m_{jz} in terms of h_{jy} using the solutions of the LL equation for each component. We then have a 4x4 system of linear equations for h_{ry}, h_{1y}, h_{2y} and h_{3y} that can be solved numerically with the help of a computer. This also requires the solution of the 6th order polynomial for the k_j's as a function of H_0 and the magnetic parameters. Using the Poynting vector the reflected power, P_r, is proportional to $|h_r|^2$. Since we use a lock-in amplifier and modulate the field we actually measure the derivative of P_r with respect to the applied field and that is what the program computes.

It is useful to consider the simpler case in which the effect of exchange on the resonance is neglected. This is a good approximation because $2Ak^2/M_s$~10-30 Oe (see Table 4.1). From equation (4.11) μ is then independent of k which therefore has only two roots given by equation (4.16), $k=\pm\sqrt{2i\mu}/\delta$. One of these k's corresponds to a wave traveling in the -z direction and is not excited in thick samples. Only the boundary conditions on **e** and **h** (equation 4.17) are then needed and this gives two linear equations with two unknowns. These are easily solved to find h_r. We then find for the ratio of reflected to incident power:

$$\frac{P_r}{P_i} = \left|\frac{(1-Z_s)}{(1+Z_s)}\right|^2 \cong 1 - 4x\text{Real}(Z_s)$$

where Z_s is the surface impedance as defined in equation (4.18). The approximation used above is valid because Z_s is small; $Z_s \sim .016(i-1)$ (see table 4.1). The absorbed power P_a is then given by:

$$\frac{P_a}{P_i} = 1 - \frac{P_r}{P_i} \cong 4x\text{Real}(Z_s) \cong \text{Real}\left[\frac{2\omega\delta}{c}\sqrt{-i\mu}\right] \tag{4.25}$$

The last step comes from equations 4.16 and 4.18. This shows clearly that the reflected power exhibits the resonant behavior of μ.

In Tables 4.1 and 4.2 we have listed the the best current magnetic parameters for Fe and Ni respectively, the effective fields at 73 GHz and room temperature and several quantities of interest. The effective fields have been calculated neglecting exchange.

Table 4.1 Magnetic Parameters and Effective Fields for Fe at Room Temperature and 73 GHz

Parameter	value	reference	Effective field	value (Oe)
M_s	1715 (Oe)	[4.10]	$4\pi M_s$	21,550
K_1	$4.79\text{x}10^5$ ergs/cm^3	[4.11]	$2K_1/M_s$	559
K_s	.5 ergs/cm^2 (a)	[1.13] [4.12]	$i\omega G/\gamma^2 M_s$	~65i
"	.7 ergs/cm^2 (b)	[1.13] [4.12]	$2Ak^2/M_s$ (c)	~107i
G	$.82\text{x}10^8$ sec^{-1}	[1.13]	ω/γ	24,928
A	$2.0\text{x}10^{-6}$ ergs-cm	[4.13]		
$\rho=1/\sigma$	$9.8\text{x}10^{-6}$ Ω-cm	[4.14]	δ ($\mu=1$)	1.0 μm
g	2.089±.006	[4.13]	μ (c)	~230i
$\gamma=g\lvert e\rvert/2mc$	$1.84\text{x}10^7$ (Oe-sec)$^{-1}$	[4.13]	Z_s (c)	~.016(i-1)

Table 4.2 Magnetic Parameters and Effective Fields for Ni at 300 K and 73 GHz

Parameter	value	reference	Effective field	value (Oe)
M_s	489 (Oe)	[4.15]	$4\pi M_s$	6,140
K_1	$-.59\text{x}10^5$ ergs/cm^3	[4.16]	$2K_1/M_s$	241
K_2	$-.28\text{x}10^5$ ergs/cm^3	[4.16]	$i\omega G/\gamma^2 M_s$	~629i
K_s	unknown		$2Ak^2/M_s$ (c)	~10i
G	$2.5\text{x}10^8$ sec^{-1}	[4.17]	ω/γ	23,765
A	$1.0\text{x}10^{-6}$ ergs-cm	[4.17]		
$\rho=1/\sigma$	$7.22\text{x}10^{-6}$ Ω-cm	[4.18]	δ ($\mu=1$)	.5 μm
g	2.187±.006	[4.17]	μ (c)	~6.1i
$\gamma=g\lvert e\rvert/2mc$	$1.93\text{x}10^7$ (Ω-cm)$^{-1}$	[4.17]	Z_s (c)	~$7\text{x}10^{-6}$

(a) covered with a ~30 Å epitaxial Au layer; (b) covered with a ~30 Å epitaxial Ag layer; (c) neglecting k in equation (4.8) for μ and using an applied field calculated from $(\omega/\gamma)^2 = H_0(H_0+4\pi M_s)$

4.3 Perpendicular Anisotropy at the (001) Surface of Bulk Fe Single Crystals

Several research groups, including ours, [1.11,1.13,4.19] have recently demonstrated the existence of a large perpendicular anisotropy in ultrathin epitaxial Fe films. These films were grown by molecular beam epitaxy (MBE) on Ag (001) and Cu (001) single crystals. In films less than 5 monolayers (ML) thick, the anisotropy is sometimes large enough to overcome the demagnetizing field, $4\pi M_S$, which holds the magnetization in-plane and to magnetize the sample normal to the surface. The magnitude of the anisotropy has excited wide interest both for its theoretical explanation and possible technological application.

Gay and Richter [4.20] calculated the perpendicular anisotropy for free (001) layers of Fe, Ni, V and Co, and Fe in contact with Ag (001). They found large values for unsupported layers of Fe, large enough to magnetize 1 ML of Fe perpendicular to its surface, and somewhat lower values for Fe on Ag. Heinrich, et al., [4.20] established experimentally that the surface anisotropy, or "pinning", scales roughly inversely with film thickness, proving it's origin is indeed at the surface or in the near surface region.

Gay and Richter's calculation is based upon the electronic properties of structurally perfect Fe. It is possible that the large surface pinning observed for thin Fe films is not a result of simple termination at the interface, but is created by imperfections such as lattice-mismatch-induced-strain, surface steps and roughness. Defects in Fe films on Ag are enhanced at substrate steps because of the large perpendicular lattice mismatch between bcc Fe and fcc Ag. An obvious question to ask is whether a large pinning exists also at the surface of bulk Fe. Frait and Fraitova [4.21] found low values for perpendicular surface anisotropy (K_S ~.1 ergs/cm^2) using ferromagnetic resonance on untreated Fe whiskers. Because of renewed interest in this question and because of the ability to prepare well-characterized surfaces by means of modern ultra high vacuum (UHV) techniques, it was worthwhile to re-examine their results. Measured values for the surface anisotropy constant, K_S, should help guide theoretical work, which Gay and Richter point out depends critically on the fine details of the calculation.

We prepared two Fe (001) single crystals in UHV with and without overlayers of Au and Ag. We determined the surface pinning by comparing experimental and theoretical frequency dependences of ferromagnetic resonance (FMR) linewidths at 24, 36.6 and 73.0 GHz [1.13]. The linewidth is defined in the usual way as the field interval between the maximum and minimum values of the derivative curve of FMR.

The preparation of samples was described in section 2.3. We used samples Fe 1 and 2 (see Table 2.1). The crystal quality of the surface was monitored *in situ* by means of reflection high energy electron diffraction (RHEED) before, during and after growth. Before growth, the RHEED patterns, particularly on sample 1, consisted of sharp streaks whose centres trace a circle characteristic of 2 dimensional diffraction. Both the Ag and Au grow in a layer-by-layer fashion on Fe as determined from the strong oscillations in RHEED intensity that occur during growth. The Ag was covered with Au to protect it from oxidation.

FMR was measured in the parallel configuration at 24.02, 36.61 and 73.01 GHz using cavities operating in the cylindrical TE_{012} mode. The samples formed the endwalls of these "doughnut" mode cavities. Standard lock-in techniques were used to detect the reflected signal from the cavity: the applied field was modulated in order to obtain the derivative of the reflected power with respect to the applied field. A lock-in ammplifier was used to stabilize the klystron frequency at the cavity resonant frequency. At 24 and 36 GHz the samples were exposed to the microwaves through a 4 mm orifice in a diaphragm cut from .001 inch thick copper foil. This covered most of the sample surfaces to reduce the inhomogeneous demagnetizing fields present near the edges in disk-shaped samples. A computer program based on a formula given by Kraus and Frait [4.22] was used to determine that the effect of this field on the FMR lineshape was < 5 Oe.

One of the problems with the use of a diaphragm is that unless it remains in intimate contact with the sample, a large asymmetry in the lineshape can be produced due to the mixing of the out-phase and in-phase parts of the surface impedance. This was taken into account in the theoretical programs and shown to have only neglible effect on the linewidth, even for large asymmetries.

We finally chose to determine K_s from the frequency dependence of the linewidth rather than the field position of the resonance, which also depends on K_s, because the dimensions of our samples made accurate field calibration difficult because of demagnetizing effects. Relative field shifts for different overlayers on the same sample at the same frequency could be measured accurately in principal but initial studies indicated some non-reproducibility. The relative effect of surface pinning on linewidth is much stronger than on the field position.

Ferromagnetic antiresonance (FMAR) was measured in reflection at 73 GHz to determine the Gilbert damping parameter G for these samples. A large modulation field was used to obtain good signal to noise. We were careful to use a range where signal was proportional to modulation amplitude in order to avoid an artificial broadening of the lineshapes.

The field dependence of the rf permeability is a complex algebraic problem which can only be solved by computer calculations. We have used a program written by Dr.J.F. Cochran which includes all relevant effective fields such as the exchange field, Gilbert damping field, cubic anisotropy, internal rf magnetic field and applied magnetic field.

Surface pinning was studied by measuring the frequency dependence of FMR linewidth. FMR linewidth is determined by exchange conductivity and intrinsic Gilbert damping. It is the exchange contribution to the linewidth (proportional to $\omega^{1/2}$) that is affected by surface pinning through the boundary conditions. It is important to realize that this line broadening is strongly frequency dependent. At low frequencies (and therefore low fields for resonance) the rf magnetization is mostly confined to in-plane motion by the strong demagnetizing field. This can be seen from equation (4.14) for m_z/m_y. At 24, 36 and 73 GHz this ratio is .33, .45 and .65 respectively. K_s affects only the perpendicular component m_z and therefore has a smaller effect on the resonance at 24 GHz than at 73 GHz.

The FMR linewidth is given by a complex combination of A, K_s, G, M_s and conductivity σ. All parameters are well known except K_s and G. To obtain a unique solution for K_s we determined G from ferromagnetic antiresonance [4.7] (FMAR) at 73.0 GHz. At FMAR the permeability is a minimum and hence from equation (4.18) k is also a minimum (skin depth ≅14 μm). Consequently exchange and surface pinning effects are insignificant. The FMAR lineshape can be fit in order to obtain a unique value for G.

FMAR measurements were made on both samples with each of the different overlayers and with M_s along both the easy (001) and hard (110) axes. The signal to noise ratio is ~50. An FMAR measurement is shown in Fig. 4.2 with a superimposed fit. Fitting was done with a multi-parameter least square fitting program, using a simple form of the surface impedance without the exchange interaction. We also included mixing of the out of phase component. We verified that these corrections have negligible effect on the choice of G, which is determined almost solely by the sharply sloped region of the curve.

The values for G for all sample preparations fall within the range $.80 \times 10^8$ –.84x108 $\sec^{-1}$. We found no consistent difference in G between easy and hard axes from FMAR even though FMR consistently shows ~10 Oe wider lines at the hard axes. In FMR calculations we used $G = .82 \times 10^8 \sec^{-1}$. This is close to recent results measured in transmission experiments by Rudd and Cochran ($.71 \times 10^8 \sec^{-1}$) [4.24] but is appreciably higher than values found by Frait and Fraitova ($.572 \times 10^8 \sec^{-1}$).

In real samples FMR is further broadened by sample magnetic inhomogeneities. It was shown in metallic samples that this linebroadening is independent of frequency [4.23]. It is common practise to use it as an additional fitting parameter in FMR linewidth studies.

The main results of this study are shown in Fig. 4.3 which depicts the frequency dependence of theoretical and experimental linewidths. The solid lines link linewidths calculated at 24.023, 36.61 and 73.01 GHz for different values of K_s. The parameters used in the calculations are listed in table 4.1 except the corrections for inhomogeneous linebroadening which are listed Fig.4.3. The corrections to the linewidths for inhomogenous linebroadening were made by requiring that the corrected values fall on a theoretical curve for a particular choice of K_s at all frequencies. Our linewidths are among the narrowest reported in the

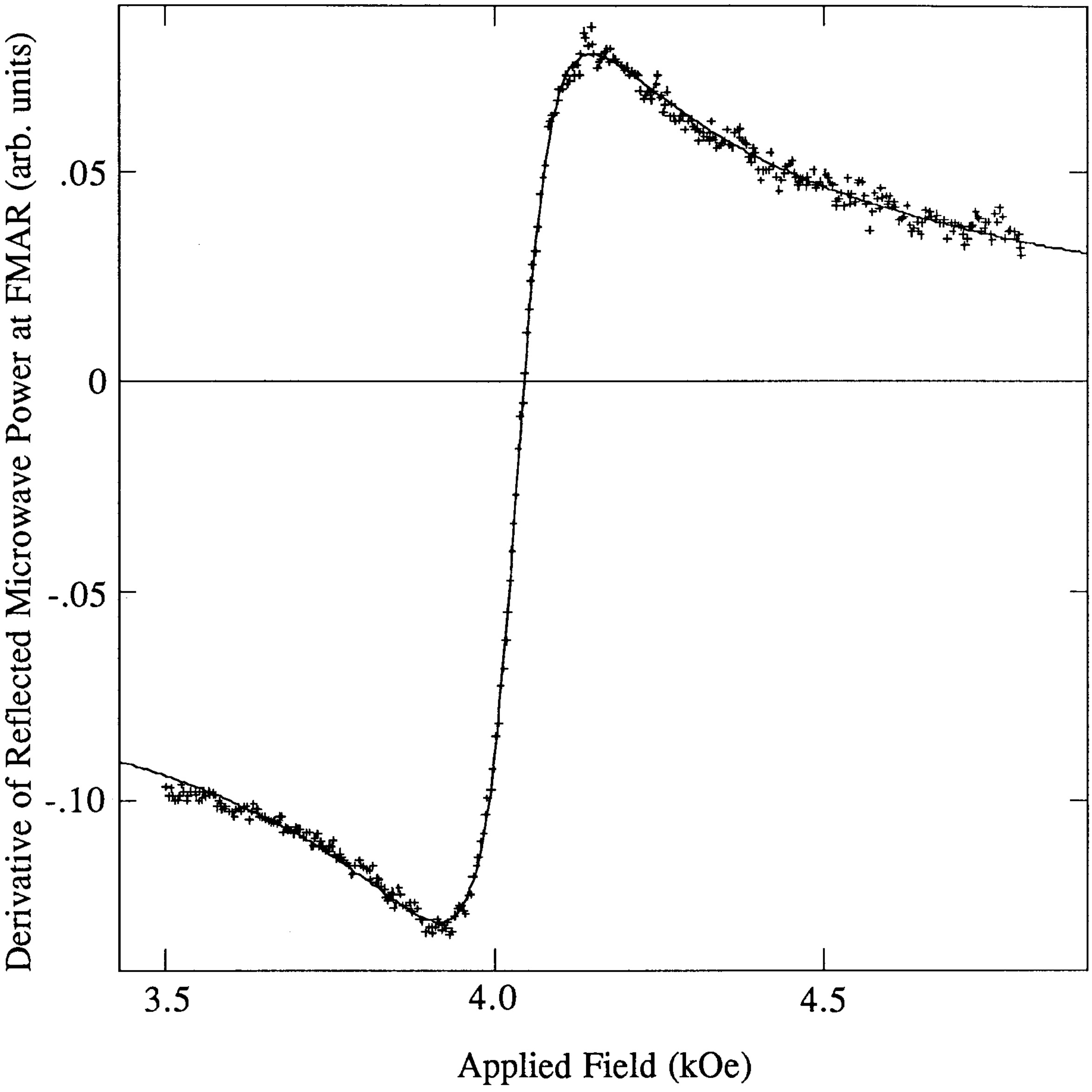

Fig. 4.2 FMAR signal at 73.01 GHz obtained from an Fe (001) single crystal (Fe sample 1) with a 30 Å Au overlayer and M_S along the [110] axis. A Minuit fit gave Gilbert damping parameter G = .82x10^8 sec^{-1}. The value of G was within the range .79-.84x10^8 sec^{-1} for fits of the data obtained for all samples.

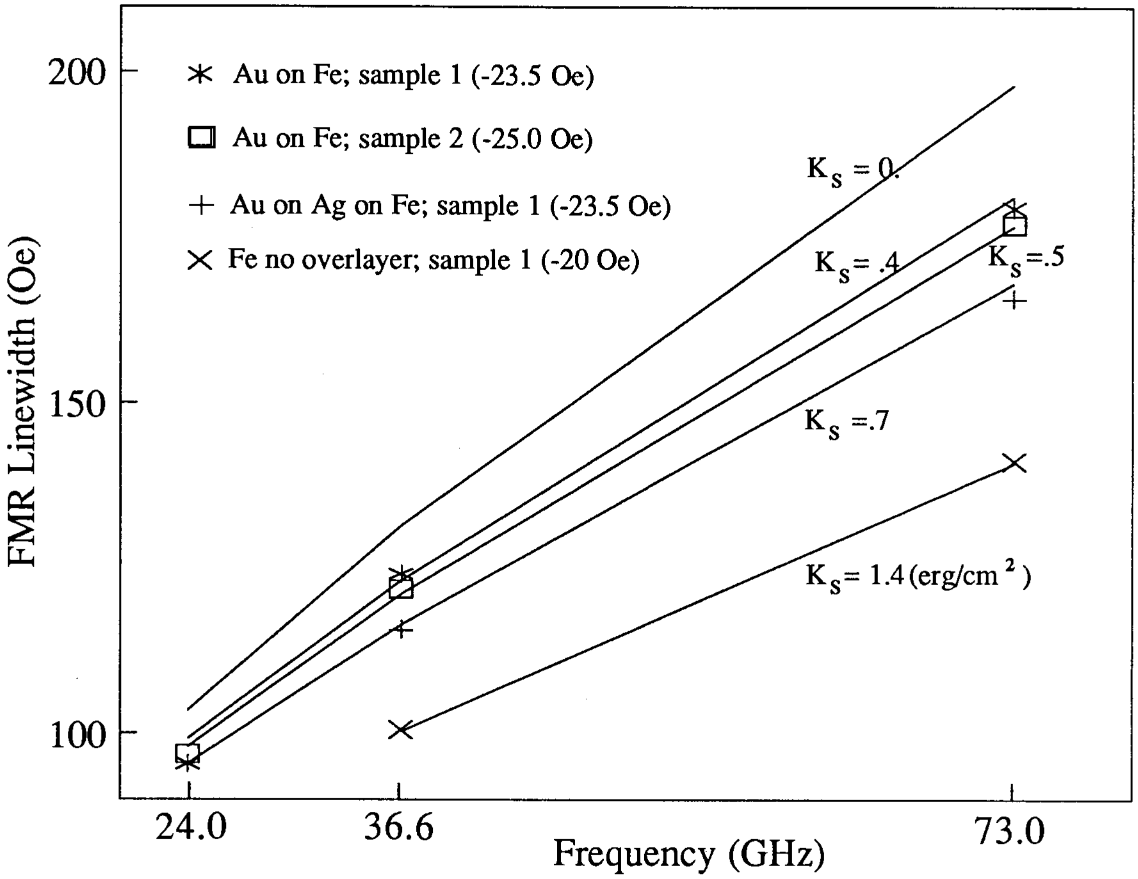

Fig. 4.3 FMR linewidth vs frequency for various values of K_S. The solid lines connect theoretical calculations at 24.023, 36.61 and 73.01 GHz. Increasing the value of K_S decreases the linewidth.

literature. We find K_s = .4 for Au on sample 1, K_s = .5 for Au on sample 2, K_s = .7 for Ag on sample 2 and an approximate value of K_s = 1.4 for no overlayer (see below), all in erg/cm^2.

The points plotted in Fig.4.3 are averaged over all easy and hard axes and thus represent four measurements each. Errors are somewhat difficult to estimate. Measurements of linewidth from FMR plots are accurate to ~±1%. There is a variation of several Oe in the linewidth between different mountings of the same samples at the different frequencies. As well, there is the uncertainty in the parameters used to fit the curves (see Fig. 4.4). For now we use the difference in the Au covered measurements on samples 1 and 2 as a basis for error estimate (±.1 erg/cm^2).

The difference in surface pinning of .3 erg/cm^2 between the Au on Fe sample 1 and Ag on Fe sample 1 was more accurately determined because no mechanical polishing was done between measurements. After the FMR measurement with the Au overlayer the sample was sputtered, annealed and covered with Ag. We note that the correction for inhomogeneous line broadening is 23.5 Oe for both fits.

In Fig. 4.5 we show the calculated shift in FMR resonance field at 24, 36.6, 50, 60 and 73 GHz for different values of K_s. Though we tried to measure this shift during the experiments, it is a more difficult because of the extra demands on calibration. We found that there was an irreproducilbility between different sample preparations and mountings. However an accurate measure of the change in FMR resonance at 73 GHz caused by replacing the Au with the Ag could be made. The change from a Au overlayer to a Ag overlayer causes a 30 ± 5 Oe shift to higher field. This is consistent with the increase in pinning from 0.4 to 0.7 ergs/cm^2 determined from the linewidth measurements.

The K_s value for the no overlayer case, 1.4 erg/cm^2, is rather large and at this time tentative. In our initial measurements at 73 GHz we found that removing a Au overlayer by sputtering and then annealing consistently narrows the line at 73 GHz by 20 - 30 Oe, indicating an increase in pinning ~ 0.5 erg/cm^2. Adding this to the K_s ~0.5 erg/cm2 found for

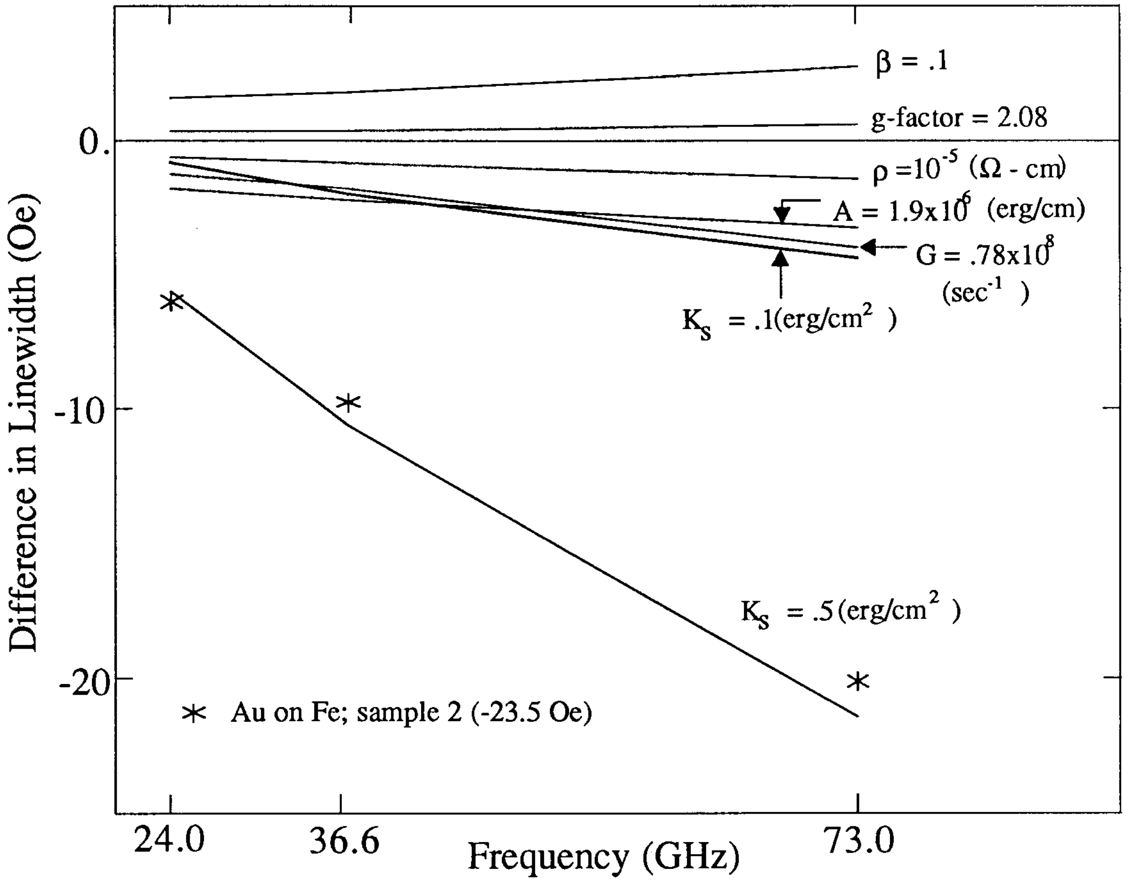

Fig. 4.4 Dependence of linewidth on magnetic parameters. We plot the difference between calculations using parameters in the text (with $K_S = 0$) and calculations varying one parameter at a time. The experimental points are also differences with the $K_S = 0$ case. Note that K_S has the strongest frequency dependence and that in-plane anisotropy leads to a frequency independent line broadening. $\beta = .1$ corresponds to mixing in 10% of the out of phase component.

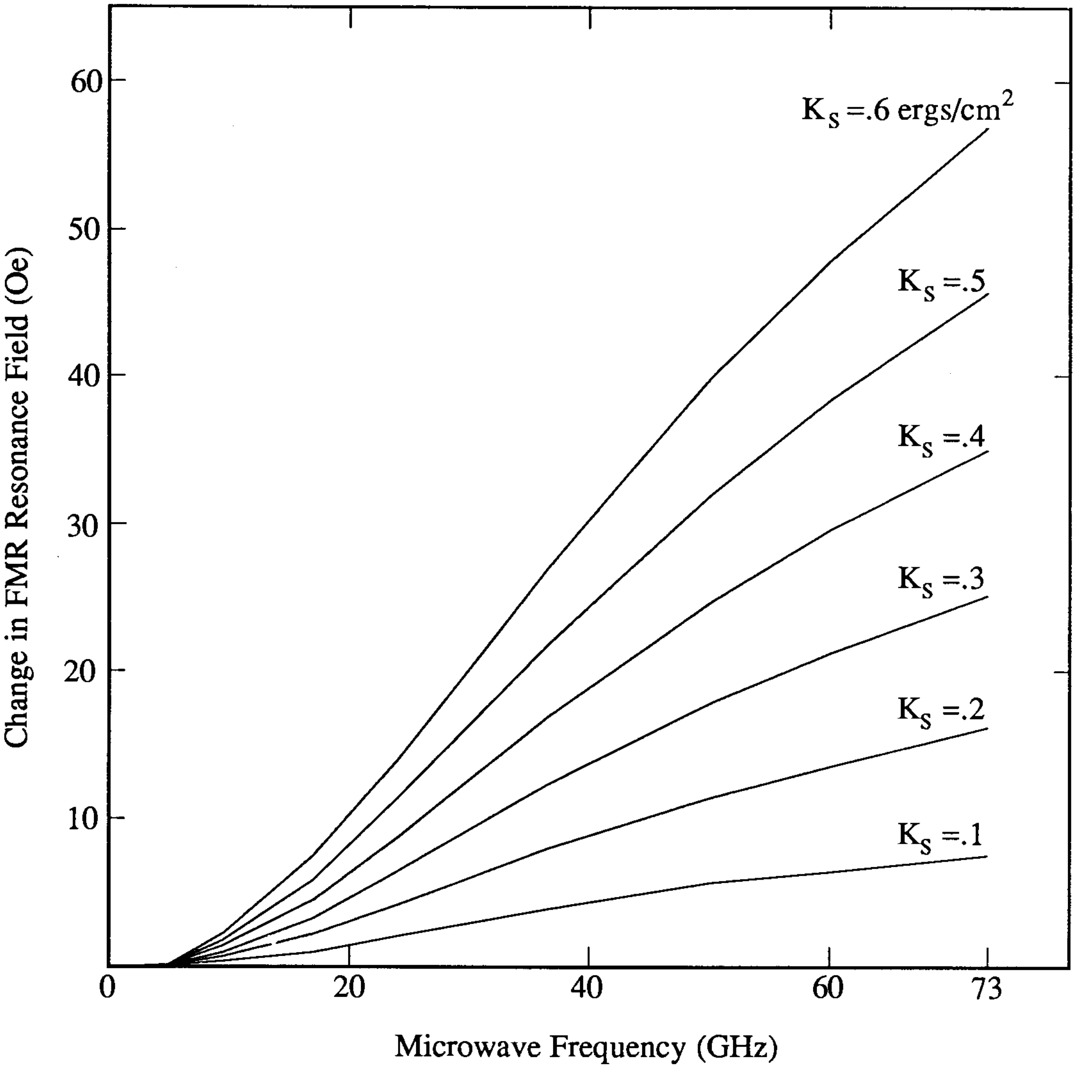

Fig. 4.5 Calculated changes in FMR resonance field between an unpinned and pinned Fe (001) sample plotted against frequency. The Fe parameters used for the calculations are listed in Table 4.1.

Au on Fe gives $K_s \cong 1$ ergs/cm^2 for Fe with no overlayer. This is close to recent estimates [4.25] (~0.9 erg/cm^2) for the free surface of ultrathin epitaxial Fe layers grown and measured in-situ. An unanswered question is how much the air that immediately comes in contact with sample on removal from UHV affects the surface pinning.

In Fig. 4.6 we show FMR spectra from Fe sample 1 with a 30 Å overlayer of Au. The fits are very good. These spectra were measured previous to the series of measurements used to determine the frequency dependence of the linewidth. The linewidths of FMR spectra taken at the time of those in Fig. 4.6 were consistently 20-25 Oe narrower than in Fig. 4.3. We found later that the increase in linewidth was caused by the use of a cheaper brand of cloth in the final diamond polishing stages. When we again used the Buehler pads the linewidths were again narrower and agreed with those in Fig. 4.6 to within 4 Oe. What is noteworthy about the fits in Fig. 4.6 is that they have require no correction for inhomogeneous linebroadening. Also the values of Gilbert damping parameter (.78x10^8 sec^{-1} and .80x10^{-1} sec^{-1}) agree very well with the FMAR measuements and the surface pinning parameter K_s = .55 ergs/cm^2 agrees well with the frequency dependence determination discussed above.

In conclusion we found large values for the surface pinning parameter K_s at well prepared Fe interfaces. They are in good agreement with recent results [4.25] using in-situ FMR on ultrathin films (K_s =0.6 for Ag/Fe interface and 0.9 for a free uncontaminated surface) and with measurements obtained using Brillouin light scattering[4.12] on a UHV prepared Fe whisker covered with Au (K_s =.54 erg/cm^2) and with Ag (K_s =.79 erg/cm^2). Our results show that the theoretical calculations of Gay and Richter that attribute the high surface pinning to the abrupt interface compare well with experiment. Disagreement in K_s with earlier work [4.21] (K_s = 0.1erg/cm^2) is likely due to the different preparation of the sample surfaces.

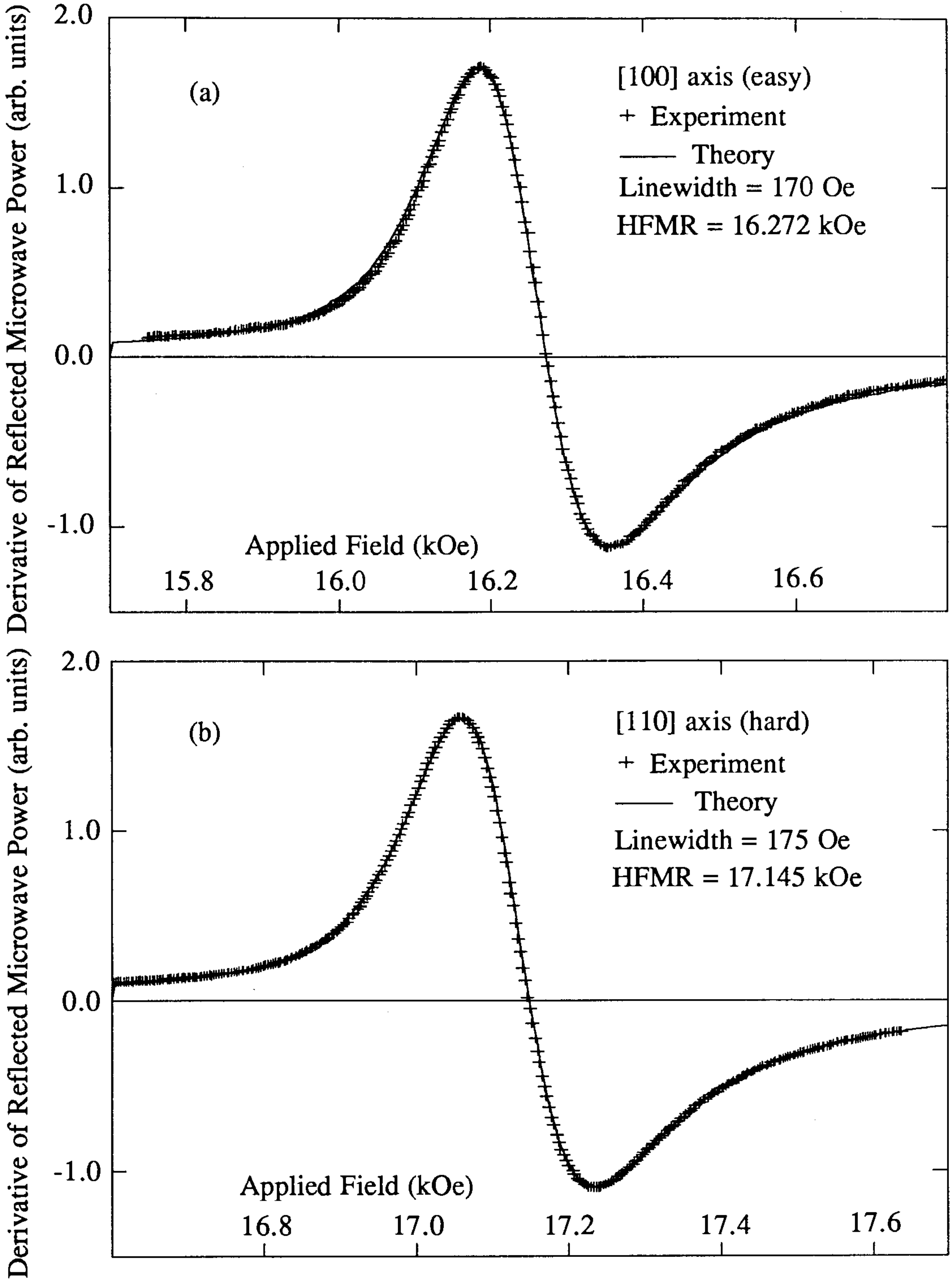

Fig. 4.6 Experimental and theoretical FMR spectra for an Fe (001) surface (sample Fe 1) covered with a 30 Å epitaxial Au layer. The magnetization is along the planer [100] axis in (a) and the [110] axis in (b). Parameters for both fits were $4\pi M_S$=21.55 kOe, H_d=412 Oe, K_1=4.8x10^5, K_s=.55 ergs/cm^2, β=.08 and g-factor=2.085. For (a) we used G=.78x10^8 sec^{-1} for (b) and G=.80x10^8 sec^{-1}.

4.4 FMR Theory of a Ferromagnetic Metal Coupled with a Ferromagnetic Overlayer

The description of the reflection of microwaves from Fe single crystals covered with an ultrathin Ni overlayer is made by extending the theory of section 4.2. This has been worked out in detail in a paper by Cochran, Heinrich and Arrott [1.6] which we outline below.

The complete solution of the problem involves writing the Landau-Lifshitz equation for both the overlayer and substrate and combining these with Maxwell's equations and the boundary conditions at the outer surface of the overlayer and at the overlayer-substrate interface. All the effective fields in equation (4.3) are included. If the exchange field is included the equation for the k-vectors is again a sixth order polynomial in both the overlayer and substrate. Since the overlayer is thin, three reflected waves are excited in it as well. Hence there are in total ten waves to calculate, a reflected wave, six overlayer waves and three waves in the substrate.

We are mostly interested in the interface boundary conditions because they control the effect that the Ni overlayer has on the Fe resonance and hence they are the key to determining the magnetic properties of the overlayer. As in section 4.1 the boundary conditions at the outer surface of the overlayer are found by balancing the torques from the surface anisotropy and exchange fields given in equations (4.20) and (4.23) respectively.

The specimen geometry and configuration of the rf driviing fields is shown in Fig. 4.7. Parameters which refer to the overlayer are superscripted with A and those which refer to the substrate are superscripted with B. The interface spins have additional torques due to surface surface anisotropy fields given by equation (4.20), the surface exchange field given by equation (4.23) and the exchange coupling across the interface. We derive the form of the exchange torques from the exchange energy per interface spin in a bcc lattice which is E_{ex}/moment = $-8J^{AB}S^{A}\cdot S^{B}$. By dividing this by a^2 and multiplying by $M^{A}M^{B}/M^{A}M^{B}$ we find the exchange energy per unit area to be:

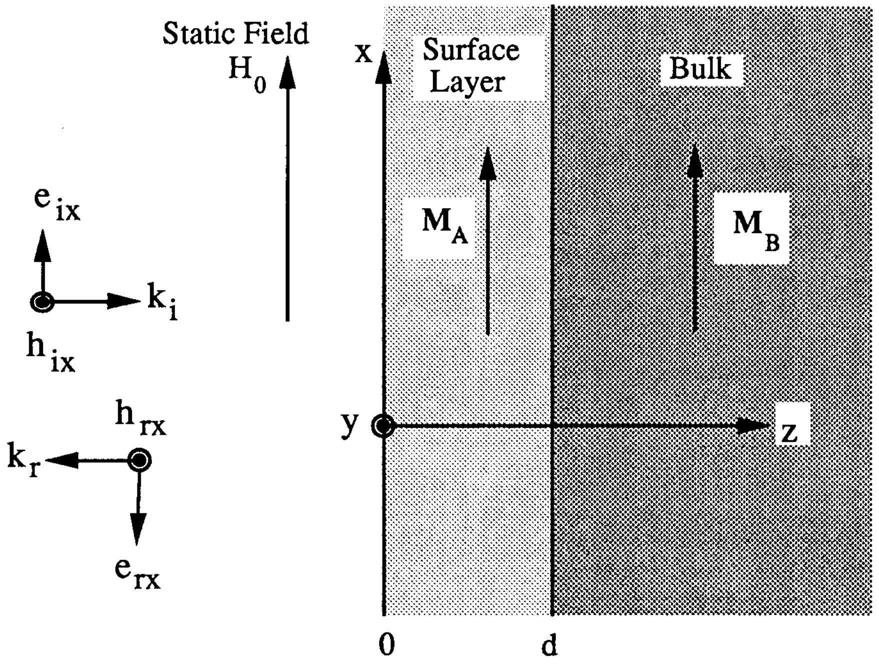

Fig. 4.7 Geometry for the theory of microwaves reflected from a ferromagnet with a ferromagnetic overlayer.

$$E_{ex}/cm^2 = -\frac{4A^{AB}}{aM^AM^B}\mathbf{M}^A\cdot\mathbf{M}^B\ . \tag{4.26}$$

We have defined the interfacial exchange constant as:

$$A^{AB} \equiv \frac{2J^{AB}S^AS^B}{a} \tag{4.27}$$

to perserve the continuity of notation with the bulk exchange parameters, A^A and A^B. We have used a constant lattice spacing throughout both the overlayer and the substrate. Allowing it to be specific to the A or B layer or the interface just changes the definitions of the exchange parameters. For Ni on Fe the interface exchange parameter A^{AB} can be expected to be about the same order as A^A and A^B ~10^{-6} ergs-cm. The fields that act on the interface surfaces of the overlayer and the substrate (in Oe-cm) are therefore:

$$\begin{aligned} \mathbf{H}^A_{int} &= -\frac{2A^A}{(M^A_s)^2}\left(\frac{\partial \mathbf{m}^A}{\partial z}\right)+\frac{4A^{AB}}{aM^A_sM^B_s}\mathbf{M}^B \\ \mathbf{H}^B_{int} &= \frac{2A^B}{(M^B_s)^2}\left(\frac{\partial \mathbf{m}^B}{\partial z}\right)+\frac{4A^{AB}}{aM^A_sM^B_s}\mathbf{M}^A \end{aligned} \tag{4.28}$$

From these boundary conditions along with the outer surface conditions, the continuity of **e** and **h** and the Landau Lifshitz equations for both media the response of the system is completely determined. A computer program which was written by Dr. Cochran [1.6] to solve the problem was used extensively to determine the Ni overlayer magnetic properties as a function of thickness by comparing calculations with experiments. This comparison is carried out in the next section.

To gain insight into the effect of the overlayer on the resonance and to qualitatively understand the results of experiment, we consider the overlayer to be almost uniformly magnetized and to be strongly coupled to the substrate. This is approximately true if the overlayer is very thin because exchange holds the spins very nearly parallel. Thus

$$\frac{\mathbf{m}^A(z)}{M^A} \cong \frac{\mathbf{m}^B(d)}{M^B} \qquad \text{and} \qquad h^A_y(0) \cong h^A_y(z) \cong h^A_y(d).$$

where h_y^A is the microwave field.

An effective set of pinning conditions on the substrate can be found [1.6] by integrating the equation of motion across the overlayer, using the above approximations and by neglecting the overlayer exchange and Gilbert damping. The approximate boundary equations for the thick substrate are:

$$\left.\frac{2A^B}{M^B}\frac{\partial m_y^B}{\partial z}\right|_d = -\frac{dM^A}{M^B}(H^B - H^A)\, m_y^B(d) \tag{4.30a}$$

$$\left.\frac{2A^B}{M^B}\frac{\partial m_z^B}{\partial z}\right|_d = -\frac{dM^A}{M^B}(B^B - B^A)\, m_z^B(d) - \frac{2K_s}{M_s^B} m_z^B(d) \tag{4.30b}$$

where

$$H^B - H^A = \left(\frac{2K^B}{M^B} - \frac{2K^A}{M^A}\right) \tag{4.31a}$$

$$B^B - B^A = 4\pi(M^B - M^A) + \frac{2K^B}{M^B} - \frac{2K^A}{M^A}\,. \tag{4.31b}$$

when $\mathbf{M}^A$ and $\mathbf{M}^B$ lie along the [100] axis and where

$$H^B - H^A = -\left(\frac{2K^B}{M^B} - \frac{2K^A}{M^A}\right) \tag{4.31c}$$

$$B^B - B^A = 4\pi(M^B - M^A) + \frac{K^B}{M^B} - \frac{K^A}{M^A}\,. \tag{4.31d}$$

when $\mathbf{M}^A$ and $\mathbf{M}^B$ lie along the [100] axis. This difference in pinning between the easy and hard axes is critical for determining the cubic magnetic anisotropy of the Ni overlayers. The K_S term accounts for the overall surface pinning due to the outer layer of the Ni and both sides of the interface. We have reversed the sign of this term from reference [1.6] because our definition of E_{K_S} has an opposite sign.

The form of the boundary conditions (4.30) is characteristic of a partially pinned surface similar to those given in equation (4.24). We see directly that the overlayer magnetic parameters will have an effect on the Fe resonance. In this approximation only M^A and K^A are present in the pinning conditions but when the full theory is used all the overlayer parameters have an effect. Quite simply the pinning comes from the difference in resonant frequencies of the overlayer and the substrate. The overlayer magnetization is forced by the interlayer exchange coupling to follow the substrate resonance which occurs at a field value very different from its own resonance. For example if $M^A = M^B$ and $K^A = K^B$ we see from equations (4.30-31) that only the usual surface pinning term enters the boundary condition.

There are several interesting aspects of the boundary conditions. Both the y and z components of the magnetization are pinned unlike the case of the perpendicular suface anisotropy. The pinning also scales linearly with the thickness of the overlayer. The pinning depends on the orientation of the magnetization and this causes shifts of opposite sign in the field values of the easy and hard axes resonances. The difference in the easy and hard resonance fields can be measured accurately because it is a relative measurement and hence, as we will see, this will provide a means of determining the overlayer anisotropy constant K^A.

The differences in the volume anisotropies and saturation magnetizations which occur in the boundary conditions will have a large effect on the substrate microwave absorbed power. For an Fe substrate with a Ni overlayer $4\pi M^A < 4\pi M^B$ and one can neglect the anisotropy terms in the boundary condition for the magnetization component perpendicular to the surface ($2K/M << 4\pi M$ for both the A and B layers). From equation (4.31b) we calculate an effective surface anisotropy constant on the z component for a 50 Å film to be $K_{seff} \sim +2$ ergs/cm^2. This is a strong surface anisotropy which shifts the resonances to higher fields and can actually split the resonance as we will see in the next section.

4.5 Experimental Results

Our initial experiments were carried out on samples having relatively thick overlayers of Ni (~60 Å) which produced large effects upon the Fe FMR signals. This allowed us to identify the large cubic anisotropy present in the Ni films which is their main unique property.

Later we grew a series of samples with different thicknesses to study the thickness dependence of the Ni magnetic properties. We start by describing the results for 60 Å films.

FMR of 60 Å Thick Ni Films on Fe(001)

Though a 10 GHz *in situ* FMR apparatus was available we wished to work at higher fields and microwave frequencies than were available in UHV. The higher applied fields force the magnetizations to be close to parallel to the applied field direction for all angular rotations. This is necessary in order to use the theory of sections 4.2 and 4.4. To carry out FMR measurements outside the vacuum we grew fcc Au epitaxially on the "bcc Ni". The FMR measurements carried out in magnetic fields ~18 kOe at 73 GHz provided the most interesting results. The 73 GHz cavity operating in the cylindrical TE_{012} mode was particularly useful for angular FMR studies because its cylindrical symmetry made the response of the system independent of the angle of the applied field.

As a preliminary to measurements of the Ni on Fe samples, we measured the angular dependence of the resonant field of the Fe with no overlayer. The angular dependence of the Fe(001) FMR peak position followed that calculated using the crystalline anisotropy constants K_1, K_2 quoted by Wohlfarth [4.26], see Fig. 4.8. This result demonstrated that there were no noticeable strains in our Fe crystal (Fe sample 2) and that it was magnetically well-behaved.

The effect of a 60 Å Ni overlayer on the FMR of Fe is shown in Figs. 4.8 and 4.9. The resonances are shifted to higher fields at all angles. The shift is strongest at the hard axis of Fe and weakest at the easy axis. The FMR peak is dramatically split for orientations near the hard axis, see Fig. 4.9. The shift in the Fe FMR line position and splitting of the FMR line around the hard axis [110] can be qualitatively explained through the effects of the boundary conditions (approximated in equations 4.30-4.31) if the "bcc Ni" overlayer is ferromagnetic. To understand the data we note that if the pinning produces a negative derivative for either dynamic component of the magnetization the resonance shifts to higher fields, while a positive derivative shifts the resonance to lower fields. This was demonstrated in section 4.3 for the case of positive K_S, which from the boundary conditions in equations 4.24 causes $\partial m_z/\partial z$ to be

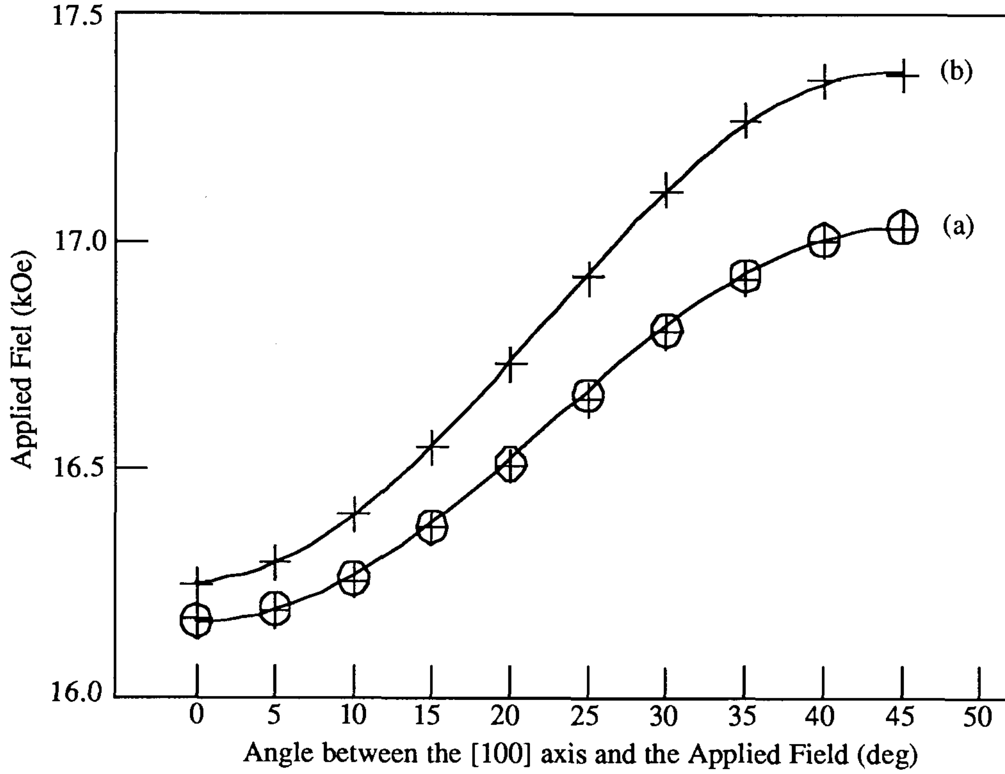

Fig. 4.8 The applied magnetic fields at which the microwave absorption is maximum are shown for 5^0 steps in angle as the applied field is rotated from the easy [100] to the planer hard [110] axis. Maxima are found from the zero crossings of the measurements of the derivative of the Ferromagnetic Resonance response at 73.55 GHz. Curve (a) is for the Fe(001) with a 30 Å Au coverlayer with the +'s for the data points and the O's for the theory points. Curve (b) is for the 60 Å Ni(bcc) overlayer on Fe(001) with a 30 Å Au coverlayer, see Fig. 4.9. The solid lines are of the form A + B cos(4θ) which are, by symmetry, the leading terms in the angular variation.

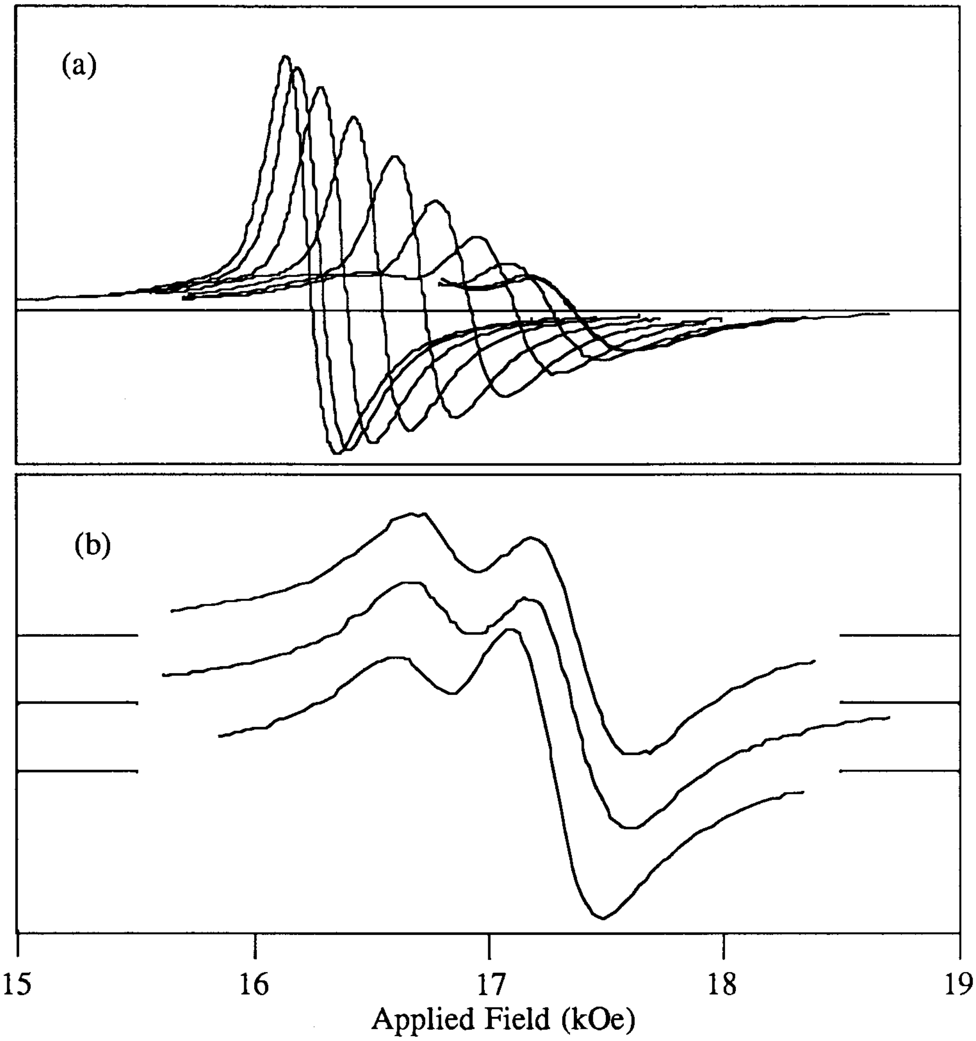

Fig. 4.9 Ferromagnetic Resonance response for 60 Å Ni(bcc) overlayer on Fe(001) with a 30 Å Au coverlayer. The measurements were made at 73.55 GHz in 5° steps in angle from left to right as the applied field is rotated from the easy [100] to the planer hard [110] axis. Note the splitting that occurs in the hard direction. The variation of the zero crossings with angle are shown in Fig. 4.8. Note also that only part of the last three curves are shown in (a). The full curves for 35^0, 40^0 and 45^0 angles are shown in (b) from bottom to top. The displaced zeros are indicated.

negative (see Fig. 4.5). An ordinary fcc Ni overlayer, which has a small anisotropy $(2K/M)_{fcc} = -200$ Oe, would shift both easy and hard axes by approximately the same amount. It would also create a similar splitting of the FMR line along both axes. This is a result of the presence of the strong pinning proportional to $-4\pi(M_{Fe}-M_{Ni})$ in the boundary condition (4.30(b)). The crystalline anisotropy term $(2K/M)_{fcc}$ is too weak and has the wrong sign to cause any anisotropic behaviour of the FMR lineshape. This can only mean that the crystalline anisotropy field, $2K^A/M^A$, of the Ni overlayer in the in-plane boundary equation (4.30a) is sufficiently large to partially overcome the out-of-plane negative surface pinning due to the difference in magnetizations between the overlayer and the Fe substrate. The difference in shifts between the easy and hard axis are caused by the difference in the pinning conditions between the easy and hard axes (equations (4.31a-b) and (4.31c-d)). This strongly suggests that the anisotropy of "bcc Ni" has the same sign as that for Fe but is larger.

The interpretation of our experimental results based on the simplified boundary conditions (4.30-31) reflects the main features but describes only crudely the FMR response of the samples. Computer calculations, using the exact theory outlined in section 4.3, shown in Fig. 4.10, were carried out using the fcc nickel parameters $A = 1.0\times10^{-6}$ ergs/cm, $g = 2.187$ and resistivity $\rho = 7.5\times10^{-7}$ Ω-cm. The parameters used for Fe are listed in the Fig. 4.10 caption. The saturation induction $4\pi M_s = 4.5$ kG was taken from the V.L. Moruzzi and P.M. Marcus [4.27] magnetic moment calculations for bcc Ni corresponding to the lattice spacing of the bcc Fe. The crystalline anisotropy constant K_1 for the "bcc Ni" was chosen to obtain the best agreement between the experimentally determined and the theoretically calculated peak positions along the [100] and [110] crystalline directions. Note that this choice of the crystalline anisotropy, $K_1 = 6.0 \times 10^5$ ergs/cc, removes the splitting along the easy axis [100]. The intrinsic Gilbert damping parameter $G = 6.0 \times 10^8$ sec^{-1} in the "bcc Ni" was chosen in order to achieve agreement between the experimental and calculated FMR lineshape for the dc magnetic field applied along the semi-hard [110] axis.

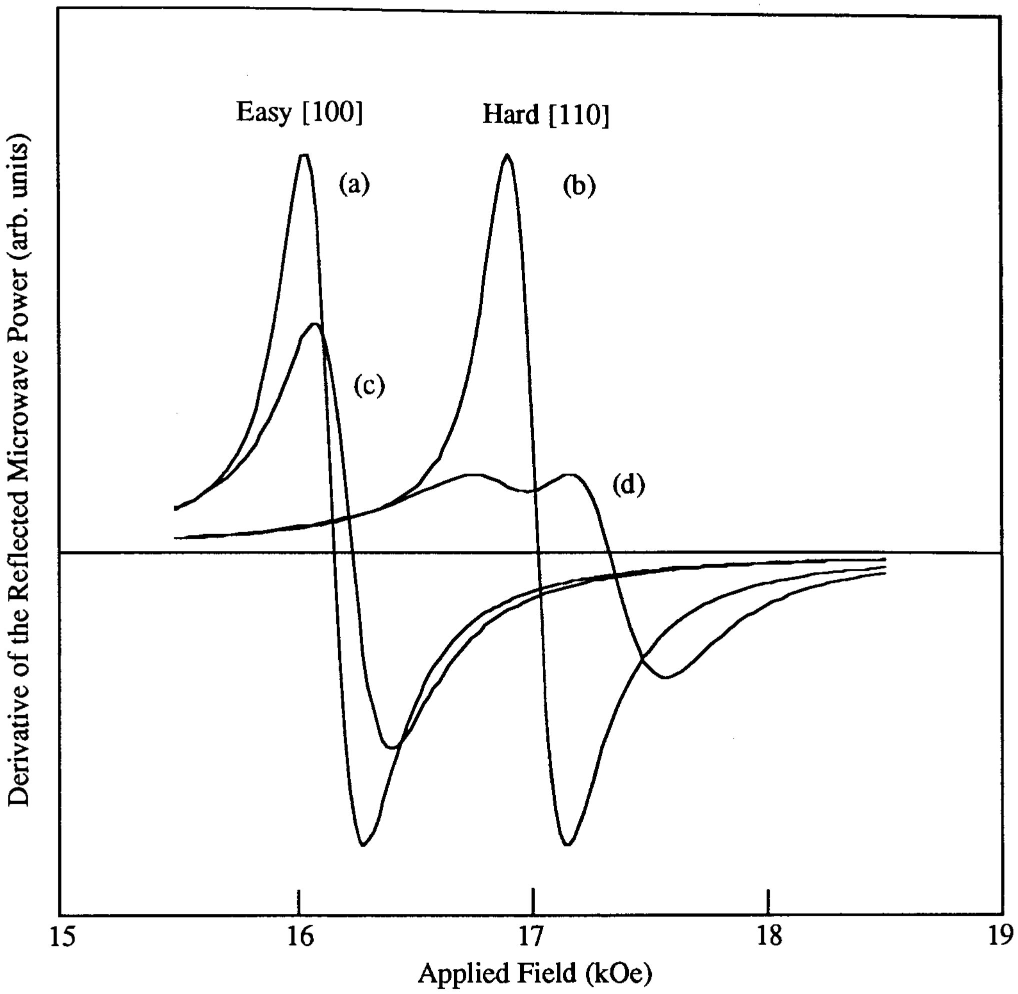

Fig. 4.10 Calculated field derivative of the microwave absorption for the (100) surface of Fe at 73.55 GHz with and without an epitaxial 60 Å bcc Ni overlayer for both the easy [100] and planer hard [110] directions. The curves (a) and (b) are for the easy and hard axis with no Ni overlayer. The curves (c) and (d) are for the easy and hard axes with the Ni overlayer. To achieve the agreement between Fig. 4.9 and Fig. 4.10, it is essential that the damping constant G be assigned a value near 6.0×10^8 sec^{-1} compared with 2.5×10^8 sec^{-1} found in fcc Ni at 300 K. The parameters used are: frequency f = 73.55 GHz; thickness of the overlayer d = 60 Å; surface exchange constant $A^{AB} = .6 \times 10^{-6}$ cm; $\omega/\gamma = 24.01$ kOe for Ni (bcc) and 25.03 kOe for Fe; $4\pi M_S = 4.5$ kOe for Ni (bcc) and 21.55 kOe for Fe; anisotropy, $K_1 = 6 \times 10^5$ ergs/cc for Ni (bcc) and 4.81×10^5 ergs/cc for Fe; $K_2 = 0$ for Ni(bcc) and 1.2×10^3 ergs/cc for Fe; resistivity $\rho = 7.2$ $\mu\Omega$-cm for Ni(bcc) and 10 $\mu\Omega$-cm for Fe; the exchange constant is $A = 10^{-6}$ ergs/cm for Ni and 2×10^{-6} ergs/cm for Fe.

Clearly, the "bcc Ni" structure exhibits a drastic change of the magnetocrystalline anisotropy: the crystalline anisotropy constant K_1 in the "bcc Ni" has the same sign as in bcc Fe, and the effective field $(2K_1/M)_{bcc} \approx 3$ kOe is more than ten times the value for K_1 measured in the fcc Ni ($|(2K/M)_{fcc}| = 0.24$ kOe).

10 GHz FMR measurements were carried out *in situ* in UHV to investigate the temperature dependence of the Ni on Fe system in the absence of Au. The resonance measured at room temperature was unchanged by heating to 200 C, that is, the Fe FMR at 200 C was still affected by the Ni magnetism. This puts a lower bound on the Curie temperature of "bcc Ni". We also verified, by using *in situ* 10 GHz FMR measurements, that the effect of Ni on the Fe resonance was not changed by covering the Ni with Au. The Au covered sample was then exposed to the air and it was verified that the FMR results were not changed by a prolonged exposure to the air. This gave us confidence that our samples could be removed from the UHV system for measurements in several FMR spectrometers without affecting their properties.

Thickness Dependence of the Magnetic Properties of the Ni Overlayers

After we had observed the effect of the 60 Å Ni overlayers on the Fe resonance we wanted to determine the thickness dependence of the magnetic parameters of the Ni, particularily of the in-plane 4-fold anisotropy. We had originally hoped to measure the magnetic parameters of the very thinnest layers (3 - 6 ML) which we know have the bcc structure. The FMR was measured on Fe sample 1 with Ni overlayer thicknesses of 0, 8.5, 19, 34.3 and 34.9 Å all covered with 30 Å of Au. The sample was not repolished between growths so that the demagnetizing field was constant. Hence we could determine the field shifts in FMR resonance accurately. Measurements were made at both room and LN_2 temperatures. FMR measurements were also made on various Fe (100) samples with overlayers of different thicknesses and demagnetizing fields.

Precision calibrations of the applied field and microwave frequency were necessary because the shifts were expected to be small for thin samples (20 - 30 Oe for eg.). We had to measure to within one part in a thousand over a period of several months. We calibrated the frequency meter and field as accurately as possible and to used a standard sample to obtain a measure of the reproducibility. The fields were calibrated each day using an NMR probe and with the sample removed from the magnet gap: the day to day drifts were observed to be ~1 - 3 Oe. The frequency meter was calibrated using the accurately known g-factor for the ESR of 2,2-diphenyl-1-picrylhydrazyl (DPPH). One problem encountered was that the magnetic moment of the sample itself could have effected the Hall probe which sat in the gap and stabilized the magnet. By assuming that the sample was a magnetic dipole we estimated that the extra field at the Hall probe was only ~2 Oe. We checked that the FMR resonance did not change appreciably when the sample and cavity were displaced in the magnet gap. As a standard we used Fe sample 2 which was prepared in the UHV and covered with 30 Å of Au. The fields at which the microwave absorption was a maximum ("FMR resonance fields") were measured by means of the zero crossings of the derivative curves and were measured for this sample during the same period as the measurements on the Fe sample covered with the Ni overlayers. The field positions of FMR were reproducible to within 10 Oe during this period and the difference in fields of the easy and hard axes resonances to within 2 Oe.

The main experimental results of this chapter are shown in Figs. 4.11 and 4.12. In Figs. 4.11 (a) and (b) we plot the FMR resonance fields as a function of the Ni overlayer thickness at 297 K and 77 K respectively. The + and x symbols are for measurements of FMR taken with the magnetization rotated 90°. In (c) and (d) we plot the difference in FMR resonance fields between the easy and hard axes which depends mainly on the bulk and overlayer cubic anisotropies. Error bars for most of the data points are no larger than the size of the symbols in both field and thickness. Most of the thicknesses at greater than 40 Å are accurate only to within ~ 5 Å because they were grown before we used RHEED oscillations or had installed a quartz crystal thickness monitor.

There are several features of the graphs to note which we relate to the magnetic parameters of the overlayer. From (a) and (b) we see that the 8.5 Å Ni overlayer causes the FMR resonances to shift to lower fields (~20 ± 5 Oe at 297 K and 35 ± 5 at 77 K). The difference

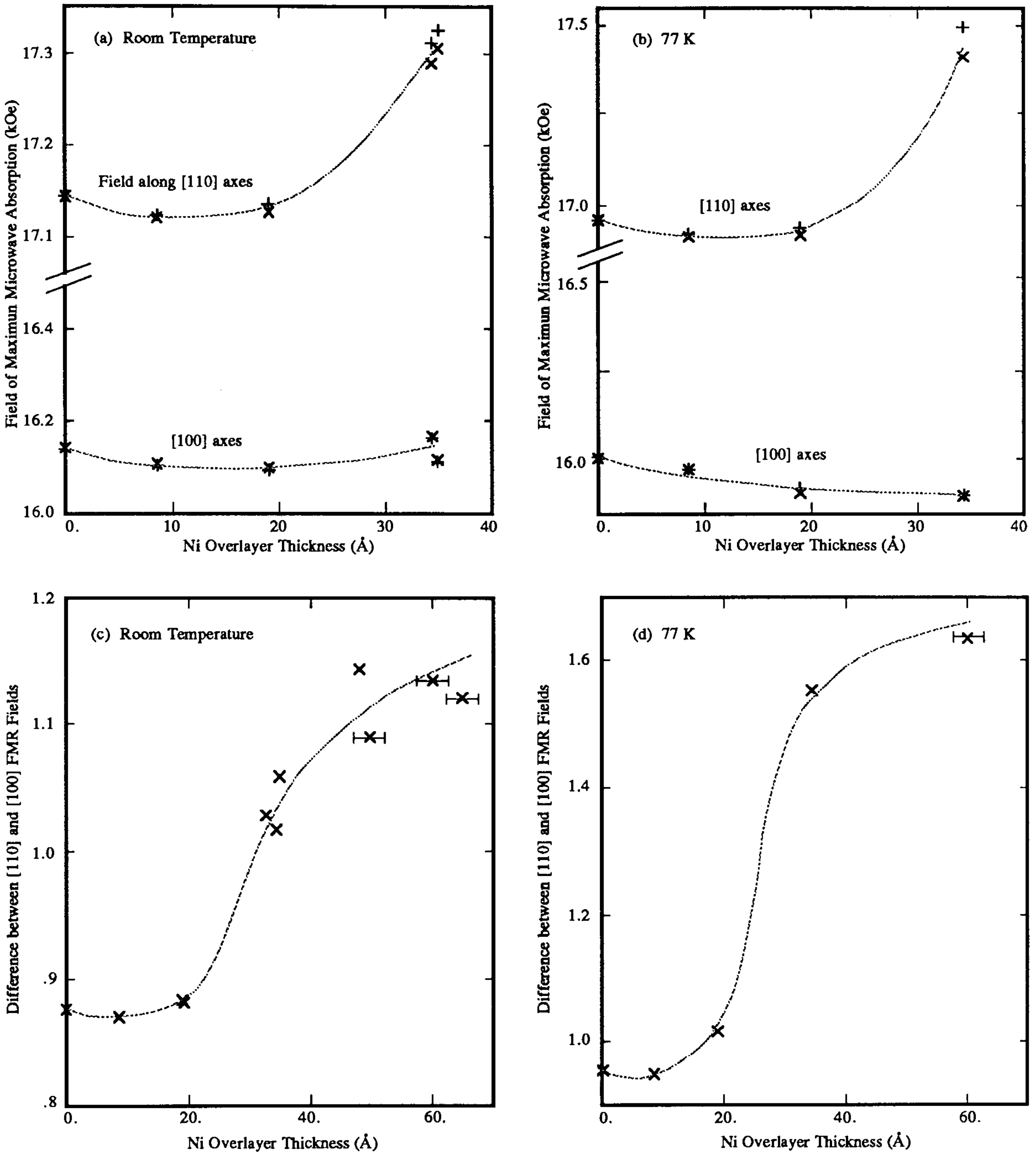

Fig. 4.11 (a)(b) The FMR resonance fields at 73 GHz as a function of Ni overlayer thickness for a series of measurements with no polishing of the sample between growths: (a) 297 K; (b) 77 K. The + and x symbols are for measurements for the in-plane angle of the magnetization 90 deg apart. In (c) and (d) we plot the difference between the resonance field when the magnetization lies along the [110] axis and when it lies along the [100] axis. Measurements that are not a part of the series for plots (a) and (b) are included. The large error bars are for samples with less precise thickness measurement. The dashed lines are there to guide the eye.

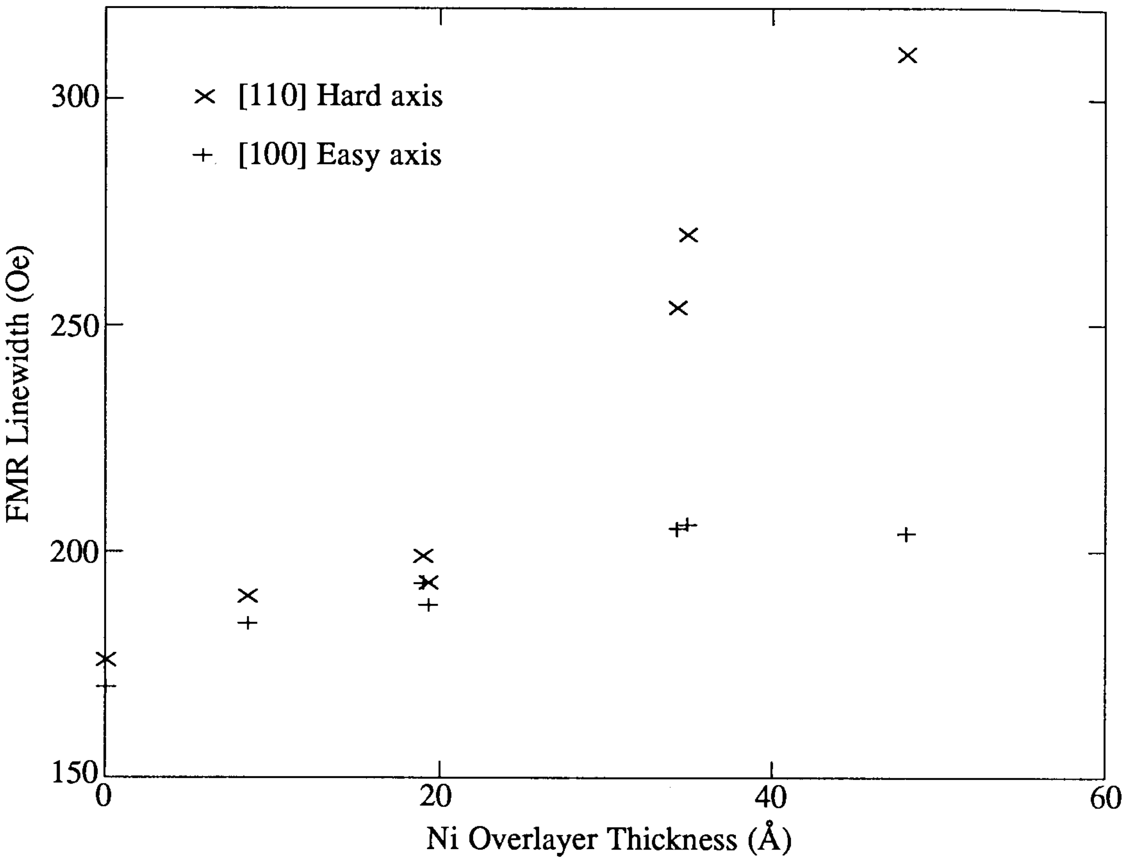

Fig. 4.12 Experimental linewidths of [110] and [100] axes FMR resonances as a function of Ni overlayer thickness. Measurements were made at 73 GHz and room temperature. Note that the hard axis linewidth increases rapidly at ~25 Å.

between the easy and the hard axis resonance fields also decreases slightly as shown in Fig. 4.11(c) (~7 ± 2 Oe). Thicker Ni overlayers cause the hard axis resonance to shift to substantially higher fields while the easy resonance field shifts only slightly. The hard axis shift increases rapidly at ~25 Å and starts to level off at ~35 - 45 Å. The behaviour of the linewidth in Fig. 4.12 is quite similiar. Whatever affects the position of the (110) resonance also increases its linewidth. We argue below that the source of this increase is inhomogeneous broadening. The shift of the hard axis resonance field caused by the overlayer is about three times larger at 77 K than at 297 K.

From (a) and (b) we see that there is a small difference between the resonance fields for the two hard axes in the plane of the sample (the + and x symbols in the figure) which increases with overlayer thickness. This shows the existence of a small thickness dependent uniaxial anisotropy with the uniaxial axis in the sample plane. In chapter 5 we will show that this is induced in the overlayer by growing the films on vicinal substrates (in this case < .5 °)

Fitting the FMR spectra to theory with a unique set of magnetic parameters is very difficult because there are many parameters, some of which affect the resonances in similar ways. Small uncertainties in field and frequency calibration become important for the small shifts due to the thinnest overlayers. Even the small uncertainties in the tabulated Fe parameters affect the accuracy of the fits. We first try to understand our measurements qualitatively using the approximate surface pinning conditions in equations 4.30-31 before describing quantitative results.

Consider the theoretical dependence of the resonance fields on the thickness of the Ni overlayers if the Ni magnetic parameters are independent of thickness. This is shown in Fig. 4.13 where we plot the theoretical shift in easy and hard axes resonance fields as a function of overlayer thickness with an anisotropy field in the overlayer of $2K^A/M^A = [(7.5\text{x}10^5 \text{ ergs/cm}^3)]/(4.5/4\pi \text{ kOe}) = 2.1$ kOe. The resonance fields and their differences are strictly increasing functions of Ni thickness unlike the experimental thickness dependence of Fig. 4.11. This is true for any physically reasonable choice of overlayer parameters. This means

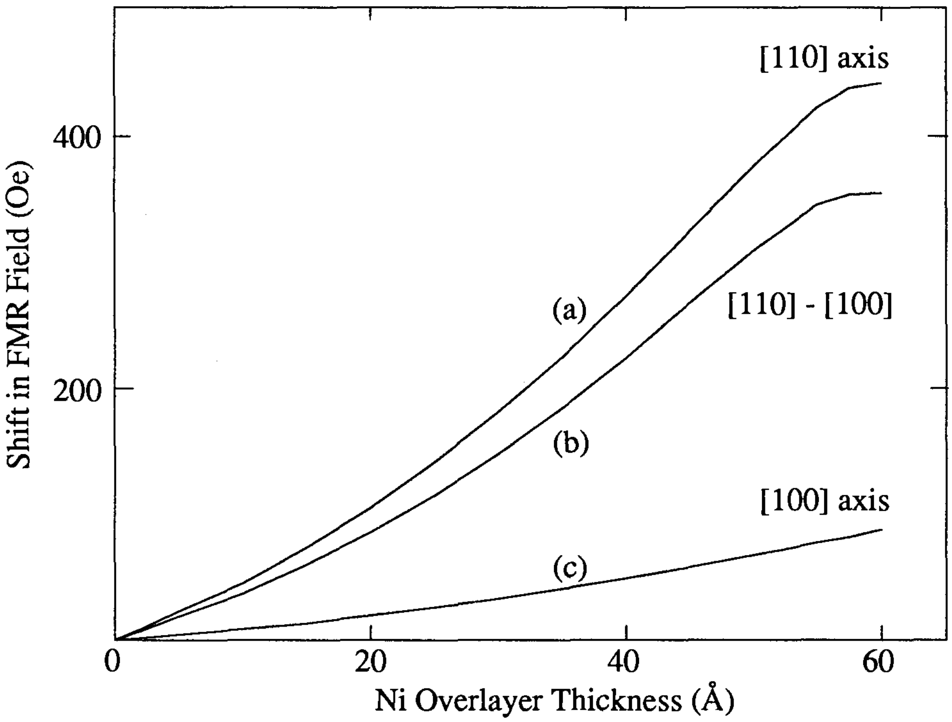

Fig. 4.13 The theoretical shift at 72.91 GHz in the field at which microwave absorption is a maximum for a Fe (001) crystal as a function of Ni overlayer thickness. Curve (a) is for the [110] hard axis, curve (c) is for the [100] (easy) axis and curve (b) is the difference between (a) and (c). The Ni overlayer is assumed to have thickness independent magnetic parameters. The Fe parameters we used were $4\pi M^B = 21.55$ kOe, g-factor=2.085, $K^B=4.85\times10^5$ ergs/cm^3, $A^A = 2.0\times10^{-6}$ ergs/cm, $\rho = .98\times10^{-5}$ Ω-cm, G=.8x10^8 sec^{-1} and demagnetizing field of 390 Oe. The Ni parameters we used were $4\pi M^A = 4.5$ kOe, g-factor=2.187, $K^A=7.5\times10^5$ ergs/cm^3, $A^A = .8\times10^{-6}$ ergs/cm, $\rho = .722\times10^{-5}$ Ω cm, G=7x10^8 sec^{-1} ([110 axis), G=2x10^8 sec^{-1} ([100 axis) and K_s=.3ergs/cm^2. We also used $\beta = .05$ (see section 4.3) and $A^{AB} = .6\times10^6$ (ergs/cm).

that the overlayer magnetic parameters are dependent on the film thickness and must be determined for each overlayer thickness.

As we noted above the results for the 8.5 Å film show a decrease in both the easy and hard axes resonance fields. From equations 4.30-4.31 the pinning due to a magnetic overlayer is dominated by the $4\pi(M^A - M^B)$ term which would shift the resonances to higher rather than to lower fields. The decrease in FMR resonance fields for the 8.5 Å films must be caused by a decrease in K_s, the surface pinning parameter. From our work in section 4.3 we know that the pinning at the Fe surface depends on the type of metal that is used as an overlayer and hence the Ni overlayer could well cause a large reduction in K_s. A decrease in K_s lowers both the easy and hard axis resonance fields by the same amount.

The measurements show that there is also a decrease in the difference between the easy and hard axes FMR fields (7 ± 2 Oe at both 77 K and 297 K). This can be explained by assuming that the Ni overlayer has a finite magnetization M^A. The source of the small decrease in the splitting between the easy and hard axes is then terms proportional to dM^AK^B/M_B^2 in the pinning conditions (equation 4.31), which causes shifts in the easy and hard axes resonances of opposite sign.

At thicker coverages the increase in the difference between the easy and hard resonance fields is clearly caused by a large cubic anisotropy in the overlayer. This is the only parameter which can cause this effect when varied within reasonable bounds (see Fig. 4.14 and discussion below). What is unique about these samples is that we have created a large 4-fold anisotropy, an order of magnitude greater than found in fcc Ni, and of the opposite sign. The leveling off of the curves in Fig 4.11 (c)(d) at ~30 Å shows that the 4-fold anisotropy in the overlayer reaches a relatively constant value in thicker samples. The approximately three times larger shift in resonance fields at 77 K relative to the shifts at room temperature shows that the anisotropy of the Ni overlayer is approximately three times larger at 77 K than at 297 K. For fcc Ni the anisotropy also has a large temperature dependence, increasing by an order of magnitude between 297 K and 77 K.

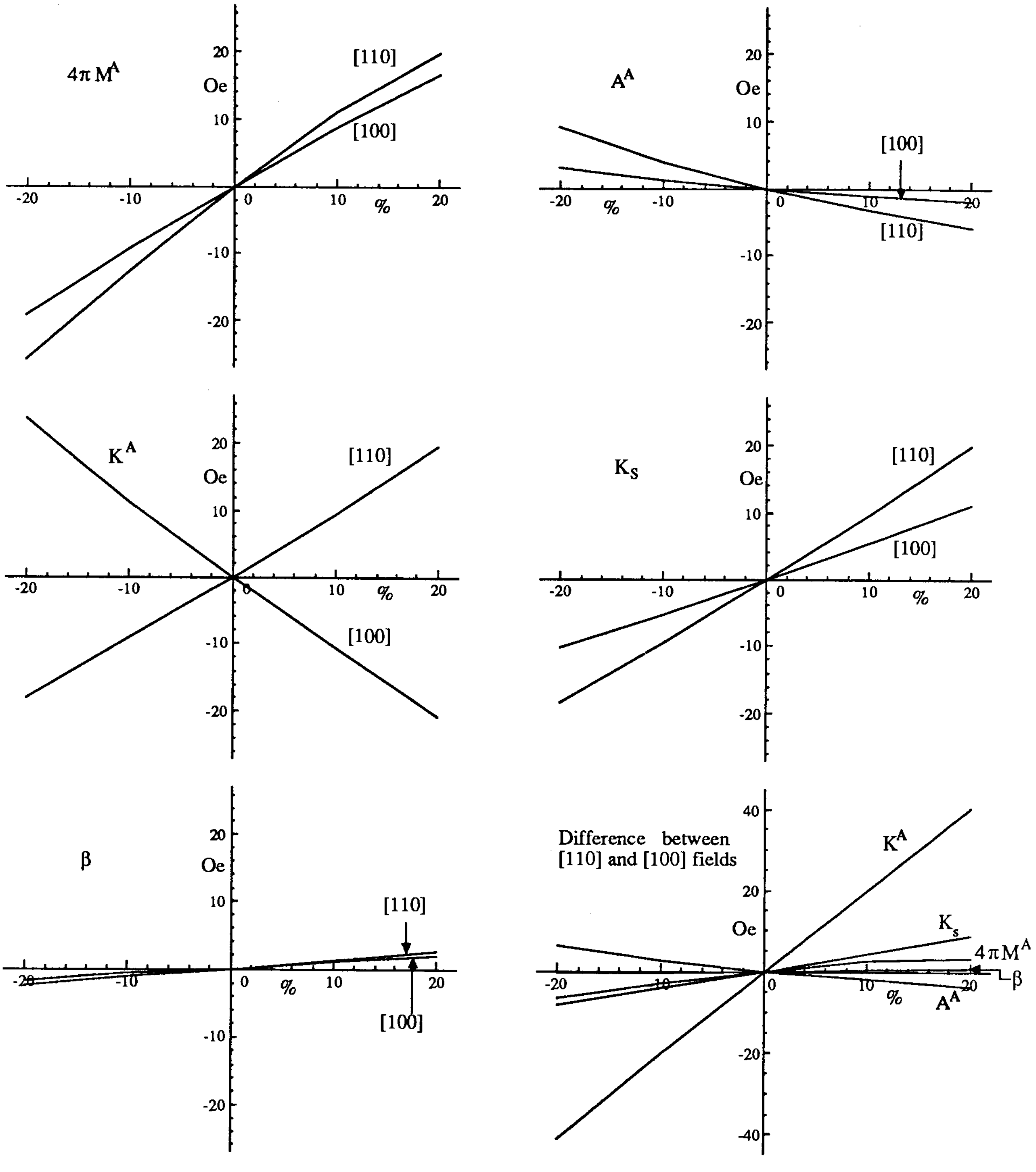

Fig. 4.14 Theoretical variations in the FMR resonance field of an Fe (001) crystal covered with a 34.9 Å film of Ni with % changes in the Ni overlayer magnetic parameters. The variations of both the easy and hard axes resonances are plotted. We started with the magnetic parameters listed in caption of Fig. 4.13 and varied one parameter at a time. Only K^A shifts the [110] and [100] axes fields in opposite directions. The difference in between easy and hard axes shifts is plotted in the lower right corner and shows that it is most dependent on K^A.

Before trying to make detailed fits to the spectra we show in Fig 4.14 how the resonance field depends on various overlayer magnetic parameters. A set of Ni parameters was found by fitting the spectra taken using the 34.9 Å sample. Calculations were carried out by varying these parameters one at a time in steps of 10%. The shift in resonance fields of the easy and hard axes due to the variation of each parameter is shown in Fig. 4.14. The saturation magnetization, the exchange constant, the perpendicular surface anisotropy, and the mixing parameter β all shift both the easy and hard axes the same direction in field. Hence the difference between the easy and hard resonance fields will be insensitive to these parameters. Only the cubic anisotropy K^A shifts the resonance fields in opposite directions. Therefore the fits are especially sensitive to this parameter. The effect of the overlayer Gilbert damping on the resonance fields is not shown in Fig. 4.14. It has negligible effect on the resonance fields and the strongest effect on the linewidth so it is also fairly well determined from fitting the linewidths.

In Fig. 4.15 we show FMR spectra from a Fe sample with a 34.9±.3 Å overlayer of Ni at 73 GHz with superimposed theoretical fits. The parameters are listed in the caption of Fig. 4.13. Of particular note are the large values of $2K^A/M^A \cong 3.3$ KOe and the anisotropic behavior of the Gilbert damping ($2\text{x}10^8$ sec^{-1} and $6.5\text{x}10^8$ sec^{-1} for the easy and hard axes respectively). For both theory and experiment the hard axis FMR has a pronounced shoulder on the low side of the first maximum which becomes a distinct peak on samples with thicker coverages. As well the field positions and linewidths of the theory and experiment are well matched.

In Fig. 4.16 we show experimental and theoretical FMR at 36.65 GHz with the fitting parameters listed in the figure caption. The parameters are fairly consistent between the two frequencies which is important and gives us confidence in our fits.

Only the value of G^A is quite different between the two frequencies having appreciably larger values at 36.65 GHz. This is because the overlayer damping has a large frequency independent part. Frequency independent losses are usually attributed to inhomogeneous line broadening which as we mentioned in section 4.2 can be caused by magnetic defects. In

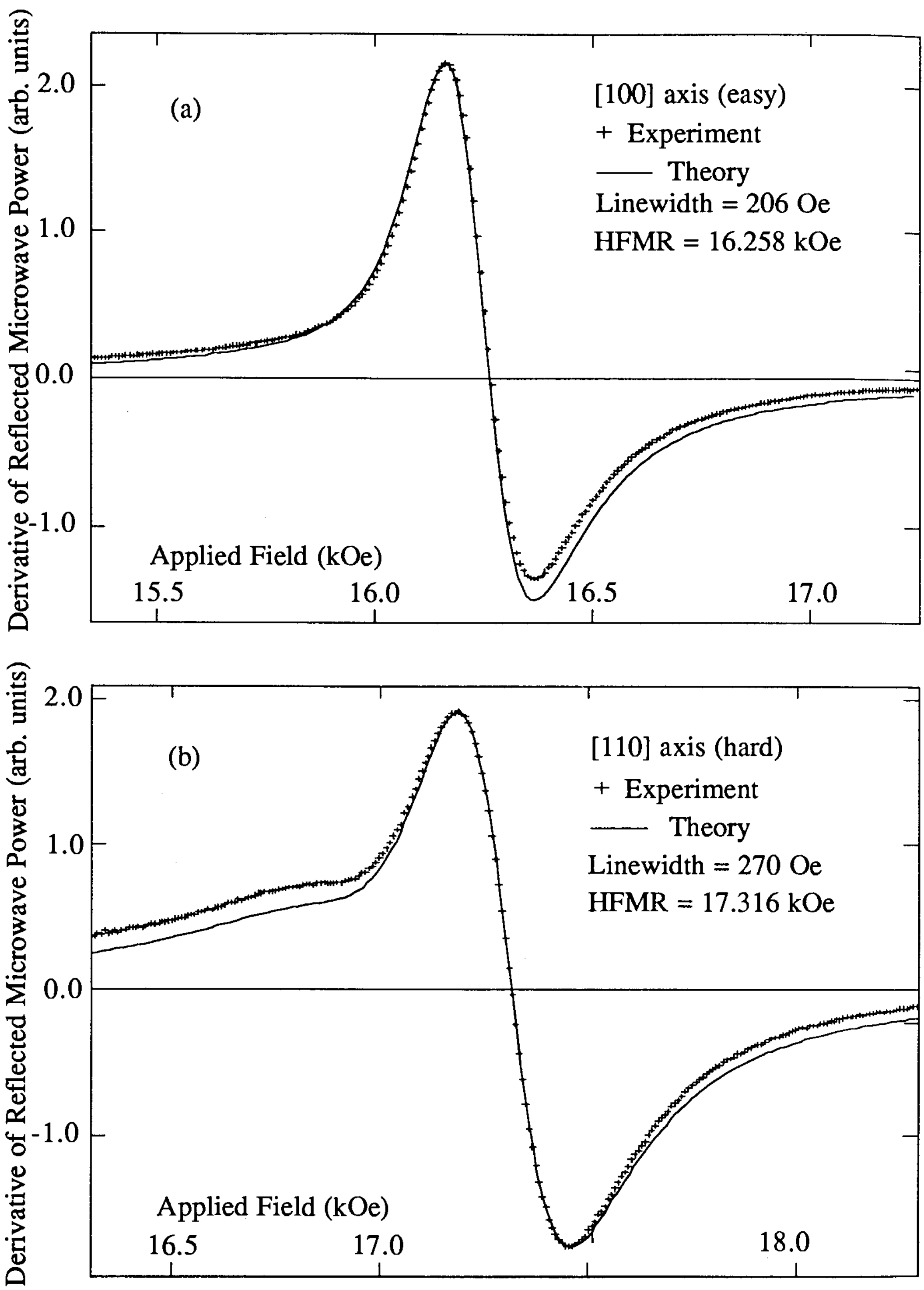

Fig. 4.15 Theoretical and experimental ferromagnetic resonance lines from a 30 Å Au/34.9 Å Ni/ Fe (100) sample at room temperature and 72.91 GHz. The magnetic parameters are listed in the caption of Fig. 4.13.

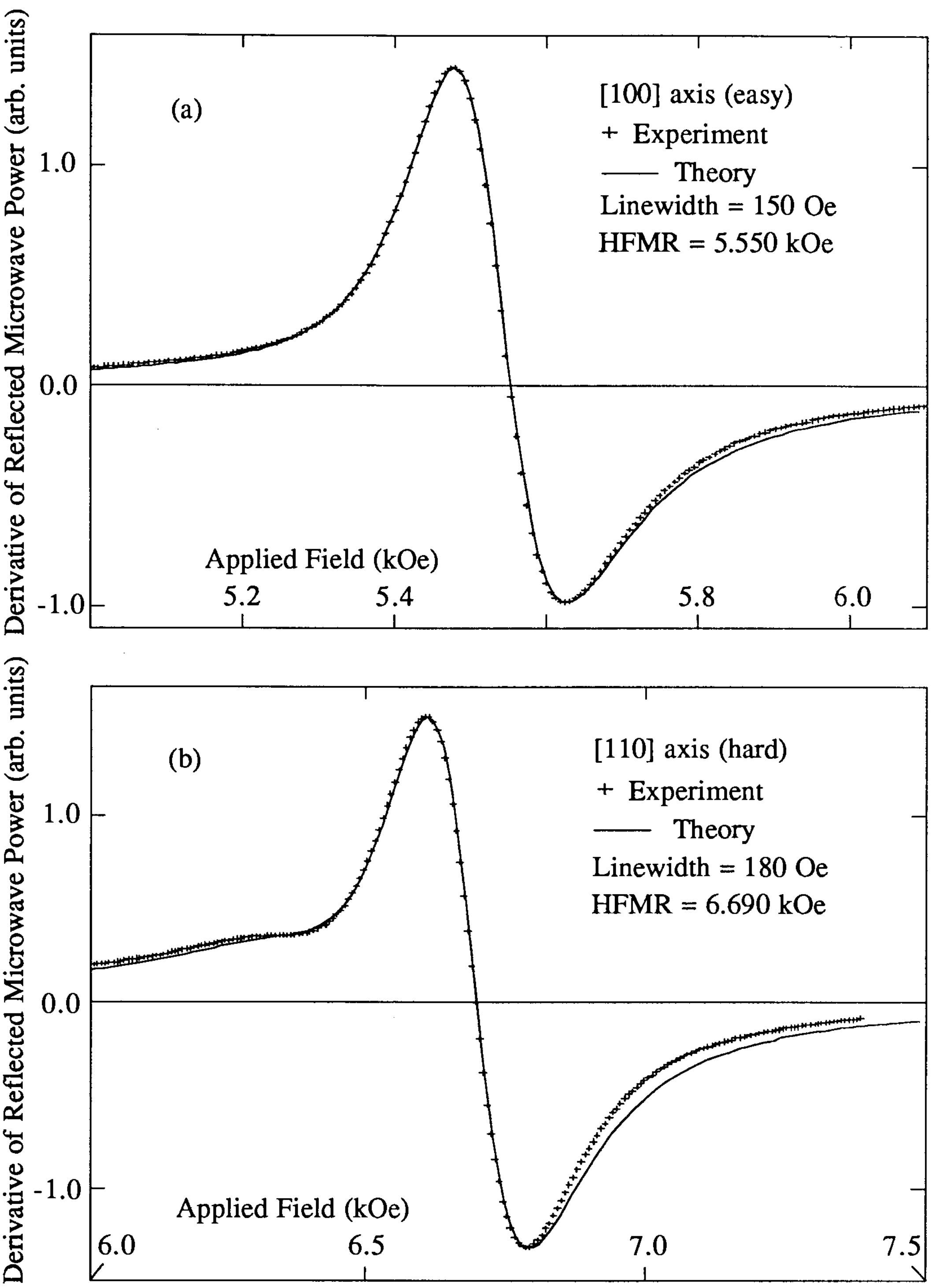

Fig. 4.16 Theoretical and experimental ferromagnetic resonance lines from a 30 Å Au/34.9 Å Ni/ Fe (100) sample at room temperature and 36.65 GHz. The magnetic parameters are the same as those listed in the caption of Fig. 4.13 except we used $K^A = 8x10^5$ ergs/cm^3, G=11x10^8 sec^{-1} ([110] axis) and G=2.8x10^8 sec^{-1} ([100] axis).

writing the theory we assumed the damping field to be proportional to frequency (see eqn. 4.9). If the damping is actually partially frequency independent, we need to fit with larger G values at lower frequencies. That is, if the linewidth is given by $\Delta H \propto fG + \text{const} = fG'$ where f is the frequency, G is the true Gilbert constant and G' is the Gilbert constant we get from fits, then $G' = G + \text{const}/f$. Therefore G' is larger at lower frequencies. As we mentioned in section 4.2 inhomogeneous line broadening is caused by magnetic inhomogenities. Both the anisotropy between the easy and hard axes linewidths and the increase in the 4-fold anisotropy occur at the same thicknesses (see Figs. 4.11 and 4.12). This indicates that the cubic anisotropy is caused by defects in the overlayers and that the defects are coordinated with the square symmetry of the substrate.

In Fig. 4.17 we plot the value of the 4-fold anisotropy field $2K^A/M^A$ as a function of Ni thickness found by fitting the FMR spectra. This field reaches a saturated value of ~1.7 kOe at ~35 Å. The value at 19 Å is higher than at first expected from inspecting the curves in Fig. 4.11(c) because it has to overcome the $2K^B/M^B$ term in the pinning conditions (equations 4.31).

We did not make fits to the low temperature data because we would have to include corrections in the theory for the anomalous skin effect (see [4.28] for example). At low temperature and GHz frequencies the mean free path of the electrons becomes comparable to the distance they travel in one microwave cycle and therefore the conductivity becomes non-local. This means we cannot use the simple relation $\mathbf{j} = \sigma\mathbf{e}$. However, as noted before, because the shifts of the FMR are roughly three times greater at 77 K than at 297 K the 4-fold anisotropy also is roughly three times greater. We will determine the 4-fold anisotropy field of ultrathin Ni/Fe films at 77 K in chapter 5.

We show the magnetic parameters we found for the 8.5, 19 and 34.9 Å Ni films in Table 4.3. As we mentioned the curve fitting is complex. We started by working with the 34.9 Å film because it is more strongly affected by the overlayer and we had measurements at both 73 and 36.6 GHz. We began with a reasonable set of Ni parameters similar to fcc Ni.

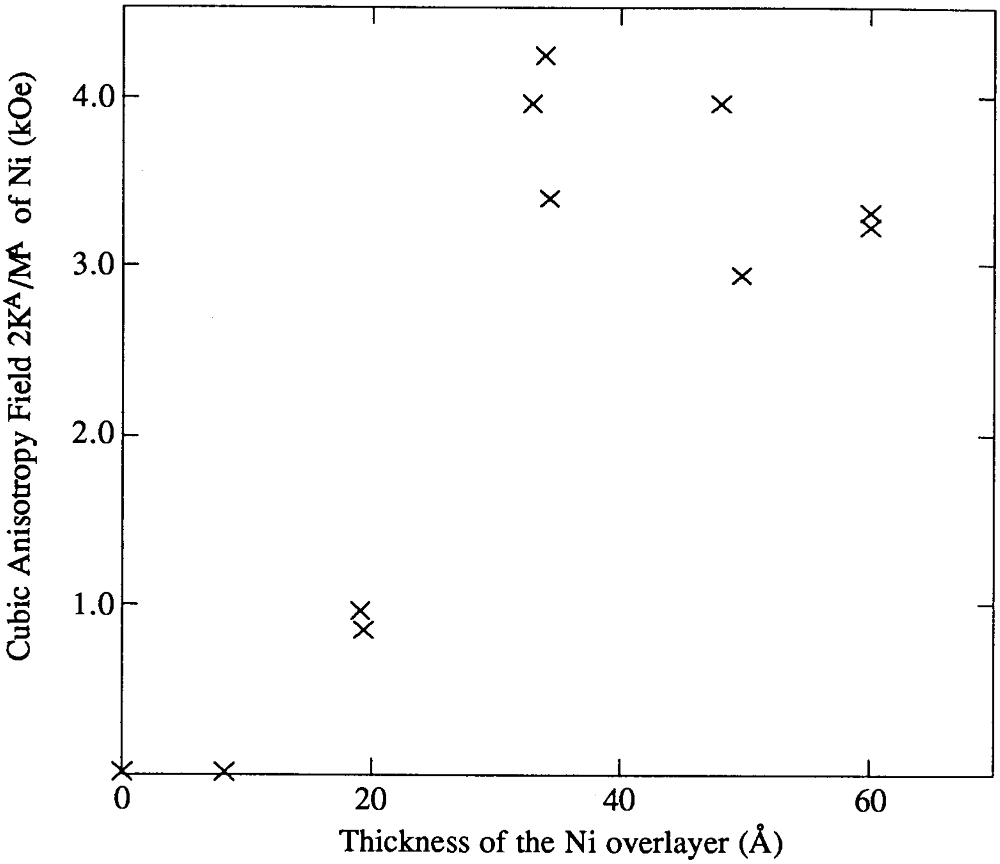

Fig. 4.17 4-fold anisotropy fields in Ni overlayers on Fe(001) substrates for different Ni thicknesses. The fields are found from fits of theory to the experimental points in Fig. 4.11(c). We used $4\pi M^A = 4.5$ kOe.

Next a value of K^A was chosen to give the correct value of the splitting between the lines. The other parameters were then varied to give the absolute position of the lines and G was varied to give the correct linewidths. This procedure was be iterated several times at both frequencies to give a consistent set of parameters. The quality of the fits achieved for both frequencies are shown in Fig. 4.15 and 4.16. We found K^A values from approximately 6.5×10^5 to 8×10^5 (ergs/cm^2) depending on the choice of the other parameters. The other thicknesses were then fit allowing only K^A, G and K_s to vary.

The value of K_s seems to vary considerably with thickness. But this is assuming that M^A and the g-factor are thickness independent. In hindsight it may have been better to have used the value of K_s obtained for the 8.5 Å sample where it is the dominant pinning effect for the other thicknesses. In the computer program K_s acted only at the outer surface of the Ni layer and not the Fe/Ni interface. Rather than rewrite the program, we assumed that to a good approximation the effects would be the same at either surface.

Table 4.3: Ni overlayer magnetic parameters at 73 GHz and 300 K determined by FMR. We used $4\pi M(\mathrm{Ni}) = 4.5$ kOe, g-factor=2.187, mixing parameter β=.05, $A^A = .8 \times 10^{-6}$ (ergs/cm) $A^{AB} = .6 \times 10^{-6}$ (ergs/cm) and the Fe parameters listed in Table 4.1 for all the thicknesses.

	thickness		
parameter	8.5 Å	19 Å	34.9 Å
K_s (ergs/cm^2)	.15	0	.3
G (sec^{-1}) [100]	2×10^8	2×10^8	2×10^8
G (sec^{-1}) [110]	2×10^8	2×10^8	6.5×10^8
K^A (ergs/cm^3)	0.0×10^5	1.5×10^5	7.8×10^5
$2K^A/M^A$ (kOe)	0	.84	4.4

Now we summarize the results of this section. The perpendicular surface anisotropy decreases by ~.4 erg/cm^2 when the Au/Fe interface is replaced by the Fe/Ni interface. The thinnest Ni sample of 8.5 Å appears to be ferromagnetic with a low 4-fold anisotropy. The 4-fold anisotropy starts to increase rapidly as a function of overlayer thickness at ~15 Å and saturates at ~ 30 Å with a value 15-20 times the fcc Ni value. Some of this increase could be explained by an increase in the Curie temperature with thickness. But to obtain such a large 4-fold anisotropy we invoke microscopic strain defects of 4-fold symmetry forced on the overlayers as it trys to lattice match to the cubic substrate. This idea will be developed further in chapter 5. The magnetic damping, as determined from the linewidth, is anisotropic in thicker Ni overlayers. That the FMR spectra for the 110 direction are affected by inhomogeneous line broadening follows from the observation that the Gilbert damping constant appears larger at lower frequencies. The increased damping in the (110) directions also provides evidence that a 4-fold strain system exists in the overlayers.

Chapter 5

Magnetic Properties of Ultrathin Ni/Fe Bilayers Grown Epitaxially on Ag(001)

5.1 Introduction

An exciting aspect of Molecular Beam Epitaxy (MBE) is the ability to grow new magnetic materials. In this chapter we present our recent results [1.15] on the growth by MBE of ultrathin bilayers of "bcc Ni"/bcc Fe grown on Ag (001) single crystal substrates. The ultrathin Ni/Fe bilayers form new materials with unique magnetic properties of their own. Their magnetic properties were studied using Ferromagnetic Resonance (FMR) and Brillouin Light Scattering (BLS). The BLS measurements were carried out by John Dutcher and are reported fully elsewhere [1.15, 5.1]. They will be mentioned only briefly here.

In Chapter 4 we discussed how FMR experiments carried out on ultrathin Ni(001) layers epitaxially deposited on bulk Fe(001) substrates revealed that Ni overlayers greater than a certain thickness exhibited a large in-plane cubic magnetic anisotropy ($2K_1/M_s \approx 3.4$ kOe). The magnetic response of these samples was dominated by the Fe substrates and weakly modified by the Ni overlayers. A unique interpretation of the FMR results was hard to achieve due to complexities arising from a strong dependence of the dynamic surface pinning on all Ni overlayer magnetic parameters. Most of these complexities could be avoided by replacing the bulk Fe substrate with ultrathin Fe films epitaxially grown on bulk Ag(001) substrates. The Ni magnetic parameters then play a larger role in the response of the samples to microwaves. The Ni thickness was held constant at 10 ML while the Fe thickness was varied in order to separate the role of the two materials. Such Fe films have suitable surfaces for epitaxial growth, as determined by RHEED (see Fig. 3.23). The interpretation of our results relies on previous work carried out on ultrathin layers of bcc Fe epitaxially grown on fcc Ag(001) substrates [1.12,4.17]. This research on the bilayers has been fully reported [1.15]. Quotes from much of that paper form the basis of this chapter which is outlined as follows:

Section 5.2: This contains a description of the samples studied in this chapter. The structural characterization has already been discussed in section 3.9.

Section 5.3: Our initial goal was to learn more about the magnetic properties of the "bcc Ni". To extract the magnetic parameters of the "bcc Ni" from the bilayer data the theory of bilayer magnetic properties was formulated in terms of the magnetic properties of the individual layers. The theory of ferromagnetic resonance for bilayers is developed in this section for the case in which the magnetization of each of the two layers is strongly coupled within the layer and the two layers are more weakly coupled with one another. This is a continuum theory. From it we deduce the scaling rules which describe the way the magnetic properties of the combined layers depend on the parameters for the two layers. As long as the coupling is not too weak this complicated problem can be understood well enough to extract those properties of the film which obey a simple scaling law that assumes that properties, such as anisotropy, of one layer are not changed by the proximity of the other layer. This may not be the case for all the properties because the electrons can move freely from one metal to the other. By comparing the experimental results for FMR with this theory we are able to see if the itinerant electron effects are discernable on properties such as the gyromagnetic ratio or the damping. Also we show in this section the theoretical existence of an optical mode in which the magnetizations in the two layers do not precess in unison, but precess 1/2 cycle out of phase.

Section 5.4: When the exchange coupling between the two materials in the bilayer is comparable to the coupling between the layers of each material it should still be possible to deduce the properties of the coupling between the layers by studying the optical modes of the bilayer. The theory of the bilayer magnetic modes was worked out by treating each monolayer as an effective spin which is exchange-coupled to its nearest neighbour monolayers.

Section 5.5: For each FMR measurement the results are fitted to obtain the magnetic properties of the material at a particular frequency and angle. The FMR studies of the bilayer systems were carried out at frequencies of 36 and 73 GHz, as a function of angle, and at temperatures of 300 K and 77 K. As in the Ni grown on bulk Fe (001) the angular dependence of the FMR exhibits anisotropies in the basal plane that are large compared to those normally found in transition series elements. The anisotropies are found by fitting the angular dependence of the FMR using the bilayer theory.

Section 5.6: The analyses of the results of the FMR experiments is carried through, showing clearly that the large anisotropy of these films is a property of the Ni layers.

Section 5.7: Conclusions: In growing the ultrathin Ni/Fe layers we have created a new magnetic material with magnetic properties that can be controlled by the choice of the individual layer thicknesses.

5.2 Sample Description

To study the magnetic properties of Ni overlayers in their pure and reconstructed bcc forms, several bilayers and one single Ni layer were epitaxially grown:

Sample NiFe(10.5/3.5):

15 ML Au(001) / 10.5 ML Ni(001) / 3.5 ML Fe(001) / Ag(001) substrate

Sample NiFe(10/6):

15 ML Au(001) / 10 ML Ni(001) / 6 ML Fe(001) / Ag(001) substrate

Sample NiFe(3.5/5.6):

15 ML Au(001) / 3.5 ML Ni(001) / 5.6 ML Fe(001) / Ag(001) substrate

Sample Ni(10):

15 ML Au(001) / 10 ML Ni(001) / Ag(001) substrate

All of the above samples were grown on the same vicinal Ag substrate (Ag sample 1, Table 2.1). A detailed inspection of Laue patterns revealed that its surface was oriented close to the (3,1,33) atomic plane, corresponding to an average misorientation of 1.8 deg. Such a vicinal surface can be viewed as a descending staircase described by kinked atomic steps along the [3,1,0] fcc direction ([2,1,0] bcc direction) see Figs. 5.1 and 5.2. Since we found that the density of atomic steps played a role in magnetic properties of ultrathin Fe layers an additional sample was grown on a singular Ag substrate (<1/4 deg misorientation, Ag sample 2).

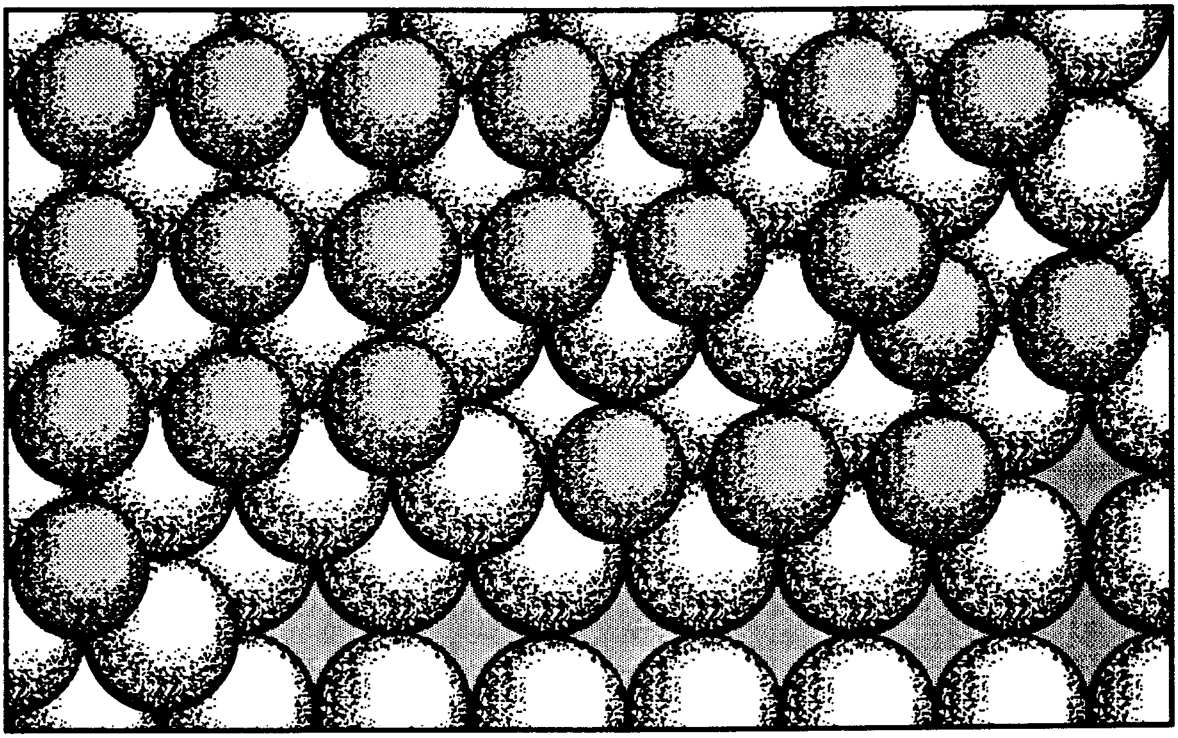

Fig. 5.1 A detailed top view of the Ag (3,1,32) vicinal surface (large balls) covered by Fe atoms (small balls). The kinked atomic steps are oriented along the [1,2,0] Fe direction. Note that the Fe stacking along the surface steps is imperfect due to the large Ag atoms.

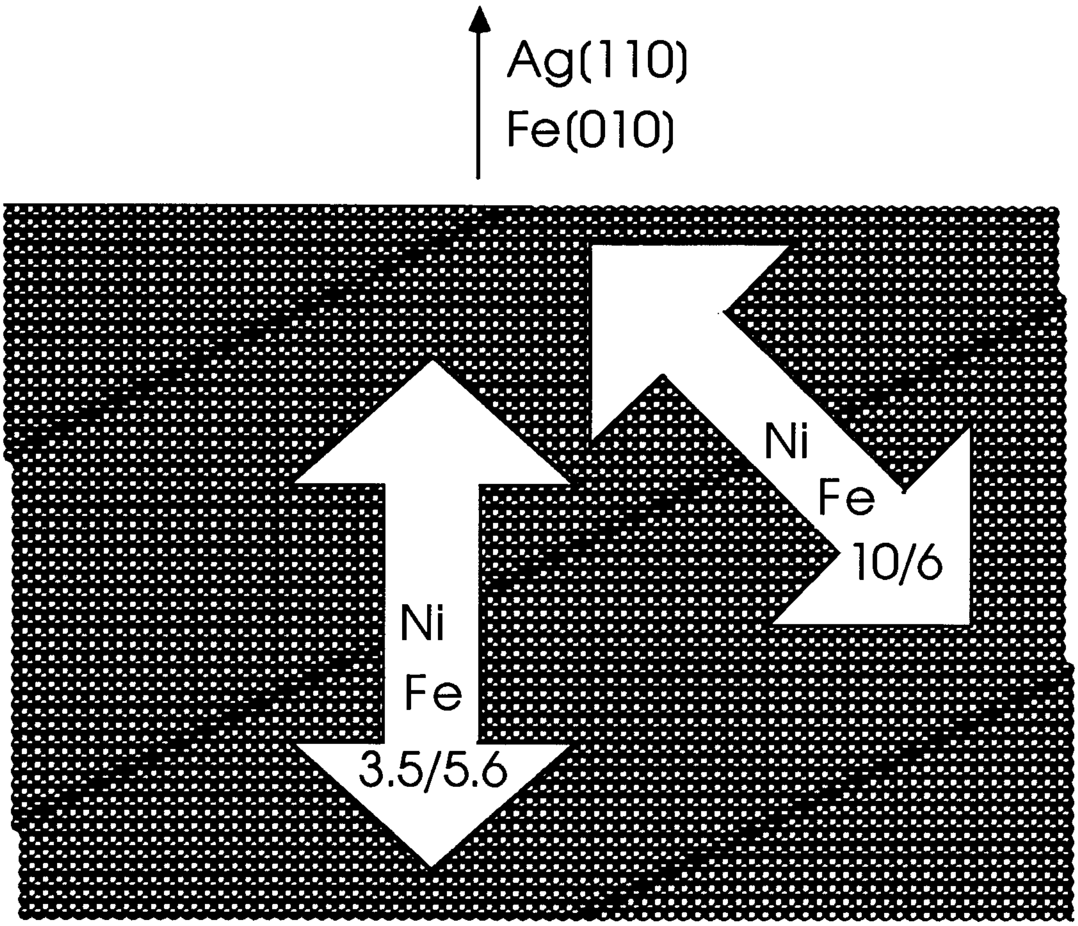

Fig. 5.2 An idealized global view of the Ag (3,1,32) vicinal surface (each square represents an atom). The vicinal surface can be described as a descending staircase of atomic terraces. The arrows indicate the direction of locked in-plane uniaxial easy axis of reconstructed Ni/Fe(10/6) and unreconstructed NiFe(3.5/5.6) bilayers. The orientation of the axes with respect to the theoretical description is shown in Fig. 5.3.

Sample NiFe(9.4/5.7):

15 ML Au(001) / 9.4 ML Ni(001) / 5.7 ML Fe(001) / singular Ag(001) substrate

This substrate came from a recently obtained boule having a much smaller mosaic spread (only single spots were visible in the Laue photos). The RHEED patterns showed well-defined short sharp diffraction streaks positioned on the Ewald circle indicating long range lattice coherence.

5.3 Eigenmodes of Ultrathin Bilayers

Magnetic ultrathin bilayers and superlattices having a strong interface exchange coupling were recently addressed in several papers [5.2-3]. Rather than solving the problem in terms of general susceptibilities, we have chosen to identify a simple set of variables which describe the overall magnetic properties as functions of single layer magnetic properties. In our calculations, the strengths of the exchange interactions were varied to explore and identify future interesting experiments.

In this section the magnetizations within the individual layers are assumed to be almost uniform due to the large interatomic exchange coupling. The strength of interlayer exchange coupling is allowed to vary. This assumption converts our simplified treatment into the well-known model of exchange-coupled sublattices [4.1]. All properties of exchange-coupled sublattices are directly applicable to our case. There are two resonance modes in this model: first, the low frequency acoustic mode in which both magnetizations are parallel and precess together; and second, the optical mode in which the magnetizations of the two layers are not parallel during precession. Optical modes occur at higher resonance frequencies due to the presence of the interface exchange field. One should note that the optical mode is observable under uniform excitation only if individual layers have different resonant frequencies.

The coordinate system appropriate for our model is shown in Fig. 5.3. The directions are different than those used in Chapter 4. The static magnetizations $\mathbf{M}_s^A$ and $\mathbf{M}_s^B$ lie in the plane of

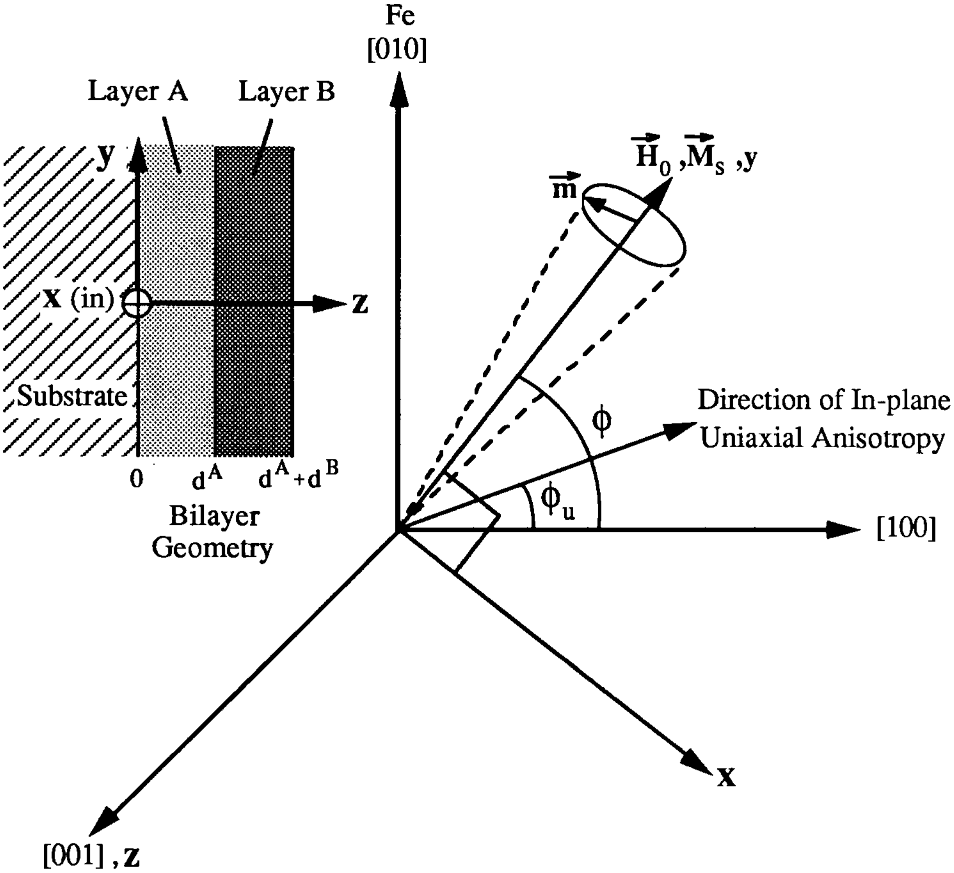

Fig. 5.3 Coordinate system used for the theory of eigenmodes of bilayers (section 5.3). Angles are measured positive *clockwise* from the [100] direction and therefore the angles ϕ and ϕ_u shown in the figure are negative.

the surface at or near the direction of the applied static in-plane magnetic field $H_0\hat{y}$. Incident microwave radiation stimulates transverse rf components of the magnetization

$$\mathbf{m}^A = m_x^A\,\hat{x} + m_z^A\,\hat{z}, \quad \mathbf{m}^B = m_x^B\,\hat{x} + m_z^B\,\hat{z}.$$

The response of the magnetic system to the applied fields is found by analyzing the Landau-Lifshitz equation of motion (L-L equation) with appropriate boundary conditions. Because the layers are assumed to be much thinner than the skin depth we can neglect eddy currents and assume that the internal rf driving fields are uniform across the layer. This makes the calculation of the rf response much simpler than in Chapter 4. Maxwell's equations only enter the problem through the boundary conditions. The boundary conditions are that the in-plane component of the microwave field **h** and the normal component of the rf magnetic field **b** are continuous across the interface.

The L-L equation for layer A is:

$$-\frac{1}{\gamma^A}\frac{\partial \mathbf{M}^A}{\partial t} = \mathbf{M}^A \times \mathbf{H}_{\text{eff}}^A \tag{5.1}$$

where γ^A is the gyromagnetic ratio, $\mathbf{M}^A = \mathbf{M}_s^A + \mathbf{m}^A$ is the total magnetization vector and $\mathbf{H}_{\text{eff}}^A$ is the effective field within the layer A given symbolically by:

$$\mathbf{H}_{\text{eff}}^A = H_0\hat{y} + \mathbf{H}_D^A + \mathbf{H}_{K1}^A + \mathbf{H}_{Ku}^A + \mathbf{H}_G^A + \mathbf{H}_{Ex}^A + h\,\hat{x} \tag{5.2}$$

The equations for layer B are found by replacing all superscripts A by B. H_0 is the externally applied static field. $h\hat{x}$ is the rf field with time dependence ~exp(iωt) which is equal to the externally applied microwave field by the boundary conditions. $\mathbf{H}_{K1}^A$, $\mathbf{H}_{Ku}^A$ are anisotropy fields which are defined by the energy expressions for cubic and in-plane uniaxial anisotropies:

$$E_{\text{cubic}} = K_1^A\,(\alpha_1^2\alpha_2^2 + \alpha_1^2\alpha_3^2 + \alpha_2^2\alpha_3^2) \tag{5.3}$$

$$E_u = -K_u^A\left(\frac{\mathbf{M}^A\cdot\mathbf{n}}{M_s^A}\right)^2 \tag{5.4}$$

where **n** is a unit vector along the in-plane uniaxial axis. The damping field is given by:

$$\mathbf{H}^A_G = -\frac{G^A}{(\gamma^A M^A_s)^2}\frac{\partial \mathbf{M}^A}{\partial t} \ .$$

where G^A is the Gilbert damping parameter. The exchange field is given by

$\mathbf{H}^A_{Ex} = (2A^A/(M^A_s)^2)\nabla^2\mathbf{m}$ where A^A is the exchange coupling coefficient (ergs/cm). The effective demagnetizing field given by $\mathbf{H}^A_D = 4\pi D_\perp M^A_s$ enters the L-L equation because of the boundary condition $b_z=0=h_z+4\pi D_\perp M^A_s$. $D_\perp \cong 1$ is the demagnetizing factor for an ultrathin layer (see [1.15] Appendix A). This enters the problem because of the boundary condition

It is useful to take explicitly into account that the experiments are sensitive to the integrated magnetization in the slab defined by:

$$\mathcal{M}^A_\alpha = \int_0^{d^A} m^A_\alpha \, dz \cong m^A_\alpha d^A ; \quad \mathcal{M}^B_\alpha = \int_{d^A}^{d^A+d^B} m^B_\alpha \, dz \cong m^B_\alpha (d^B - d^A).$$

where α = x or z and d^A, d^B are the slab thicknesses.

The following equations of motion are obtained from equation (5.1) and (5.2) by using the time dependence ~ exp(iωt) and integrating across the slab. One obtains the expressions:

$$-i\frac{\omega}{\gamma^A}\mathcal{M}^A_x + \left[H_0 + 4\pi D_\perp M^A + \frac{K^A_1}{2M^A_s}(3+\cos(4\varphi)) + \frac{K^A_u}{M^A_s}(1+\cos(2(\varphi-\varphi_u))) + i\frac{G^A}{\gamma^A M^A_s}\frac{\omega}{\gamma^A} \right]\mathcal{M}^A_z$$

$$= 2\frac{A^A}{M^A_s}\frac{\partial m^A_z}{\partial z}\Bigg|_0^{d^A} \qquad (5.5a)$$

$$\left[H_0 + \frac{2K^A_1}{M^A_s}\cos(4\varphi) + \frac{2K^A_u}{M^A_s}\cos 2(\varphi-\varphi_u) + \frac{iG^A}{\gamma^A M^A_s}\frac{\omega}{\gamma^A} \right]\mathcal{M}^A_x + i\frac{\omega}{\gamma^A}\mathcal{M}^A_z$$

$$= M_s^A d^A h + 2\frac{A^A}{M_s^A}\frac{\partial m_x^A}{\partial z}\Bigg|_0^{d^A} \qquad (5.5b)$$

A similar pair of equations can be written for the second layer (layer B); they can be obtained from (5.5a), (5.5b) by replacing the superscript A by B, and by changing the sign in front of the derivative terms (because the derivative must be evaluated at the interface which is the rear surface for slab A but the front surface for slab B).

The derivatives in the equations of motion, (5.5a) and (5.5b) can be evaluated from the torque equations which describe the motion of the spins at the outer surfaces of the A and B layer and the interface between the A and the B layers. As in chapter 4 the interface spins have been assumed to couple through a pair interaction characterized by J^{AB}. The interface exchange stiffness parameter is given by $A^{AB} \equiv 2J^{AB}S^A S^B/a$.

For layers of bcc material having four nearest neighbors, the effective exchange fields acting on an interface spin are given by equation 4.28. There are additional torques due to second order perpendicular anisotropy fields at each interface of the form of equation 4.20. The effective surface and interface fields can now be used to write the Landau-Lifshitz equations of motion for the magnetizations $\mathbf{m}^A$, $\mathbf{m}^B$ at the interface between layers A and B. In these equations all fields other than the exchange fields and pinning fields are negligible. This procedure gives all the derivatives $\mathbf{m}^A$ and $\mathbf{m}^B$:

$$\frac{2A^A}{M_s^A}\frac{\partial m_x^A}{\partial z}\Bigg|_0 = 0$$

$$\frac{2A^A}{M_s^A}\frac{\partial m_z^A}{\partial z}\Bigg|_0 = -\frac{2K_s^A(0)}{d^A M_s^A}\mathcal{M}_z^A$$

$$\frac{2A^A}{M_s^A}\frac{\partial m_x^A}{\partial z}\Bigg|_{d^A} = \frac{4A^{AB}}{a}\left[\frac{1}{d^B}\left(\frac{\mathcal{M}_x^B}{M_s^B}\right) - \frac{1}{d^A}\left(\frac{\mathcal{M}_x^A}{M_s^A}\right)\right]$$

$$\frac{2A^A}{M_s^A}\frac{\partial m_z^A}{\partial z}\bigg|_{d^A} = \frac{4A^{AB}}{a}\left[\frac{1}{d^B}\left(\frac{\mathcal{M}_z^B}{M_s^B}\right) - \frac{1}{d^A}\left(\frac{\mathcal{M}_z^A}{M_s^A}\right)\right] + \frac{2K_s^A(d^A)}{d^A M_s^A}\mathcal{M}_z^A \qquad (5.6)$$

plus four equivalent equations for the surface and interface derivatives of $\mathbf{m}^B$. The surface anisotropy terms only come into the derivative of m_z. Hence they only enter equation (5.5a) and not (5.5b). They can therefore be added to the $4\pi D_\perp M^A$ term to make the effective demagnetizing field:

$$(4\pi D_\perp M_s^A)_{eff} = 4\pi D_\perp M_s^A - \frac{2K_s^A}{d^A M_s^A}$$

where K_s^A is the sum of the surface anisotropies on the A layer. Because the surface anisotropy enters the equation of motion in this way, the effective demagnetizing field is what is measured in experiment.

The 4x4 system of equations which results from the elimination of the derivative terms from equations (5.5a) and (5.5b) using equations (5.6) (and their analogues for layer B) can be solved by straightforward matrix algebra. The numerator and denominator of the effective susceptibility ($\chi = (M_x^A + M_x^B) / h_x$) are quadratic polynomials in the interface coupling A^{AB}. A general expression for the susceptibility, χ, is extremely long and impractical. However, for strong interlayer exchange coupling, only and the quadratic terms in A_{AB} are important. The resulting expression for the resonance condition simplifies significantly and can be interpreted in terms of a high frequency optical mode and a low frequency acoustic mode. The low frequency resonance is given by the root of the coefficient of the $(A^{AB})^2$ term. Algebraic evaluation of the denominator results in the following equation:

$$\frac{\mu_A N_A}{\mu^B N^B}\left[H_1^A H_2^A - \left(\frac{\omega}{\gamma^A}\right)^2\right] + \frac{\mu_B N_B}{\mu^A N^A}\left[H_1^B H_2^B - \left(\frac{\omega}{\gamma^B}\right)^2\right] + \left[H_1^A H_2^B + H_2^A H_1^B - 2\left(\frac{\omega\,\omega}{\gamma^A \gamma^B}\right)\right] = 0 \qquad (5.7)$$

where $$H_1^A = B_{\mathrm{eff}}^A + \frac{K_1^A}{2M_s^A}(3+\cos(4\varphi)) + \frac{K_u^A}{M_s^A}(1+\cos(2(\varphi-\varphi_u))) + \frac{iG^A}{\gamma^A M_s^A}\frac{\omega}{\gamma^A} \tag{5.7a}$$

and $$H_2^A = H_0 + \frac{2K_1^A}{M_s^A}\cos(4\varphi) + \frac{2K_u^A}{M_s^A}\cos2(\varphi-\varphi_u) + \frac{iG^A}{\gamma^A M_s^A}\frac{\omega}{\gamma^A}\,. \tag{5.7b}$$

H_1^B and H_2^B are found by replacing the superscripts A by B in the above equations. N^A, N^B are the number of monolayers for A and B and $\mu^A = M_s^A a^3/2$, $\mu^B = M_s^A a^3/2$ are the magnetic moments per atom.

Equation (5.7) can be further rewritten as:

$$\omega^2\left[\frac{\mu^A N^A}{\gamma^A} + \frac{\mu^B N^B}{\gamma^B}\right]^2 - (\mu^A N^A H_1^A + \mu^B N^B H_1^B)\;(\mu^A N^A H_2^A + \mu^B N^B H_2^B) = 0$$

Dividing this equation by $(\mu^A N^A + \mu^B N^B)^2$ leads to

$$\omega^2\left[\frac{\mu^A N^A}{\gamma^A(\mu^A N^A + \mu^B N^B)} + \frac{\mu^B N^B}{\gamma^B(\mu^A N^A + \mu^B N^B)}\right]^2 -$$

$$\left[\frac{\mu^A N^A H_1^A}{(\mu^A N^A + \mu^B N^B)} + \frac{\mu^B N^B H_1^B}{(\mu^A N^A + \mu^B N^B)}\right]\left[\frac{\mu^A N^A H_2^A}{(\mu^A N^A + \mu^B N^B)} + \frac{\mu^B N^B H_2^B}{(\mu^A N^A + \mu^B N^B)}\right] = 0$$

Introducing the bilayer scaling parameter α given by

$$\alpha = \frac{\mu^A N^A}{\left(\mu^A N^A + \mu^B N^B\right)} = \frac{M_s^A N^A a^3/2}{\left(M_s^A N^A a^3/2 + M_s^B N^B a^3/2\right)} \tag{5.8}$$

the low frequency condition can be written in its final form:

$$\omega^2\left[\frac{\alpha}{\gamma^A} + \frac{(1-\alpha)}{\gamma^B}\right]^2 - \left[\alpha H_1^A + (1-\alpha)H_1^B\right]\left[\alpha H_2^A + (1-\alpha)H_2^B\right] = 0 \tag{5.9}$$

The comparison of equation (5.9) with an effective single layer resonance condition given by:

$$\left(\frac{\omega}{\gamma}\right)^2 = \left[B_{eff} + \frac{1}{4}H_{K1}(3+\cos(4\varphi)) + \frac{1}{2}H_{Ku}(1+\cos(2(\varphi-\varphi_u))) + i\Delta H\right]$$

$$\times \left[H + H_{K1}\cos(4\varphi) + H_{Ku}\cos(2(\varphi-\varphi_u)) + i\Delta H\right] \qquad (5.10)$$

leads to the scaling laws for effective fields of strongly exchange coupled bilayers:

$$H_{K1} = \alpha\frac{2K_1^A}{M_s^A} + (1-\alpha)\frac{2K_1^B}{M_s^B}; \qquad H_{Ku} = \alpha\frac{2K_u^A}{M_s^A} + (1-\alpha)\frac{2K_u^B}{M_s^B}$$

$$\frac{\omega}{\gamma} = \alpha\frac{\omega}{\gamma^A} + (1-\alpha)\frac{\omega}{\gamma^B}; \qquad \Delta H = \alpha\frac{\omega\, G^A}{(\gamma^A)^2 M_s^A} + (1-\alpha)\frac{\omega\, G^B}{(\gamma^B)^2 M_s^B} \qquad (5.11)$$

$$(4\pi D_\perp M_s)_{eff} = \alpha(4\pi D_\perp M_s^A)_{eff} + (1-\alpha)(4\pi D_\perp M_s^B)_{eff}$$

All expressions in eqs. (5.11) are effective fields and hence the effective fields of individual layers form the set of natural variables of magnetic bilayers. The general scaling law can therefore be written in the form:

$$H_{eff}^{bilayer} = \alpha H_{eff}^{A} + (1-\alpha) H_{eff}^{B} \qquad (5.12)$$

Equation (5.12) can be used recursively with equations (5.10) to form a generalized expression for the effective field associated with a multilayer structure:

$$H_{eff}^{multilayer} = \sum_i \alpha^i H_{eff}^{i}, \qquad (5.13)$$

where

$$\alpha^i = \mu^i N^i \Big/ \sum_j \mu^j N^j$$

The bilayer magnetic response for small and intermediate values of A^{AB} is more complex and can be investigated only by computer calculations. In the limit $A^{AB} = 0$, the layers A and

B behave independently in FMR measurements. In BLS studies of the optical mode resonance, the layers are still coupled by the rf demagnetizing fields which are a consequence of an in-plane spatial dependence of the magnetization [5.4-5].

Calculations were carried out to demonstrate the role of variable interface exchange coupling on the bilayer magnetic response. We chose a bilayer composed of a 10 ML Fe layer weakly coupled to a 6 ML Fe layer. These layers act as two distinct magnetic materials with different resonant frequencies because of the 1/d dependence of the perpendicular uniaxial anisotropy. For an arbitrary value of A^{AB} the rf susceptibility denominator leads to two resonance modes. The modes can be described either by fixing the field and scanning the frequency (BLS), or by fixing the frequency and scanning the field (FMR). The character of the modes in the BLS is shown in Fig. 5.4. As A^{AB} is increased from zero, the lower branch reaches a fixed frequency given by equation (11). The upper branch is almost linear with A^{AB} and will be called the soft optical mode. Since BLS measurements can be extended to 500 GHz, one can study the interlayer exchange up to a value of 1×10^{-7} ergs/cm which is a significant portion of the bulk exchange (~ 10^{-6} erg/cm).

Fig. 5.5 illustrates the FMR dependence on interlayer exchange (A^{AB}). In contrast to BLS, the FMR optical resonance field shifts downwards to lower d.c. magnetic fields with increasing A^{AB}. The antiferromagnetic coupling ($A^{AB} < 0$) would result in reverse trends (see Figs. 5.4 and 5.5). Both BLS and FMR can therefore distinguish between ferro- and antiferromagnetic interface exchange coupling.

The above calculations show that BLS and FMR are well suited to the study of small interlayer exchange coupling. FMR is a better technique for investigating the onset of interlayer exchange since BLS is affected by dipolar interactions even in the absence of exchange coupling. Assuming that the interlayer exchange decreases exponentially with a decay length corresponding to the interlayer spacing, spacer layers ~6-8 ML thick could be used to investigate the role of long range exchange coupling in itinerant ultrathin bilayers which form the building blocks of magnetic superlattices. Such measurements would be complementary to

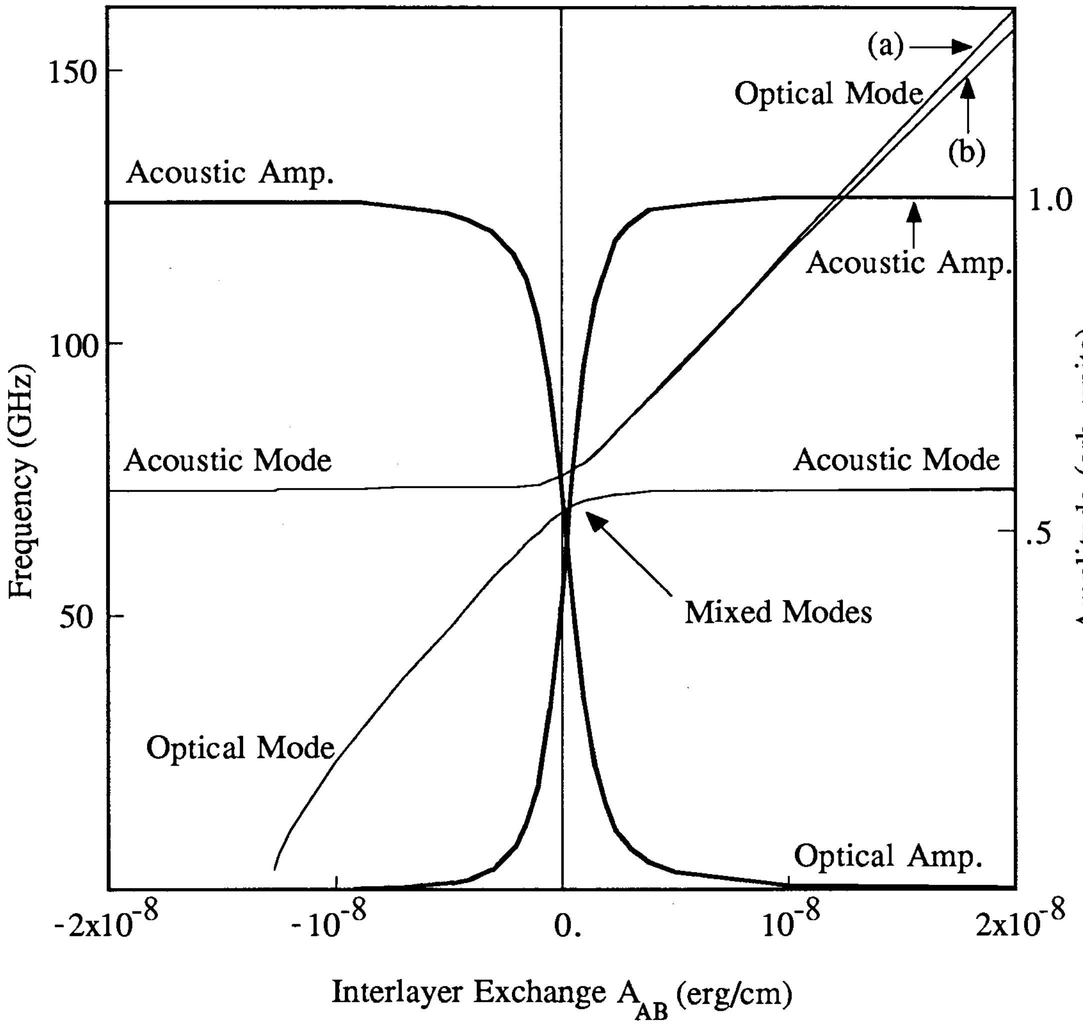

Fig. 5.4 Calculated resonant frequencies and amplitudes of low frequency modes in a bilayer composed of a 10 ML Fe layer weakly exchange-coupled to a 6 ML layer. The applied field is fixed at 20 kOe. See Fig. 5.6 caption for the Fe magnetic parameters. Curve (a) is calculated using the simplified theory of section 5.3. Curve (b) and the amplitude curves use the discrete model extended to include demagnetizing and anisotropy fields and Gilbert damping.

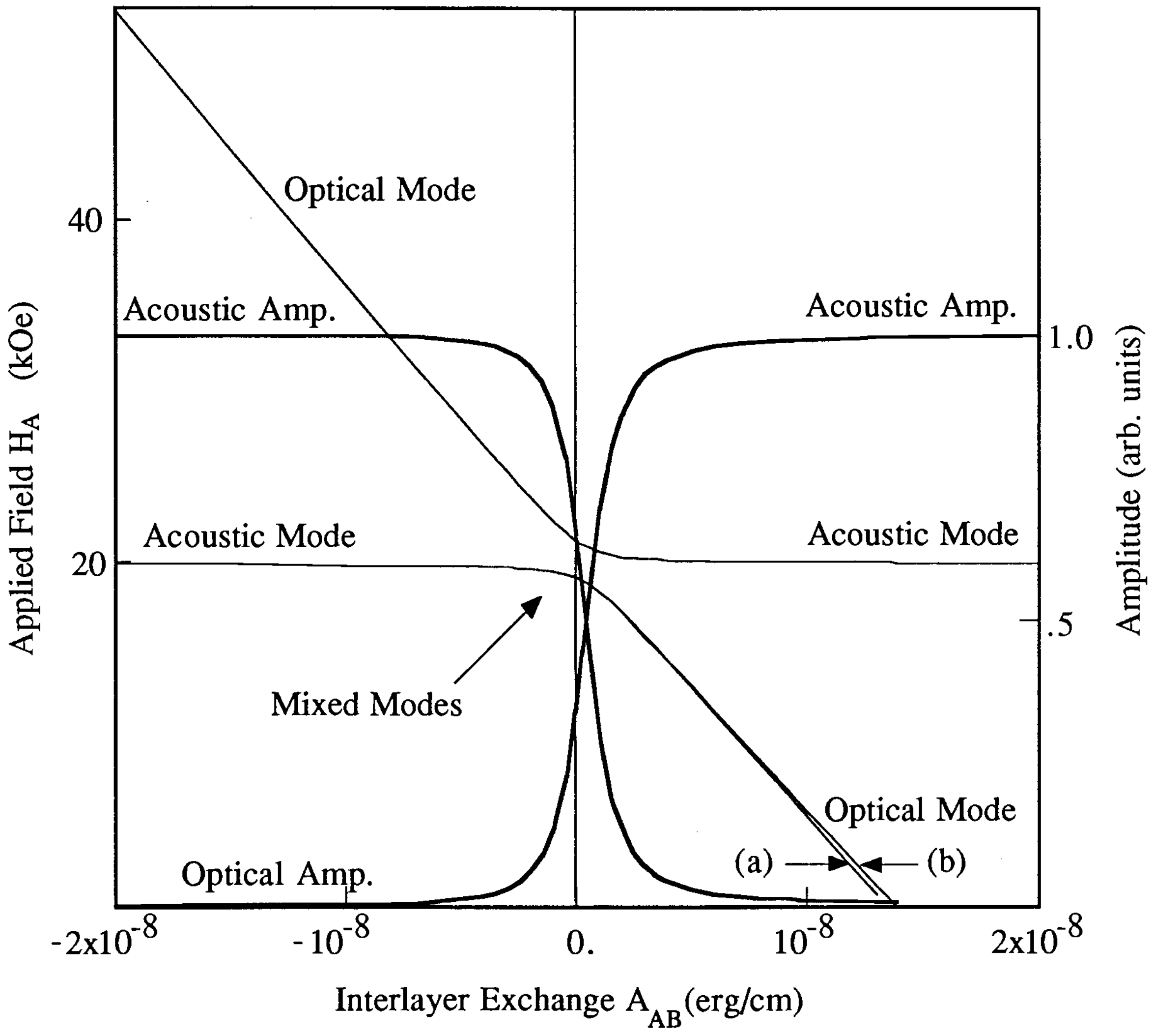

Fig. 5.5 The curves are calculated as in Fig. 5.4 but using a fixed frequency of 73 GHz and varying the applied magnetic field.

the experimental work on thick magnetic bilayers carried by Grünberg and co-workers [5.4] and corresponding theoretical work by J.F. Cochran and J.R. Dutcher [5.5] for BLS and K. Vayhinger and H. Kronmüller [5.6 for FMR.

In the limit of a strong interface exchange coupling, the soft optical mode becomes the first optical mode of the tightly exchange-coupled atomic layers.

5.4 The Discrete Model of Exchange-coupled Bilayers:

The theoretical treatment of optical modes requires further refinement. The simplified model of exchange-coupled magnetic layers discussed above fails completely when the interface exchange becomes comparable to the interplanar exchange. True optical modes should be described by taking the full exchange coupling between all atomic layers into account. Since our MBE studies are carried out on ultrathin ferromagnetic films, a discrete model of exchange-coupled atomic planes can be used without introducing too much computational complexity.

The Landau-Lifshitz equations have been written for each atomic plane coupled by exchange to its nearest-neighbor planes. Each plane can in principle have different magnetic properties. In-plane 4-fold and 2-fold anisotropies, surface anisotropy, Gilbert damping and demagnetizing fields have been included. The general equations are complicated. They form a system of 2n×2n linear equations for the transverse components of the spins where n is the number of atomic planes. To make an easier connection to macroscopic parameters we have converted the equations from spin variables to magnetizations by dividing the L-L equations by the volume per spin.

The effective exchange field on the ith spin is found from the interaction energy expression which is $E_i = - 8J^{j-1,j}S^{j-1}\cdot S^j - 8J^{j,j+1}S^j\cdot S^{j+1}$ for a bcc lattice with 4 nearest neighbours. Note that $J^{j-1,j} = J^{j,j-1}$, etc. Using $\gamma\hbar S^j = \mu^j = (a^3/2)M^j$ for a bcc lattice where μ^j is the magnetic moment per atom we can convert the exchange energy to:

$$E_j/(\text{unit vol}) = -\frac{8}{a^2 M^j}\left(\frac{A^{j-1,j}\mathbf{M}^{j-1,j}}{M^{j-1,j}} - \frac{A^{j,j+1}\mathbf{M}^{j,j+1}}{M^{j,j+1}}\right)\cdot \mathbf{M}^j \equiv \mathbf{H}^j_{ex}\cdot \mathbf{M}^j$$

which defines the exchange field, $\mathbf{H}^j_{ex}$, acting on the jth plane. We used $A^{j,k} = J^{j,k}S^jS^k/a^2$.

Also we have assumed for simplicity that the lattice spacings is the same for all layers.

The forms of the anisotropy fields are given in equations (5.7a,5.7b). After substituting all the effective fields into the L-L equation and neglecting second order terms we get:

$$\begin{aligned} i\frac{\omega}{\gamma^j}m^j_x &= \left[m^j_y\left(H_0+\beta^{j-1,j}+\beta^{j,j+1}+H^j_1\right) - \left(\beta^{j-1,j}m^{j-1}_y - \beta^{j,j+1}m^{j+1}_y\right)\right] \\ i\frac{\omega}{\gamma^j}m^j_y &= -\left[m^j_x\left(H_0+\beta^{j-1,j}+\beta^{j,j+1}+H^j_2\right) - \left(\beta^{j-1,j}m^{j-1}_x - \beta^{j,j+1}m^{j+1}_x\right)\right] \end{aligned} \tag{5.14}$$

where $\beta^{j-1,j} = \dfrac{8A^{j-1,j}}{a^2M^{j-1,j}}$, $\beta^{j,j+1} = \dfrac{8A^{j,j+1}}{a^2M^{j,j+1}}$

and H^j_1 and H^j_1 are found from equations (5.7a) and (5.7b) respectively with interchanging A for i in the superscripts.

A computer program was written which solves this system of equations. As mentioned above, the first optical resonance corresponds to the soft optical mode in the limit of strong interfacial exchange coupling. The calculations shown in Fig. 5.6 were carried out for an asymmetric 6 ML Fe layer with different pinnings on its two surfaces and a [10 ML Ni/6 ML Fe] bilayer having a strong interfacial exchange coupling ($A^{AB} = 1.5\text{x}10^{-6}$ erg/cm). The resonance modes are in the range of Raman Light Scattering (RLS) experiments and there are as many modes as there are atomic planes. In Fig. 5.6 we have plotted the integral of the optical response for each mode as a function of the mode frequency. The optical response is defined as the sum over all atomic planes of the area under the peak of the transverse magnetization (m_x) vs frequency assuming a uniform driving field. Note that optical modes of

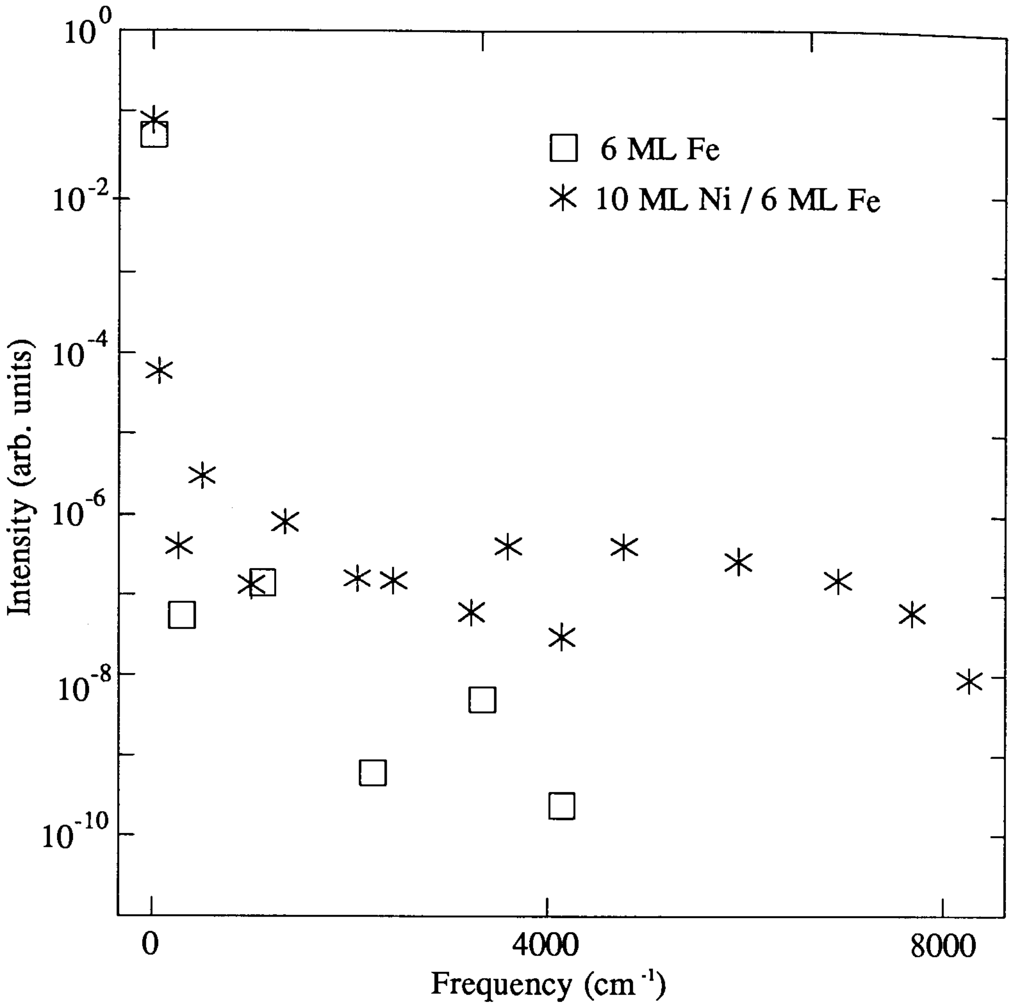

Fig. 5.6 Intensity of optical modes vs frequency (cm^{-1}) for a 6 ML Fe single layer and a [10 ML Ni]/ [6 ML Fe] bilayer. The parameters of the Fe are $4\pi M_s = 21.55$ kG, g-factor = 2.09, Gilbert damping parameter = $1\text{x}10^8$ sec^{-1}, $K_1 = 4.8\text{x}10^5$ erg/cm^3 and the exchange coefficient $A = 2.0\text{x}10^{-6}$ erg/cm. The parameters of the Ni are $4\pi M_s = 6.14$ kG, g-factor = 2.21, Gilbert damping parameter = $3\text{x}10^9$ sec^{-1}, $K_1 = 8.5\text{x}10^5$ erg/cm^3 and the exchange coefficient $A = 1.0\text{x}10^{-6}$ erg/cm. The coupling exchange was $1.5\text{x}10^{-6}$ and the applied field was 20 kOe. The 6 ML Fe has surface pinning $K_s = .7$ erg/cm^2 on one surface and .5 erg/cm^2 on the other. This models an Fe layer grown on Ag and covered by a Au overlayer [1.13]. A value $K_s = .5$ erg/cm^2 was used for the Fe in the bilayer

single magnetic layers pinned equally on both surfaces have zero intensity because they do not couple to a homogeneous driving field. Different values of surface pinning on the interfaces or different magnetic parameters of the layers of a bilayer break the symmetry of the system and couple the optical modes to a homogeneous driving field. For the above parameters the calculated intensities of the optical modes are weak (see Fig. 5.6); a very high sensitivity would be required to observe them. The intensities are weak because the exchange fields holds the spins nearly parallel. Hence these modes will be stronger and more easily observable in systems with low exchange, for example if the nonmagnetic spacer layers are inserted between ferromagnetic layers. A search for optical modes in Ni/Fe bilayers using Raman light scattering is in progress.

5.5 Experimental Results

To determine $4\pi M_{eff}$, H_{K1}, H_{Ku} and the g-factor we carried out FMR measurements at 9.5, 24.0, 36.6 and 73.0 GHz for each of the samples listed in section 5.2. The samples formed the end plates of TE_{01N} cylindrical cavities (doughnut mode) for the latter three frequencies and formed an endplate of a waveguide mode cavity for the 9.5 GHz measurements. The waveguide cavities gave constant sensitivity independent of the orientation of the magnetic field in the plane of the specimen while the waveguide cavity sensitivity had `90 deg symmetry. The d.c. magnetic field was rotated in the sample plane over the full 360° to measure the in-plane anisotropies. We used standard lock-in amplifier detection techniques with 127 Hz field modulation to detect the signal and 60 kHz repeller modulation to stabilize the frequency of the klystron to the cavity containing the sample. FMR sensitivity was excellent. FMR lines as wide as 1000 Oe were readily detectable in samples 2-3 ML thick. FMR measurements were carried out at room and liquid nitrogen (LN_2) temperatures.

The most striking difference between the reconstructed Ni/Fe bilayers and single Fe layers is the presence of a large in-plane 4-fold anisotropy in the bilayer samples, see Figs. 5.7, 5.8 and 5.9, whereas in ultrathin Fe films the 4-fold anisotropy is weak. Fe samples less than 3.5

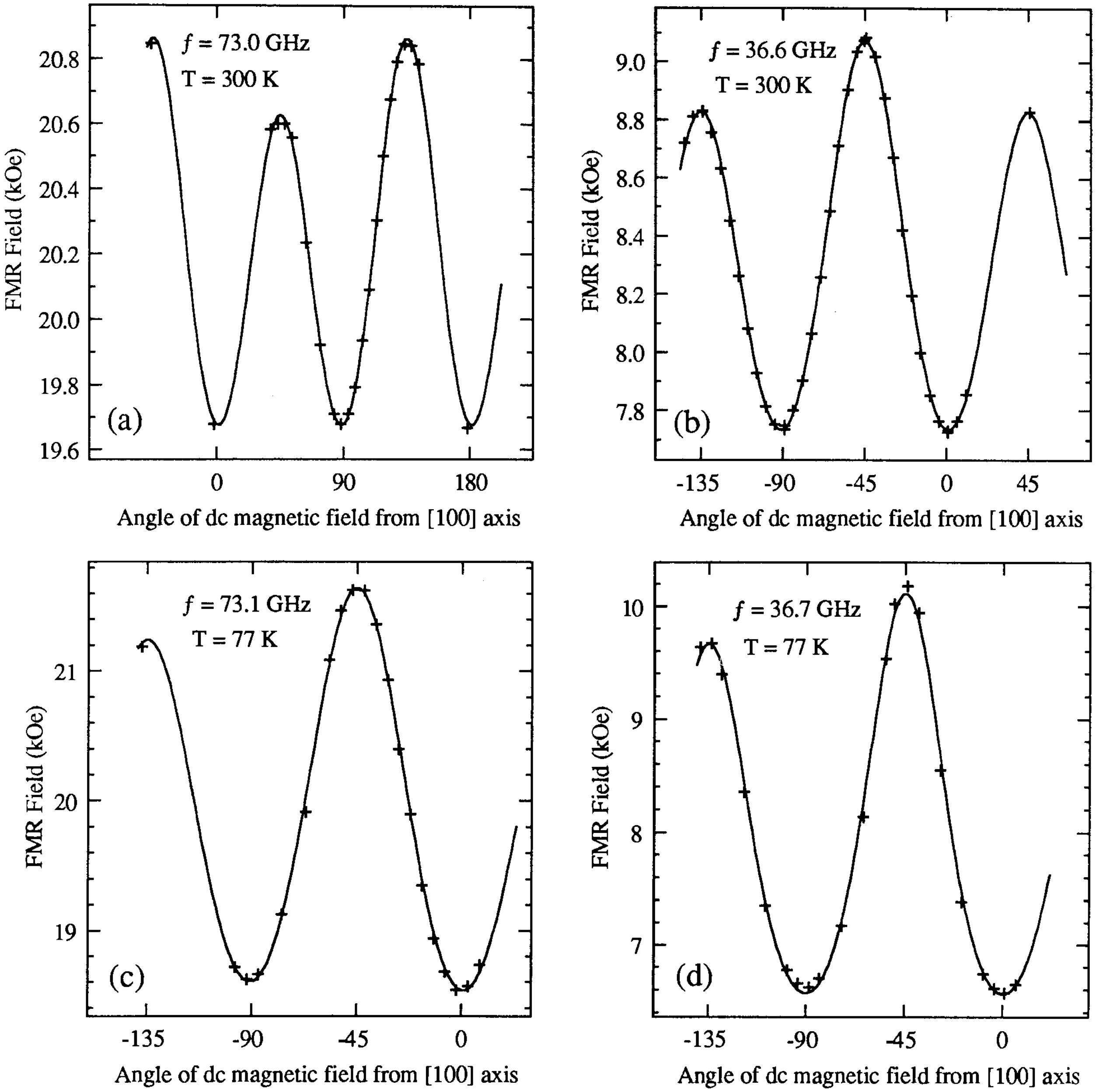

Fig. 5.7 The in-plane dependences of measured FMR field for the the [15 ML Au(001)]/ [10 ML Ni(001)]/ [6 ML Fe(001)]/ [bulk Ag(001)] (sample NiFe(10/6)) at room and LN_2 temperatures. Solid lines are calculated angular dependences of the FMR field. Calculations were carried out with magnetic parameters obtained from a multi-parameter chi-squared function minimization routine. (a) f=72.925 GHz; H_{K1}=.760 kOe; H_{Ku}=–.149 kOe; φ_u=45° (along Fe [110]); g-factor=2.1; $(4\pi D_\perp M_s)_{eff}$=9.75 kG; T=300 K. (b) f=36.62 GHz; H_{K1}=.789 kOe; H_{Ku}=–.143 kOe; φ_u=45° (along Fe [110]); g-factor=2.1; $(4\pi D_\perp M_s)_{eff}$=9.75 kG; T=300 K. (c) f=72.97 GHz; H_{K1}=2.04 kOe; H_{Ku}=–.253 kOe; φ_u=41°; g-factor=2.103; $(4\pi D_\perp M_s)_{eff}$ =9.346 kG; T=77 K. (d) f=36.76 GHz; H_{K1}=2.14 kOe; H_{Ku}=–.257 kOe; φ_u=41°; g-factor=2.103; $(4\pi D_\perp M_s)_{eff}$ =9.346 kG; T=77 K.

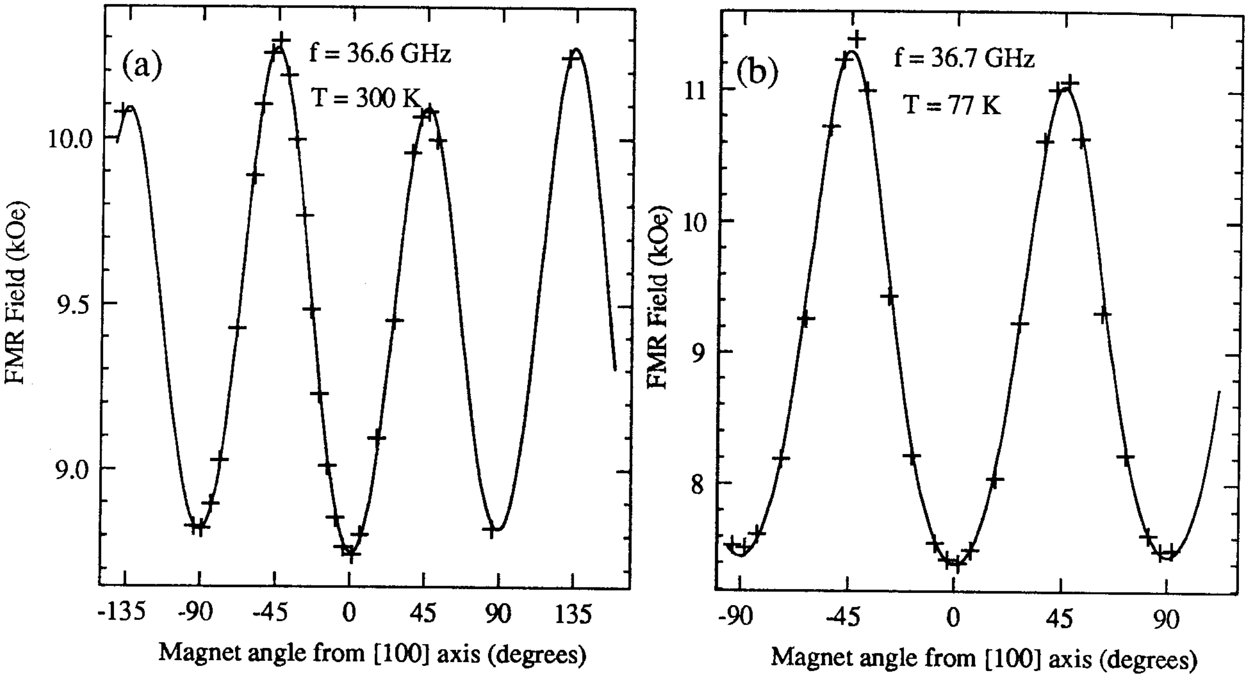

Fig. 5.8 The in-plane angular dependence of measured FMR field for the [15 ML Au(001)]/ [10.5 ML Ni(001)]/ [3.5 ML Fe(001)]/[bulk Ag(001)] sample NiFe(10.5/3.5). (a) f=36.627 GHz; H_{K1}=.974 kOe; H_{Ku}=.119 kOe; φ_u=35°; g-factor=2.149; $(4\pi D_\perp M_s)_{eff}$ =5.376 kG; T=300 K. (b) f=36.71 GHz; H_{K1}=2.57 kOe; H_{Ku}=.164 kOe; φ_u=38°; g-factor=2.149; $(4\pi D_\perp M_s)_{eff}$ =4.83 kG; T=77 K.

ML thick show no in-plane anisotropies even at LN_2 temperatures, see Table 5.1. The in-plane 4-fold anisotropy of the Ni/Fe bilayers can be as large as ~ 6 kOe at LN_2 temperature, appreciably exceeding those observed in bulk Fe. Consequently, the bilayer saturation magnetization, when oriented away from the planar [100] easy axis, lagged behind the in-plane d.c. magnetic field. The angular dependence of the FMR field is thus not described by simple 4-fold and 2-fold symmetry terms, but exhibits a somewhat smaller curvature around the easy axis and sharper curvature around the [110] hard axis, see Figs. 5.7-9. Note that there is also a weak 2-fold in-plane anisotropy for samples grown on the vicinal substrates (Figs. 5.7 and 5.8) which are significantly decreased (~x4) in the bilayer grown on singular Ag (001) substrate Fig. 5.9.

The FMR linewidth, ΔH, in the samples NiFe(10.5/3.5), NiFe(10/6) and NiFe(9.4/5.7) had a very large angular dependence with the narrowest lines along the [100] easy axes and the widest lines along the [110] hard axes, see Fig. 5.10. This contrasts sharply with all previous measurements carried out on Fe films where FMR linewidths were nearly isotropic. In fact, no similar large anisotropic behaviour in ΔH has been observed in any 3d transition metals or their alloys.

The similarity between the angular dependence of ΔH and the FMR field is even more surprising, see Fig. 5.10. Obviously the 4-fold anisotropy energy and FMR linebroadening have a common physical origin. The frequency dependence of ΔH in all samples studied showed a linear dependence with a zero frequency offset, ΔH(0), see Fig. 5.11. It has been shown [4.23] that the linear slope is proportional to the intrinsic Gilbert damping parameter and that the frequency independent offset, ΔH(0), is caused by the presence of magnetic inhomogeneities in the sample: this is often referred to as the 2-magnon scattering mechanism [5.7].

Another interesting aspect of sample NiFe(10/6) is the observation of hysteresis with much smaller coercive fields than H_{K1}. This proves the existence of domains in this ultrathin sample. The microwave absorption at 9.5 GHz near zero field, with the dc field along the easy

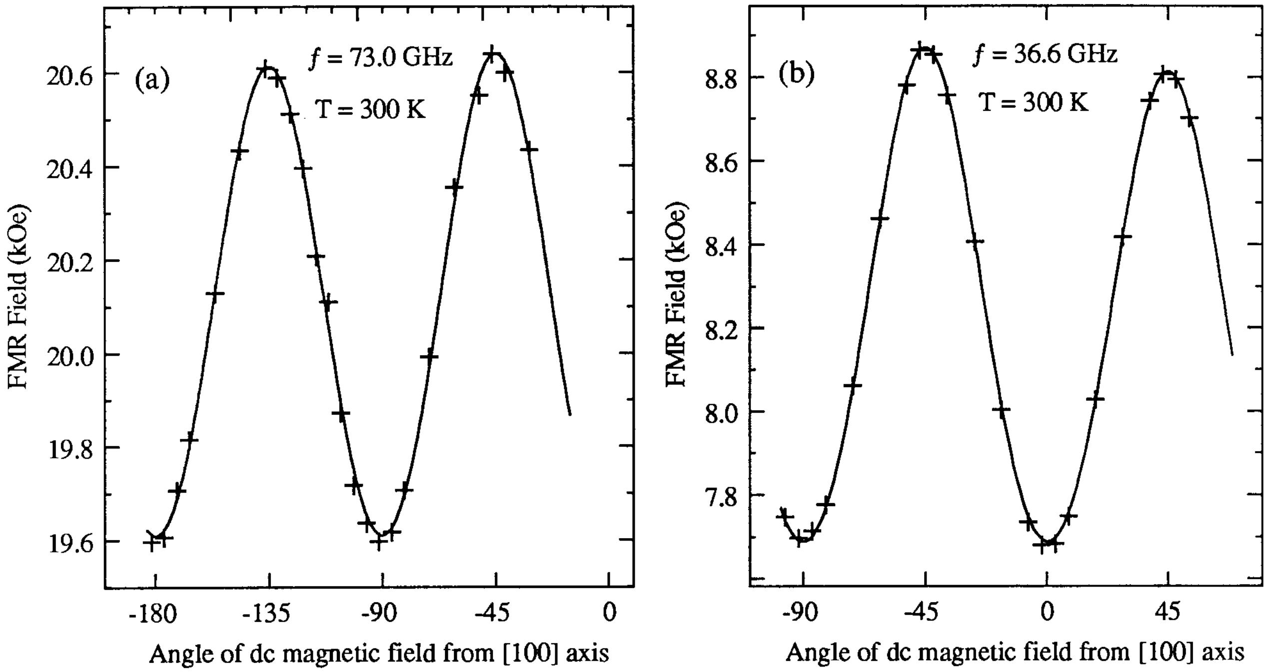

Fig. 5.9 The in-plane angular dependence of measured FMR field for the [15 ML Au(001)]/ [9.4 ML Ni(001)]/ [5.7 ML Fe(001)]/ [bulk singular Ag(001)] sample NiFe(9.4/5.6). (a) f=73.01 GHz; H_{K1}=.723 kOe; H_{Ku}=.017 kOe; $\varphi_u=0^o$ (along Fe [001]); g-factor=2.107; $(4\pi D_{\perp}M_s)_{eff}$ = 9.816 kG; T=300 K. (b) f=36.61 GHz; H_{K1}=.749 kOe; H_{Ku}=.033 kOe; $\varphi_u=0^o$ (along Fe [100]); g-factor=2.107; $(4\pi D_{\perp}M_s)_{eff}$=9.816 kG; T=300 K.

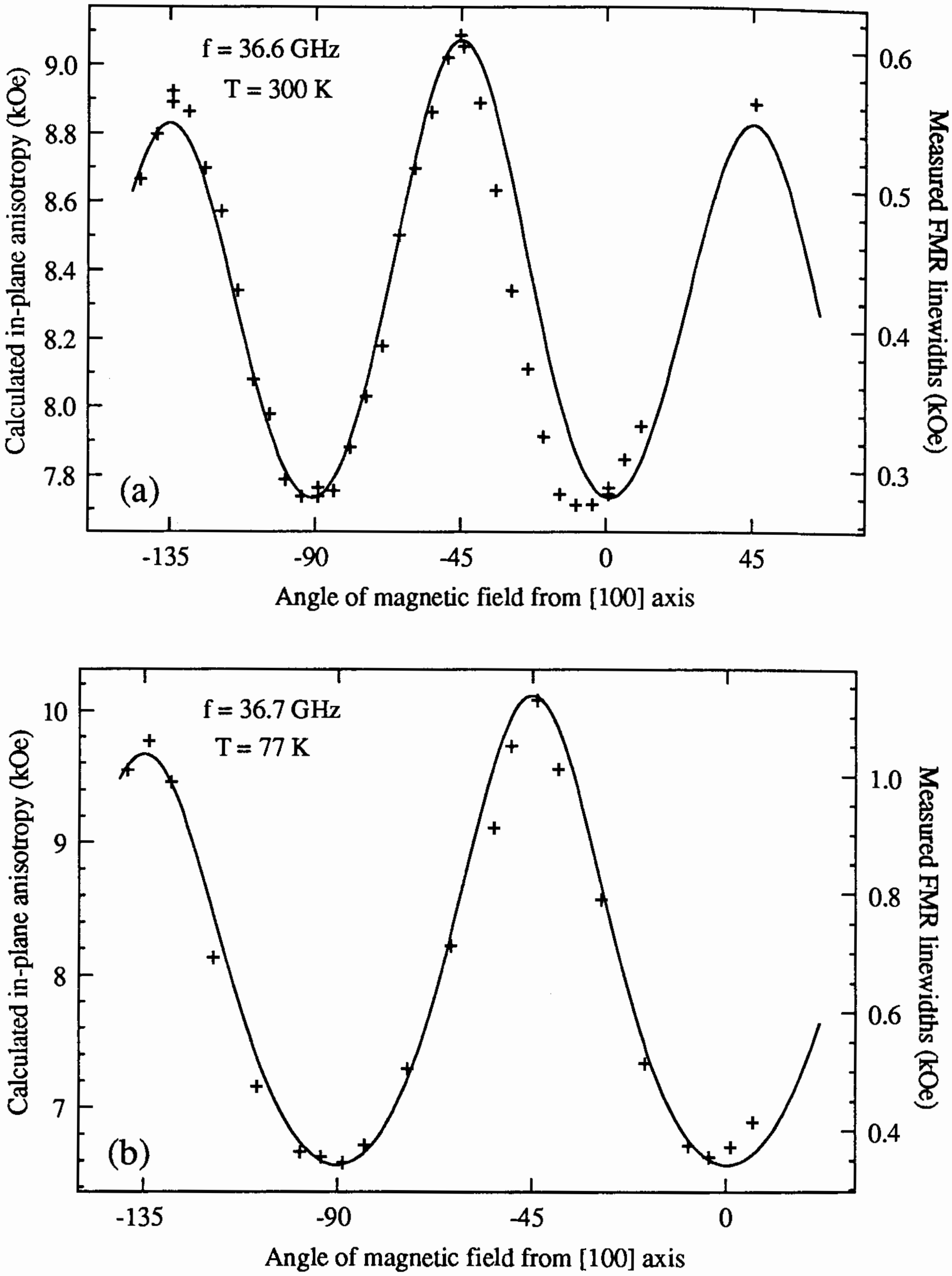

Fig. 5.10(a),(b). The in-plane angular dependences of FMR linewidth for sample NiFe(10/6) using the 36.6 GHz system at (a) room temperature and (b) LN_2 temperature. The superimposed solid curves in (a) and (b) were taken from Fig. 5.7(b) and Fig. 5.7(d) respectively to demonstrate a similarity between the in-plane anisotropy of FMR field and linewidth.

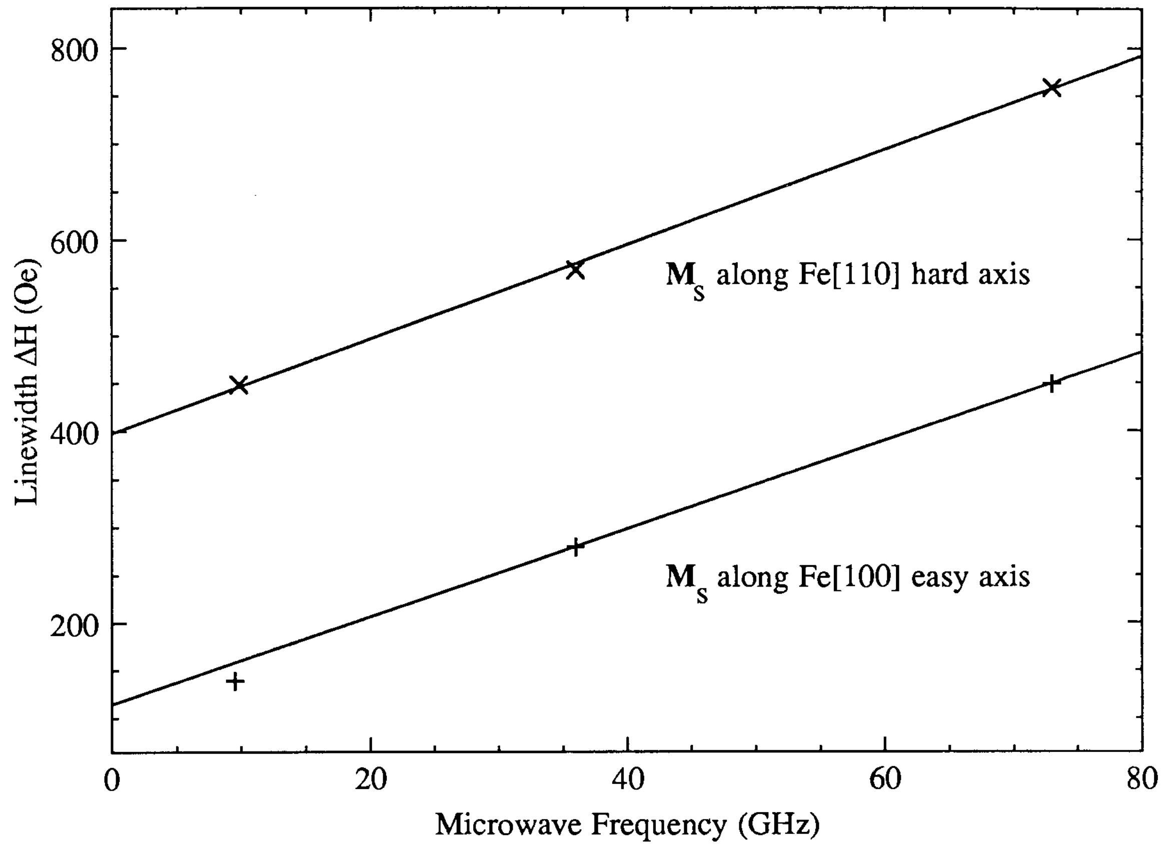

Fig. 5.11 The frequency dependence of FMR linewidth for sample NiFe(10/6) at room temperature. The linewidth is linear with microwave frequency. The zero frequency intersects, ΔH(0), originate in sample inhomogeneities. The slopes of the solid lines are caused by the intrinsic Gilbert damping. Note that the intrinsic damping is almost isotropic whereas ΔH(0) exhibits a strong angular dependence. ΔH(0) along the easy axis is very small and is comparable to the narrowest FMR linewidths measured in thick epitaxial Fe films.

axis, is shown in Fig. 5.12. The FMR peak is shifted to low fields by the large cubic crystalline anisotropy. The loop is actually defined by the tails of the FMR peaks which occur on either side of zero field. The coercive field is ~25 Oe whereas H_{K1} ~770 Oe. Thus the domains nucleate in the sample at very low fields (~13 Oe) and spread easily through the sample to reverse the magnetization.

It was important to discover whether magnetic properties of the ultrathin layers of unreconstructed bcc Ni could be found. If the properties of the first few layers of Ni on Fe were at all like the scaling law prediction based on the thicker "bcc Ni", the 4-fold anisotropy field in the NiFe(3.5/5.6) sample should have been relatively large, $H_{k1} = 250$ Oe, and easily measurable using FMR. FMR measurements at room and LN_2 temperatures, see Fig. 5.13 showed that the 4-fold in-plane anisotropies in the NiFe(3.5/5.6) sample were almost identical to those expected for a single 5.6 ML thick Fe layer sandwiched between a Ag(001) substrate and a Au(001) coverlayer, see Table 5.1. Evidently the 4-fold anisotropy in the pure bcc Ni is significantly smaller than that observed in lattice reconstructed Ni. Furthermore, all other properties of the NiFe(3.5/5.6) bilayer were almost identical with those observed in the 5.6 ML thick Fe film. However we cannot conclude yet that the pure unreconsructed bcc Ni is non-magnetic. This is because the scaling laws predict that even if the 3.5 ML Ni film were magnetic it would affect the magnetic properties of the bilayer only slightly. To determine whether the thinnest Ni films are magnetic measurements sensitive to the total moment of the films are necessary and such studies are in progress.

5.6 Analysis and Discussion of Results:

Before we disscuss the determination of the magnetic parameters it is important to realize the form of the anisotropy we are sensitive to in the parallel FMR configuration. The 4th-order magnetic anisotropy energy in ultrathin films epitaxially grown in the (001) plane, can be described by:

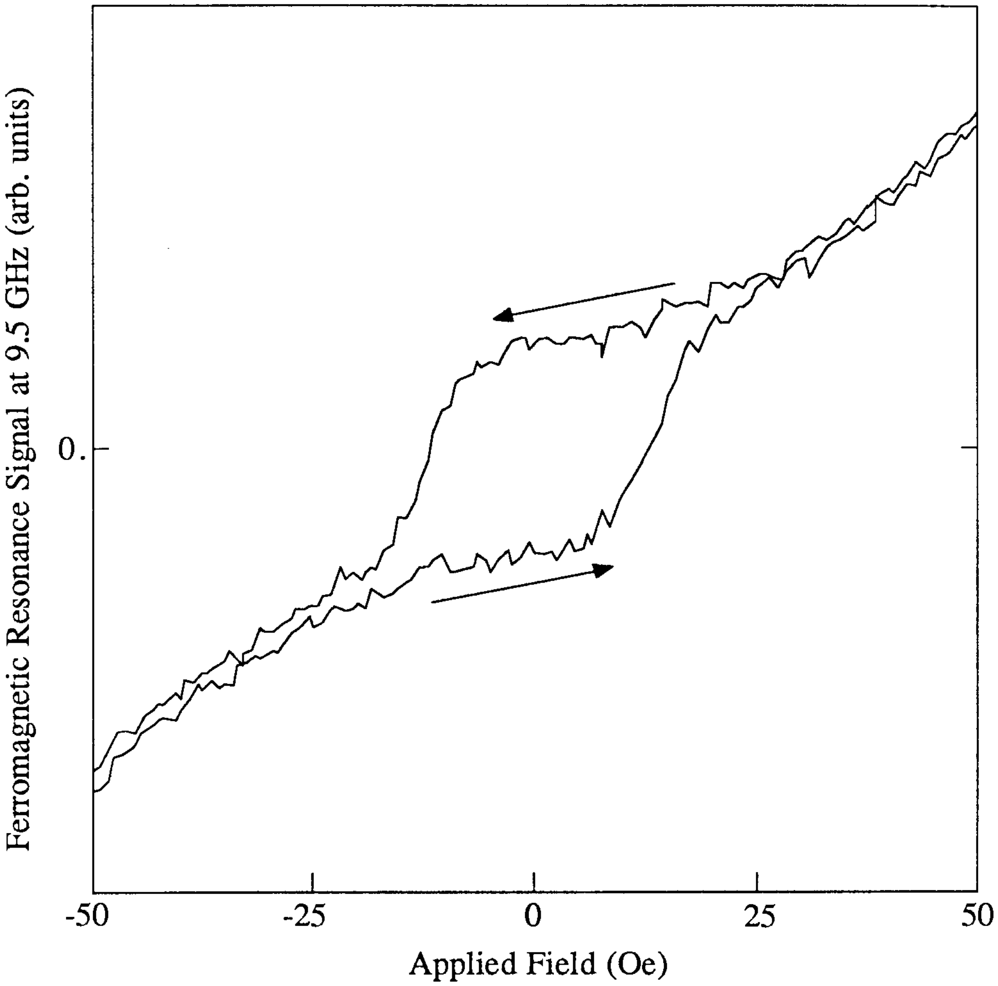

Fig. 5.12. Hysteresis in FMR from sample NiFe(10/6) at 9.5 GHz with the applied field along the easy axis (Fe (001)). H_{K1} = 770 Oe for this sample while the coercive field is ~ 25 Oe. The arrows show the directions in which the applied field was swept.

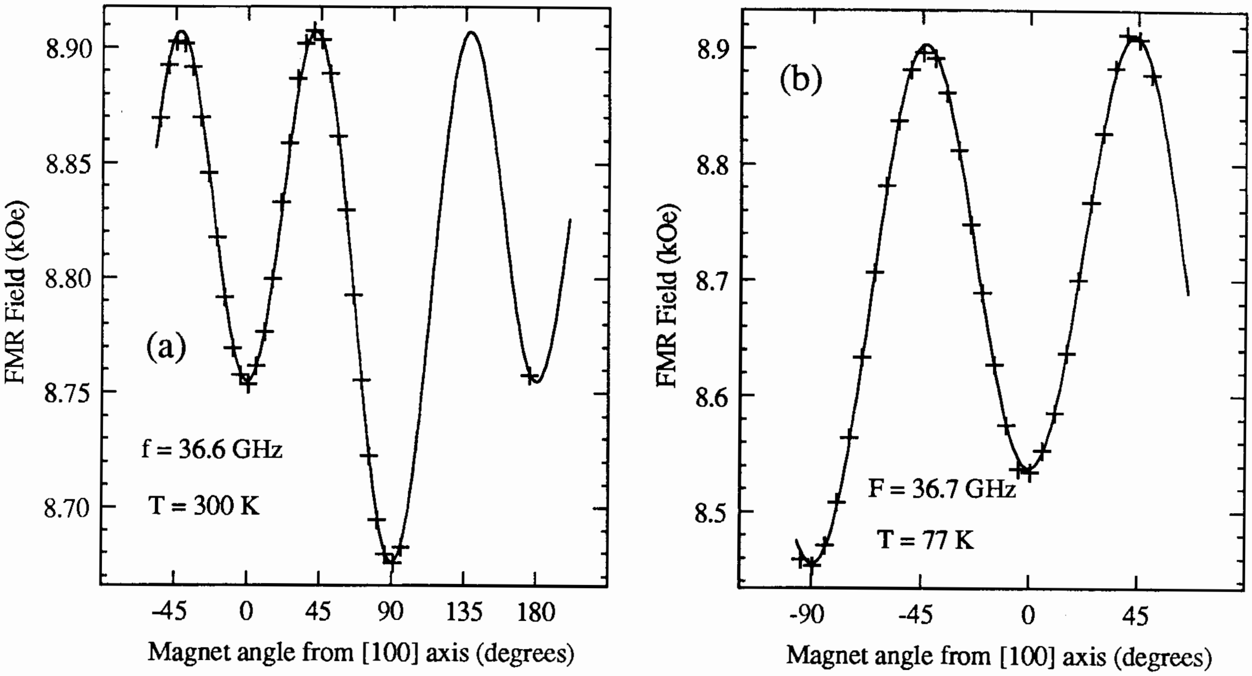

Fig. 5.13 The in-plane angular dependence of measured FMR field for the [15 ML Au(001)]/[3.5 ML Ni(001)]/[5.6 ML Fe(001)]/ [bulk Ag(001)] sample (NiFe(3.5/5.6)). (a) f=36.615 GHz; H_{K1}=.126 kOe; H_{Ku}=.048 kOe; 2-fold axis along the Fe [001] direction; g-factor=2.09; $(4\pi D_{\perp}M_s)_{eff}$=8.92 kG; T=300 K. (b) f=36.745 GHz; H_{K1}=.271 kOe; H_{Ku}=.049 kOe; 2-fold axis along the Fe [001] direction; g-factor=2.09; $(4\pi D_{\perp}M_s)_{eff}$=9.29kG; T=77 K.

Table 5.1: Properties of Ni/Fe bilayers and single Fe overlayers at room and liquid nitrogen temperatures.

Sample	Temp. (K)	$(4\pi D_\perp M_s)_{eff}$ (kOe)	g	H_{k_1}[a] (kOe)	H_{k_u}[b] (kOe)	φ_u[c] (degrees)	ΔH (36.6 GHz) (kOe) easy	hard
3.5 ML Ni / 5.6 ML Fe (vicinal Ag substrate)	300	8.9	2.09	0.14	−0.044	0	0.230	0.170
	77	9.29	2.09	0.280	−0.050	0	0.200	0.165
9.4 ML Ni / 5.7 ML Fe (singular Ag substrate)	300	9.82	2.107	0.735	0.025	45	0.253	0.525
10 ML Ni / 6 ML Fe (vicinal Ag substrate)	300	9.75	2.1	0.770	0.146	45	0.285	0.611
	77	9.346	2.103	2.090	0.254	41	0.350	1.130
10.5 ML Ni / 3.5 ML Fe (vicinal Ag substrate)	300	5.376	2.149	0.992	0.120	35	0.307	0.757
	77	4.83	2.149	2.570	0.160	38	0.380	1.313
3.5 ML Fe[d] (vicinal Ag substrate)	300	3.5	2.09	0.0	0.0	—	0.34[e]	
	77	3.84	2.09	0.0	0.0	—	0.47[e]	
5.6 ML Fe[d] (vicinal Ag substrate)	300	7.7	2.09	0.14	−0.044	0	0.15[e]	
	77	8.7	2.09	0.26	−0.13	0	0.17[e]	
6 ML Fe[d] (vicinal Ag substrate)	300	8.1	2.09	0.16	−0.044	0	0.14[e]	
	77	9.16	2.09	0.29	−0.13	0	0.16[e]	

[a] H_{k_1} is the effective 4-fold in-plane anisotropy field defined by $2K_1/M_S$. The values quoted are the averaging of data obtained at 36 and 73 GHz.

[b] H_{k_u} is the effective 2-fold in-plane anisotropy field defined by $2K_u/M_S$. The values quoted are the averaging of data obtained at 36 and 73 GHz.

[c] angular direction of the uniaxial anisotropy axis with respect to the in-plane Fe [100] direction.

[d] the parameters for single Fe films were obtained by interpolation from previously measured Fe films of similar thicknesses.

[e] the easy and hard axis FMR linewidths were nearly the same and are represented by their average values.

$$E_4 = -\frac{1}{2}K_{1\parallel}\left[\alpha_x^4 + \alpha_y^4\right] - \frac{1}{2}K_{1\perp}\alpha_z^4 \qquad (5.15)$$

where α_x, α_y, and α_z are the directional cosines of the magnetization vector with respect to the cubic crystalline axes. $K_{1\parallel}$ and $K_{1\perp}$ describe the strength of the 4th-order anisotropy parallel and perpendicular to the sample surface respectively. They may be different in thin films.

This expression can be rewritten in the form

$$E_4 = -\frac{1}{2}K_{1\parallel}\left[\alpha_x^4 + \alpha_y^4 + \alpha_z^4\right] - \frac{1}{2}(K_{1\perp} - K_{1\parallel})\,\alpha_z^4 \qquad (5.16)$$

The first part of the expression is equivalent to a regular cubic anisotropy term:

$$E_{cubic} = K_{1\parallel}\left[\alpha_x^2\alpha_y^2 + \alpha_y^2\alpha_z^2 + \alpha_z^2\alpha_x^2\right] \qquad (5.17)$$

The remaining part of the 4th-order anisotropy energy corresponds to a 4th-order perpendicular uniaxial energy having its symmetry axis perpendicular to the sample surface. For the saturation magnetization oriented in the plane of the specimen a 4th-order perpendicular uniaxial anisotropy plays no role in FMR measurements since the corresponding effective field is proportional to the third power of the r.f. perpendicular magnetization component and is negligible. Therefore, in our geometry, the full 4th-order anisotropy energy term and the cubic anisotropy term, eqs. (5.15) and (5.17), are indistinguishable. Determination of $K_{1\perp}$ is possible if measurements are made in the perpendicular configuration for which the static magnetization and the applied field are aligned perpendicular to the surface of the sample.

The angular dependence of the FMR field was analyzed using the full treatment of the cubic and in-plane uniaxial anisotropies. This included the non-collinearity of the saturation magnetization with the in-plane d.c. magnetic field. Computer fits carried out with MINUIT, a multi-parameter chi-squared function minimization routine, are excellent, see Figs. 5.7-9, 5.13 The results are summarized in Table 5.1 along with the some results from [4.19] which we use in our analysis.

For clean Ni/Fe interfaces the inter-layer exchange coupling is expected to be strong and should result in FMR and BLS responses corresponding to the pure acoustic mode. It can be anticipated that the scaling formulae should be followed. Epitaxially grown bilayers should borrow their magnetic properties from both the bcc Fe, which has a large saturation magnetization, and the bcc Ni, which has a large in-plane 4-fold anisotropy. Indeed, the magnetic bilayers with 10 ML thick Ni show a robust FMR signal like Fe with a strong in–plane 4-fold anisotropy like "bcc Ni".

In the simplest case the bilayers interact only through the interface exchange coupling. In this limit the scaling laws are exactly valid and in principle magnetic properties of "bcc Ni" can be extracted from FMR measurements carried out on Ni/Fe bilayers and appropriate single Fe layers. However, real bilayers do not behave in this simple manner. The itinerant nature of valence electrons, which becomes particularly important when the bilayer thickness becomes comparable to the electron mean free path, assures that some of these properties will be affected by valence band hybridization.

An analysis of FMR results obtained on epitaxially grown Ni/Fe bilayers was carried out assuming that the scaling laws were valid. The comparison of "bcc Ni" magnetic properties, obtained on different Ni/Fe bilayers, showed which of these magnetic parameters followed a simple bilayer scaling and which magnetic parameters were strongly affected by the collective nature of the valence electrons. Results of this analysis are presented in Table 5.2. The scaling parameters, α, used in Table 5.2 were evaluated using the saturation magnetization of bulk Fe ($4\pi M_S = 21.55$ kG), and employed either the saturation magnetization of bulk fcc Ni ($4\pi M_S = 6.13$ kG) or the saturation magnetization of bcc Ni as theoretically predicted by Moruzzi, et al. [5.8], ($4\pi M_S = 4.5$ kG). Epitaxially grown Ni layers in NiFe(10.5/3.5), NiFe(10/6) and NiFe(9.4/5.7) bilayers were thicker than the critical thickness and therefore were reconstructed.

All of these bilayers exhibited large 4-fold anisotropies, see Table 5.1. Note also that the 4-fold anisotropy field scales extremely well (H_{K1} agrees within 5% for the three bilayers with reconstructed Ni which is within the accuracy of the thickness measurements, see Table 5.2).

Table 5.2: Magnetic properties of ultrathin "bcc Ni" films grown on ultrathin bcc Fe(001) films deposited on bulk fcc Ag(001) substrates. The linewidths were calculated for a microwave frequency of 36.6 GHz using the scaling law.

Sample	$4\pi M_S$ (Ni) (kOe)	$(4\pi D_\perp M_S)_{eff}$ (kOe)	g	H_{k_1} (kOe)	H_{k_u} (kOe)	ΔH[expt. Fe][c] (kOe)		ΔH[selected Fe][d] (kOe)	
						easy	hard	easy	hard
Magnetic properties of "bcc Ni" overlayers measured at room temperature (T = 300 K).									
9.4ML Ni / 5.7ML Fe	6.14[a]	14.33	2.14	2.00	0.078	0.472	1.32	0.323	1.17
	4.50[b]	15.98	2.16	2.46	0.097	0.552	1.61	0.348	1.41
10ML Ni / 6ML Fe	6.14[a]	13.22	2.12	2.06	0.36	0.590	1.602	0.408	1.385
	4.50[b]	14.5	2.13	2.52	0.44	0.701	1.964	0.445	1.614
10.5ML Ni / 3.5ML Fe	6.14[a]	7.57	2.22	2.16	0.260	0.264	1.241	0.422	1.434
	4.50[b]	8.37	2.25	2.58	0.311	0.249	1.417	0.471	1.734
Magnetic properties of "bcc Ni" overlayers measured at liquid nitrogen temperature (T = 77 K).									
10ML Ni / 6ML Fe	6.14[a]	9.737	2.131	5.876	0.523	0.760	3.183	0.497	2.919
	4.50[b]	9.88	2.14	7.256	0.622	0.910	3.931	0.551	3.572
10.5ML Ni / 3.5ML Fe	6.14[a]	6.00	2.22	5.6	0.347	0.270	2.300	0.496	2.521
	4.50[b]	6.41	2.25	6.67	0.415	0.230	2.652	0.539	2.961

[a] the scaling calculation was carried out using the saturation magnetization corresponding to fcc Ni, $4\pi M_S = 6.14$ kOe.

[b] the scaling calculation was carried out using $4\pi M_S = 4.5$ kOe, the saturation magnetization corresponding to bcc Ni [4.27].

[c] these FMR linewidths were calculated using the bilayer scaling law and the Fe film properties given in Table 5.1.

[d] these FMR linewidths were calculated assuming the ΔH of a bilayer Fe films was 220 Oe at 300K and 280 Oe at 77 K.

The Gilbert damping in NiFe(10.5/3.5) and NiFe(10/6) samples is isotropic. It is the frequency independent part, ΔH(0), which shows a strong anisotropic behaviour and which resembles the 4-fold in-plane anisotropy field. It could be argued that the anisotropic ΔH behaviour is a consequence of the lagging of the saturation magnetization behind the applied field. In this respect, BLS studies are particularly useful because the applied field is held constant and the spectra are obtained by sweeping the frequency. BLS measurements [1.15] showed the same cubic anisotropy in linewidth as the FMR measurements. This proves that the anisotropic dependence of ΔH is dynamic in origin and is not caused by magnetostatic effects. Since the 4-fold anisotropy and the anisotropy in ΔH(0) have a common origin, it follows that the strong 4-fold in-plane anisotropy is not a consequence of the intrinsic spin-orbit interaction. Rather, it is a result of crystallographic defects generated during the Ni overlayer reconstruction.

As previously mentioned small 2-fold in-plane anisotropies were observed in all epitaxial bilayers and in most of the ultrathin single Fe films grown on vicinal Ag substrates. Note that there is a significant decrease in this anisotropy in the sample NiFe(9.4/5.7) and single Fe layers [4.25] grown on singular Ag substrates.

Table 5.2 shows that the 4-fold in-plane anisotropy field in all reconstructed Ni/Fe bilayers satisfies the bilayer scaling law given by equation (5.11) well, see Table 5.2, column 4. This is true for samples grown on both the singular and vicinal substrates. The 4-fold anisotropy field, H_{K1} = 2.6 kOe, in a 10 ML thick overlayer of "bcc Ni" is very close to that observed in a 60 Å thick "bcc Ni" layer epitaxially grown on the bulk Fe substrate (H_{K1} = 3.2 kOe). Therefore, it is reasonable to assume that the observed large in-plane 4-fold anisotropies belong to bulk properties of the reconstructed "bcc Ni".

Magnetostatic and magnetoelastic energies stored in growth defects become a part of the total magnetic energy and generate restoring torques of their own. However, well defined in-plane 4-fold anisotropy requires a corresponding degree of symmetry in the lattice defects. A network of mutually perpendicular misfit dislocations in (001) epitaxial structures have been previously observed [5.9] and could be the origin of the 4-fold anisotropy. Such a "checkerboard" surface pattern possesses the required symmetry for the behaviour of the 4-fold in-plane magnetic anisotropy and FMR linewidth. The easy axis of these anisotropies is along the [100] direction.

The other Ni parameters, such as $4\pi M_{eff}$, g-factor, and in-plane uniaxial anisotropies, do not scale well. Some parameters, like $4\pi M_{eff}$ and g-factor, are very dependent on the collective behaviour of valence electrons and their lack of scaling is not surprising. Other parameters, like H_{Ku} and ΔH, are less easy to understand. However all of these parameters have distinct trends worth noting.

The perpendicular uniaxial anisotropy decreases $\approx 10\%$ ($4\pi M_{eff}$ increases) with decreasing temperature in all single Fe films covered by Au layers, see Table 5.1. On the other hand, the Fe films covered by Ag(001) increase their perpendicular uniaxial anisotropy with decreasing temperature [4.19]. In this respect reconstructed bilayers behave like Fe films covered with Ag(001) and unreconstructed bilayers behave like Fe films covered with Au(001).

The in-plane 2-fold anisotropies in bilayers were enhanced by reconstructed Ni overlayers. For example, the sample NiFe(10.5/3.5) with a 3.5 ML Fe film showed an appreciable in-plane anisotropy while no in-plane anisotropies were observed in the single 3.5 ML thick Fe films. This increase is also accompanied by a rotation in the uniaxial axis (in all bilayers with reconstructed Ni) from the [100] to the [110] direction. The locking of the in-plane uniaxial anisotropies along major crystallographic axes is remarkable. However it should be pointed out that the locking in some cases deviates by ~10 deg from a principal axes, see Table 5.1. The in-plane uniaxial anisotropy is appreciable only in samples grown on vicinal substrates and therefore is a consequence of the presence of atomic steps in the Ag substrate that break the symmetry of the 4-fold (001) plane.

The mechanism of the in-plane uniaxial anisotropies can be discussed from two perspectives. Firstly, they can be caused by growth defects formed around atomic steps. In this case the lowest symmetry, the second order in-plane uniaxial anisotropy (described by equation (5.4)), can be expected. Secondly, the broken symmetry of vicinal surfaces can result in an asymmetric 4-fold anisotropy. Misfit dislocations may not form an ideal square array; e.g. they may have unequal dislocation densities in mutually perpendicular in-plane directions. The asymmetric in-plane 4-fold anisotropy can be described by

$$E_{4\text{-fold}} = -\frac{1}{2}\left(K_{1x}\,\alpha_x^4 + K_{1y}\,\alpha_y^4\right) = -\frac{1}{2}K_{1x}\left(\alpha_x^4 + \alpha_y^4\right) - \frac{1}{2}K_{1f}\,\alpha_y^4 \qquad (5.18)$$

where $K_{1f} \equiv K_{1y} - K_{1x}$. This asymmetry results in an additional 4th order in-plane uniaxial anisotropy which originates directly in the dominant 4-fold anisotropy. Since the 4th order anisotropy is locked to principal 4-fold axes, the direction of the uniaxial axis along the [100] direction in single Fe bilayers is a direct consequence of this model.

We reanalyzed our data by using the 4th order in-plane uniaxial anisotropy, see Table 5.3. The angular dependence of the FMR field can be equally well fit for samples with the uniaxial axis locked closely to {100} and {110} axes. However numerical fits were noticeably worse in samples with the uniaxial axis oriented away from the cubic principal axis. These fits can be improved by adding the 2nd order uniaxial anisotropy. However, the resulting in-plane 4-fold and 2-fold anisotropies were not consistent for different microwave frequencies and therefore were rejected. Furthermore, the 4-fold uniaxial anisotropies have a significantly weaker temperature dependence than the main 4-fold anisotropies. This would indicate that the 4-fold and 4th order uniaxial anisotropies are not caused by an identical mechanism. Therefore we believe that the uniaxial anisotropy is better described by the 2nd order in-plane anisotropy.

The bilayer g-factor exhibits a simple behaviour. With a decreasing Fe thickness, the bilayer g-factor converges towards the fcc Ni value of g = 2.187. However, the bilayer g-factor approaches the Fe value faster than expected from the scaling law, equation (5.11). This result clearly shows that Fe-Ni valence band hybridization is indeed significant and affects the spin-orbit contribution to the overall valence band behaviour.

The FMR linewidth in the reconstructed bilayers NiFe(10.5/3.5) and NiFe(10/6) scales poorly. Deviations from the scaling law are more serious for results obtained for easy axes

Table 5.3: Properties of Ni/Fe bilayers and single Fe overlayers at room and liquid nitrogen temperatures when a fourth order, in-plane, anisotropy is assumed to be present.

Sample	Temp. (K)	$4\pi M_{eff}$ (kG)	g	$2K_1/M_s$ (kOe)	$2K_F/M_s$ (kOe)
3.5 ML Ni / 5.6 ML Fe	300	8.87	2.09	0.086	–0.039
	77	9.1	2.09	0.228	–0.042
10 ML Ni / 6 ML Fe	300	10.9	2.097	0.657	0.119
	77	12.58	2.092	1.89	0.205
10.5 ML Ni / 3.5 ML Fe	300	6.93	2.147	1.08	0.090
	77	8.79	2.147	2.69	0.126

than hard axes. However, scaling predicts correctly that the Ni FMR linewidth is much larger when the magnetization points along the [110] direction than when it points along the [100] direction. The main reason for the discrepancy in scaling of FMR linewidths can be found by a re-examination of the data. NiFe(10.5/3.5) and NiFe(10/6) have almost identical FMR linewidths along the easy axis at both room and LN_2 temperatures, see Table 5.1, whereas ΔH in a 3.5 ML thick Fe single layer is almost twice that observed in the 6 ML thick Fe single layer. Consequently the scaling law, equation (11), using the single layer iron linewidths gives appreciably different values for the FMR linewidth of the two Ni overlayers even though they have almost the same thicknesses. However, if we assume that the FMR linewidths in both the 3.5 ML and 6 ML Fe layers were identical, then the Ni linewidth follows the scaling law, see columns 8,9 in Table 5.2. Our previous measurements [4.19], carried out on single Fe layers covered by Au(001) and Ag(001) overlayers, showed that FMR linewidths are sensitive to the particular interface. It is therefore possible that FMR linewidths in Fe layers are changed by contact with the Ni layers. FMR linewidths along the hard axis are dominated by misfit dislocations and hence we expect them to obey the bilayer scaling, as is observed for the 4-fold anisotropy. However, this conclusion implies that the FMR linewidths in bilayer Fe layers are only weakly dependent on their thickness, contrary to the behavior of individual Fe layers in contact with Ag or Au.

We tried to observe the FMR and BLS resonance signals in the single 10 ML thick "bcc Ni" layer epitaxially grown on Ag(001) substrate, sample Ni(10), but none could be observed. The Ni(10) sample was difficult to study. Its large resonance damping and small saturation magnetization reduced FMR and BLS signals close to the detectable limits. The rougher surface of single "bcc Ni" , see section 3.9, would lead to a further resonance linebroadening and very likely resulted in our inability to measure its resonance peak.

For completeness, one has to entertain the idea that the reconstructed Ni is also nonmagnetic and all results are due to a possible propagation of misfit dislocations into the Fe layer. However, recent measurements [5.10] based on the intensity of the FMR signal from a

Ni/Fe bilayer with a 10 ML Ni layer have shown conclusively that the Ni in the film is magnetic with $4\pi M_S \cong 6$ kG.

It is possible that the large anisotropy that we attribute to the Ni layers is actually created in the Fe layers by the Ni overlayers. There are several arguments against this. Firstly, the bilayer scaling for the in-plane 4-fold anisotropy works if the anisotropy is attributed to the Ni. Secondly, no large anisotropies have been found to exist in pure Fe films grown by MBE on any substrate even though there are generally some degrees of lattice misfit. For example the Fe on Ag has a .8 % in-plane lattice misfit and a large vertical misfit.

We believe that the experimental results, obtained on ultrathin bilayers and Ni layers on bulk iron, strongly support our original inference: the reconstructed "bcc Ni" is magnetic and possesses a large in-plane 4-fold anisotropy.

5.7 Conclusions:

We have successfully grown epitaxial ultrathin Fe/Ni bilayers on Ag(001) bulk substrates. RHEED studies showed that Ni films less than 6 ML thick grow homomorphously in the pure bcc structure when epitaxially grown on Fe (001). Lattice reconstructions, which follow after the Ni overlayers reach a critical thickness, suggest that the equilibrium atomic spacing of the metastable "bcc Ni" does not exactly match the Fe (001) spacing.

Magnetic properties of the Fe/Ni bilayers were investigated using FMR and BLS. The lattice reconstructed Fe/Ni bilayers exhibited large in-plane 4-fold anisotropies. This is in sharp contrast with single Fe layers for which the 4-fold in-plane cubic anisotropy decreases with the Fe layer thickness and becomes negligible in 3-4 ML thick films.

The in-plane angular dependence of the FMR field and FMR linewidth helped to identify the origin of the 4-fold in-plane anisotropy. Large 4-fold anisotropies observed in Fe/Ni bilayers do not originate in the intrinsic spin-orbit contribution to the valence electron energy bands, but are a consequence of lattice reconstruction. The pure bcc Ni overlayer does not contribute to 4-fold in-plane magnetic anisotropies. In fact unreconstructed Ni layers play a very minor role in bilayer magnetic properties. We cannot say at this time whether the unreconstructed Ni layers are non-magnetic. If they have a low anisotropy they influence the bilayer magnetic properties weakly because the value of the saturation magnetization of Ni is expected to be small in comparison with that of Fe.

At clean Fe/Ni interfaces the interlayer exchange is strong and results in a tightly coupled system. A theory of exchange-coupled bilayers was formulated. It was shown that the effective fields of individual layers form a set of natural variables; the bilayer effective fields are expressed as a linear combination of the scaled effective fields of the individual layers, see equation (5.11). The scaling parameter α, for a particular layer, is given by the product of the magnetic moment per atom and the number of atomic planes in the layer. The validity of scaling is limited to the simplest interlayer interaction in which only Heisenberg-like exchange coupling plays a role. The itinerant nature of valence electrons in 3d transition metals assures that some magnetic properties are strongly affected by valence band interlayer hybridization. The compliance of bilayer magnetic properties with scaling was checked by comparison of "bcc Ni" magnetic properties obtained on different Ni/Fe bilayers. We found that the scaling in ultrathin Fe/Ni bilayers is satisfied remarkably well for the 4-fold in-plane anisotropy field at both room and LN_2 temperatures. However, the perpendicular and in-plane uniaxial anisotropies, g-factor and resonance linewidths did not satisfy the scaling law because they are strongly affected by 3d interband hybridization.

Magnetostatic and magnetoelastic energies, stored in growth defects during the Ni reconstruction, contributed to the total magnetic energies and resulted in effective fields which affected the magnetic response. It is very surprising that growth defects can create well-defined in-plane anisotropies which surpassed those originating in the spin-orbit mechanism. Apparently the defects in the (001) plane formed a "checkerboard" surface pattern. This pattern possessed the required 4-fold symmetry and therefore could be responsible for the observed 4-fold magnetic anisotropies. Furthermore, as a consequence of the scaling property, it is possible to control the strength of the 4-fold anisotropies by choice of the layer materials and thicknesses. In-plane uniaxial anisotropies were observed in all samples grown on vicinal Ag (001) substrates. The samples prepared on singular surfaces exhibited a negligible in-plane uniaxial anisotropy and therefore the in-plane uniaxial anisotropies originated in the Ag atomic steps. Other magnetic properties such as $(4\pi D_{\perp}M_S)_{eff}$, g-factor and particularly the in-plane 4-fold anisotropy are very weakly dependent on the density of atomic steps of the Ag substrates.

The ability to control quantitatively magnetic properties is one of the ultimate goals facing the magnetic community working with MBE technologies. In this respect we believe that the results of our studies on ultrathin Fe/Ni bilayers have helped to advance the atomic engineering of new magnetic structures.

References

[1.1] for example, R. Feder, editor, **Polarized Electrons at Surfaces,** World Scientific Publishing Co. Pte. Ltd., Singapore (1985).

[1.2] for example, C.L. Fu, A.J. Freeman and T. Oguchi, Phys. Rev. Lett. **54**, 2700 (1985), and references therein.

[1.3] A.S. Arrott, B. Heinrich, S.T. Purcell, J.F. Cochran and K.B. Urquhart, J. Appl. Phys. **61**, 3721 (1987).

[1.4] B. Heinrich, A.S. Arrott, J.F. Cochran, C. Liu and K. Myrtle, J. Vac. Sci. Technol. **A 4**, 1376 (1986).

[1.5] M. De Crecenzi, L. Papagno, G. Chiarello, R. Scarnozzino, E. Colavita, R. Rosei and S. Mobilio, Sol. St. Comm. **40**, 613 (1981).

[1.6] J.F. Cochran, B. Heinrich and A.S. Arrott, Phys. Rev. B **34**, 7788 (1986).

[1.7] B. Heinrich, A.S. Arrott, J.F. Cochran, S.T. Purcell, K.B. Urquhart, N. Alberding, and C. Liu, **Thin Film Techniques for Low Dimensional Structures**, eds. R.F.C. Farrow et al., Plenum Press, New York (1987), pp. 521-548.

[1.8] B. Heinrich, A.S. Arrott, J.F. Cochran, S.T. Purcell, K.B. Urquhart and K. Myrtle, J. Cryst. Growth, **81**, 562 (1987).

[1.9] S.T. Purcell, B. Heinrich and A.S. Arrott, Rapid Comm. Phys. Rev. B. **35**, 6458 (1987).

[1.10] S.T. Purcell, A.S. Arrott and B. Heinrich, J. Vac. Sci. Technol. B **6(2)**, 794 (1988).

[1.11] B.T. Jonker, K.H. Walker, E. Kisker, G.A. Prinz, and C. Carbone, Phys. Rev. Lett,. **57**, 142 (1986).

[1.12] B. Heinrich, K.B. Urquhart, A.S. Arrott, J.F. Cochran, K. Myrtle and S.T. Purcell, Phys. Rev. Lett., **59**, 1756 (1987).

[1.13] M. Stampononi, A. Vaterlaus, M. Aeschlimann, and F. Meier, Phys. Rev. Lett. **59**, 2483 (1987).

[1.14] S.T. Purcell, B. Heinrich and A.S. Arrott, J. Appl. Phys. **64**, 5337 (1988).

[1.15] B. Heinrich, S.T. Purcell, J.R. Dutcher, K.B. Urquhart, J.F. Cochhran and A.S. Arrott, Phys. Rev. B15 **38**, 879-896 (1988).

[2.1] C. Liu, **Ultrathin Metallic Films of Mn, AgMn and VMn Grown By Molecular Beam Epitaxy**, Ph.D. thesis, Simon Fraser University, (1986).

[2.2] L.E. Davis, N.C. MacDonald, P.W. Palmberg, G.E Riach and R.E. Weber, **Handbook of Auger Electron Spectroscopy**, Physical Electronics, Minnesota, (1978), and C.D. Wagner, W.M. Riggs, L.E. Davis, J.F. Moulder and G.E. Muilenberg, **Handbook of X-ray Photoelectron Spectroscopy** Physical Electronics, Minnesota, (1978).

[2.3] J.M. Van Hove, C.S. Lent, P.R. Pukite and P.I. Cohen, J. Vacuum Sci. **B1, 741** (1983).

[2.4] T. Takeuchi and S. Ikeda, Trans. ISJI **9**, 484 (1969).

[2.5] S. Kadeckova and K. Volenik, Czech. J. Phys. B **17**, 649 (1967).

[2.6] S.S. Brenner, Acta Metall. **4**, 62-74 (1956).

[2.7] R.L. Lyles, Jr., S.J. Rothman and W. Jager, Metallography **11**, 363 (1978).

[2.8] K. Urquhart, **Magnetic Propeties of Ultrathin Fe Layers Grown On Bulk Ag (001)**, Ph.D. thesis, Simon Fraser University, 1989.

[3.1] U. Berttocci, J. Electrochem. Soc. **119**, 822 (1972).

[3.2] J.W. Matthews, ed., **Epitaxial Growth B**, Academic Press, N.Y. (1975).

[3.3] A.A. Chernov, **Modern Crystallography III**, Springer Verlag, N.Y. (1984).

[3.4] J. Woltersdorf, Thin Solid Films **32**, 277 (1976).

[3.5] J.H. Van Der Merwe, **Epitaxial Growth B**, Edit. by J.W. Matthews, Academic Press (1975) chapter 6.

[3.6] D.A. Steigerwald and W.F. Egelhoff, Jr., Surf. Sci. **191**, L887 (1987).

[3.7] T. Beier, H. Jahrreiss, D. Pescia, Th. Woike and W. Gudat, Phys. Rev. Lett. **61**, 1875 (1988).

[3.8] W.F. Egelhoff, Jr. and I. Jacob, Phys. Rev. Lett. **62**, 921 (1989).

[3.9] E. Bauer, in **Techniques of Metals Research**, Edited by R.F. Bunshah (Wiley-Interscience, N.Y. (1969), Vol 2, p. 201.

[3.10] P.R. Pukite, **Reflection High Energy Electron Diffraction of Interface Formation**, Ph.D Thesis, University of Minnesota (1988).

[3.11] P.A. Maksym and J.L. Beeby, Surf. Sci. **110**, 423 (1981).

[3.12] C.J. Humphreys, Rept. Prog. Phys. **42**, 1825 (1979).

[3.13] J.M. Van Hove, P.R. Pukite, P.I. Cohen and C.S. Lent, J. Vac. Sci. Technol. A **1(2)**, 609 (1983).

[3.14] C.S. Lent and P.I. Cohen, Surf. Sci. **139**, 121 (1984).

[3.15] K.O. Legg, F. Jona, D.W. Jepsen and P.M. Marcus, Phys. Rev. B **16**, 5271 (1977).

[3.16] M. Horn and M. Henzler, J. Cryst. Growth **81**, 428 (1987).

[3.17] G.K. Binnig, H. Rohrer, Ch. Gerber and E. Stoll, Surf. Sci. **144** 321-335 (1984).

[3.18] S.T. Purcell, B. Heinrich and A.S. Arrott, Rapid Comm. Phys. Rev. B. **35**, 6458 (1987).

[3.19] T. Kaneko, M. Imafuku, C. Kokubu, R. Yamamoto and M. Doyama, J. Phys. Soc. Jap. **55**, 2903-2904 (1986).

[3.20] T. Sakamoto, H. Funabashi, K. Ohta, T. Nakagowa, N.J. Kawai and T. Kojiima, Jpn. J. Phys. **23**, L657 (1984).

[3.21] J. Aarts, W.M. Gerits and P.K. Larsen, Appl. Phys. Lett. **48**, 931 (1986).

[3.22] P.J. Dobson, B.A. Joyce, J.H. Neave and J. Zhang, J. Crystal Growth **81**, 1 (1987).

[3.23] J.M. Van Hove, C.S. Lent, P.R. Pukite and P.I. Cohen, J. Vac. Sci. Technol. **B1**, 741 (1983).

[3.24] S.V. Ghaisas and A. Madhukar, J. Vac. Sci. Technol. **B3**, 563 (1985).

[3.25] L.A. Kolodziejski, R.L. Gunshor, and N. Otsuka, B.P. Gu, Y. Hefetz and A.V. Nurmikkom, J. Crystal Growth **81**, 491 (1987).

[3.26] S.T. Purcell, A.S. Arrott and B. Heinrich, J. Vac. Sci. Technol. **B6**, 794 (1988).

[3.27] J.M. Van Hove, C.S. Lent, P.R. Pukite and P.I. Cohen, J. Vac. Sci. Technol. **B1**, 563 (1985).

[3.28] J.H. Neave, P.J. Dobson, B.A. Joyce and J. Zhang, Appl. Phys. Lett. **47**, 400 (1985).

[3.29] Y. Iimura and M. Kawabe, Japan. Appl. Phys. **25**, L81 (1986).

[3.30] A.S. Arrott, B. Heinrich and S.T. Purcell, Denver Symposium, (to be published).

[3.32] Whaley and P.I. Cohen, J. Vac. Sci. Technol. B (1988).

[3.31] Z.Q. Wang, Y.S. Li, F.Jona and P.M. Marcus, Sol. St. Com. **61**, 623 (1987).

[3.33] M.P. Seah and W.A. Dench, Surface and Interface Analysis, **1**, 1 (1979).

[3.34] L. Papagno, M. De Crescenzi, G. Chiavello, E. Colavita, R. Scarnozzino, L.S. Caputi and R. Rosei ,Surf. Sci. **117**, 525 (1982).

[3.35] A.P. Hitchcock and C.H. Teng, Surface Sci. **149**, 558 (1984) and C.H. Teng and A.P. Hitchcock, J. Vac. Sci. Technol. **A1**, 1209 (1983).

[3.36] F.W. Lytle, D.E. Sayers and E.A. Stern, Phys. Rev. **B11**, 4825 (1975) and E.A. Stern, D.E. Sayers and F.W. Lytle, Phys. Rev. **B11**, 4836 (1975).

[3.37] D.T. Jiang, N. Alberding, A.J. Seary, B.Heinrich and E.D. Crozier, Proceedings of the 5th International Conference on X-ray Absorption Fine Structure, August 1988, Seattle.

[4.1] A.G. Gurevich, **Ferrites at Microwave Frequencies**, Consultants Bureau, New York, (1963).

[4.2] S.V. Vonskovskii, (ed.), **Ferromagnetic Resonance**, Pergamon Press, London, (1965).

[4.3] J.M. Rudd, **Ferromagnetic Resonance in Nickel at Low Temperature**, M.Sc. thesis, Simon Fraser University, (1985).

[4.4] J.R. MacDonald, Proc. Phys. Soc. London **A64**, 968 (1951).

[4.5] W.F. Brown, **Micromagnetics**, Interscience Publishers, New York (1963).

[4.6] J.F. Cochran, B. Heinrich and G. Dewar, Can. J. Phys. **55**, 787 (1977).

[4.7] B. Heinrich and V.F. Meshcharyakov, Zh. Eksp. Teor. Fiz. **59**, 424 (1970), translated Sov. Phys. JETP **32**, 232 (1971).

[4.8] W.S. Ament and G.T. Rado, Phys. Rev. **97**, 1558 (1955).

[4.9] G.T. Rado and J.R. Weertman, J. Phys. Chem. Solids **11**, 315 (1959).

[4.10] J. Crangle and G.M. Goodman, Proc. Roy. Soc. London **A321**, 477 (1971).

[4.11] H. Gengnagel and U. Hofmann, Phys. Stat. Sol. **29**, 91 (1968).

[4.12] J.R. Dutcher, J.F. Cochran, B. Heinrich and A.S. Arrott, J. Appl. Phys. **64**, 6095 (1988).

[4.13] Z. Frait, ICM IV Moscow, Proc. Int. Conf. Magn. **4**, (1973).

[4.14] Y.S. Touloukian and C.Y. Ho, **Properties of Selected Ferrous Alloying Elements**, McGraw-Hill, New York, 1981.

[4.15] R. Kaul and E.D. Thompson, J. Appl. Phys. **40**, 1383 (1969).

[4.16] T. Tokunaga, J. Sci. Hiroshima Univ. Ser. **A 38**, 215 (1968).

[4.17] G. Dewar, B. Heinrich and J.F. Cochran, IEEE Trans. Mag. **16**, 660 (1980).

[4.18] M.T. Laubitz, T. Matsumura and P.J. Kelly, Can. J. Phys. **54**, 92 (1976).

[4.19] B. Heinrich, K.B. Urquhart, J.R. Dutcher, S.T. Purcell, J.F. Cochran, A.S. Arrott, D.A. Steigerwald and W.F. Egelhoff, Jr., J. Appl. Phys. **63**, 3863 (1988).

[4.20] J.G. Gay and R. Richter, J. Appl. Phys. **61**, 3362 (1987).

[4.21] Z. Frait and D. Fraitova, J. Magn. Mag. Mat. **15-18**, 1081 (1980).

[4.22] L. Kraus and Z. Frait, Czech. J. Phys. **B**, 23 (1973).

[4.23] J.F. Cochran, K. Myrtle and B. Heinrich, J. Appl. Phys. **53**, 2261 (1982),
B. Heinrich, J.F. Cochran and R. Hasegawa, J. Appl. Phys. **57**, 3690 (1985) and references therein.

[4.24] Rudd and J.F. Cochran, (private communication).

[4.25] K.B. Urquhart, B. Heinrich, J.F. Cochran, K. Myrtle and A.S. Arrott, J. Appl. Phys. Nov. (1988).

[4.26] E.P. Wohlfarth, Iron, Cobalt and Nickel, in: **Ferromagnetic Materials, Vol. 1**," E.P. Wohlfarth, ed., North-Holland, Amsterdam (1980).

[4.27] V.L. Moruzzi, P.M. Marcus, K. Schwarz and P. Mohn, Phys. Rev. B. **34**, 1784 (1986).

[4.28] A.B. Pippard, **The Dynamics of Conduction Electrons**, Gordon and Breach, New York (1964).

[5.1] J.R. Dutcher, **Brillouin Light Scattering Studies of Epitaxial Ferromagnetic Films**, Ph.D. thesis, Simon Fraser University, (1988).

[5.2] N. Raj and D.R. Tilley, Phys. Rev. B **36**, 7003 (1987).

[5.3] N.S. Almeida and D.L. Mills, (to be published).

[5.4] P.A. Grunberg, J. Appl. Phys. **57**, 3673 (1985).

[5.5] J.F. Cochran and J.R. Dutcher, J. Appl. Phys. Nov. (1988).

[5.6] K. Vayhinger and H. Kronmüller, J. Magn. and Mag. Mat. **72**, 307 (1988).

[5.7] M. Sparks, **Ferromagnetic Relaxation Theory**, McGraw-Hill, New York (1964).

[5.8] V.L. Moruzzi, P.M. Marcus, K. Schwarz and P. Mohn, Phys. Rev B **34**, 1748 (1986).

[5.9] M.J. Stowell, **Epitaxial Growth B**, Edit. by J.W. Matthews, Academic Press (1975).

[5.10] B. Heinrich (private communication).